

A Thesis Submitted for the Degree of PhD at the University of Warwick

Permanent WRAP URL:

<http://wrap.warwick.ac.uk/169282>

Copyright and reuse:

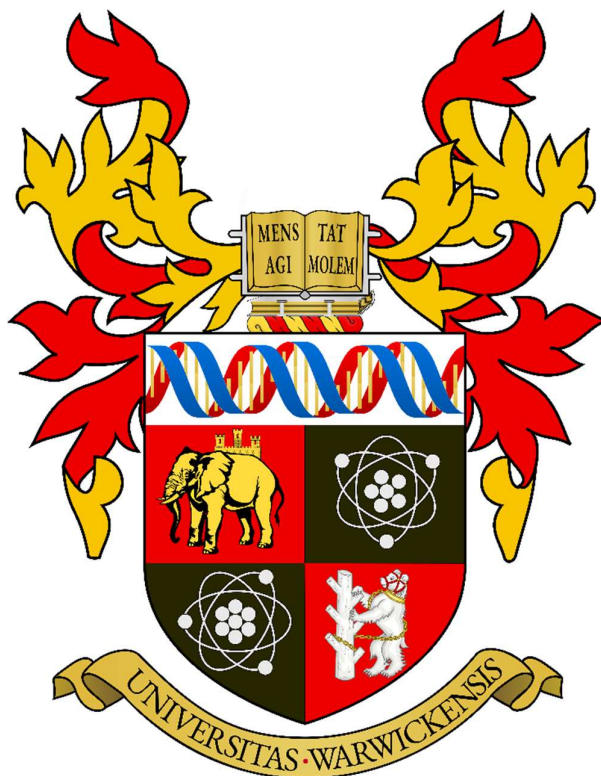
This thesis is made available online and is protected by original copyright.

Please scroll down to view the document itself.

Please refer to the repository record for this item for information to help you to cite it.

Our policy information is available from the repository home page.

For more information, please contact the WRAP Team at: wrap@warwick.ac.uk



Determination and localisation of post
translational modifications using Fourier
transform ion cyclotron resonance and two-
dimensional mass spectrometry

Johanna Paris

A thesis submitted for the degree of Doctor of Philosophy in
Analytical Chemistry

Department of Chemistry

University of Warwick

June 2022

Acknowledgement

I would like to thank my two supervisors Peter O'Connor and John O'Hara, for the opportunity of this PhD. Thank you for the help, the supervision, the advice along this scientific adventure. Under the mentoring of Peter O'Connor, I learned a lot about mass spectrometry. His deep knowledge of the field and his encyclopaedic memory of the literature as well as his eagle eye for good data and high resolution, taught me what I needed to know to better understand mass spec and conduct my research. I would like to thank the trust of John O'Hara all along the way, and as a role model for the last eight years.

I would like to thank Tomos Morgan. Thank you for the long hours of supervision and training, the fun, and the terrible humour. It has been a bless. Thanks to Anisha Harris and Bryan Marzullo, nothings work but finally we did it! Thanks to Cookson for his supervision. Thanks to Christopher Wootton, Maria Van Agthoven, Alina Thiesen, Diana Palacio Lozano and Mark Barrow for their knowledge, their help, and their work with the instrument. Thanks to all the ICR lab for the constructive talks. I would also like to thank MAS CDT, and Naomi for her help and smile.

I would like to thank UCB, and especially the characterisation group. I arrived in UK in 2014 and joining your group has been a life changer. You were the first to train me, Sarah Hamilton and Will Burkitt, and welcoming me into these ions of madness. Thanks to Andrew, you are probably the one who put the idea of a PhD in my head.

I would like to thank my family, my parents, grandparents, and siblings, for their support. A special thought to Amandine, Anna, Maeva and Arnaud, who helped me all along the way.

I would like to thank my partner in life, Adrien, for his love and support. Thanks for sharing the stress of the PhD, particularly during the pandemic, helping me every step of the way, and keeping me sane. It would not have been possible without you. And I will never be sufficiently grateful.

And finally, a last word to my brother. Now it's your turn!

Author information

and curriculum vitae

Education

2008 - Baccalaureat (A-level) in Auray, France.

2008-2011 - **BCPST** (Biology, Chemistry, Physics, and Geology) in Caen, France. Intensive program preparation for the national competitive exam for admission to engineering schools in Caen, France.

2011-2015 - **ENSTBB** – A highly selective graduate school in biotechnology in Bordeaux, France. Specialised in Biotechnology, Proteomics, Immunology, Characterisation, Chromatography, Genetics, Microbiology.

2018-2022 - **PhD in Mass spectrometry** at the University of Warwick under the supervision of Peter O'Connor, and John O'Hara (UCB).

Main focus: Development of two-dimensional mass spectrometry for the analysis of post translational modification in proteomic mixtures.

Teaching: Demonstrating - Master and Undergraduate modules (GCMS) Supervision of 2 URSS students (2 months), one Mchem Student (10 months)

Organisation: Organisation of the EU FT-ICR school at Warwick, 2019.

Organisation of MAS-CDT weekly seminars: Invitation of Speakers.

MAS_CDT Modules: Mass spectrometry, nuclear magnetic resonance, statistics, and frontier in analytical science - Postgraduate award with distinction.

Work Experience

06/12 - 08/12 - Internship at Toulouse hospital, France.

Development and validation of a RP-UHPLC method: Methotrexate quantification in blood for the laboratory of pharmacology and clinic toxicology.

09/13 - 02/14 - Internship at SANOFI PASTEUR, Marcy l'Etoile, France.

Monitoring tools for High Throughput Process Development robots: Development of RP-UHPLC and UHP-SEC methods for the quantification and characterisation of proteins.

07/14 - 02/15 - Work Placement at UCB, Slough, UK.

Development of a mass spectrometry method to quantify post translational modifications of an antibody: Manufacture of a stable isotope-labelled internal standard (¹⁵N labelling) with CHO cells, development of LC-MS/MS peptide mapping quantification method for PTMs.

08/15- 04/18 - **Scientist in bioanalytical processes** at UCB, Slough, UK.

Mass Spectrometry: LC-MS/MS QToF and Orbitrap. Analysis of antibodies. Intact mass and peptide mapping, identification of post-translational modifications, disulphides bridges.

Innovation Project: Development of mass spectrometry methods for the quantification of post-translational modifications with isotopic labelling.

Glycan Analysis: Method development, comparability studies, clone selection, cell line stability.

Project Management: Collaboration between Upstream, Downstream and Characterisation team to produce ¹⁵N antibodies. In charge of the glycan analysis, development, and submissions, for the characterisation group.

Papers

Paris, J.; Morgan, T. E.; Wootton, C. A.; Barrow, M. P.; O'Hara, J.; O'Connor, P. B. Facile determination of phosphorylation sites in peptides using two-dimensional mass spectrometry. Anal. Chem. 2020.

Paris, J.; Morgan, T. E.; Marzullo, B. P.; Wootton, C. A.; Barrow, M. P.; O'Hara, J.; O'Connor, P. B. Two-Dimensional Mass Spectrometry Analysis of IgG1 Antibodies. JASMS 2021.

Morgan, T. E.; Wootton, C. A.; Marzullo, B.; **Paris, J.;** Kerr, A.; Ellacott, S. H.; van Agthoven, M. A.; Barrow, M. P.; Bristow, A. W.; Perrier, S.; O'Connor Peter B. Characterization across a dispersity: polymer mass spectrometry in the second dimension. JASMS 2021.

Paris, J.; Theisen A.; Marzullo, B. P.; Haris A.; Morgan, T. E.; Barrow, M. P.; O'Hara, J.; O'Connor, P. B. Multimodal tandem mass spectrometry techniques for the analysis of phosphopeptides. JASMS 2022.

Conference presentations

Poster presentations

BMSS Birmingham 2015, ProteoMMX Chester 2016, Glycobiotech Berlin 2017, BMSS Manchester 2017, Uppcon Leeds 2018, BMSS Cambridge 2018, EMPW Lincoln 2018, EU FT-ICR Finland 2018, 1st ECTD Paris 2019, Native MS Oxford 2019, BMSS Manchester 2019, EU FT-ICR Warwick 2019

Oral presentations

EU FT-ICR Warwick 2019 – Two dimensional mass spectrometry of phosphopeptides.

East Midlands Proteomic Workshop 2019 – Unravel posttranslational modifications with two-dimensional mass spectrometry.

Declaration

Declaration I hereby declare that except where specifically stated/references are made to other sources, the thesis entitled 'Determination and localisation of post translational modifications using Fourier transform ion cyclotron resonance and two-dimensional mass spectrometry' is the original work of the named Author. It has been composed by myself and co-authors where stated and has not been submitted in whole or in part for any other degree, diploma, or qualification.

Johanna Paris,

June 2022

Abstract

Proteins are the building blocks of life; after translation from the genome, they are post translationally modified by enzymes and environmental conditions, which affects their functions, interactions, localisation, and degradation. The characterisation of their post translational modifications (PTMs) is crucial to understand their pivotal role in the regulation, control, and formation of the cellular environment.

The high resolution of mass spectrometry instruments is essential to accurately detect the mass change as a result of a PTM, which could be smaller than one Dalton apart. Tandem mass spectrometry is one of the fundamental methods to localise PTM(s) in proteins and to distinguish between proteoforms. Fragmentation can be performed by the collision of gases, the capture or collision of electrons, and the absorption of photons, through various dissociation mechanisms, giving complementary information on the molecule of interest.

Analysing post translational modifications in complex mixtures such as a proteomics sample is challenging, but possible via data dependant or data independent approaches. The samples are often chemically or enzymatically digested into peptide mixtures, which are separated via liquid chromatography and then analysed in the mass spectrometer. Two-dimensional mass spectrometry (2DMS) is an alternative tool which allows the characterisation of complex mixtures without the need of extensive peptide separations, and isolation of the molecules of interest in the mass spectrometry instrument.

This thesis focuses on the method development and applications of high-resolution mass spectrometry and two-dimensional mass spectrometry in the analysis of proteomics samples and post translational modifications characterisation. Fragmentations of phosphopeptides were achieved with collision gas, electrons, and photons and compared, in a high-resolution instrument. Two-dimensional mass spectrometry applications in the analysis of proteomics samples were developed using the specifics of the 2D technique: the neutral loss lines and the 3D resolution. One of the main breakthroughs of this thesis is the use of 2DMS to detect and localise post translational modifications in complex mixtures.

Table of Contents

ACKNOWLEDGEMENT	2
AUTHOR INFORMATION	3
DECLARATION	6
ABSTRACT	7
TABLE OF CONTENTS	8
TABLE OF FIGURES AND TABLES.....	12
ABBREVIATIONS.....	25
CHAPTER 1. INTRODUCTION	30
1.1. PROTEIN MASS SPECTROMETRY	31
1.1.1. Structure of Proteins.....	31
1.1.1.1. Sequence of amino acids	31
1.1.1.2. The structure of a protein	33
1.1.1.3. The example of the antibody	34
1.1.2. Post translational modifications	35
1.1.2.1. Phosphorylation	35
1.1.2.2. Common antibody post translational modifications	37
1.2. PROTEIN MASS SPECTROMETRY	40
1.2.1. Protein ionization.....	40
1.2.1.1. Matrix-assisted laser desorption ionization (MALDI)	41
1.2.1.2. Electrospray Ionization (ESI)	42
1.2.2. Transfer of ions and quadrupole isolation	44
1.2.3. Fourier Transform Ion Cyclotron Resonance Mass Spectrometry.....	47
1.2.3.1. Cyclotron motion	47
1.2.3.2. Trapping motion.....	48
1.2.3.3. Magnetron Motion	49
1.2.3.4. Ion motion in the ICR cell.....	50
1.2.3.5. Ion excitation	51
1.2.3.6. Ion detection.....	54
1.2.3.7. FT-ICR Data.....	55

1.2.4.	Tandem mass spectrometry (MS/MS)	59
1.2.4.1.	Collision activated dissociation	60
1.2.4.2.	Electron-based dissociation (ExD)	62
1.2.4.3.	Photodissociation	64
1.2.5.	Analyzing proteins	65
1.2.5.1.	Intact mass	65
1.2.5.2.	Bottom-up vs top-down strategy	67
1.2.5.3.	Data dependent vs independent acquisition	68
1.3.	TWO-DIMENSIONAL MASS SPECTROMETRY	71
1.3.1.	Ion modulation in the ICR cell	72
1.3.2.	2DMS pulse sequence	73
1.3.3.	Visualization and modelling of the ion's modulation	75
1.3.4.	2DMS fragmentation techniques	78
1.3.5.	2DMS spectrum	82
1.3.6.	Data processing of 2DMS data	83
1.3.7.	Noise and	84
1.3.8.	Resolution in the second dimension	86
1.3.9.	Applications	88
1.3.10.	Alternative mass spectrometers for 2DMS	94
1.3.11.	References	94

CHAPTER 2. MULTIMODAL TANDEM MASS SPECTROMETRY TECHNIQUES FOR THE ANALYSIS OF PHOSPHOPEPTIDES 113

3.1.	DECLARATION	114
3.2.	ABSTRACT	116
3.3.	INTRODUCTION	116
3.4.	EXPERIMENTAL SECTION	118
2.4.1.	Material	118
2.4.2.	Ionisation	119
2.4.3.	Tandem MS parameters	119
3.5.	RESULTS AND DISCUSSION	120
2.5.1.	RDSLGP TYSSR – Phosphothreonine peptide	120
2.5.2.	EVQAEQPSSpSSPR – Phosphoserine peptide	124
2.5.3.	VIEDNEpYTAR – Phosphotyrosine peptide	129

3.6.	CONCLUSION AND OUTLOOK.....	132
3.7.	ACKNOWLEDGEMENT.....	133
3.8.	REFERENCES.....	134
3.9.	ASSIGNMENT TABLES.....	139
CHAPTER 3. FACILE DETERMINATION OF PHOSPHORYLATION SITES IN PEPTIDES USING TWO-DIMENSIONAL MASS SPECTROMETRY		155
4.1.	DECLARATION.....	156
4.2.	ABSTRACT.....	158
4.3.	INTRODUCTION.....	158
4.4.	EXPERIMENTAL SECTION.....	160
2.4.1.	Material.....	160
2.4.2.	Ionisation.....	161
2.4.3.	2DMS Sequence.....	161
2.4.4.	2DMS Workflow.....	162
4.5.	RESULTS AND DISCUSSION.....	163
2.5.1.	Modulation of intensities.....	163
2.5.2.	A 2DMS spectrum.....	164
2.5.3.	Resolution of the experiment.....	169
2.5.4.	Extraction of the neutral loss lines.....	170
2.5.5.	Cleavage coverage of the phosphopeptides.....	172
4.6.	CONCLUSION AND OUTLOOK.....	174
4.7.	ACKNOWLEDGEMENT.....	174
4.8.	REFERENCES.....	175
4.9.	ASSIGNMENT TABLES.....	179
CHAPTER 4. TWO-DIMENSIONAL MASS SPECTROMETRY ANALYSIS OF IGG1 ANTIBODIES.		186
4.1.	DECLARATION.....	187
4.2.	ABSTRACT.....	189
4.3.	INTRODUCTION.....	189
4.4.	EXPERIMENTAL SECTION.....	193
2.4.1.	Material.....	193
2.4.2.	Protein Oxidation.....	193

2.4.3.	Protein reduction, alkylation, and digestion.....	194
2.4.4.	Mass spectrometry analysis.....	194
2.4.5.	Data analysis	195
4.5.	RESULTS AND DISCUSSION	195
2.5.1.	Raw Data Modulation of intensities	195
2.5.2.	A 2DMS spectrum	197
2.5.3.	Sequence coverage	198
2.5.4.	Fragmentation efficiency	200
2.5.5.	PTM identification.....	204
2.5.6.	Resolution in 2DMS.....	206
1.5.6.1.	2DMS zoom	206
1.5.6.2.	Extraction of lines	207
1.5.6.3.	3D visualization	209
1.5.6.4.	Peak picking algorithm.....	210
1.5.6.5.	Precursor view of two peptides	211
4.6.	CONCLUSION AND OUTLOOK	212
4.7.	ACKNOWLEDGEMENT	212
4.8.	REFERENCES	213
4.9.	NOMENCLATURE OF THE IGG1 PEPTIDES	220
4.10.	ASSIGNMENT TABLES.....	222
CHAPTER 5. CONCLUSION AND OUTLOOK.....		240
	CONCLUSION AND OUTLOOK	241
	THE FUTURE OF 2DMS	243

Table of Figures and Tables

Figure 1. 1: Primary structure of proteins. Blue sphere: amino acid.....	31
Figure 1. 2: Essential amino acids and their characteristics.	32
Figure 1. 3: Structure of proteins.....	33
Figure 1. 4: Disulphide bond (green square) between two cysteines (blue spheres).	33
Figure 1. 5: Structure of an IgG1 antibody. Red: light chains. Blue: heavy chains. Constant (CH) and variable (VH) heavy chain, constant (CL) and variable (VL) light chain immunoglobulin domains. Reprinted from Rouet et al ¹⁰ with permission from Copyright 2014, John Wiley and sons.	34
Figure 1. 6: Complexity of the proteome.....	35
Figure 1. 7: Phosphorylation/dephosphorylation of the serine. Structure of the three main phosphoamino acid residues.	36
Figure 1. 8: Common antibody N-glycans. Mass of the sugars: fucose (~146 Da), mannose (~162 Da), galactose (~162 Da), N-acetylglucosamine (~203 Da), sialic acid (various). Reprinted from Liu ⁵² Copyright 2015 with permission from Elsevier.....	38
Figure 1. 9: Deamidation pathway. Reprinted from Vlasak et al ⁵⁹ Copyright 2009 with permission from Elsevier.	39
Figure 1. 10: pKa of charged amino acids. Numbers corresponds to pKa. Percentages corresponds to the occurrence of the amino acids in proteins.....	40
Table 1. 1: Proton affinity in peptides.....	40
Figure 1. 11: Schematic of the MALDI principle.....	41
Figure 1. 12: Diagram of an ESI source. Blue spheres: analyte.....	42
Figure 1. 13: Models of formation of ions. Blue: analyte. Grey: solvent. Adaptation. ⁷⁸ ..	43
Figure 1. 14: Schematics of the 12T solariX instrument. A: ESI source. B: glass capillary. C: Deflector plate. D, F: Ion funnels. E, G, I: skimmers. H: split octupole. J: quadrupole. K: argon. L: hexapole collision cell. M: beam valve. N: hexapole transfer optic (TOF). O: ICR cell. P: hollow electron emitting cathode. Q: lasers. R: nCl source.	44
Figure 1. 15: Electrodes in grey. Ion in orange. Trajectory of ejected ion in red. Trajectory of filtered ion in green.	45
Figure 1. 16: Matthieu diagram for the stability of ion trajectories in quadrupoles. Red line: scan line.....	46
Equation 1. 1	47

Figure 1. 17: Cyclotron motion. Reprinted Marshall and Grosshans ⁸⁶ with permission from Copyright 1991 American Chemical Society.	47
Equation 1. 2	48
Equation 1. 3	48
Equation 1. 4	48
Equation 1. 5	48
Figure 1. 18: Analyser cell schematics. Reprinted from Yukin et al ⁸⁷ with permission from Copyright 2014 Wiley Periodicals.	48
Figure 1. 19: Plot of the electric potential in the xy plane due to the trapping voltage in the z axis. The potential has its maximum in the centre of the cell, producing an outward-directed force on ions. Reprinted from Amster ⁸² with permission from Copyright 1996 John Wiley & Sons.	49
Equation 1. 6	50
Figure 1. 20: Ion motion in the ICR cell. Reprinted from Madeira et al ⁸⁹ Copyright 2012 InTech.....	50
Figure 1. 21: Ion motion in the x-y axis in (A) collision free environment and (B) under collision gas conditions. Reprinted from Amster ⁸² with permission from Copyright 1996 John Wiley & Sons.....	51
Figure 1. 22: Ion excitation in the ICR cell. E: excitation plates. D: detection plates. Reprinted from Madeira et al ⁸⁹ Copyright 2012 InTech.	52
Equation 1. 7	52
Figure 1. 23: Time domain (left) and frequency-domain (right) excitation waveform. Reprinted from Marschall et al ⁸¹ with permission from Copyright 1998 John Wiley & Sons.	53
Figure 1. 24: Excitation and detection of the ions in an ICR cell.....	54
Equation 1. 8	54
Equation 1. 9	54
Figure 1. 25: Nyquist frequency. Grey lines: sampling rate. Grey dots: data points. Blue and black lines: frequencies.....	55
Table 1. 2: Mass calibration procedures for FT-ICR MS. Reprinted from Gross et al ⁹⁴ with permission from Copyright 2004 Wiley Periodicals.....	56
Equation 1. 10	56
Equation 1. 11	57

Figure 1. 26: Representation of several processing (a) transient (b) Hanning function apodization and (c) zero-filling. Results (d) for no processing: dot dash (· - · -), zero-filling only: dash (---) and after applying Hanning function and zero filling solid (—). Reproduced from Methodologies for Metabolomics Experimental Strategies and Techniques ¹⁰² with permission of Cambridge university press through PLSclear.	58
Figure 1. 27: Localisation of the fragmentation tools in the 12T solariX instrument.	59
Figure 1. 28: Nomenclature of peptide cleavages. ¹⁰⁴	60
Figure 1. 29: Collision activated mechanism.	60
Figure 1. 30: Fragments obtained with CAD.	61
Figure 1. 31: ECD and ETD fragments.	62
Figure 1. 32: EDD fragments.	62
Figure 1. 33: Utah Washington mechanism. Reprinted from Tureček ¹²¹ with permission from Copyright 2003, American Chemical Society.	63
Figure 1. 34: Energy diagram of photodissociation mechanisms. Black lines: electronic states. Grey lines: vibrational excited states.	64
Figure 1. 35: IRMPD fragments.	65
Figure 1. 36: UVPD fragments.	65
Figure 1. 37: Intact mass of an IgG1 antibody. 0.1 g/L at 50:50 ACN:Water + 0.1% FA. 1000 acquired scans. 262K. Q1: 1200 <i>m/z</i> . CAD: 9V. In-source CAD: 80V.	66
Figure 1. 38: Intact mass of the light chain of an IgG1 antibody. 0.4g/L 30:70 ACN:Water + 0.1% FA. 100 acquired scans. 1MW, Q1: 800 <i>m/z</i> . CAD: 2V. In-source CAD: 60V.	67
Figure 1. 39: Example of an antibody digestion protocol.	68
Figure 1. 40: Illustration of few characteristics of 2DMS.	71
Figure 1. 41: ICR signals of C ₉ F ₂₀ N ⁺ from perfluorotributylamine (<i>m/z</i> 501.971) after resonant excitation. Filled circle: constant phase. Open triangles: phase shifted through 180° after 1.0 ms. Reprinted from Marshall et al. ¹⁶⁶ with permission from copyright 1984 Elsevier.	72
Figure 1. 42: Pulse Sequence developed by Gäumann et al. ¹⁶⁵	73
Figure 1. 43: (A) Modulation of the CH ₃ ⁺ , CH ₄ ⁺ and CH ₅ ⁺ species depending on t1. (B) 2DMS spectrum. Reproduced from Pfändler et al ¹⁷² with permission from copyright 1988, American Chemical Society.	75

Figure 1. 44: Modulation of the ion depending on the phase of the P2 excitation. Reprinted from Guan et al ¹⁷⁷ with the permission of AIP Publishing.	76
Equation 1. 12	76
Equation 1. 13	76
Figure 1. 45: Modulation of the ion depending on the phase of the excitation. Reproduced from Sehgal et al ¹⁷⁶ with permission.	77
Figure 1. 46: Pulse Sequence for the method development of 2DMS experiment and the mapping of the fragmentation zone. ¹⁸⁴	79
Figure 1. 47: Theoretical shapes of the fragmentation zones.	79
Figure 1. 48: Modulation of intensities during the IRMPD 2DMS experiment. (A) Modulation of precursors during the scans (B-spline smoothed). (B) Modulations of fragments and corresponding precursors (B-spline smoothed). Gray lines correspond to 5 periods. Reprinted with permission from Paris et al. Figure 2. ¹⁸⁵ Copyright 2021 American Chemical Society.	80
Figure 1. 49: IRMPD 2DMS experiment. Left side: Ion intensity vs. RF excitation voltage for (a) MH ³³⁺ of angiotensin, (b) the b ₉₂ ⁺ fragment, and (c) the IH ⁺ internal fragment. Right side: Ion intensity vs. encoding delay t1 for (d) MH ³³⁺ of angiotensin, (e) the b ₉₂ ⁺ fragment, and (f) the IH ⁺ internal fragment. Reproduced from Van Agthoven et al ¹⁸⁴ with permission from Copyright 2019 American Chemical Society.	81
Figure 1. 50: Schematic of a 2DMS spectrum.	82
Equation 1. 14	83
Equation 1. 15	83
Figure 1. 51: Schematics of the main noises in 2DMS. ac: autocorrelation line.	84
Figure 1. 52: 2D IRMPD mass spectrum of bovine serum albumin without (a) and with (b) urQRd denoising. Reproduced with permission from Van Agthoven et al. ¹⁸⁶	86
Figure 1. 53: Schematics of 2D mass spectra obtained in broadband (left) and narrowband mode (right). All precursors are centred in a small <i>m/z</i> window (big dots). The folding of the autocorrelation line (central diagram) does not mix the signals. Reproduced with permission from Halper et al. ¹⁹⁸	87
Figure 1. 54: Comparison between the absorption mode and magnitude mode in the precursor (A) and fragment (B) ion dimensions. Reproduced from Delsuc et al. Figures 2 and 3. ¹⁹⁶	88

Figure 1. 55: ECD 2DMS mass spectrum of the mixture of custom synthetic glycopeptides (M1: YSPTS(β -O-GlcNAc)PSK-NH ₂ , M2: SVES(β -O-GlcNAc)GSADAK-NH ₂ , M3: SVET(β -O-GlcNAc)GSADAK-NH ₂ at 1 pmol/ μ L in MeOH/water, 50:50, with 0.1% formic acid). Self-correlation line corresponds to the autocorrelation line. Reprinted with permission from Van Agthoven et al. Figure 4. ¹⁸¹ Copyright 2012 American Chemical Society.....	89
Figure 1. 56: 2D FT-ICR mass spectrum of the collagen tryptic digest mixture. Orange/yellow lines show the regions of the spectrum corresponding to the fragment ion scans in the four insets at precursor <i>m/z</i> (a) 951.81, (b) 850.41, (c) 634.34, and (d) 659.34. Reprinted from Simon et al. Figure 2. ⁶ Copyright The Royal Society of Chemistry 2016.	90
Figure 1. 57: CAD-MS/IRMPD-2DMS of ubiquitin in denaturing conditions. (a) Two-dimensional mass spectrum. (b) Extracted autocorrelation line. (c) Fragment ion scan of the ion y_{589}^+ (<i>m/z</i> 726.2838) and respective cleavage coverage. (d) Precursor ion scan of the ion y_{244}^+ (<i>m/z</i> 682.3820), constituting important information for the assignment of y ions on the autocorrelation line (b). Reprinted with permission from Floris et al. Figure 2. ²⁰⁷ Copyright 2018 American Chemical Society.	91
Figure 1. 58: Zoom of the 2DMS spectrum of the hydrogen-terminated polyacrylamide species showing the different fragment lines and the corresponding precursors to those species. Reprinted with permission from Morgan et al. Figure 4.b. ²⁰⁹ Copyright 2021 American Chemical Society.	92
Figure 1. 59: (A) The 2D-EID-MS of the 7 agrochemicals. (B) Extracted autocorrelation line. The extracted fragmentation line of the protonated (C) azoxystrobin and (D) pirimiphos-methyl species. Reprinted with permission from Marzullo et al. Figure 3. ¹⁸² Copyright 2020 American Chemical Society.	93
Figure 1. 60: (A) 2D-UVPD-MS spectrum of the 14 agrochemical mixture. (B) Extracted autocorrelation line. (C) 2D-UVPD fragmentation spectrum of azoxystrobin with the cleavage diagram. Reprinted with permission from Marzullo et al. Figure 2. ¹⁸⁰ Copyright 2021 American Chemical Society.	93
Figure 2. 1: Graphical Abstract.....	115
Figure 2. 2: NanoESI set-up.....	119
Figure 2. 3: CAD fragmentation of RDSLGP ₆ TYSSR. p: fragment with phosphate attached. ' loss of water.....	121

Figure 2. 4: IRMPD fragmentation of RDSLGPpTYSSR. p: fragment with phosphate attached. ' loss of water.....	121
Figure 2. 5: UVPD fragmentation of RDSLGPpTYSSR. p: fragment with phosphate attached. ' loss of water. " loss of two water molecules.....	122
Figure 2. 6: ECD fragmentation of RDSLGPpTYSSR. p: fragment with phosphate attached.	123
Figure 2. 7: CAD fragmentation of EVQAEQPSSpSSPR. p: fragment with phosphate attached. ' loss of water. " loss of two waters.	124
Figure 2. 8: IRMPD fragmentation of EVQAEQPSSpSSPR. p: fragment with phosphate attached. ' loss of water. " loss of two waters.	125
Figure 2. 9: UVPD fragmentation of EVQAEQPSSpSSPR. p: fragment with phosphate attached. ' loss of water. " loss of two waters.	125
Figure 2. 10: ECD fragmentation of EVQAEQPSSpSSPR. p: fragment with phosphate attached. ' loss of water.....	126
Figure 2. 11: EDD fragmentation of EVQAEQPSSpSSPR. p: fragment with phosphate attached. ': loss of water. Swirl: harmonics.....	128
Figure 2. 12: CAD fragmentation of VIEDNEpYTAR. p: fragment with phosphate attached. ': loss of water.....	129
Figure 2. 13: IRMPD fragmentation of VIEDNEpYTAR. p: fragment with phosphate attached. ': loss of water.....	130
Figure 2. 14: UVPD fragmentation of VIEDNEpYTAR. p: fragment with phosphate attached. ': loss of water. "': loss of two water molecules.....	130
Figure 2. 15: ECD fragmentation of VIEDNEpYTAR. p: fragment with phosphate attached.	131
Table 2. 1: Peaks assignment for RDSLGPpTYSSR CAD spectrum. ': loss of water. p: fragment with phosphate.	140
Table 2. 2: Peaks assignment for RDSLGPpTYSSR IRMPD spectrum. ': loss of water. p: fragment with phosphate.	141
Table 2. 3: Peaks assignment for RDSLGPpTYSSR UVPD spectrum. ': loss of water. p: fragment with phosphate.	143
Table 2. 4: Peaks assignment for RDSLGPpTYSSR ECD spectrum. p: fragment with phosphate.	144

Table 2. 5: Peaks assignment for EVQAEQPSSpSSPR CAD spectrum. '': loss of water. '': loss of two waters. p: fragment with phosphate.....	145
Table 2. 6: Peaks assignment for EVQAEQPSSpSSPR IRMPD spectrum. '': loss of water. '': loss of two waters. p: fragment with phosphate.....	146
Table 2. 7: Peaks assignment for EVQAEQPSSpSSPR ECD spectrum. '': loss of water. p: fragment with phosphate. w: z-C ₃ H ₅ NO	147
Table 2. 8: Peaks assignment for EVQAEQPSSpSSPR UVPD spectrum. '': loss of water. '': loss of two water. p: fragment with phosphate.	149
Table 2. 9: Peaks assignment for VIEDNEpYTAR CAD spectrum. '': loss of water. '': loss of two waters. ''': loss of three water. p: fragment with phosphate.	150
Table 2. 10: Peaks assignment for VIEDNEpYTAR IRMPD spectrum. '': loss of water. '': loss of two waters. ''': loss of three water. p: fragment with phosphate.....	152
Table 2. 11: Peaks assignment for VIEDNEpYTAR ECD spectrum. '': loss of water. p: fragment with phosphate.	152
Table 2. 12: Peaks assignment for VIEDNEpYTAR UVPD spectrum. '': loss of water. '': loss of two waters. ''': loss of three water. p: fragment with phosphate.....	154
Figure 3. 1: Graphical Abstract.....	157
Figure 3. 2: Fragmentation efficiency defined as $-\ln(P/F + P)$, with F being the sum of fragment abundances and P the abundance of the intact precursor. Reprinted (adapted) with permission from Correia et al. ¹¹ Copyright 2007 American Chemical Society.....	159
Figure 3. 3: NanoESI set-up.....	161
Figure 3. 4: Fundamentals of 2DMS. Illustration of the ICR Cell, 37 2DMS pulse sequence and corresponding ion motions within the ICR cell. ³⁵	162
Figure 3. 5: Modulation of intensities of the precursor Ph06 in black and in red the fragment of Ph06 corresponding to the loss of phosphate. (B-spline).....	163
Figure 3. 6: 2DMS spectrum of the phosphopeptides mixture. In pink and purple, precursor lines respectively at 3+ and 2+. In black, auto-correlation line. In blue and green, neutral loss lines.	164
Figure 3. 7: Extracted zooms of the 2DMS spectrum of [Ph09+3H] ³⁺ and [Ph04+2H] ²⁺ . 165	
Figure 3. 8: Precursors of the MS Phosphomix 1 Light Sample (A) 1D standard MS scan. (B) Extracted 2D autocorrelation line.	166

Figure 3. 9: Loss of Ph07 (A) 1D standard MS scan. (B) Extracted 2D autocorrelation line. (C) Extracted 1D scan of the 2DMS experiment (scan #224 at 4.75min). (D) Extracted 1D scan of the 2DMS experiment (scan #1004 at 21min). (E) Extracted 1D scan of the LCMS experiment (at 5min). (F) Extracted 1D scan of the LCMS experiment (at 20min).	168
Figure 3. 10: Resolution of the 2DMS experiment, zoom on [Ph01+2h] ²⁺ and extracted lines in the two dimensions.	169
Figure 3. 11: Zoom of the 2DMS spectrum, showing in purple the fragment lines of three precursors, in blue the water loss lines, and in green the phosphate loss lines. ...	170
Figure 3. 12: Extracted H ₃ PO ₄ loss lines, at 2+ and 3+.	171
Figure 3. 13: Extracted fragment line of Ph06. -w: loss of water. p: fragment containing the phosphorylation. M: ADEPpSSEESDLEID (precursor Ph06).	172
Diagram 3. 1: Cleavage diagram for Ph06. In green and bold: fragments with phosphorylation. In red: fragments without phosphate group.....	172
Table 3. 1: Observed cleavage coverage of the detected phosphopeptides by 2DMS. Green, bold: b/y fragment containing a single phosphate, Green, double lined: b/y fragment containing two phosphates, red: b/y fragment without a phosphate group, green box: localisation of the phosphate group.	173
Table 3. 2: Peaks assignment of the 1D Standard MS Scan. Internal calibration points are in bold. Absolute error is 0.154 ppm, absolute standard deviation is 0.184 ppm.	179
Table 3. 3: Peaks assignment of the extracted autocorrelation line of the 2DMS spectrum. Internal calibration points are in bold. Absolute error is 0.594 ppm, absolute standard deviation is 0.997 ppm.....	179
Table 3. 4: Peaks assignment of the extracted 2+ phosphate neutral loss (H ₃ PO ₄). Internal calibration points are in bold. Absolute error is 0.283 ppm; absolute standard deviation is 0.301 ppm.....	180
Table 3. 5: Peaks assignment of the extracted 3+ phosphate neutral loss (H ₃ PO ₄). Internal calibration points are in bold. Absolute error is 0.033 ppm; absolute standard deviation is 0.021 ppm.....	180
Table 3. 6: Peaks assignment of the extracted [Ph01+2H] ²⁺ precursor line. Ph01: VLHSGpSR. Internal calibration points are in bold. Absolute error is 0.267 ppm; absolute standard deviation is 0.288 ppm.....	180

Table 3. 7: Peaks assignment of the extracted [Ph02+2H] ²⁺ precursor line. Ph02: RSpYpSRSR. Internal calibration points are in bold. Absolute error is 0.194 ppm; absolute standard deviation is 0.087 ppm.....	181
Table 3. 8: Peaks assignment of the extracted [Ph03+2H] ²⁺ precursor line. Ph03: RDSLgPTYSSR. Internal calibration points are in bold. Absolute error is 0.678 ppm; absolute standard deviation is 0.889 ppm.....	181
Table 3. 9: Peaks assignment of the extracted [Ph04+2H] ²⁺ precursor line. Ph04: pTKLlpTQLRDAK. Internal calibration points are in bold. Absolute error is 0.459 ppm; absolute standard deviation is 0.726 ppm.	182
Table 3. 10: Peaks assignment of the extracted [Ph05+2H] ²⁺ precursor line. Ph05: EVQAEQPSSpSSPR. Internal calibration points are in bold. Absolute error is 0.497 ppm; absolute standard deviation is 0.550 ppm.	182
Table 3. 11: Peaks assignment of the extracted [Ph08+2H] ²⁺ precursor line. Ph08: FEDEGAGFEESpSETGDYEEK. Internal calibration points are in bold. Absolute error is 0.617 ppm; absolute standard deviation is 0.626 ppm.	183
Table 3. 12: Peaks assignment of the extracted [Ph06+2H] ²⁺ precursor line. Ph06: ADEPpSSEESDLEIDK. Internal calibration points are in bold. ' : water loss. Absolute error is 0.482 ppm; absolute standard deviation is 0.446 ppm.....	184
Table 3. 13: Peaks assignment of the extracted [Ph09+3H] ³⁺ precursor line. Ph09: ELSNpSPLRENSFGpSPLEFR. Internal calibration points are in bold. Absolute error is 0.668 ppm; absolute standard deviation is 0.896 ppm.	185
Table 3. 14: Peaks assignment of the extracted [Ph10+3H] ³⁺ precursor line. Ph10: SPTEYHEPVpYANPFYRPTpTPQR. Internal calibration points are in bold. Absolute error is 1.290 ppm; absolute standard deviation is 1.368 ppm.....	185
Figure 4. 1: Graphical Abstract.....	188
Figure 4. 2: Fundamentals of 2DMS. Illustration of the ICR Cell, ⁴² and 2DMS pulse sequence and corresponding ion motions within the ICR cell. ³⁷	192
Figure 4. 3: Protocol of Digestion. Red dot line: disulphide bond. Red dot: free cysteine. Blue dot: alkylated cysteine.	194
Figure 4. 4: Modulation of intensity of three different precursors during the 2DMS scans (B-spline smoothed). Grey lines correspond to 5 periods.	195

Figure 4. 5: Modulations of intensity of fragments (right) and corresponding precursors (left) during the 2DMS experiment. (B-spline smoothed). Grey lines correspond to 5 periods.	196
Figure 4. 6: Full IRMPD 2DMS spectrum of the tryptic digest of an IgG1.....	197
Figure 4. 7: Extracted autocorrelation line from the 2DMS spectrum (Figure 4.6) showing all detected precursors.....	198
Figure 4. 8: Sequence of the IgG1. Sequence coverage in blue, from the peptides observed on the autocorrelation line. Cysteine in bold. Square is the site of the N-glycosylation.	199
Figure 4. 9: Extracted m/z 904 fragment line from the 2DMS Spectrum showing the b/y fragments of HC23. ‘: loss of water. ‘’: loss of NH ₃ . 2’: loss of two water molecules.	201
Figure 4. 10: Extracted m/z 973 fragment line from the 2DMS Spectrum showing the b/y fragments of LC11. ‘: loss of water. ‘’: loss of NH ₃ . 2’: loss of two water molecules.	202
Figure 4. 11: Sequence of the IgG1. Sequence coverage in blue, obtained from the autocorrelation line. Cleavage of the b/y ions in black obtained from the fragment lines analysis. Cysteine in bold. Square is the site of the N-glycosylation.....	203
Figure 4. 12: Detection and Identification of posttranslational modifications. Extracted autocorrelation lines of the IgG1 sample and the IgG1 sample after oxidative stress, between m/z 830 and 860. 2DMS zoom into m/z 830-860. In black HC18, in blue oxidised HC18.....	204
Figure 4. 13: Detection and Identification of posttranslational modifications. Extracted fragments lines at m/z 851.4 for the oxidative sample, and m/z 835.4 for the IgG1 sample, compared to extracted 2DMS contour plot related to the species.	205
Figure 4. 14: Zoom of the m/z 839-843, m/z 833-847 region on the 2DMS spectrum, and extracted horizontal and vertical lines. HC20: purple. HC27: green. The horizontal lines on the 2DMS spectrum are every two datapoint lines and correspond to: 1, black: m/z 840.059692, 2, brown: m/z 840.527520, 3, orange: m/z 840.995870, 4, red: m/z 841.464741, and 5, pink: m/z 841.934136.....	206
Figure 4. 15: Extracted intensities of precursors (A) b7, y6, and y4 fragments of HC27. (B-D) y8, b11, and y5 fragments of HC20. (E-G) on the 5 lines marked on Figure 4.14. (+1 is the second isotope peak).	208

Figure 4. 16: Isotope envelope of b11 (A) Zoom of the 2DMS spectrum (m/z 1346-1349, m/z 840-843) showing the b11 fragment of HC20. (B) Extracted scans of the b11 fragment, across the marked lines from Figure 4.14.....	208
Figure 4. 17: 3D visualisation. (A, B) 3D plot of the two precursors. (C) Zoom showing the 2DMS resolution between the first isotope of HC20 and the second isotope of HC27.....	209
Figure 4. 18: Zoom on the 2DMS spectra. Dots represent result of the 3D peak picking algorithm. HC20 in purple. HC27 in green.	210
Figure 4. 19: Fragment ion spectra extracted from Precursor View from the two peak picked points in Figure 4.18. (A) Fragment ion spectrum from the peak picked first isotope of HC27 (dark green, circle) and from the peak picked second isotope of HC27 (light green, triangle). (B) Fragment ion spectrum from the peak picked first isotope of HC20.....	211
Table 4. 1: Light chain peptides	220
Table 4. 2: Heavy chain peptides	221
Table 4. 3: Peaks assignment for HC01 extracted fragmentation line. HC01: EVQLVESGGGLVQPGGSLR. Internal calibration points are in bold. *: not observed. ‘: loss of water.....	222
Table 4. 4: Peaks assignment for HC02 extracted fragmentation line. HC02: LSCAASGFAFSTYDMSWVR. Internal calibration points are in bold. *: not observed. ‘: loss of water.....	223
Table 4. 5: Peaks assignment for HC04 extracted fragmentation line. HC04: GLEWVATISSGGSYTYLDSVK. Internal calibration points are in bold. *: not observed. ‘: loss of water.....	224
Table 4. 6: Peaks assignment for HC06 extracted fragmentation line. HC06: FTISR. No internal calibration. *: not observed. ‘: loss of water.....	224
Table 4. 7: Peaks assignment for HC08 extracted fragmentation line. HC08: NTLYLQMNSLR. Internal calibration points are in bold. *: not observed. ‘: loss of water.	225
Table 4. 8: Peaks assignment for HC10 extracted fragmentation line. HC10: GPSVFPLAPSSK. Internal calibration points are in bold. *: not observed. ‘: loss of water	225

Table 4. 9: Peaks assignment for HC11 extracted fragmentation line. HC11: STSGGTAALGCLVK. Internal calibration points are in bold. *: not observed. †: loss of water.	226
Table 4. 10: Peaks assignment for HC17 extracted fragmentation line. HC17: THTCPPCPAPELLGGPSVFLFPPKPK. Internal calibration points are in bold. *: missing assignment. †: loss of water.	227
Table 4. 11: Peaks assignment for HC19 extracted fragmentation line. HC19: TPEVTCVVVDVSHEDPEVK. Internal calibration points are in bold. *: not observed. †: loss of water.....	228
Table 4. 12: Peaks assignment for HC20 extracted fragmentation line. HC20: FNWYVDGVEVHNAK. Internal calibration points are in bold. *: not observed. †: loss of water. ††: loss of NH ₃	229
Table 4. 13: Peaks assignment for HC23 extracted fragmentation line. HC23: VVSIVLTVLHQDWLNGKK. Internal calibration points are in bold. *: not observed. †: loss of water.....	230
Table 4. 14: Peaks assignment for HC27 extracted fragmentation line. HC27: ALPAPIEK. Internal calibration points are in bold. *: not observed. †: loss of water.	230
Table 4. 15: Peaks assignment for HC31 extracted fragmentation line. HC31: EPQVYTLPPSR. Internal calibration points are in bold. *: not observed. †: loss of water.	231
Table 4. 16: Peaks assignment for HC32 extracted fragmentation line. HC32: DELTK. Internal calibration points are in bold. *: not observed. †: loss of water.	231
Table 4. 17: Peaks assignment for HC33 extracted fragmentation line. HC33: NQVSLTCLVK. Internal calibration points are in bold. *: not observed. †: loss of water. ††: loss of NH ₃	231
Table 4. 18: Peaks assignment for HC35 extracted fragmentation line. HC35: TTPPVLDSDGSFFLYSK. Internal calibration points are in bold. *: not observed. †: loss of water.....	232
Table 4. 19: Peaks assignment for HC39 extracted fragmentation line. HC39: SLSLSPG. Internal calibration points are in bold. *: not observed. †: loss of water.	232
Table 4. 20: Peaks assignment for LC01 extracted fragmentation line. LC01: DIQMTQSPSSLSASVGDR. Internal calibration points are in bold. *: not observed. †: loss of water. <i>Italic: high ppm assignments due to overlapping of peaks</i>	233

Table 4. 21: Peaks assignment for LC02 extracted fragmentation line. LC02: VTITCK. Internal calibration points are in bold. *: not observed. ′: loss of water.	234
Table 4. 22: Peaks assignment for LC03 extracted fragmentation line. LC03: ASQNVN. Internal calibration points are in bold. *: not observed. ′: loss of water.	234
Table 4. 23: Peaks assignment for LC04 extracted fragmentation line. LC04: TVVAWYQQKPGK. Internal calibration points are in bold. *: not observed. ′: loss of water.	235
Table 4. 24: Peaks assignment for LC07 extracted fragmentation line. LC07: HTGVPSR. Internal calibration points are in bold. *: not observed. ′: loss of water.	235
Table 4. 25: Peaks assignment for LC11 extracted fragmentation line. LC11: TVAAPSVFIFPPSDEQLK. Internal calibration points are in bold. *: not observed. ′: loss of water.	236
Table 4. 26: Peaks assignment for LC12 extracted fragmentation line. LC12: SGTASVCLLNLFYPR. Internal calibration points are in bold. *: not observed. ′: loss of water.	237
Table 4. 27: Peaks assignment for LC15 extracted fragmentation line. LC15: VDNALQSGNSQESVTEQDSK. Internal calibration points are in bold. *: not observed. ′: loss of water. ′′: loss of NH ₃	237
Table 4. 28: Peaks assignment for LC16 extracted fragmentation line. LC16: DSTYLSSTLTLTK. Internal calibration points are in bold. *: not observed. ′: loss of water.	238
Table 4. 29: Peaks assignment for LC17 extracted fragmentation line. LC17: ADYEK. Internal calibration points are in bold. *: not observed. ′: loss of water.	238
Table 4. 30: Peaks assignment for LC19 extracted fragmentation line. LC19: VYACEVTHQGLSPVTK. Internal calibration points are in bold. *: not observed. ′: loss of water. ′′: loss of NH ₃	239
Figure 5. 1: Summary of 2DMS specifics useful for the analysis of proteomics samples.	242
Figure 5. 2: Number of 2DMS publications.	243

Abbreviations

2DMS two-dimensional mass spectrometry

AC alternating current

ACN acetonitrile

ADP adenosine diphosphate

AGE advanced glycation end products

AI activated ion

AI-ECD activated ion-electron capture dissociation

APCI atmospheric pressure chemical ionisation

APPI atmospheric pressure photo-ionisation

ATP adenosine triphosphate

CAD collisionally activated dissociation aka CID

CDR complementary-determining region

CEM chain ejection model

CH constant heavy chain

CID collisionally induced dissociation aka CAD

CL constant light chain

CRM chain residue model

CytC cytochrome C

DC direct current

DDA data dependant analysis

DIA data independent analysis

DMSO DimethylSulfoxide

DNA deoxyribonucleic acid

ECD electron capture dissociation

EDD electron detachment dissociation

EI electron impact / electron ionisation

EID electron-induced dissociation

ESI electrospray ionisation

ESR electron spin resonance

ETD electron transfer dissociation

ETnoD electron transfer no dissociation

eV electron volt

ExD electron-based dissociation

Fc fragment crystallisable

FcRN neonatal Fc receptor

FFT fast-Fourier transform

FT Fourier transform

FT-ICR Fourier transform-ion cyclotron resonance

FTMS Fourier transform mass spectrometry

GC gas chromatography

GCMS gas chromatography mass spectrometry

HC heavy chain

hECD hot-electron capture dissociation

hot-ECD hot-electron capture dissociation

HPLC high pressure liquid chromatography

ICP-MS inductively coupled plasma mass spectrometry

ICR ion cyclotron resonance

IEM ion ejection model

IgG immunoglobulin G

IMS ion mobility spectrometry

IR Infrared

IR-ECD infrared-electron capture dissociation

IRMPD infrared multiphoton dissociation

ISD in-source dissociation/decay

LC light chain

LC liquid chromatography

LCMS liquid chromatography mass spectrometry

LC-MS/MS liquid chromatography tandem mass spectrometry

m/z mass to charge ratio

MALDI matrix-assisted laser desorption ionisation

man5 mannose-5 glycan

MeOH methanol

MRM multiple reaction monitoring

MS mass spectrometry

MS/2DMS tandem mass spectrometry followed by 2DMS

MS/MS tandem mass spectrometry

MS3 two-stage tandem mass spectrometry

MS_n mass spectrometry with n stages

MW weighted average

MW microwave spectroscopy

nano-ESI nano-electrospray ionization

nCI negative chemical ionization

nESI nano-electrospray Ionisation

nETD negative-electron transfer dissociation

niECD negative ion- electron capture dissociation

nLC nano-liquid chromatography

NMR nuclear magnetic resonance

NOESY nuclear overhauser effect spectroscopy

PAcIFIC precursor acquisition independent from ion count

ppm part-per-million

PSD post-source decay

PTM post translational modification

RF radio frequency

RP resolving power

SORI sustained off-resonance irradiation

SORI-CAD sustained off-resonance irradiation-collisionally activated dissociation

SORI-CID sustained off-resonance irradiation-collisionally induced dissociation

SPIKE spectrometry processing innovative KErnel

SRM selected reaction monitoring

SWATH sequential window acquisition of all theoretical mass

SWIFT stored-waveform Inverse Fourier transform

SWIM stored-waveform ion modulation

ToF time of flight

urQRd uncoiled random QR denoising

UV ultraviolet

UVPD ultraviolet photodissociation

VH variable heavy chain

VL variable light chain

Vp-p voltage peak to peak

WiSIM-DIA wide selected-ion monitoring

CHAPTER 1.

Introduction: Mass spectrometry in the analysis of proteins

1.1. Protein mass spectrometry

Proteins are found in all living systems and make up over 50 percent of the dry weight of cells. They intervene in all biological functions, from the cytoskeletal structure to the transportation and storage of oxygen, electrons, and nutrients, from the production of energy to the communication within the cell and/or the organism, from the reading of the desoxyribonucleic acid (DNA) to the directed transformation of molecules and other proteins. Proteins are the building blocks of life, providing structural and functional framework for cellular life.

Understanding the functions, complexity and interactions of proteins is a step forward understanding life itself. Proteomics is the study of proteins and their interactions.^{1,2} The first proteomics experiments, in 1975, used two dimensional gel electrophoresis, which allowed the visualisation of the proteins.³⁻⁵ Since, many analytical tools have been developed to study proteomics sample. Mass spectrometry (MS) is especially a powerful tool in the analysis of proteins; MS allows the detection, identification, structure elucidation, post translational modification identification, and localisation of proteins.^{6,7}

1.1.1. Structure of Proteins

1.1.1.1. Sequence of amino acids

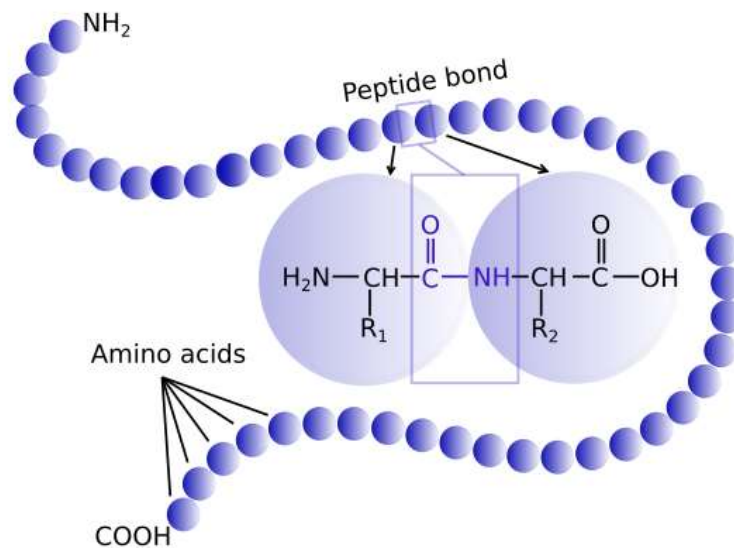


Figure 1. 1: Primary structure of proteins. Blue sphere: amino acid.

Proteins are polymers of amino acids (Figure 1.1). Each amino acid contains an amino group, a carboxyl group and a carbon linked to side chain, called radical group. Amino acids are joined together by peptide bonds, formed between the amino group of one residue and the carboxyl group of another. A polypeptide is a chain of multiple amino acids.

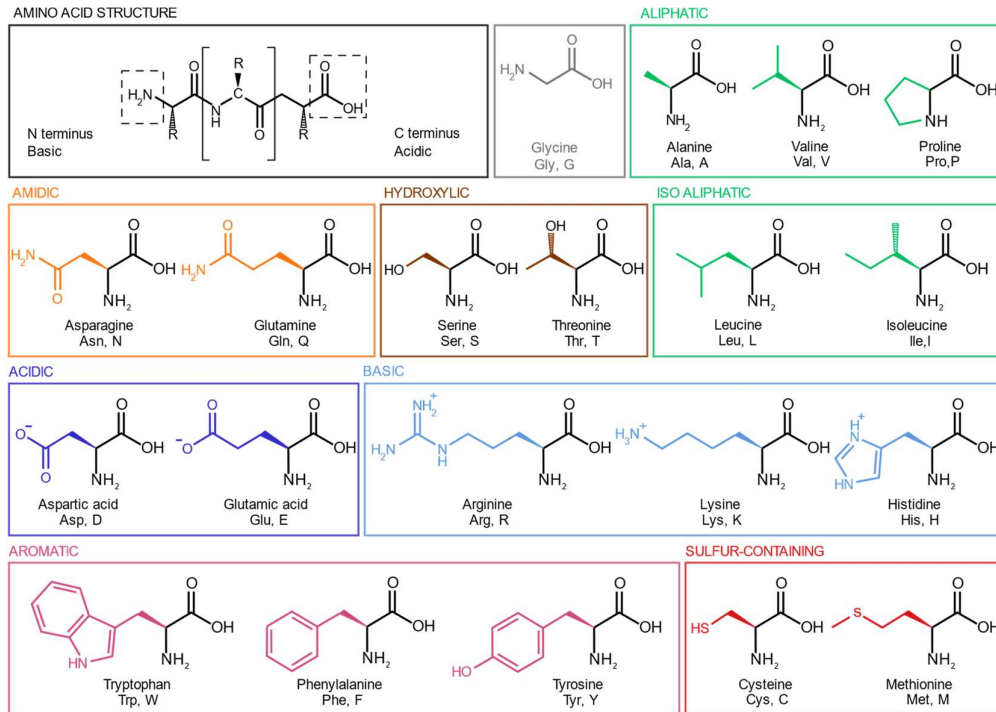


Figure 1. 2: Essential amino acids and their characteristics.

There are 20 essential amino acids with various characteristics (Figure 1.2). Two can be charged negatively, aspartic acid and glutamic acid, three can be charged positively, lysine, arginine, and histidine. The interactions between the radical groups of amino acids form the structure of the polymer chain.

1.1.1.2. The structure of a protein

The activity of proteins is dependant of their structure.

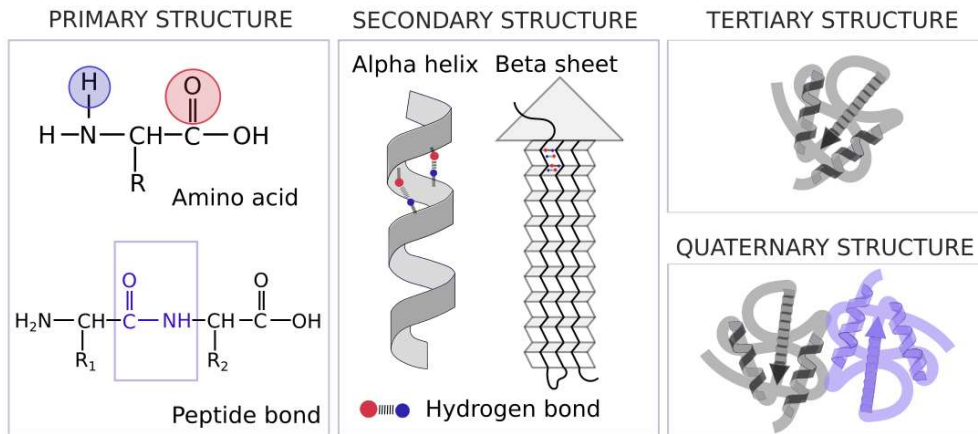


Figure 1. 3: Structure of proteins.

The sequence of amino acids constitutes the primary structure of proteins. The folding of the polypeptide chain via hydrogen bonds between the amino group and carboxyl group of amino acids forms secondary structures called alpha-helix and beta-pleated sheet. The tertiary structure corresponds to all secondary structures and hydrogen bonds, ionic bonds, salt-bridges, disulphide bonds between the side chains of amino acids, giving the 3D structure of the protein. Disulphide bonds are covalent bonds that form between cysteines (Figure 1.4).

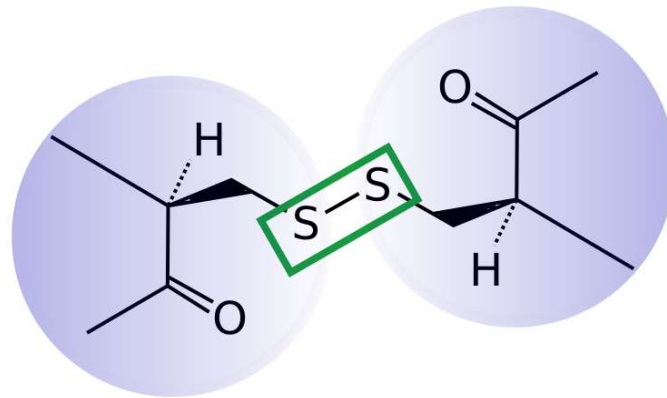


Figure 1. 4: Disulphide bond (green square) between two cysteines (blue spheres).

Some proteins are made of multiple polypeptide chains linked together via disulphide bonds and/or non-covalent bonds. The quaternary structure corresponds to the structure of such proteins.

1.1.1.3. The example of the antibody

Immunoglobulin G1 (IgG1) antibodies are complex proteins, composed of two heavy chains (HC) of ~50kDa and two light chains (LC) of ~25kDa, linked together by 4 inter-chain disulphides bonds and 12 intra-chain disulphides bonds.^{8,9}

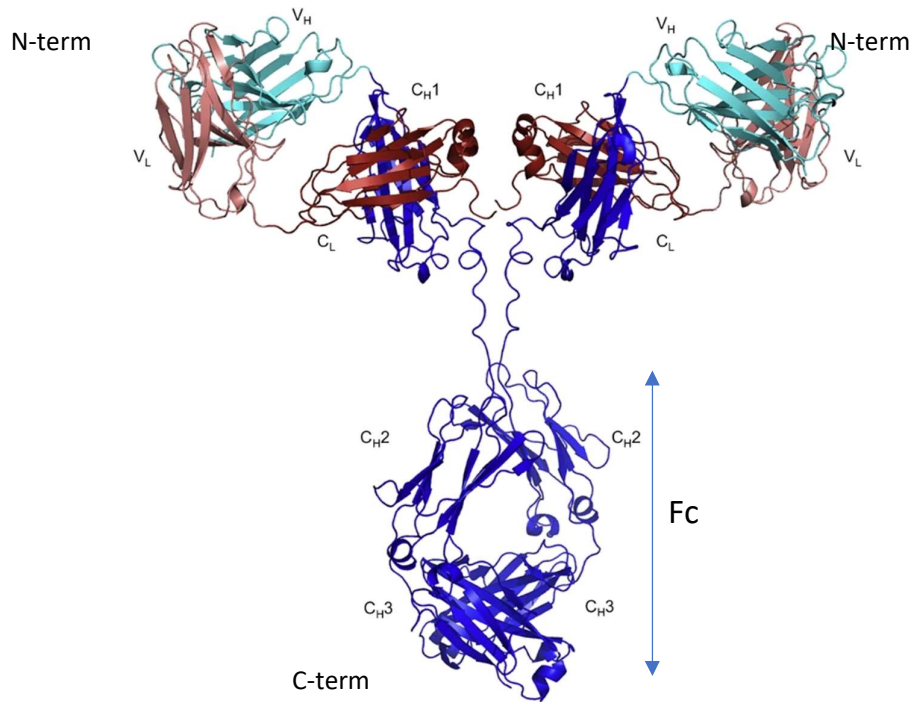


Figure 1. 5: Structure of an IgG1 antibody. Red: light chains. Blue: heavy chains. Constant (CH) and variable (VH) heavy chain, constant (CL) and variable (VL) light chain immunoglobulin domains. Reprinted from Rouet et al¹⁰ with permission from Copyright 2014, John Wiley and sons.

The chains are composed of homology regions (2 in the LC, 4 in the HC), called immunoglobulin domains, forming β -barrel structures bridged via an intra-chain disulphide bond.¹¹ Most of the sequence of IgG1 is constant within a species. However, there are three hypervariable regions in the antibody composed of six complementarity-determining regions (CDRs) near the N-terminus of the light and heavy chains.¹² The regions are brought into spatial proximity by the immunoglobulin fold, and form unique and highly specific epitope-binding paratopes.¹³

The fragment crystallisable (Fc) region interacts with activating and inhibitory FcγR receptors to mediate cellular and complement response for efficient pathogen clearance, and the neonatal receptor for IgG (FcRN) which impacts the antibody half-life in blood.¹⁴

1.1.2. Post translational modifications

Post translational modifications (PTMs) are modifications occurring on proteins after the translation. PTMs enhance biological complexity (Figure 1.6).¹⁵ They are part of the activation, structure, function, localisation, and degradation of proteins.

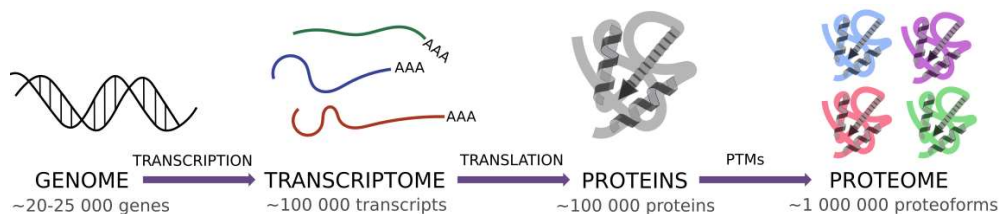


Figure 1. 6: Complexity of the proteome.

A single human gene often expresses as a family of related forms of a protein, called proteoforms. Understanding the proteome is understanding the proteoforms, and the consequences of the PTMs on the behaviour of the protein. To date, data are still being gathered for the human proteoforms.¹⁶

1.1.2.1. Phosphorylation

Thousands of proteins are expressed in mammalian cells; a third of them are thought to be phosphorylated.¹⁷ Protein phosphorylation is one of the major known signal transduction mechanisms for controlling and regulating intercellular processes.¹⁸ Phosphorylation also alters protein activity, subcellular location, degradation, and interactions with other proteins.¹⁹ Phosphorylation predominantly occurs on serine, threonine, or tyrosine, through the formation of a phosphoester linkage between the amino acid and the phosphate group at the side-chain hydroxyl oxygen on the action of a kinase (Figure 1.7). Non-canonical phosphorylation may occur on other residues such as histidine, lysine, and arginine through phosphoamidate bonds, and on aspartic acid and glutamic acid through anhydride linkages.²⁰⁻²⁴

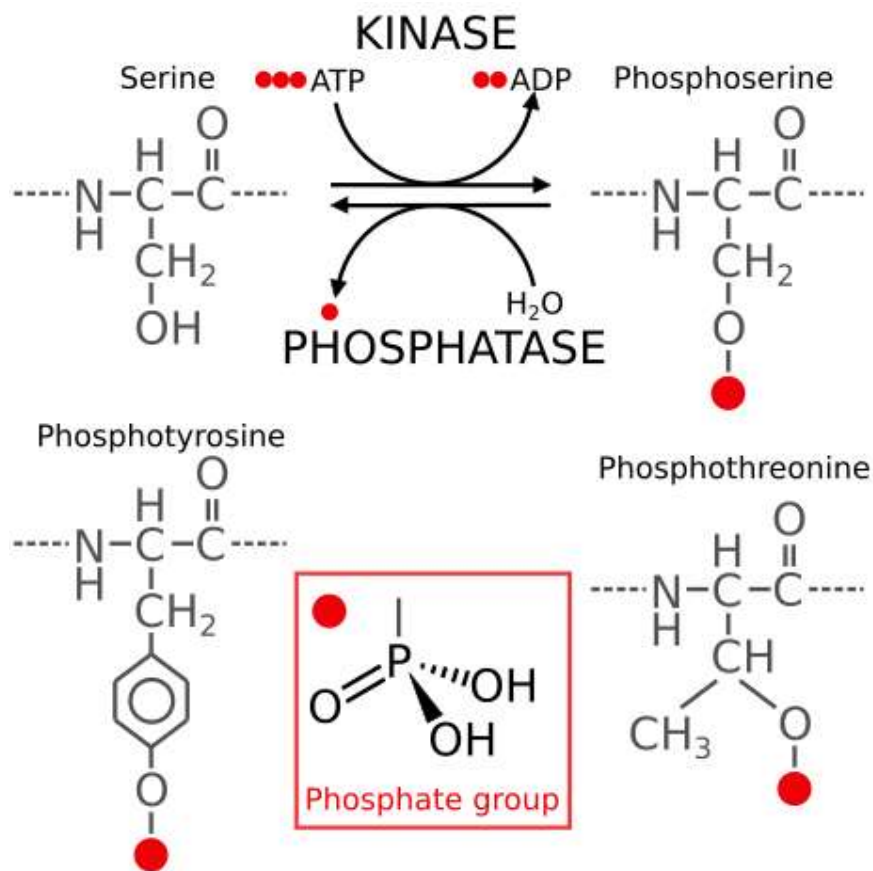


Figure 1. 7: Phosphorylation/dephosphorylation of the serine. Structure of the three main phosphoamino acid residues.

On phosphopeptides with basic residues, the phosphate group can exist in a deprotonated form and can form salt-bridges with protonated side chains.^{25, 26} Salt-bridges are electrostatic interactions between amino acids of different charges.²⁷ Basic residues are common around phosphorylation sites suggesting that salt-bridges could be part of their formation.²⁸

The phosphoryl group is a labile modification that can be lost during the mass spectrometry experiment, either by the hydrolysis of the phosphoramidate group by acidic additives frequently added to aid protonation of the analyte molecules during electrospray, or by the dissociation technique itself. High resolution mass spectrometry, or fragmentation pattern, are needed to distinguish phosphorylation to sulfation, as the mass change between the addition of the sulfonyl and the phosphoryl group is less than 9.5 mDa apart.²⁹ Loss of phosphoric acid (H₃PO₄) or metaphosphoric acid (HPO₃) can be observed in positive mode and loss of phosphite (PO₃) in negative mode. When the loss is

induced by the fragmentation techniques, the phosphopeptides can be identified by immonium ions,³⁰⁻³² or the neutral losses can be used as a signature.³³⁻³⁵ Other strategies also allow the identification of phosphopeptides by accurate mass alone, using the mass defect of the phosphorus-31 isotope, ³¹P (– 0.0262 Da)³⁶, or with the specific detection of ³¹P by inductively coupled plasma mass spectrometry (ICP-MS),³⁷ or by tagging the phosphate groups.³⁸ However, the loss of the phosphate from the sequence ions makes phosphorylation site assignment difficult. The loss depends on the fragmentation techniques, the charge states of the precursor, the residue the phosphate is linked to, and the neighbouring amino acids.^{39, 40}

1.1.2.2. Common antibody post translational modifications

Antibodies are complex proteins, with a wide range of post translational modifications.⁴¹ Some are part of their structures such as their N-glycosylation, and are the reason why therapeutic antibodies are produced in mammalian tissue cell cultures.⁴² Some can be occurring during the translation of the antibody, such as misincorporations. Some can be caused by the manufacturing process, formulation, and storage.⁴³ The PTMs modifications affect the efficacy,^{44, 45} immunogenicity,⁴⁶ stability,⁴⁷ and clearance of the antibody.⁴⁸⁻⁵¹

Common antibody PTMs include N-glycosylation, oxidation, deamidation, glycation, N-terminal pyroglutamic acid formation, and C-terminal lysine clipping.

N-glycosylation is an enzyme-mediated ATP-dependent attachment of sugars to protein and it is required for the function of antibodies. In the endoplasmic reticulum, high mannose glycans are attached to the asparagine of the consensus glycosylation motif (N-X-S/T) in the heavy chain and then matured with the stepwise addition of sugars in the Golgi apparatus via the action of enzymes. The N-glycan biosynthesis produce a N-glycan profile composed of high mannose glycans (man5) and complex glycans (such as G0F, G1F, G2F) for antibodies (Figure 1.8).⁵²

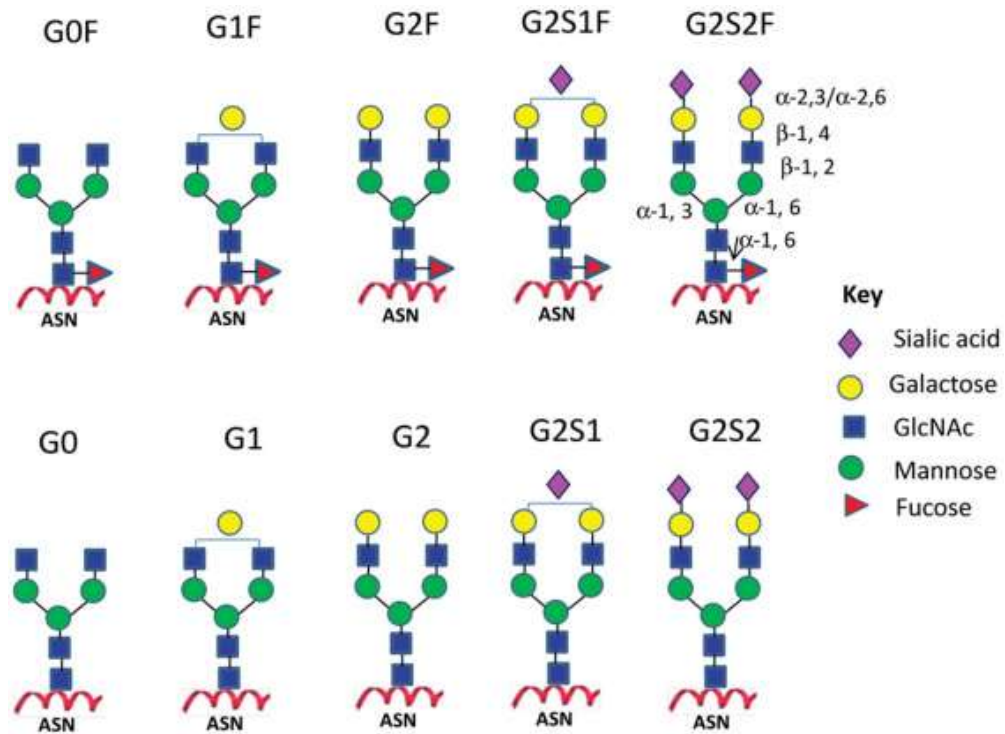


Figure 1. 8: Common antibody N-glycans. Mass of the sugars: fucose (~146 Da), mannose (~162 Da), galactose (~162 Da), N-acetylglucosamine (~203 Da), sialic acid (various). Reprinted from Liu⁵² Copyright 2015 with permission from Elsevier.

Oxidation can occur during the formulation, the storage or under the oxidative stress of the antibody. The addition of oxygen (mass shift ~16 Da) can occur on methionine⁵³ and tryptophan,⁵⁴ and, more rarely, on cysteine⁵⁵ and histidine⁵⁶ residues.

Deamidation of asparagine residues (mass shift ~1Da) is a common protein degradation pathway, and is commonly occurring at the PENNYK peptide of antibodies.^{57,58} The protonation of the peptide nitrogen bond leads to the formation of the succinimide intermediate, which is unstable and hydrolyses into a 1:3 ratio of isoaspartic acid and aspartic acid (Figure 1.9).⁵⁹

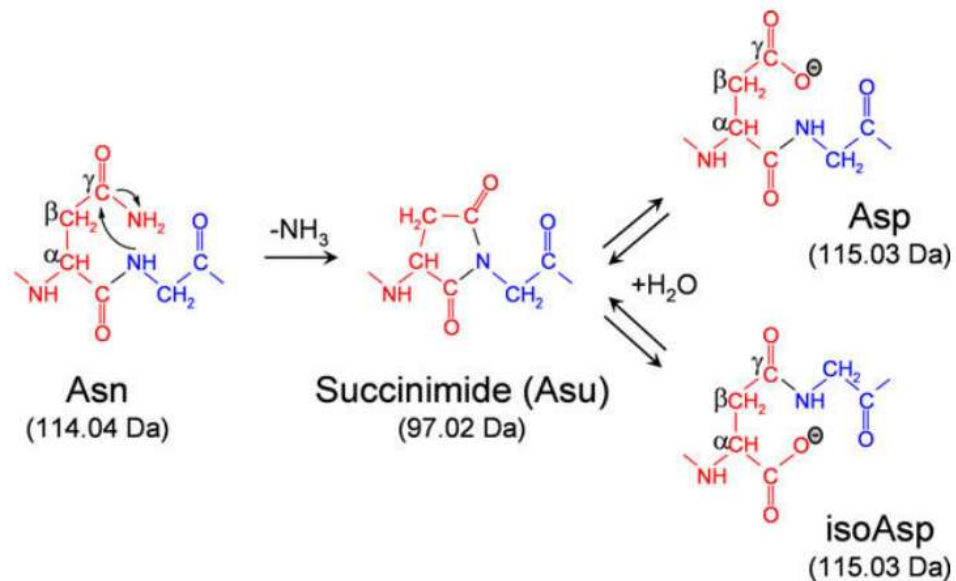


Figure 1. 9: Deamidation pathway. Reprinted from Vlasak et al⁵⁹ Copyright 2009 with permission from Elsevier.

Glycation is the covalent non-enzymatic attachment of sugars to the serine and threonine residues.⁶⁰ During production, the antibody is exposed to sugars and therefore, low levels of glycations are often detected.⁶¹ The glycation is the first step of Maillard reactions leading to advanced glycation end products (AGEs).⁶⁰

PTMs are often arising at the extremities of the antibodies.⁶² At the N-terminus glutamine and glutamic acid residues, pyroglutamic acid formation ($\sim 17/18$ Da) occurs spontaneously during production and storage. At the C-terminus of the antibody, the lysine is often clipped.⁶³ Both do not have impact on the pharmacokinetics and safety of the antibody.

1.2. Protein mass spectrometry

Mass spectrometry is an analytical tool measuring the mass-to-charge (m/z) ratio of molecules. It was first developed in 1913 by Sir J. J. Thompson⁶⁴ and Francis Aston,⁶⁵ but protein mass spectrometry waited 70 years more, and the discovery of soft ionisation sources, to be developed.

1.2.1. Protein ionization

To be analysed via mass spectrometry, molecules need to be ionised. The development of soft ionisation techniques such as matrix-assisted laser desorption ionization (MALDI) and electrospray ionisation (ESI) in the 1980's allowed the ionisation and analysis of proteins.

Proteins can be charged at their extremities (C-terminus COOH or the N-terminus NH₂) or at the side chain of the five charged amino acids. Aspartic acid and glutamic acid are negatively charged at pH7. Lysine and arginine are positively charged at pH7. Histidine is neutral at pH7.

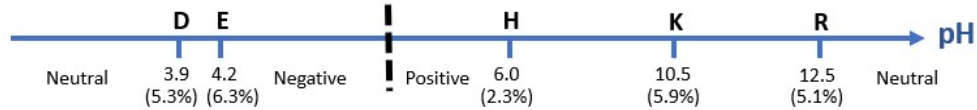


Figure 1. 10: pKa of charged amino acids. Numbers corresponds to pKa. Percentages corresponds to the occurrence of the amino acids in proteins.

When adding acidic additives in the sample, aspartic acid and glutamic acid are neutral and histidine, lysine and arginine are positives, enhancing ionisation rate. Proteins are usually analysed in positive mode, neither the less they can also be analysed in negative mode.⁶⁶

Site of protonation	Arginine	Histidine	Lysine	Backbone Amide
Proton affinity (kcal/mol)	315	290	110	~40

Table 1. 1: Proton affinity in peptides.

When ionised, the peptides are protonated first at arginine, histidine, lysine residues and then at the backbone.

1.2.1.1. Matrix-assisted laser desorption ionization (MALDI)

MALDI was first developed by Karas and Hillenkamp,^{67, 68} in 1985 they ionized amino acids⁶⁹ and, in 1987, polypeptides (mellitin MW 2843),⁶⁸ followed by Tanaka and al,⁷⁰ which ionised several proteins up to 34kDa demonstrating the possible application of MALDI in the analysis of proteins.

MALDI is a soft pulsed ionization technique, where the analyte is mixed to a matrix composed of molecules of strong absorption at the laser wavelength, dried into a plate, and then irradiated with a laser (Figure 1.11). The intense irradiation induces heating of the solid sample, and the photoionization of the matrix molecules, until the ablation of bulk portions of the mix.^{71, 72} The analyte is ionised via proton transfer from the matrix molecules. Desorption of the compounds produces analyte ions which are then accelerated due to the electrostatic field between the MALDI plate and the MS analyser.

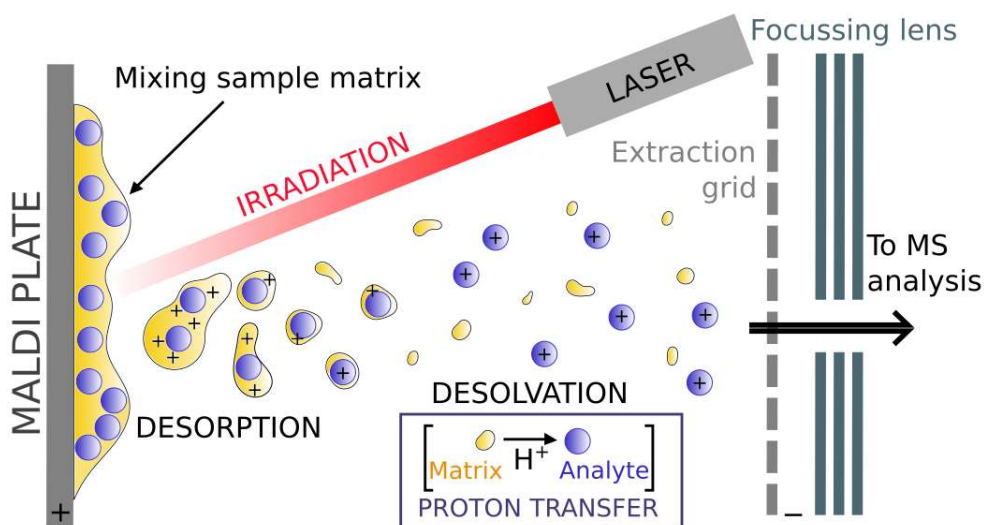


Figure 1. 11: Schematic of the MALDI principle.

MALDI is a sensitive technique. The analyte is at low concentration in the sample matrix to avoid clustering. The matrix crystals absorb most of the laser induced energy, protecting the analyte, and increases the efficiency of the energy transfer between the laser and the analyte. However, fragmentation of the ions (in-source decay (ISD)) can still occur due to internalisation of excess energy, or collision with neutral molecule in the source. If happening before or during the desorption, it is called prompt fragmentation, if

happening directly after the desorption, it is called fast fragmentation, and finally, if happening after the acceleration of the ions, it is called post-source decay fragmentation (PSD). MALDI ionisation produces mostly single-charged ions, leading to easier spectra to interpret.

1.2.1.2. Electrospray Ionization (ESI)

ESI was first developed in 1985 by John Fenn for the analysis of proteins,⁷³⁻⁷⁵ following the investigation of supersonic free jets as sources for molecular beams by Johnson in 1927.⁷⁶ The ESI process can be carried out in molecules in solution, leading to easy coupling with liquid chromatography systems.

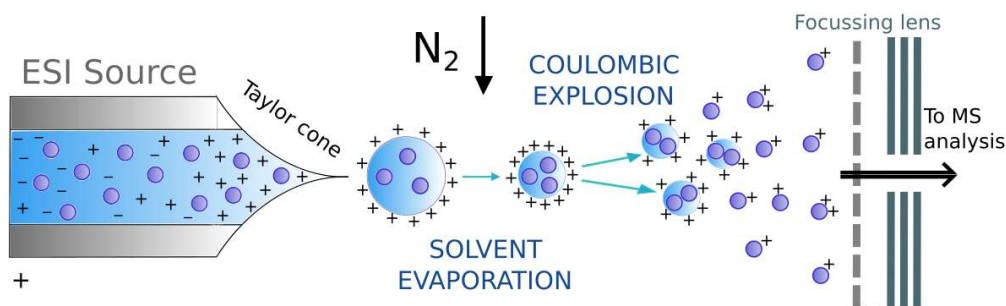


Figure 1. 12: Diagram of an ESI source. Blue spheres: analyte.

Between the ESI source and the MS analyser, a strong electric field is applied (generally with a potential difference of ~2-6 kV), generating an accumulation of charges in the ESI capillary and forming a Taylor cone. The high pressure on the surface tension leads to the production of a plume composed of droplets. The insertion of heated inert gas (usually nitrogen) or the passage through a heated capillary glass, evaporate the solvent surrounding the analyte molecules, until the ratio of charge-to-volume increases to a Rayleigh limit. The charge density of the droplet becomes greater than the stabilisation of the surface tension inducing the Coulombic explosion of the droplets. The new highly droplets evaporate further solvent, in a cycle of evaporation/explosion, until the desorption of the ions (Figure 1.12).⁷⁷

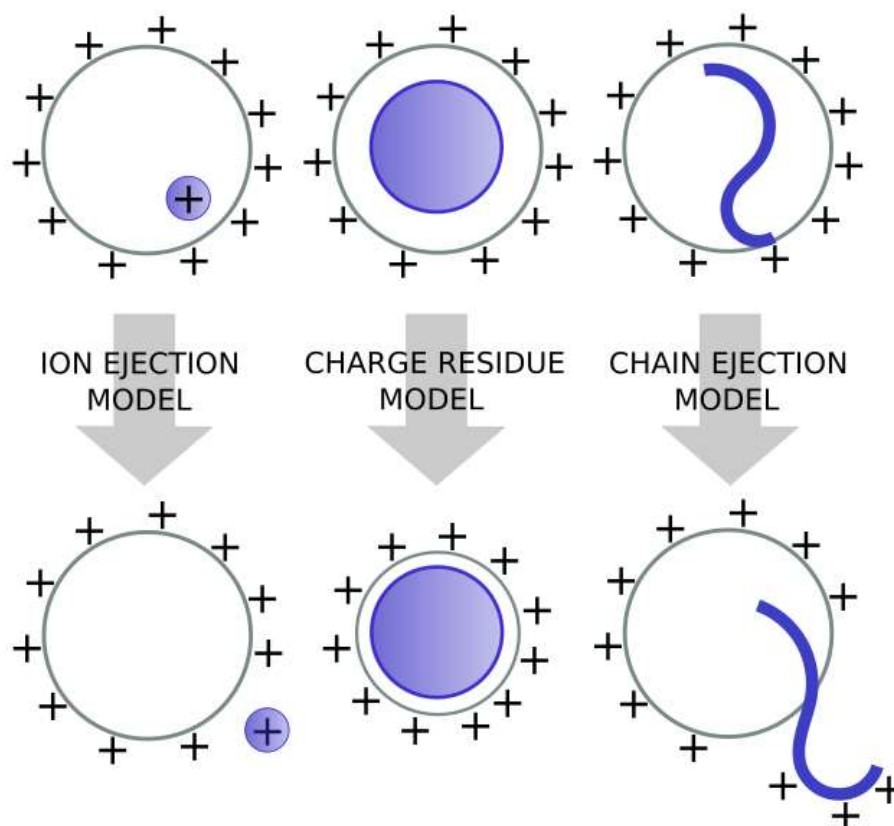


Figure 1. 13: Models of formation of ions. Blue: analyte. Grey: solvent. Adaptation from Konermann et al, 2013.⁷⁸

There are three models depending on the analyte size and shape in the droplet explaining the formation of ion (Figure 1.13).⁷⁸ In the ion ejection model (IEM), the small charged analyte is expelled out of the droplet. In the charge residue model (CRM), the progressive evaporation of the solvent around a molecule with 3D structure (globular protein) continues until full desorption, suspending the molecule in the gas phase without altering its 3D structure. In the chain ejection model (CEM), unfolded or denatured proteins are ejected out of the droplet, with charges moving from the surface of the droplet onto the chain, pushing further away the analyte out.

The ESI process reduces the energy needed to ionise the analyte, and therefore fragile and large molecules can be charged without fragmenting. Protein ions can carry a great number of charges, if the protein has enough basic or acidic amino acids,^{73, 74} leading to the possibility of electron capture fragmentation, or the analysis of large molecule in a lower dynamic range analyser.

1.2.2. Transfer of ions and quadrupole isolation

From the ionisation of the analyte to the detection of a signal, the ions are transferred, focussed, accelerated or stored, and even fragmented through the various optics. The manipulation of the ions permits to get through the different compartments of the MS analyser from high to low pressure, where higher resolution experiments can be achieved.

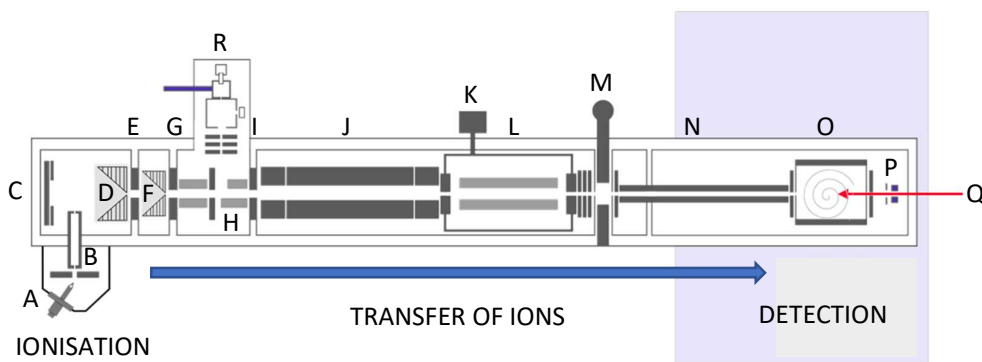
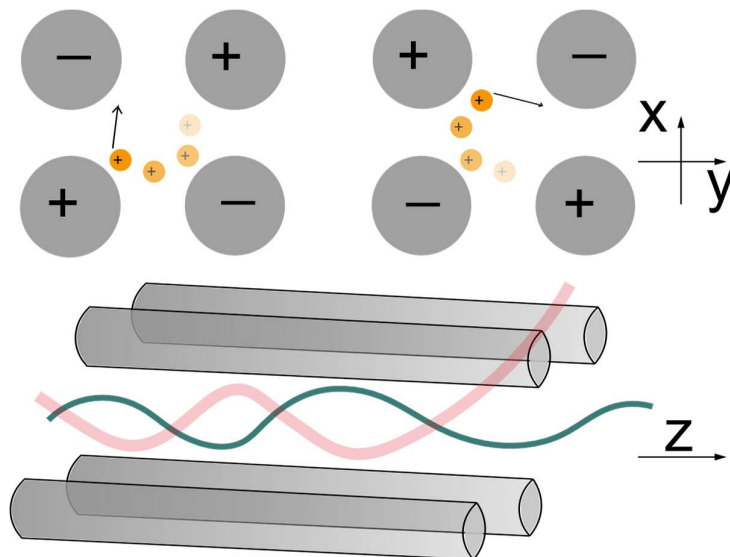


Figure 1. 14: Schematics of the 12T solariX instrument. A: ESI source. B: glass capillary. C: Deflector plate. D, F: Ion funnels. E, G, I: skimmers. H: split octopole. J: quadrupole. K: argon. L: hexapole collision cell. M: beam valve. N: hexapole transfer optic (TOF). O: ICR cell. P: hollow electron emitting cathode. Q: lasers. R: nCl source.

In the 12T solariX instrument used through this thesis, the ionisation was achieved via atmospheric pressure nano-ESI source. The voltage applied to the deflector plate pushed the charged molecules into the mass spectrometer analyser. The ions were transferred, in the front end of the mass spectrometer to the ion cyclotron resonance (ICR) cell via focussing lenses, skimmers, quadrupole and octopole optics, stabilizing the ion trajectories.

From the diverted ESI plume, ions are focussed into ion packets using skimmers and ion funnels. The voltage applied to the skimmers repels the ions outside the centre of the trajectory and increases the energy of the ions passing through the narrow orifice (~1mm). Skimmers are separating the different pumping regions; the narrow orifices allow lower vacuum pressure achievement. Higher skimmer voltage causes ion collisions helping in the desolvation of protein ions but could also fragment fragile ions. The trajectory of ions is focused via ion funnels. The alternative voltages on the coupled plates

and rings of the ion funnels attract and direct ions from a wide cloud to a condensed central cloud. The ions are accelerated through the ion funnel barrier via the voltage gradient in the front end.



**Figure 1. 15: Electrodes in grey. Ion in orange. Trajectory of ejected ion in red.
Trajectory of filtered ion in green.**

Ions are transported, stored, and filtered in the front end via multipoles. Alternative polarity electrodes are used to confine the ions radially and guide them through the analyser (Figure 1.15). Electrode polarities are coupled, two by two with quadrupoles, and switched regularly. Rods with the same polarity than the ions, repel the ions, preventing their radial ejection, and then attract the ions, when the polarity is switched. The constant attraction and repulsion of the ions from the electrodes confines them at the centre of the guide. The frequency of the polarity switch and the amplitude can filter the ions depending on their m/z . Although octopoles and hexapoles are used for the transport of ions, quadrupoles allow the possibility of selective isolation of ions up to mass windows of 1Da in front of the ICR cell.^{79, 80}

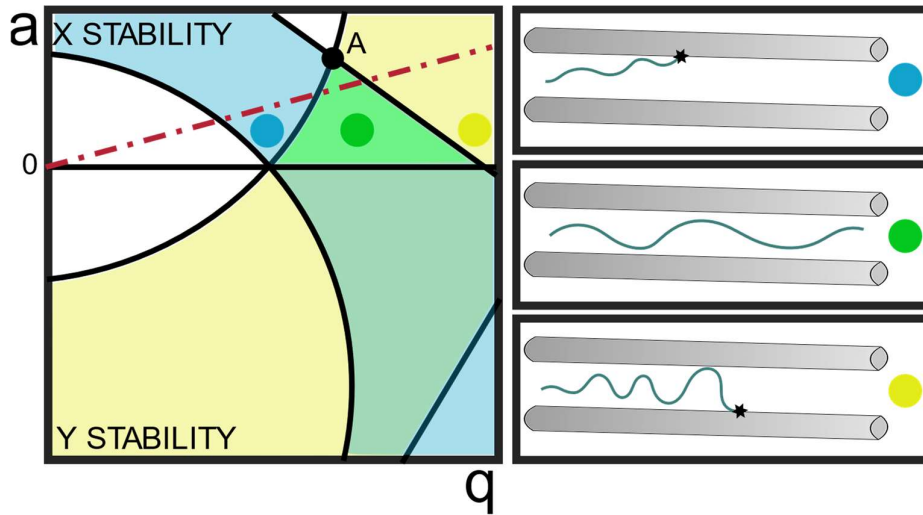


Figure 1. 16: Mathieu diagram for the stability of ion trajectories in quadrupoles. Red line: scan line.

$$a_x = -a_y = \frac{8 z U}{m r_0^2 \Omega^2} \quad -q_x = q_y = \frac{4 z V}{m r_0^2 \Omega^2}$$

Stability of ion trajectories depends on the tuning of the a and q parameters for a certain m/z . a and q are inversely proportional of m/z . a and q depend on the distance between the centre of the pole and the electrode (r_0), the RF frequency (Ω) (both stable for a giving quadrupole), the potential applied to the rodes (U), and the RF amplitude (V), (both can be modulated during experiments).

Ions in the stable a/q region (in green in Figure 1.16) have a stable trajectory through the quadrupole. Ions in the blue region have a stable amplitude trajectory but are displaced from the centre of the quadrupole; ions in the yellow region have a stable trajectory around the centre of the quadrupole but an increasing amplitude, they both hit the rods and neutralise.

When the quadrupole behaves as a mass filter, the scan line pass through the peak of the stability diagram (A). If U and V are fixed, only the ion of this m/z have a stable trajectory and pass through the quadrupole. If U and V are ramped up, with a stable U/V ratio, the ions of a wider mass-to-charge windows are filtered. If $a=0$, all ions pass through the quadrupole without mass selection.

1.2.3. Fourier Transform Ion Cyclotron Resonance Mass Spectrometry

Fourier transform ion cyclotron resonance (FT-ICR) mass spectrometry^{81, 82} was first developed by Comisarow and Marshall in 1974.⁸³⁻⁸⁵ The ions are analysed using a phenomenon known as the Lorentz force, in a penning trap enclosed at the centre of a magnet.

1.2.3.1. Cyclotron motion

In an FT-ICR cell, the ion motion is induced by the magnetic field (B) and the electric field (E). The sum of forces at the surface of an ion is named Lorentz force (F). It depends on its charge (q) and its velocity (v) arising from the interactions of the ion to the electric and magnetic field. If the ions maintain constant speed (if they encounter no collision), the magnetic field bends the ion paths into a circle.

$$F = qE + q(v \times B) \quad \text{Equation 1. 1}$$

The magnetic field is uniform, unidirectional, and homogeneous. The electrical field is from the voltage applied on the electrodes of the analyser cell. The Lorentz force is perpendicular to the magnetic field and to the velocity of the ion. It causes the ion to travel in circular orbit perpendicular to the magnetic field, called cyclotron motion.

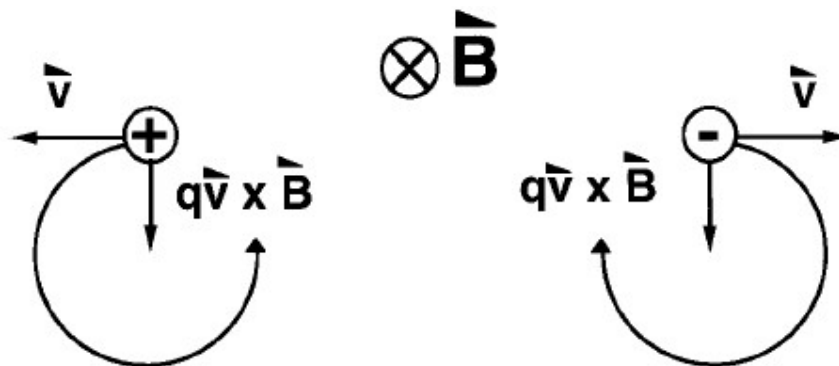


Figure 1. 17: Cyclotron motion. Reprinted Marshall and Grosshans⁸⁶ with permission from Copyright 1991 American Chemical Society.

The cyclotron frequency (f_c) of an ion is the frequency of the ion to repeat its orbit. It is independent of the velocity and therefore to its kinetic energy. The cyclotron frequency is used to calculate the masse-to-charge ratio.

$$f_c = \frac{qB}{2\pi m} \quad \text{Equation 1. 2}$$

All ion from the same m/z have the same ICR frequency, independent of their velocity.

$$w_c = 2\pi f_c \quad \text{Equation 1. 3}$$

$$w_c = \frac{v}{r} \quad \text{Equation 1. 4}$$

The cyclotron oscillation (w_c) depends, per definition, on the velocity and the radius of the ion. For an m/z ion in an FT-ICR cell the f_c is constant, therefore the w_c is constant. The radius of the ion depends on its velocity, and consequently to the square of its kinetic energy.

1.2.3.2. Trapping motion

The analyser cell is composed of 6 plates. Two plates are perpendicular to the magnetic field and called trapping plates. A small voltage is applied to the trapping plates creating a potential well that trap the ions into the cell. Ions undergo harmonic oscillations between the trapping plates, in the z axis. The trapping motion (w_z) depends on the trapping voltage (V) and the geometry of the cell (α and a are respectively measures of shape and size of the trap).

$$w_z = \sqrt{\frac{2qV\alpha}{ma^2}} \quad \text{Equation 1. 5}$$

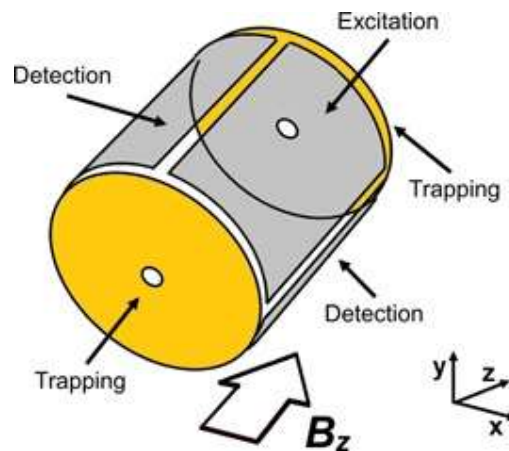


Figure 1. 18: Analyser cell schematics. Reprinted from Yulin et al⁸⁷ with permission from Copyright 2014 Wiley Periodicals.

1.2.3.3. Magnetron Motion

The magnetic field confined the ions radially; however, the electric field generated by the trapping plates generates the magnetron motion.

In the z-axis, the electric potential induced at the trapping plates extends to the centre of the cell (Figure 1.19). In the x and y axis, at the excitation and detection plates, the voltage is ground (0V). Since the electric field at the centre of the cell is not zero (Laplace equation),⁸⁸ ions are repelled toward lowest energy point, against the force of the magnetic field confining the ions radially, resulting in an increase of the ion orbit in the x-y plan around the z-axis.

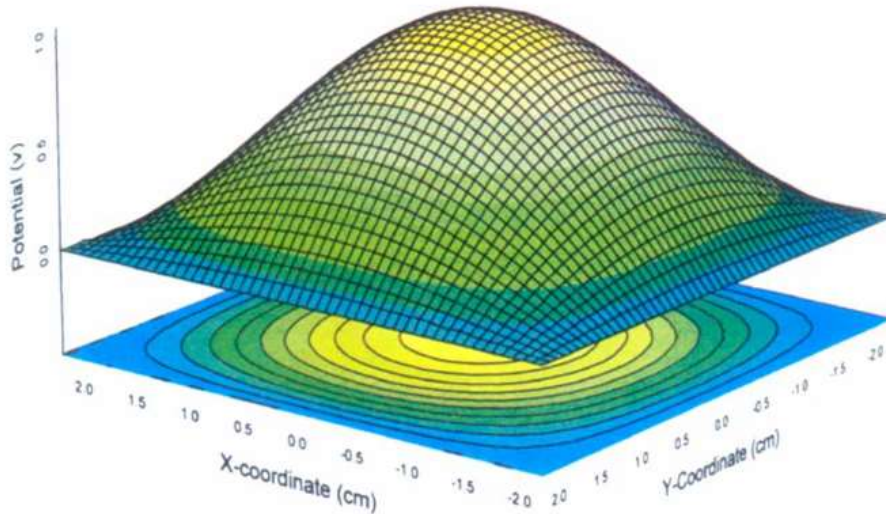


Figure 1. 19: Plot of the electric potential in the xy plane due to the trapping voltage in the z axis. The potential has its maximum in the centre of the cell, producing an outward-directed force on ions. Reprinted from Amster⁸² with permission from Copyright 1996 John Wiley & Sons.

The magnetron motion is independent to m/z , and the orbit expands slowly with time. The magnetron radius of an ion is determined by the initial displacement of the ion from the principal axis of the cell. The magnetron frequencies are lower than cyclotron

frequencies, they are function of the trapping voltage (V), the magnetic field (B), and the geometry of the cell (α and a are respectively measures of shape and size of the trap).

$$f_m = \frac{\alpha V}{2\pi a^2 B} \quad \text{Equation 1. 6}$$

The magnetron motion decreases the resolution and the mass accuracy by inducing radial ion diffusion. To minimize it, the ions are injected or created along the principal axis of the cell, parallel to the magnetic field.

1.2.3.4. Ion motion in the ICR cell

Ions motion in the ICR is the combination of the cyclotron frequency (x-y axis), magnetron motion (x-y axis), and trapping motion (z-axis).

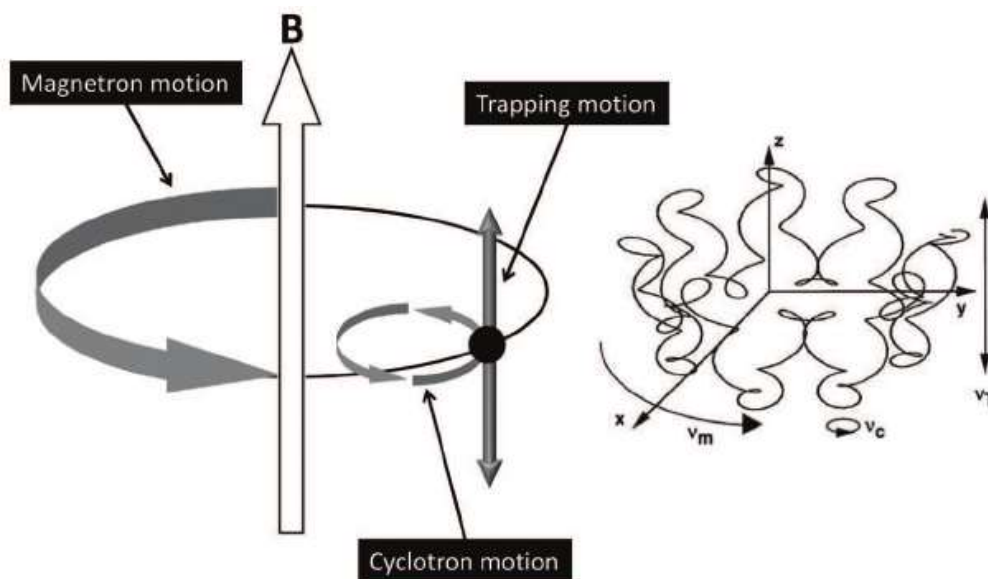


Figure 1. 20: Ion motion in the ICR cell. Reprinted from Madeira et al⁸⁹ Copyright 2012 InTech.

Ion motions can also be affected by collision with neutral molecules, or interferences with other ions which cause coulombic repulsion.

The ICR cell is maintained at 10^{-9} Torr. Under higher pressure, the collision between the ion and the neutral molecules could occur, inducing a decrease of the kinetic energy of the ion. The frictional damping force inhibits the trapping oscillation along the z-axis, decreases the radius of the cyclotron motion and increases the radius of the magnetron

motion. The ions drift away from the centre of the cell and neutralize at the detection and excitation plates.

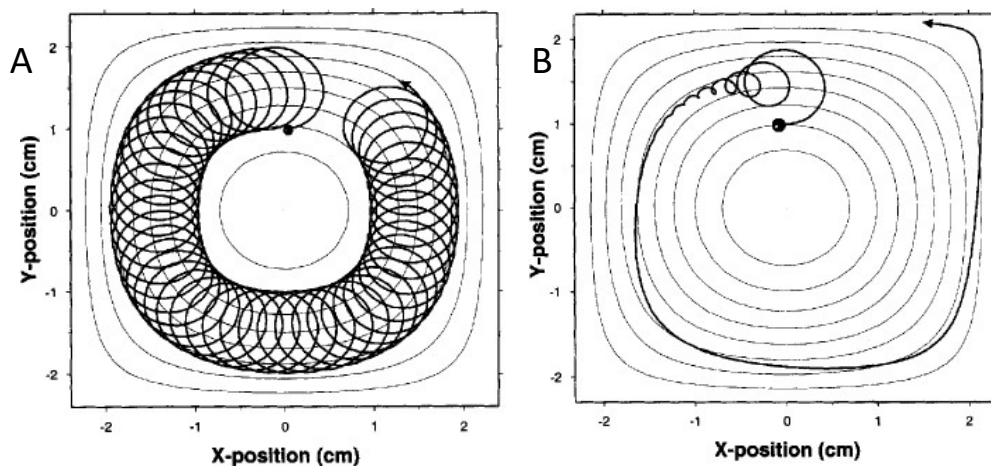


Figure 1. 21: Ion motion in the x-y axis in (A) collision free environment and (B) under collision gas conditions. Reprinted from Amster⁸² with permission from Copyright 1996 John Wiley & Sons.

Ion-ion interactions in the cell can occur, especially with a high number of ions in the cell. The coulombic repulsion between the ions broadens the ions clouds, leading to coalescence of the ions cloud of near m/z , and broadening of the signal. This phenomenon is called space charge.

1.2.3.5. Ion excitation

The ions are detected at the detection plates; however, the radius of the ions (<1mm) is small compared to the radius of the ICR cell (~3 cm), and the phase of the ions are random when injected or created in the ICR cell. The incoherent state produces destructive interference of the already low signal emitted by the ions, if they are not excited.

Resonant excitation expands the ions radius and put the ions in a coherent state, which allow the detection of a signal. To do so, a RF pulse is applied to the excitation plates.

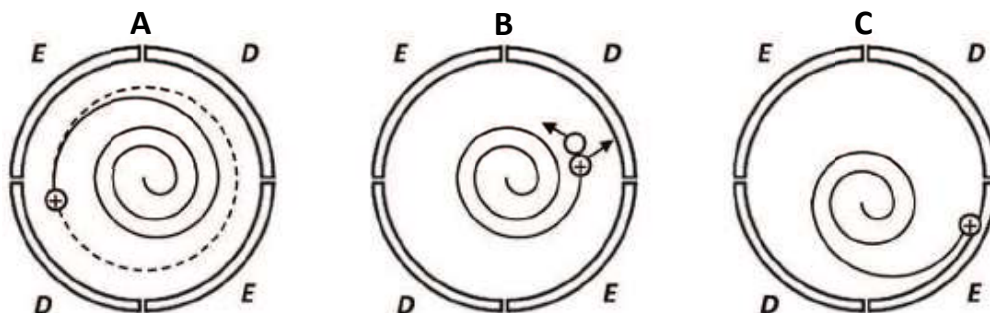


Figure 1. 22: Ion excitation in the ICR cell. E: excitation plates. D: detection plates. Reprinted from Madeira et al⁸⁹ Copyright 2012 InTech.

When the cyclotron frequency is resonant with the frequency of the RF pulse, the ions absorb the energy, move faster but at the same cyclotron frequency, and therefore at an increasing radius, until the voltage is stopped. In this case, the ions precess at the new cyclotron orbit (A). If the increase of kinetic energy is above the threshold of ion dissociation, the ions fragment (B). If the voltage is applied continuously, the ions hit the plates and get neutralised (C). The ions which are not in resonance with the excitation stay at the centre of the cell.

The post-excitation radius (r) is function of the period of excitation T_{excite} , the magnetic field (B_0) and the electric field (E_0) induced by the voltages applied at the excitation plates.

$$r = \frac{E_0 T_{excite}}{2B_0} \quad \text{Equation 1. 7}$$

r is therefore independent to m/z ; ions are excited to the same ICR orbital radius.

During single-frequency excitation, ions with close m/z can also be excited; however, doubling the duration of the excitation narrows the corresponding frequency-domain spectral width (Figure 1.23, A and B).

To collect a mass spectra containing various m/z ions, broadband excitation must be performed. The CHIRP excitation (Figure 1.23.C) is a frequency-sweep which allows the excitation of ions from a broader frequency-domain spectral width.^{85, 90} However, the excitation is non-uniform, and the selectivity is limited at the start and end frequencies of the sweep.

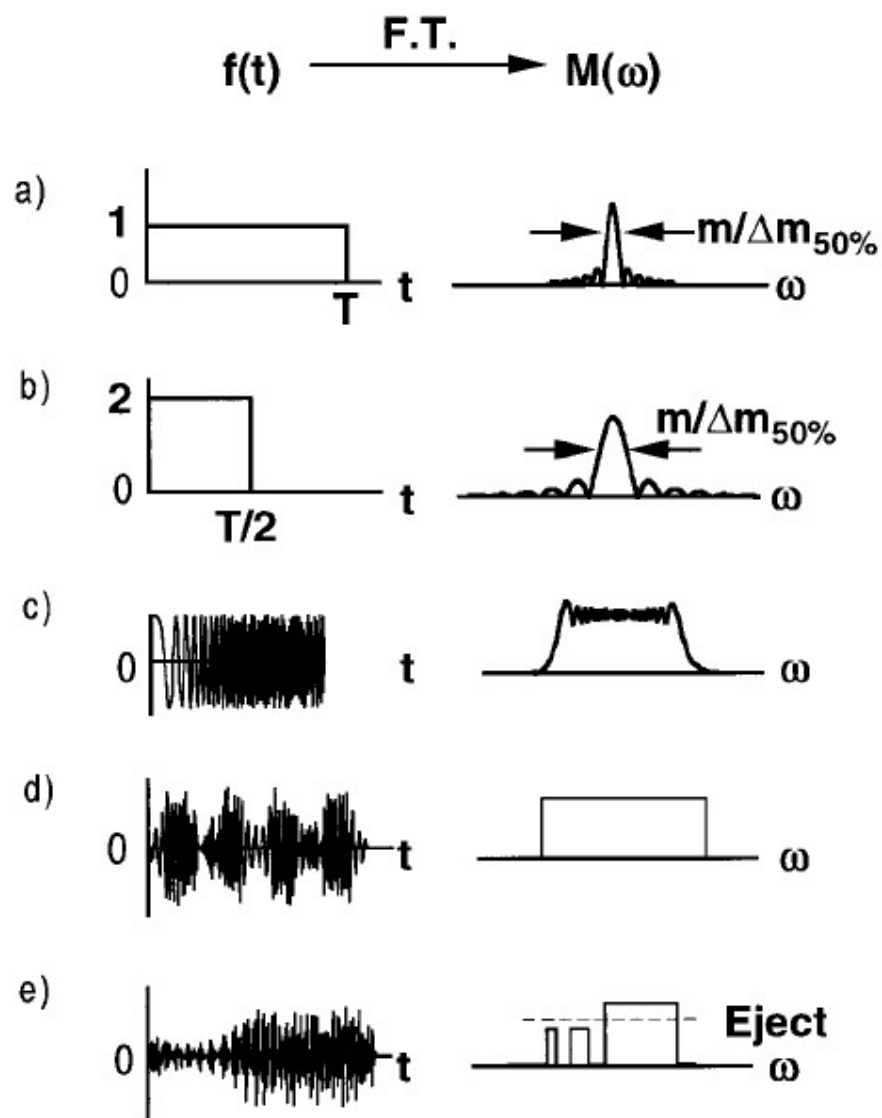


Figure 1. 23: Time domain (left) and frequency-domain (right) excitation waveform. Reprinted from Marschall et al⁸¹ with permission from Copyright 1998 John Wiley & Sons.

The alternative broadband excitation is the stored waveform inverse Fourier transform excitation (SWIFT).^{91,92} The desired excitation profile in the mass-domain is converted into a frequency-domain excitation spectrum and transformed with the inverse Fourier to generate the desired time-domain excitation waveform (Figure 1.23.D). This technique also allows a better selectivity of the excited m/z ions (Figure 1.23.E) and produce uniform excitation of the ions.

1.2.3.6. Ion detection

When excited, the ions in coherent packets evolve at their cyclotron frequencies on a wide orbit near the detection and excitation plates. When near, the ions attract electrons from the detection plates, inducing an image current, and producing an ICR signal. Therefore, the detection plates record the cyclotron frequency of the ions. The resulting measurement is amplified,⁹³ digitized and called the transient. This detection technique is powerful because the ions are not destroyed, they stay in the ICR cell and can undergo further analysis. The ions can also be ejected by applying a voltage pulse (quench pulse) to the trapping plates.

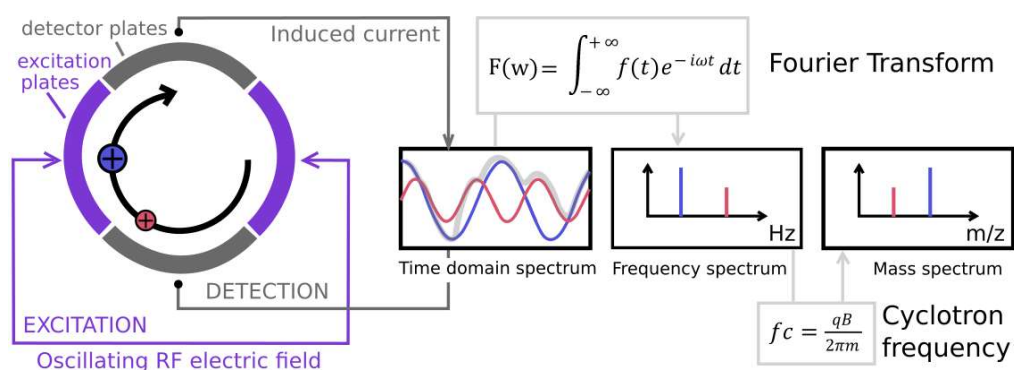


Figure 1. 24: Excitation and detection of the ions in an ICR cell.

The image current is a composite of all the different ions motion, that the Fourier transform can solve into a frequency spectrum.

$$F(\omega) = \int_{-\infty}^{+\infty} f(t)e^{-i\omega t} dt \quad \text{Equation 1. 8}$$

The data is recorded in a discrete transient at two times the Nyquist frequency. The Nyquist frequency (f_N) is the highest detected frequency correctly that can be accurately determined in an experiment and is calculated with the sampling period (Δt).

$$f_N = \frac{1}{2\Delta t} \quad \text{Equation 1. 9}$$

The Nyquist-Shannon theorem states that the sampling frequency (f_s) must be equal or greater to twice the maximum frequency of the signal to convert this signal without

loss or aliasing of the frequencies. As an illustration, at the sampling rate of the Figure 1.25, the blue frequency can be miscalculated to the black frequency.

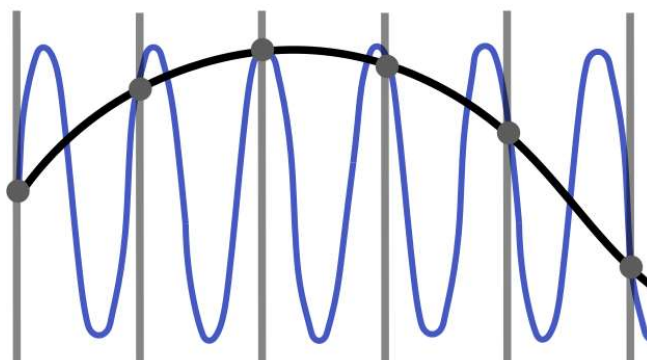


Figure 1. 25: Nyquist frequency. Grey lines: sampling rate. Grey dots: data points. Blue and black lines: frequencies.

1.2.3.7. FT-ICR Data

1.2.3.7.1. Frequency to mass conversion

The true recorded frequency of ions is called the reduced cyclotron frequency and includes the effects of the magnetron motion and the other ions within the cell, to the cyclotron frequency. To achieve high accuracy data, the instrument is calibrated daily using standard compound mixture. The frequencies are converted into m/z ratio using different calibration equations⁹⁴ and the data is often internally calibrated using the theoretical m/z of the analysed compounds.

The parameters (a, b, c) permit a better fit of the calibration curve to the data, take in account the static electric fields caused by the trapping voltages and the ion space charge, and allow high accuracy of the measurements.

$f = \frac{a}{m}$	basic law of ions in a B field
$f^2 = \frac{a}{m^2} + \frac{b}{m}$	(Beauchamp-Armstrong et al., 1969)
$f^2 = \frac{a}{m^2} + \frac{b}{m} + c$	(Ledford et al., 1980)
$f_{\text{sideband}} = \frac{a}{m}$	(Allemann et al., 1981)
$f = \frac{a}{m} + c$	(Francl et al., 1983)
$\left(\frac{M}{Z}\right) = \frac{a}{f_{\text{obsd}}} + \frac{b}{f_{\text{obsd}}^2}$	(Ledford et al., 1984b)
$f_{\text{estimated}} = f_{\text{measured}} + c(I_{\text{calibrant}} - I_{\text{analyte}})$	
$\frac{m}{z} = \frac{A}{f_{\text{estimated}}} + \frac{B}{f_{\text{estimated}}^2} + \frac{C}{f_{\text{estimated}}^3}$	(Easterling et al., 1999)
$M = \left(\frac{kB}{f_n + \Delta f}\right)n - n(M_c)$	(Bruce et al., 2000)
$\left(\frac{M}{Z}\right)_i = \frac{a}{f_{\text{obsd}}} + \frac{b}{f_{\text{obsd}}^2} + \frac{CI_i}{f_{\text{obsd}}^2}$	(Masselon et al., 2002)
$\frac{m}{z} = \frac{A}{v} + \frac{B}{v^2} + \frac{C}{v^3} + \frac{BC}{Av^4}$	(Wang et al., 1988)

Table 1. 2: Mass calibration procedures for FT-ICR MS. Reprinted from Gross et al⁹⁴ with permission from Copyright 2004 Wiley Periodicals.

1.2.3.7.2. Performance metrics

The resolving power is the ability of the mass spectrometer to resolve/separate two spectral peaks.

$$\text{Resolving power} = \frac{m}{\Delta m} \quad \text{Equation 1. 10}$$

The resolving power is calculated with m (mass to charge ratio of the peak) and Δm (width of the peak at half its height). Two peaks are considered baseline resolved when there is baseline noise between the two peaks. FT-ICR mass spectrometers are ultra-high resolving power instruments and have a consistent resolving power above 100,000 at 400 m/z , reaching millions with careful tuning.^{95, 96} However, FT-ICR MS shows a linear decrease of $1/x$ in resolving power with increasing m/z values.

High resolving power allows the fine structure elucidation of compounds, or isotope resolution, separating the isotopes of each molecule.⁹⁷ The isotope resolution allows the charge state determination of the analytes, calculated often with the isotopic spacing of the ¹²C-¹³C isotopes.

The mass accuracy is calculated for each identified peaks and is a value on how accurate the assignment is.

$$\text{mass accuracy (ppm)} = \frac{m/z(\text{experimental}) - m/z(\text{theoretical})}{m/z(\text{theoretical})} \times 10^6 \quad \text{Equation 1. 11}$$

Exact mass measurements allow the molecule identification on the m/z alone.⁹⁸ Each atom has a mass defect, which corresponds to the difference between the exact mass of the atom and the nearest-integer mass (0 Da for ¹²C, 0.007825032 Da for ¹H, 0.003074005 Da for ¹⁴N, 0.005085378 Da for ¹⁶O, etc.). Computing the exact mass of a monoisotopic peak permit to identify the elemental composition of the analysed molecule.^{95, 99} FT-ICR MS are extremely accurate instruments which can reach part-per-billion mass accuracy.¹⁰⁰

1.2.3.7.3. Processing of the data

To increase the performance metrics of a dataset, few post-acquisition manipulations are commonly done.

The data has a finite duration; when processed, the brutal start and end of the transient lead to extra small peaks at the feet of each peak of the data called Gibbs oscillations, a phenomenon known as 'causality'. These peaks contain no information and can interfere with low intensity peak identification. The apodization is the multiplication of the transient by a windowing function and is performed to smooth the end of the transient and therefore, minimize the side peaks.¹⁰¹

The resolving power is dependent of the size of the transient. The low pressure of the ICR cell allows the excited ions to travel theoretically infinitely. However, due to collisions, coulombic repulsions, or ineffective ion trapping, the transient is damped, and the length of the transient is limited. Moreover, the signal is recorded into a discrete transient, and the peaks are plotted by connecting the frequency points, leading to the distortion of the peaks shape, and possible miscalculation of the peak centroids. Zero-filling processing is

applied to double the length of the transient, adding zeros at the end of it, and therefore, doubling the sampling resolution of the FT. It adds data points in the processed spectrum, smoothing the signal and improving the accuracy of the centroid calculation and the peak fitting.

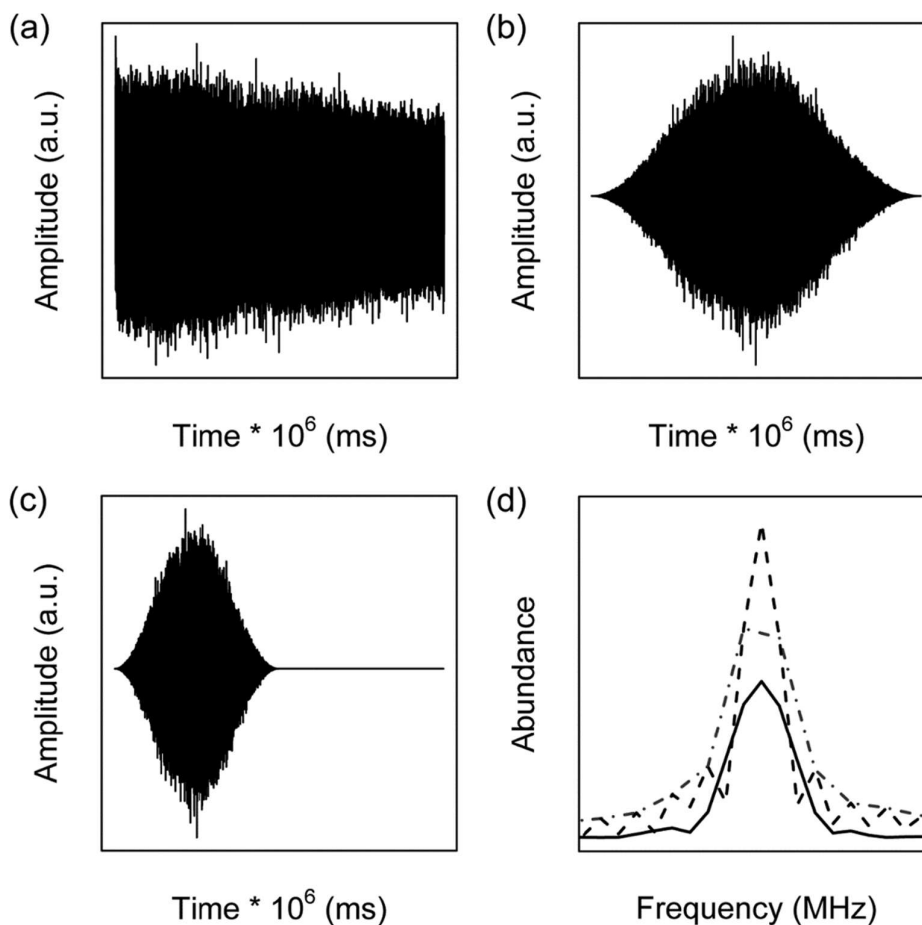


Figure 1. 26: Representation of several processing (a) transient (b) Hanning function apodization and (c) zero-filling. Results (d) for no processing: dot dash (· - · -), zero-filling only: dash (- - -) and after applying Hanning function and zero filling solid (-). Reproduced from Methodologies for Metabolomics Experimental Strategies and Techniques¹⁰² with permission of Cambridge university press through PLSclear.

1.2.4. Tandem mass spectrometry (MS/MS)

Mass spectrometers measure the m/z ratio of molecules, at high accuracy allowing their identification. In addition, they are also able to fragment ions to elucidate their structure. In a usual tandem MS instrument, the ions of interest (precursors) at a single m/z ratio are isolated and accumulated in the quadrupole and then fragmented. Current fragmentation techniques rely on the interaction of the ion to neutral molecules, electrons, and/or photons.

FT-ICR are versatile instruments, which could be implemented with various dissociation techniques. In the instrument used for collecting the data of this thesis, collision activated dissociation were possible at the front end of the mass spectrometer, via the insertion of argon in the collision cell. Electron and photon-based fragmentations were executed in the ICR cell, via the implementation of a hollow cathode and lasers.¹⁰³

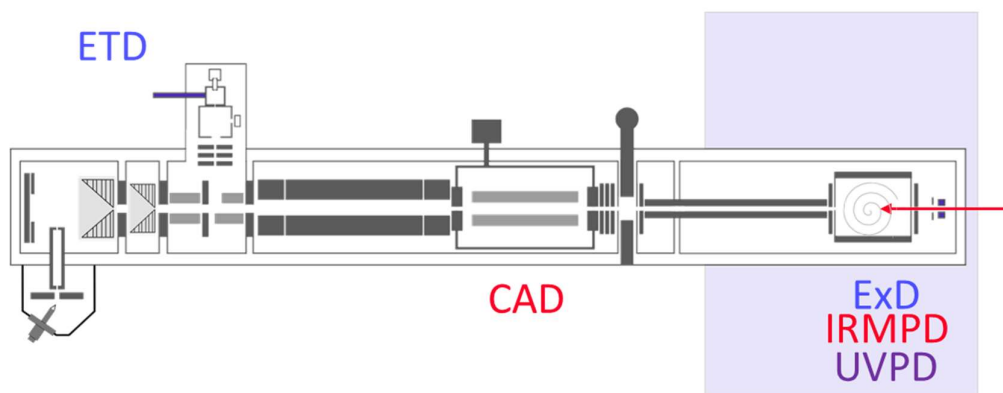


Figure 1. 27: Localisation of the fragmentation tools in the 12T solariX instrument.

During protein analysis, dissociation occurs at different bonds of the peptide backbone chain (Figure 1.28). Fragmentation at the peptide backbone give a, b, c, x, y or z ions.¹⁰⁴ Fragmentation at the sidechains of the residue give d, v or w ions.¹⁰⁵ Internal ions are the product of multiple fragmentations at the C-terminus and N-terminus. Immonium ions are single side chain only ions.

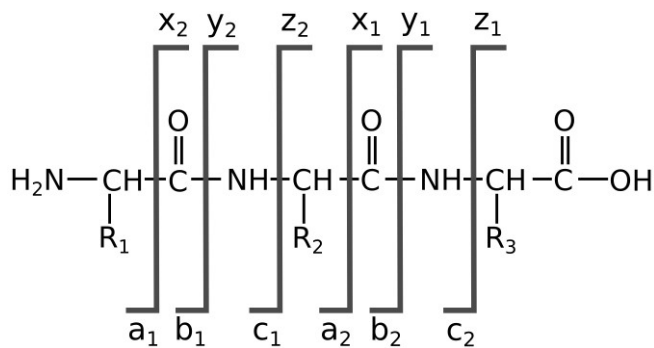


Figure 1. 28: Nomenclature of peptide cleavages.¹⁰⁴

To elucidate amino acid sequences, and PTMs localisation, the fragmentation must occur between each amino acid of the backbone, and the PTM must be retained attached. Labile post translational modifications such as phosphorylation are especially fragile and prone to fragment depending on the dissociation technique, leading to the loss of their localisation. The cleavage coverage calculates the number of separated amino acids by fragmentation compared to the number of peptide bonds, giving an estimation of the efficiency of the fragmentation.

1.2.4.1. Collision activated dissociation

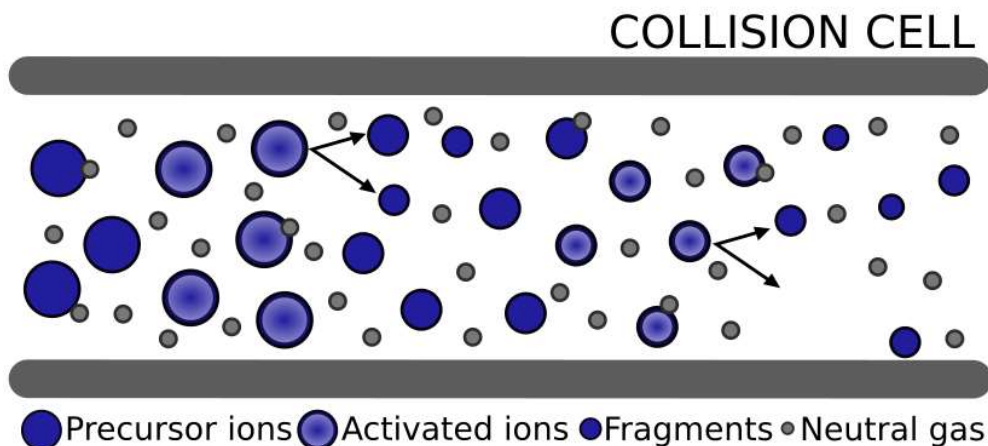


Figure 1. 29: Collision activated mechanism.

Collision activated dissociation (CAD) is the most common and widely use dissociation technique.¹⁰⁶ In a collision cell, the accelerated analyte ions collide with the neutral gas molecules (usually nitrogen or argon) (Figure 1.29). The energy of the multiple collisions is converted into internal vibrational energy. The stepwise deposition of energy activates

the analyte until a threshold of dissociation where fragmentation occurs.¹⁰⁷⁻¹⁰⁹ The fragmentation is controlled by the activation of the ions (collision voltage).

This slow fragmentation process deposits and spreads the energy throughout the molecule; moreover, the final accumulated energy is just slightly higher than the threshold; therefore, the cleavage preferentially occurs at the weakest bonds. Labile PTMs are usually cleaved first, leading to the loss of their localisation information. CAD fragments are typically b and y ions (Figure 1.30), generated by the preferential cleavage of the amide bond (the weaker in the backbone structure). Some amino acids promote specific cleavage bonds.¹¹⁰ The proline residue enhances dissociation N-terminally, yielding intense y-type ions at the X-P amide bond.¹¹¹ The aspartic acid and the glutamic acid, direct fragmentation at the C-terminal amide bond.^{110, 112, 113}

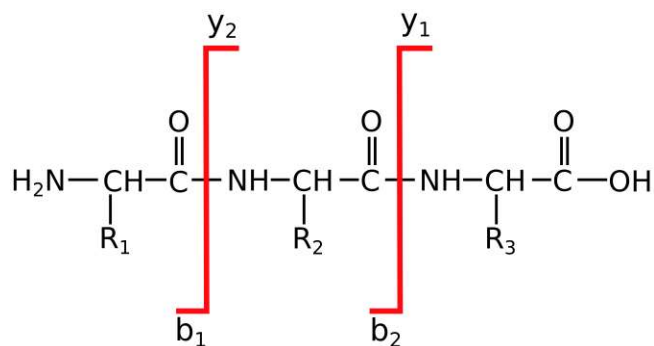


Figure 1. 30: Fragments obtained with CAD.

When ionised, the peptides are protonated first at arginine, histidine, lysine residues and then at the backbone. The mobile proton model¹¹⁰ suggests that peptide fragmentation is driven by charge-directed cleavages. If the protons are captured at the residues, the threshold of fragmentation is higher, and the peptide is likely to fragment nearby. If the protons are captured by the backbone, they are called mobile protons, and more diverse fragments are observed on the spectrum.

In the FT-ICR instrument, it is also possible to do high energy CAD, often resulting in high ion losses, or sustained off resonance irradiation collision activated dissociation (SORI-CAD).¹¹⁴ In this technique, once the pressure has been raised, the ions are accelerated in the ICR cell. They encounter the neutral gas molecules and fragment in the same way than in a collision cell. Then, the pressure is pumped out to allow the high-

resolution analysis to be done. This technique is not commonly used in current studies because it requires an increase of pressure, and consequently induces a loss in resolution.

1.2.4.2. Electron-based dissociation (ExD)

FT-ICR instruments are implemented with hollow cathode which release low energy electrons into the ICR cell. The capture of a low-energy electron by a multiply positively charged ions provoke the fragmentation, in a process called electron capture dissociation (ECD).¹¹⁵ The fragmentation occurs at the N-C α bond of the peptide backbone, producing predominantly c- and z-type product ions (Figure 1.31).¹¹⁶

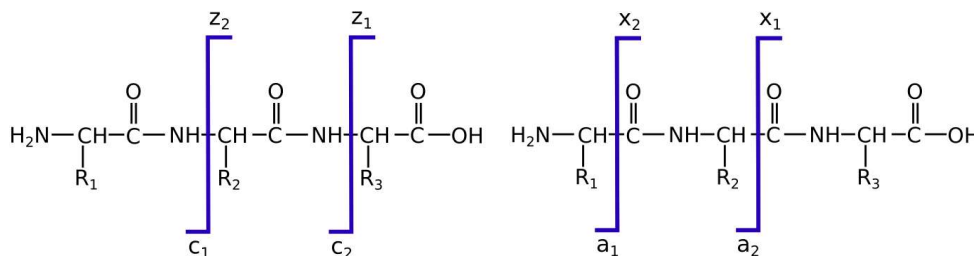


Figure 1. 31: ECD and ETD fragments.

Figure 1. 32: EDD fragments.

Electron based fragmentation (ExD) techniques are radical-driven dissociation methods; the fragmentation does not proceed via vibrational energy distribution and selectivity is based on where the electron is captured. Consequently, the analyte does not fragment at its weakest bonds and the labile groups are often retained,^{117, 118} allowing identification and localization of PTMs. The cleavage coverage obtained with ECD is generally higher than the cleavage coverage obtained with the slow heating processes. Noncovalent interactions are kept intact, and the fragments can be held together if not activated by vibrational energy using CAD or IRMPD.^{103, 119, 120}

The capture of electrons produces a decrease in charge which can lead to the neutralisation of the analyte and its loss. High charged species greatly enhance the capture of electrons. The Utah-Washington mechanism propose a fragmentation pathway (Figure 1.33),¹²¹ however the mechanism of dissociation is still under investigation.¹¹⁸

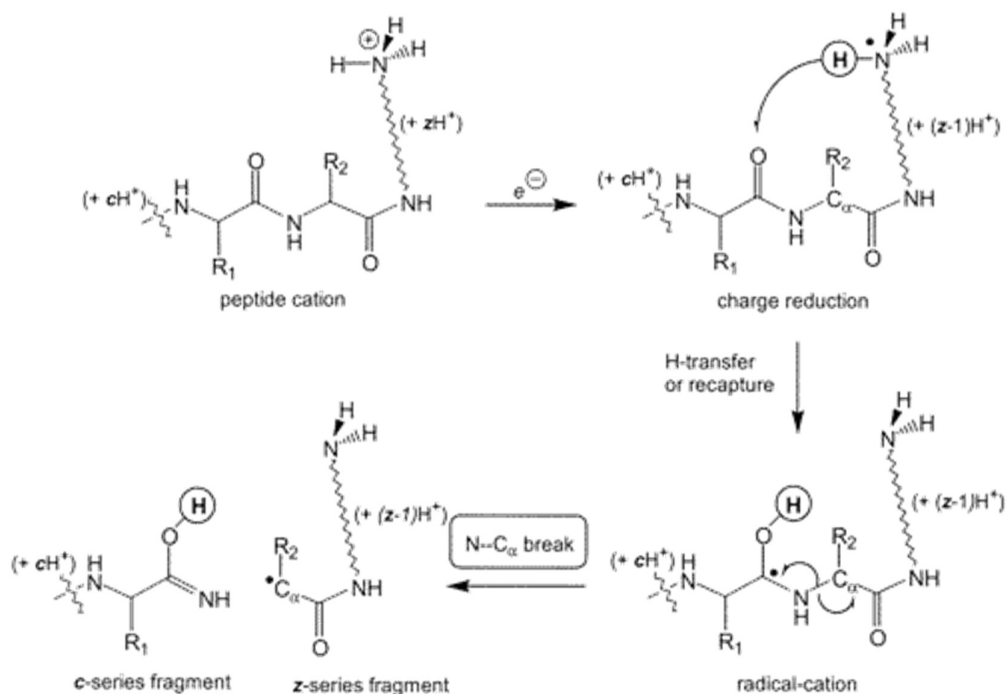


Figure 1. 33: Utah Washington mechanism. Reprinted from Tureček¹²¹ with permission from Copyright 2003, American Chemical Society.

Electron transfer dissociation (ETD) is an alternative to ECD where the multiply charged ions are charge reduced using an electron-donating reagent to start an ion-radical fragmentation process.¹²² The fragmentation process is similar, generating the same c/z fragments.

Electron detachment dissociation (EDD) consists of the use of electrons with kinetic energies above 10 eV to detach electrons from a negatively-charged precursor in negative mode analysis.¹²³ The negative charges are located at the amide nitrogen bond along the backbone, and therefore produce a./x fragments (Figure 1.32), or at the amino acid side chain, producing neutral losses.^{124, 125}

1.2.4.3. Photodissociation

In photodissociation techniques, ions are irradiated by lasers of fixed wavelengths and absorb photon(s) leading to dissociation.¹²⁶ The energy of the fragmentation depends on the photon wavelength, the higher the wavelength, the lower the energy (Figure 1.34).

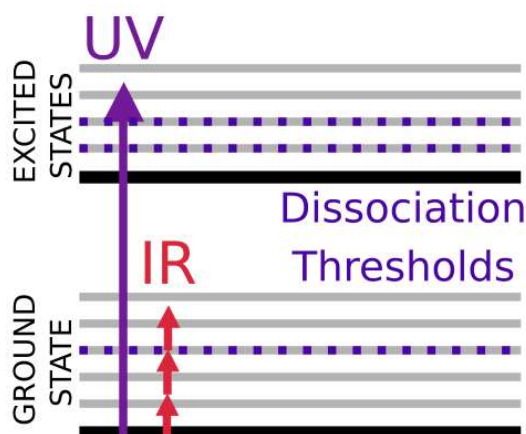


Figure 1. 34: Energy diagram of photodissociation mechanisms. Black lines: electronic states. Grey lines: vibrational excited states.

The 10.6 μm IR photons of the CO_2 laser have low energy (0.117 eV per photon), and many need to be absorbed to reach the threshold of ground state dissociation of the analyte, in a process called infrared multiphoton dissociation (IRMPD).¹²⁷⁻¹³⁰ The stepwise absorption of photons causes low energy proton rearrangement leading to destabilization and cleavage of an amide bond, in a similar process than CAD and producing the same ions (Figure 1.35).^{131, 132} In ultraviolet photodissociation (UVPD), the absorption of a single UV photon is enough to pop an electron into a higher electronic orbital generating excited state dissociation of a protein. UVPD access high-energy dissociation channels, resulting in the generation of all complementary ion pairs (Figure 1.36).^{126, 133, 134} The dissociation can occur via three pathways: the absorption leads to an electron shifting to an electronic excited state, breaking a double bond into two radicals, one of high energy and one of low energy. The high energy radical is beyond the threshold of dissociation resulting in direct cleavage (a/x fragments) and the low energy radical undergoes radical rearrangements similar to ECD (c/z fragments). Internal conversion of the electronic energy into vibrational modes results in even-electron fragmentation similar to CAD (b/y fragments).

Depending on the wavelength of the UV photon, the absorption may require specific chromophores. For example, peptide backbone dissociation at 266 nm can only occur if the sequence contains aromatic amino acids (tyrosine, tryptophan, phenylalanine). However, at 193 nm (6.4 eV per photon), the amide bond absorbs and there is no need for further chromophores.^{133, 135}

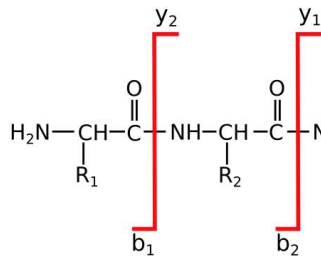


Figure 1. 35: IRMPD fragments.

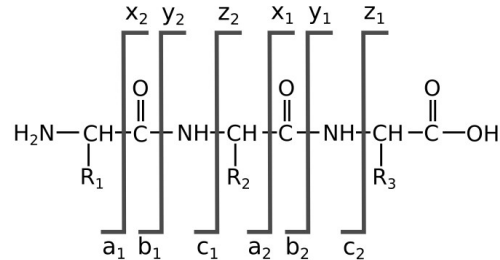


Figure 1. 36: UVPD fragments.

1.2.5. Analyzing proteins

1.2.5.1. Intact mass

Intact proteins are usually ionised with ESI, which produce multi charged ions.^{73, 136} However, MALDI experiments are also possible, generating single-charged ions of ultra-high m/z that can be analysed if the ionisation source is coupled with a high resolving time-of-flight (TOF).

High resolution is required to baseline resolved the highly charged species and to distinguish their PTMs (deamidation for example has a mass shift of 1 Da). High sensitivity is also a key factor: the ionised proteins have a broad charge state and isotopic distributions, spreading the signal from a single species across many peaks. Figure 1.37 is an example of intact mass spectrum from an IgG1 antibody (~150kDa) showing charge states from 44+ to 70+. The charge states are resolved; however, the isotopic distribution is not. To baseline resolve the 55+ species, a resolving power of 150000 is needed at 2700 m/z , so a resolving power of 1 million at 400 m/z . If this resolving power can be achieved easily with FT-ICR, that is not the resolving power which is effectively needed. The protein sample is a mixture of the proteoforms of the antibody, the glycosylation profile is resolved in the Figure 1.37, but the others PTMs are not resolved (deamidation, oxidation, etc).

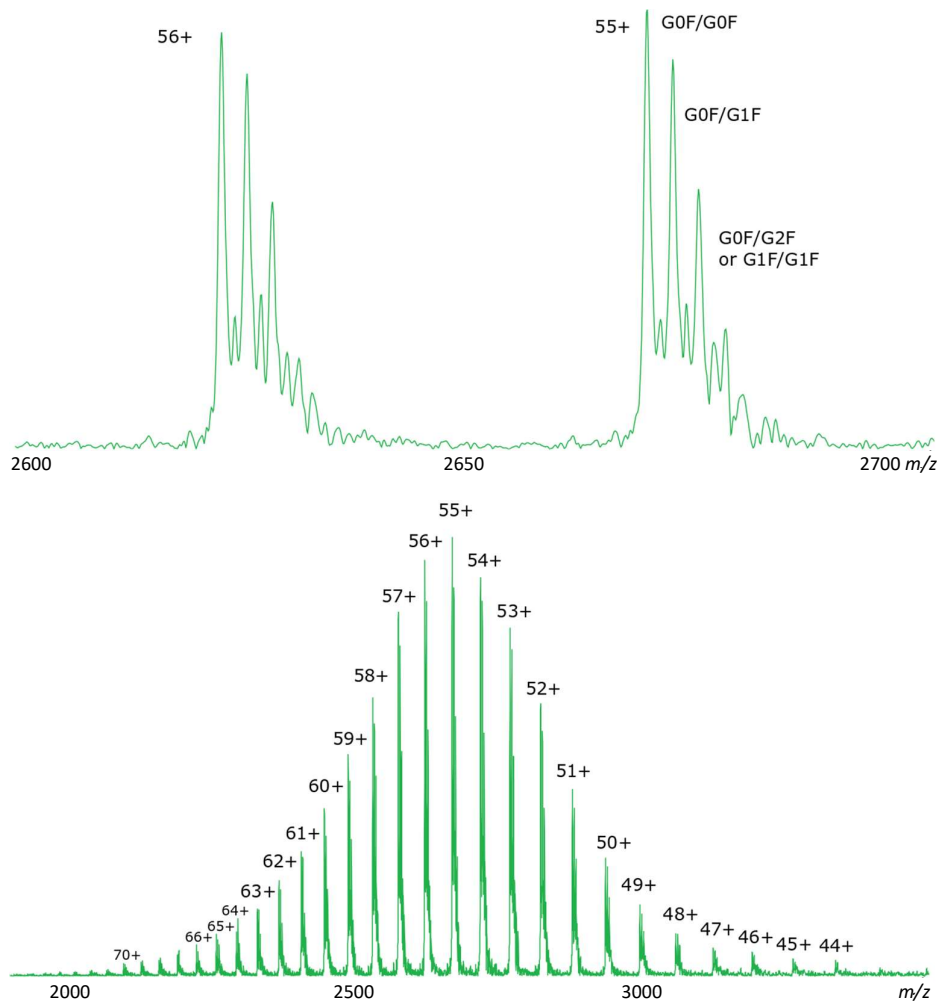


Figure 1. 37: Intact mass of an IgG1 antibody. 0.1 g/L at 50:50 ACN:Water + 0.1% FA. 1000 acquired scans. 262K. Q1: 1200 m/z. CAD: 9V. In-source CAD: 80V.

Figure 1.38 is a mass spectrum of the light chain of the antibody (~25 kDa), which is charge state resolved, and isotopically resolved. The light chain signal is spread over 13 charges states, and ~15 isotopes per charge state.

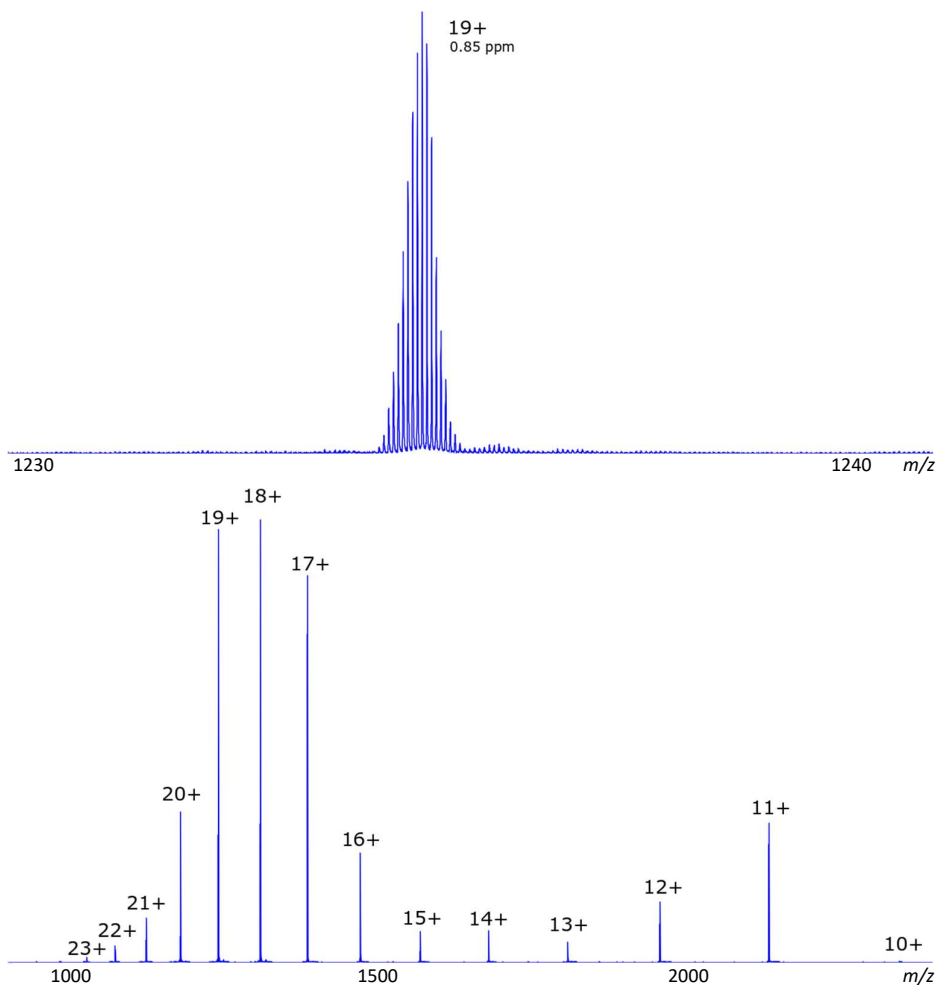


Figure 1. 38: Intact mass of the light chain of an IgG1 antibody. 0.4g/L 30:70 ACN:Water + 0.1% FA. 100 acquired scans. 1MW, Q1: 800 m/z. CAD: 2V. In-source CAD: 60V.

1.2.5.2. Bottom-up vs top-down strategy

Two fundamental strategies for protein identification, and PTMs characterisation, are currently employed in proteomics mass spectrometry.¹³⁷

In the top-down approach, the intact proteins are directly fragmented. The fragmentation of the intact proteins leads to a lot of fragments of different charges, scattered along the dynamic range, which are often difficult to assign. The discrimination occurring with the slow dissociation techniques are enhanced, leading to a fragmentation of the weak sites of the protein structure. Therefore, ExD dissociation techniques are often useful. However, they necessitate longer experiment time, due to their low

efficiencies. The top-down analysis of proteins is shown complicated for protein over 50kDa. For example, the highest cleavage coverage obtained for fragmenting an intact antibody in the literature is ~35%.¹³⁸

The alternative is to analyse the protein after either enzymatic or chemical digestion. In the bottom up approach, the proteins are digested into peptides which are then separated by liquid chromatography, fragmented and analysed in the mass spectrometer (LC-MS/MS).⁶ This approach allows the identification and localisation of PTMs, but does not keep the information on which PTM corresponds to which proteoforms.

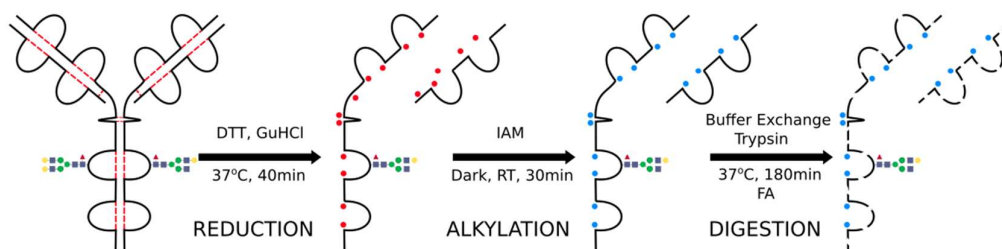


Figure 1. 39: Example of an antibody digestion protocol.

1.2.5.3. Data dependent vs independent acquisition

Bottom-up proteomics are widely used and developed. In the liquid chromatography tandem mass spectrometry (LC-MS/MS) analysis of complex mixtures such as proteins, the separation of all peptides is rarely obtained. Three main approaches exist: the data dependant analysis (DDA),¹³⁹ the multiplexed-data acquisition¹⁴⁰ and data independent analysis (DIA).¹⁴¹

In the data dependant analysis, the ions are selected to be isolated and fragmented.¹³⁹ In shotgun/discovery proteomics, 10 or 20 peptides are fragmented each cycle.^{142,140} Through the full experiment most of the peptides of the complex mixture are analysed; however the low intensity peptides can be missed¹⁴³ and the automatic selection of different subset of peptides causes high variation across replicates.¹⁴⁴ This technique allowed the first comprehensive analysis of a yeast proteome in 2008, with an identification of 4499 proteins and an experiment time of 9h.¹⁴⁵ Since, multiple optimisations have been made. In 2014, the yeast proteome was analysed in 1.8h¹⁴⁶ and in 2017 the DDA approach allowed the full analysis of a single cell type.¹⁴⁷

The other approach in data dependant analysis is called targeted proteomics. The mass spectrometer is operated in selected reaction monitoring (SRM), or multiple reaction monitoring (MRM), mode. In this approach, only some peptides are investigated. They are, with their fragments, selected beforehand, and preferentially acquired.^{148,148} The goal of a targeted proteomics experiment is to monitor selected proteins of interest with high sensitivity, reproducibility and quantitative accuracy.¹⁴⁹ Targeted proteomics is an alternative tool for the analysis of biomarkers¹⁵⁰ or system biology studies.^{151, 152}

Data dependant analysis is a very well-established technique, which built extensive spectral libraries, retaining the elution time and fragment ions of peptides. These libraries are now useful for the data analysis of multiplexed-data acquisition and data independent experiments, where the precursors ions are co-selected and co-fragmented in parallel, and the fragments allocated to the precursor using database search strategy.

Contrary to DDA, where peptides are fragmented one at a time, in the multiplexed acquisition approach, peptides are simultaneously selected and fragmented.¹⁵³ Data-dependant SWIFT isolation waveforms were for example applied to multiplexed tandem acquisition.¹⁵⁴ A multiplexed method was proposed by McLafferty et al¹⁵⁵ in order to measure parent ion spectra using the Hadamard transform instead of the Fourier Transform. In this approach, all the precursor ions are isolated with a SWIFT pulse and fragmented producing a MS/MS spectrum. Instead of selecting one by one the n precursors, it is possible to fragment n combinations of $0.5n$ precursors ions, and identifying which fragment comes from which precursor.^{156,157}

Data independent acquisition methods are independent to prior information collected on the sample, they do not select the ions based on the precursor scans, but fragment all the ions entering the mass spectrometer at a time (broadband DIA) or divide the m/z range into small m/z windows that are fragmented one by one.

Shotgun CID is a broadband DIA with in-source fragmentation of the ions.¹⁵⁸ Using search algorithms, this approach can assign fragments of the assigned precursor of a file. Broadband DIA was further developed into an in-cell fragmentation approach called MS^E.¹⁵⁹ In the collision cell, energy is switched to low and high voltages in a rapid succession. The precursor ion masses are recorded during low voltages scans, and their associated high voltage scans (MS^E scans) record their fragments m/z .

In a main data-independent acquisition approach, called sequential window acquisition of all theoretical fragment ion spectra mass spectrometry (SWATH),¹⁶⁰ peptides in a narrow mass-to-charge window are fragmented simultaneously. This acquisition is repeated in successive stepped windows to analyse fully the dynamic range of the mixture. The window was originally 25 m/z ,¹⁶⁰ but since various window were investigated, to a minimum window of 3 m/z , advised for in-depth analysis of complex proteomic sample.¹⁶¹ Peptides with no spectral library can be missed. However, algorithms are developed to create a dataset similar to DDA from the DIA data (untargeted peptide identification or untargeted DIA).

Sequential window acquisition of all theoretical mass (SWATH) is a fragment-ion centric approach, where quantitation is done on the fragment. WiSIM-DIA (wide selected-ion monitoring) is an alternative DIA analysis¹⁶² with a precursor-centric approach.¹⁶³ In this approach, the resolution is high for the MS scan and low for the MS/MS scan, which are for identification only of the peptides.

Precursor acquisition independent from ion count (PAcIFIC) is a combination of the DDA and the DIA approaches where the analysed sample is divided in m/z windows precursors, then isolated and fragmented one by one.¹⁶⁴ The DDA process is forced to examine ions of lower abundance.

Interference can occur when there is a high number of fragment ions in a coeluting peptides elution time. Peptides with broad elution time produces chimere peaks. The stepped ion isolation leads to long experiments and high sample consumption. Moreover, the DIA methods are usually coupled with short duty cycle mass spectrometer (1ms), and if it is possible to coupled them to FT-ICR analyser, the duty cycle (~1s) of such instruments would lead to even longer experiments, and the production of very large datasets. Consequently, they are not the best suited for FT-ICR analysis. However, the characteristics of the ICR cell, with the possibility to modulate the ions in the cell, and the in-cell spatially-resolved fragmentations techniques give the possibility of an alternative data independent approach, called two-dimensional mass spectrometry (2DMS).

1.3. Two-dimensional mass spectrometry

Two-dimensional mass spectrometry (2DMS) was introduced in the late 1980's.¹⁶⁵ Due to the improvement of computational capabilities, it was further investigated in 2010. It has been since developed and applied to the analysis of small molecules and macromolecules.

Usually, complex samples are analysed by chromatographic separations followed by tandem mass spectrometry (LC-MS/MS), the compounds are separated by liquid chromatography (LC) and then fragmented into ions in the mass analyser. 2DMS is an alternative tool that allows analysis of the sample, without the isolation of the species, and retains the information of which ions are fragmented from which precursors.

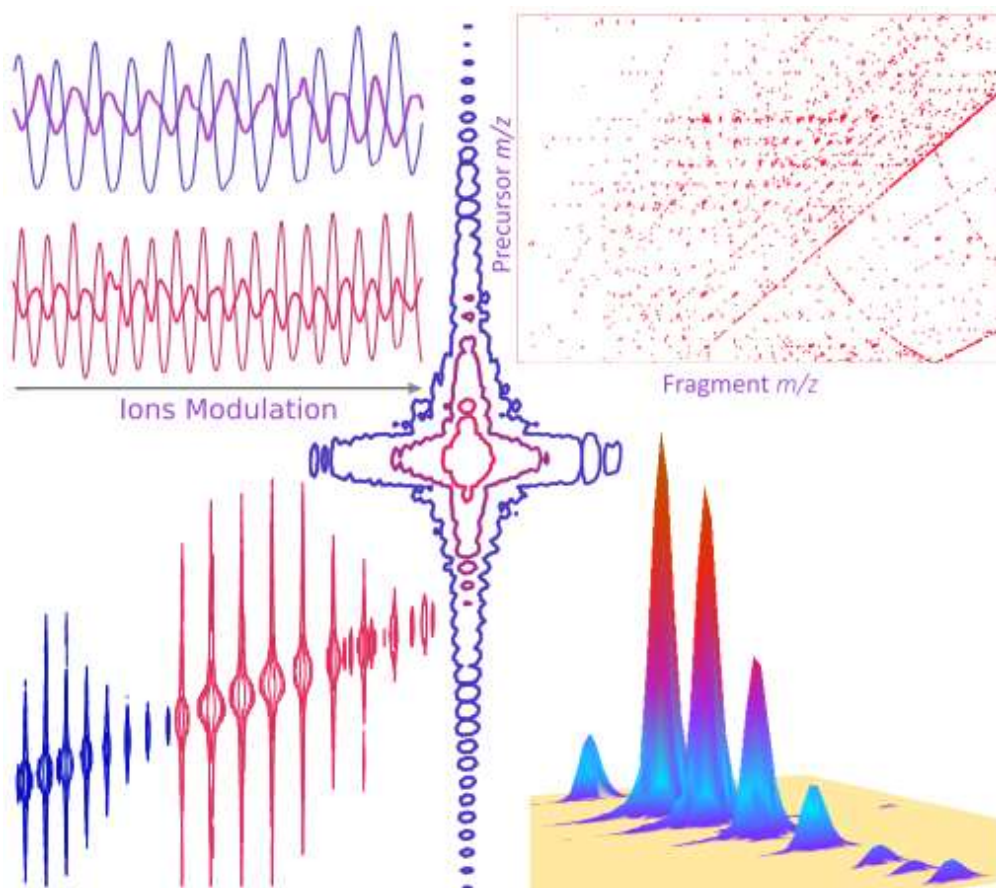


Figure 1. 40: Illustration of few characteristics of 2DMS

1.3.1. Ion modulation in the ICR cell

2DMS is possible because of the ions' behaviour in the ICR cell. Marshall et al,¹⁶⁶ in 1984, have shown that it is possible to excite an ion to a larger orbit and then de-excite the ions back to its starting point. Midway through the excitation period, they changed the phase of the oscillating electric field by 180°. The radius increased during the first part of the excitation, producing a higher detected signal, and then, after the phase shift, the signal decreased indicating that the ions were more distant to the detection plates. In the Figure 1.41 is shown the two cases, the usual case when the ions are excited until they are ejected out the cell (solid curve) and the case of the de-excitation (dashed curve) that occurs during the 2DMS pulse sequence.

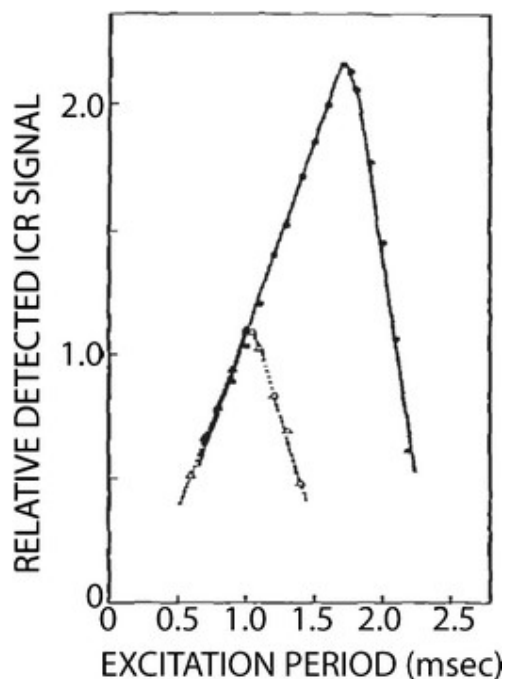


Figure 1. 41: ICR signals of $C_9F_{20}N^+$ from perfluorotributylamine (m/z 501.971) after resonant excitation. Filled circle: constant phase. Open triangles: phase shifted through 180° after 1.0 ms. Reprinted from Marshall et al.¹⁶⁶ with permission from copyright 1984 Elsevier.

1.3.2. 2DMS pulse sequence

Two-dimensional Fourier spectroscopy was first used for nuclear magnetic resonance (NMR), and continues to be commonly used in that field with pulse sequences like 2D nuclear overhauser effect spectroscopy (NOESY).^{167,168} Other applications to the idea underlying 2D NMR were developed in other fields of spectroscopy with pulse excitation such as electron spin resonance (ESR)¹⁶⁹, rotational microwave spectroscopy (MW) and ion cyclotron resonance (ICR).¹⁶⁵

Gäumann's team was inspired by the 2D NMR experiment and proposed a new pulse sequence¹⁶⁵ for FT-ICR mass spectrometer that is equivalent to the NOESY pulse sequence.^{170,171}

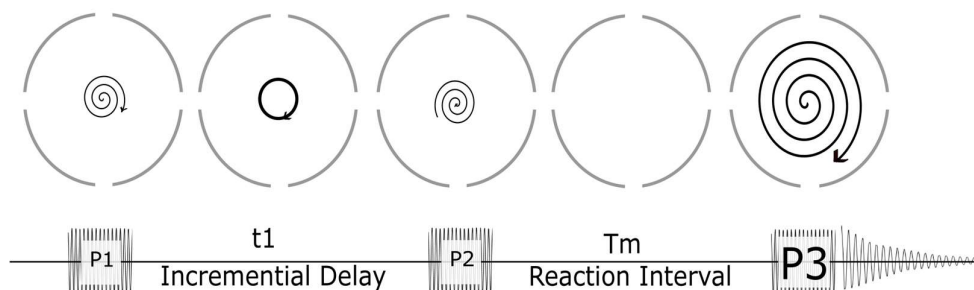


Figure 1. 42: Pulse Sequence developed by Gäumann et al.¹⁶⁵

After a quench pulse, ions are generated or loaded into the centre of the cell. P1 is the first RF pulse; it acts on an incoherent state system (the Zeeman polarisation in NMR and the trapped ions in ICR) and excites coherence (transverse magnetisation in NMR and ion packets on cyclotron trajectories in ICR). The ion packets spiral out from the centre of the cell into an orbit of increasing radius; they are parked at a small orbital radius (3-5 mm) at the end of P1. During the evolution time (t_1), the ions precess at that orbital radius and separate themselves depending on their m/z . Depending on the phase of the ion packets at the time of start of the second RF pulse (P2), P2 provokes a de-excitation or a further excitation of the ions, or something in-between. Therefore, the ions are separated in radius depending on their m/z . During the reaction interval (T_m), called mixing interval in

NMR, fragmentation can be induced. The produced fragments have different cyclotron frequencies and different phases than the precursor. The third RF pulse (P3), corresponding to the usual excitation event, excites all the ions to a large radius (typically about 25 mm) and puts them in a coherent state. They are then detected during the detection period. The signal for the 2DMS is recorded by increasing systematically t_1 in a set of a large number (1k – 8k, typically) of spectra, generating several thousand transients.

Few improvements have been made on the initial pulse sequence as its capabilities have not yet been exhausted. In Gäumann et al 1987,¹⁶⁵ the 2DMS was originally a narrow-band experiment due to computational dataset limitations; P1, P2 and P3 were derived from a continuously running frequency generator. This experiment had limited applications. In Gäumann et al 1988,¹⁷² they implemented a broadband experiment, where P1, P2 and P3 are swept through the relevant range of frequencies (chirped). The broadband experiment needs phase continuity. In Gäumann et al 1989,¹⁷³ they demonstrated that by varying simultaneously t_1 and the phase of P2, it is possible to generate the phase continuity required to overcome bandwidth limitation problems. Ross et al, 1993,^{174, 175} developed another strategy where the excitation period is fixed with a single excitation time-domain waveform (stored-waveform inverse Fourier Transform (SWIFT)⁹¹) whose magnitude varies sinusoidally from one waveform to the next; this approach is called stored-waveform ion modulation (SWIM).

Sehgal et al¹⁷⁶ developed a second theory model in 2016, in order to optimise the pulse sequence. They calculated that during the first pulse (P1), when the ions move away from the centre of the ICR cell, the ions also gain kinetic energy. The movement of the ion during t_1 is therefore off-centre. If the second pulse (P2) is not a multiple of 2π (not a matched pulse), the ions are not brought back to the centre. These trajectories induce a loss in efficiency of cell-centred fragmentation techniques. However, they find out that if the pulses are short in duration, the overlap between the fragmentation zone and the ions are not compromised. The short pulses also induce fewer harmonic signals.

1.3.3. Visualization and modelling of the ion's modulation

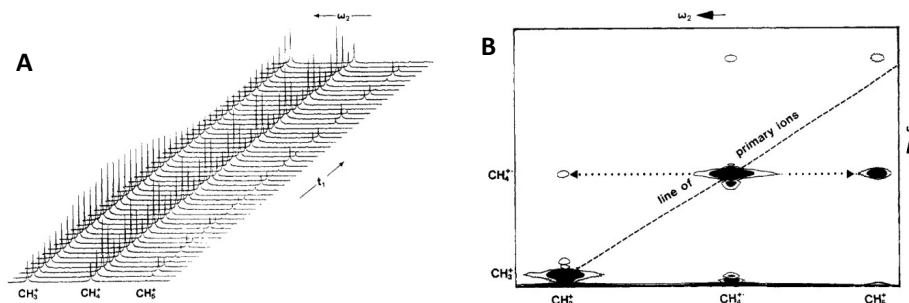


Figure 1. 43: (A) Modulation of the CH_3^+ , CH_4^+ and CH_5^+ species depending on t_1 . (B) 2DMS spectrum. Reproduced from Pfändler et al¹⁷² with permission from copyright 1988, American Chemical Society.

The Figure 1.43 is the first visualisation of the original 2DMS results from Pfändler et al.¹⁷² It highlights evidence that CH_5^+ is produced from CH_4^+ as only CH_3^+ and CH_4^+ were introduced in the ICR cell and that the modulation of CH_4^+ and CH_5^+ are inversely opposite. The Figure 1.43 is Fourier transformed in respect to t_1 , producing a 2D broadband FT-ICR spectrum. The dotted line indicates that the modulation of CH_4^+ is the same than CH_3^+ and CH_5^+ , and therefore that CH_3^+ and CH_5^+ are produced from CH_4^+ ($2 \text{CH}_4^+ \rightarrow \text{CH}_3^+ + \text{CH}_5^+$).

Guan et al in 1989¹⁷⁷ proposed a model for 2DMS. The fragment ions (B and P) were produced by the collision of the precursor A with N neutral molecules. The Figure 1.44 shown the variation of A and B depending on t_1 . A higher radius cyclotron motion had the same frequency, and therefore moved at higher speed in the cell. After P2, during the reaction interval, a higher radius ion will be more likely to encounter neutral molecules.

The modulations of the primary and product ions were opposite of phase. This model is consistent with the sustained off-resonance irradiation (SORI)¹¹⁴ fragmentation or the in cell collision induced dissociation (CID).¹⁷⁸

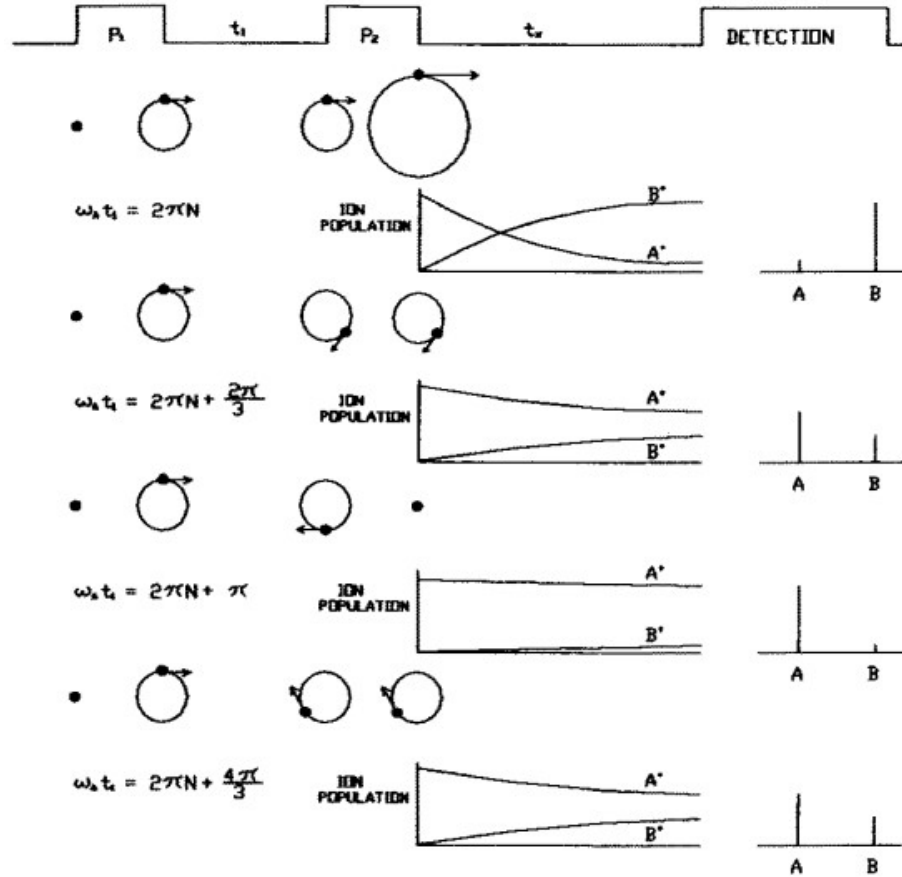


Figure 1. 44: Modulation of the ion depending on the phase of the P2 excitation.

Reprinted from Guan et al¹⁷⁷ with the permission of AIP Publishing.

They modelled the modulation of the ions and concluded that the modulation of the ions was not sinusoidal but square root cosinusoidal, producing higher harmonics.

$$[A^+] = \begin{cases} [A^+]_0 e^{-c \sqrt{1 + \cos(\omega_A t_1)}}, & E > E_{threshold} \\ [A^+]_0, & E < E_{threshold} \end{cases} \quad \text{Equation 1. 12}$$

$$c = \sqrt{2} t_x \sigma_0 V_{A0} [N] \quad \text{Equation 1. 13}$$

V_{A0} is the ion speed at the end of P1, σ_0 is the reaction cross section when the energy (E) is higher than the threshold of dissociation ($E_{threshold}$). With an increase in the reaction interval (t_x) or the concentration of neutral [N], the parameter c increases, giving an increase in the higher harmonic component but also in the absolute intensity of the fundamental frequency as well.

Sehgal et al¹⁷⁶ calculated the trajectories of the ions (Figure 1.45).

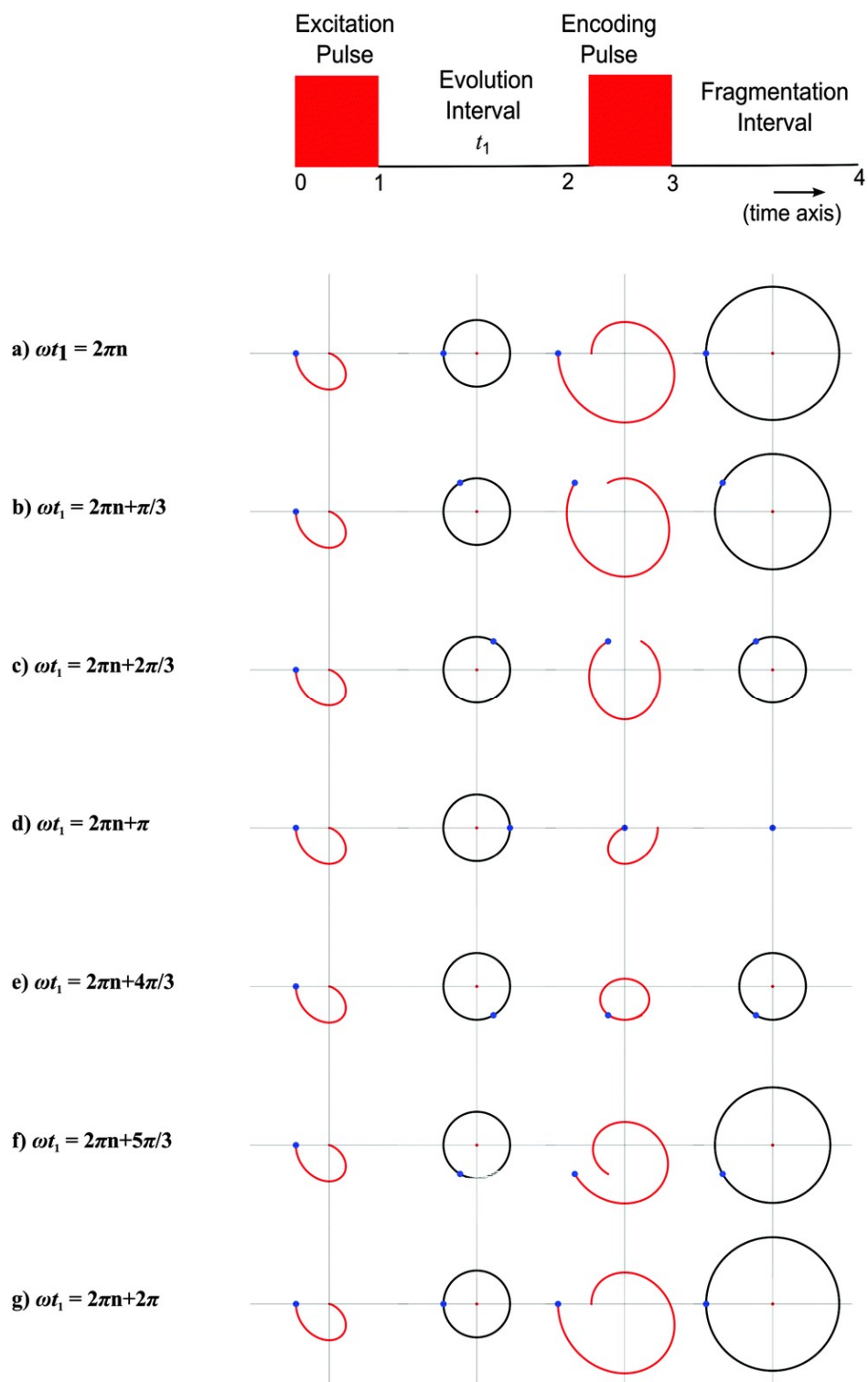


Figure 1. 45: Modulation of the ion depending on the phase of the excitation. Reproduced from Sehgal et al¹⁷⁶ with permission.

1.3.4. 2DMS fragmentation techniques

In the first 2DMS experiments, Gäumann and Ross used CID fragmentation, where higher radii ions were evolving at higher speed in the ICR cell and therefore encountering more neutral molecules and fragmenting more than the lower radii ions. Consequently, the fragments had high magnetron and cyclotron radii, as well as random phase, which limited the technique.

Due to the excitation-delay-excitation event in the 2DMS sequence and the incremental delay, the precursors modulate in radius at the end of the event in each iteration of the sequence. Therefore, any radii spatially resolved fragmentation technique could be used for a 2DMS experiment. The cell-centred approach produces fragments at low radius with low magnetron/cyclotron radii which are much easier to excite/detect afterwards.

In Gäumann et al 1989,¹⁷³ the first IRMPD 2D experiment was carried out to study ion-molecule reactions and multiphoton dissociation of ions in the gas phase on the CF₃I. In Van Agthoven et al 2011,¹⁷⁹ the potential of IRMPD as a fragmentation tool for 2DMS was further investigated. With gas-free fragmentation techniques, the resolution in space of the ion after the second excitation pulse allows the selective fragmentation of some of the precursors. In the case of the laser pulse, ions with a high cyclotron radius are outside the laser beam and therefore do not fragment. The de-excited ions are in the path of the laser beam and fragment. UVPD 2DMS experiment¹⁸⁰ was also conducted, following the same principle.

Electron-based dissociations such as ECD, EID, EDD, are also gas-free radius-dependant fragmentation techniques.^{181, 182} In the FT-ICR cell, the hollow cathode produces a cloud of electrons of the shape of a hollow cylinder. However, the low ExD fragmentation efficiency could be a problem.

The design of the ICR cell¹⁰³ also allows instruments, to do 2DMS infrared activated electron capture dissociation (IR-ECD).¹⁸³ In this case, the ions are excited by the IR laser, which increases their fragmentation by ECD.

The difference in size and shape of the fragmentation zone for the laser dissociation techniques and the electron-based fragmentations leads to different abundance modulation for IRMPD and UVPD, IR-ECD, and ECD fragments and therefore difference in their vertical harmonics.

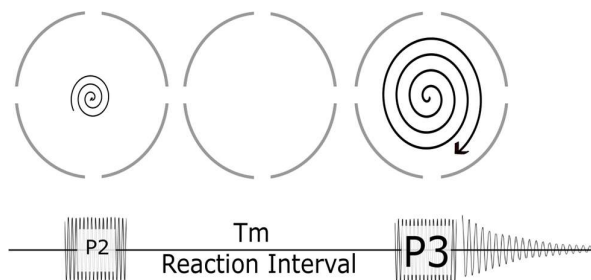


Figure 1. 46: Pulse Sequence for the method development of 2DMS experiment and the mapping of the fragmentation zone.¹⁸⁴

When starting a 2DMS experiment, the pulse sequence in Figure 1.46 can be used to build the fragmentation zone shape of the dissociation technique inside the ICR cell (Figure 1.47).

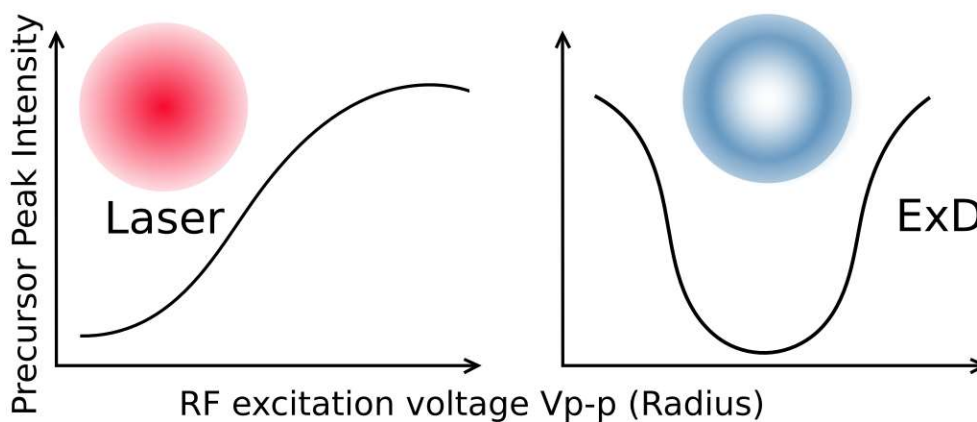


Figure 1. 47: Theoretical shapes of the fragmentation zones.

Computing the modulation of intensities of the ions, scan to scan, allow the identification of which precursors produce which fragments.

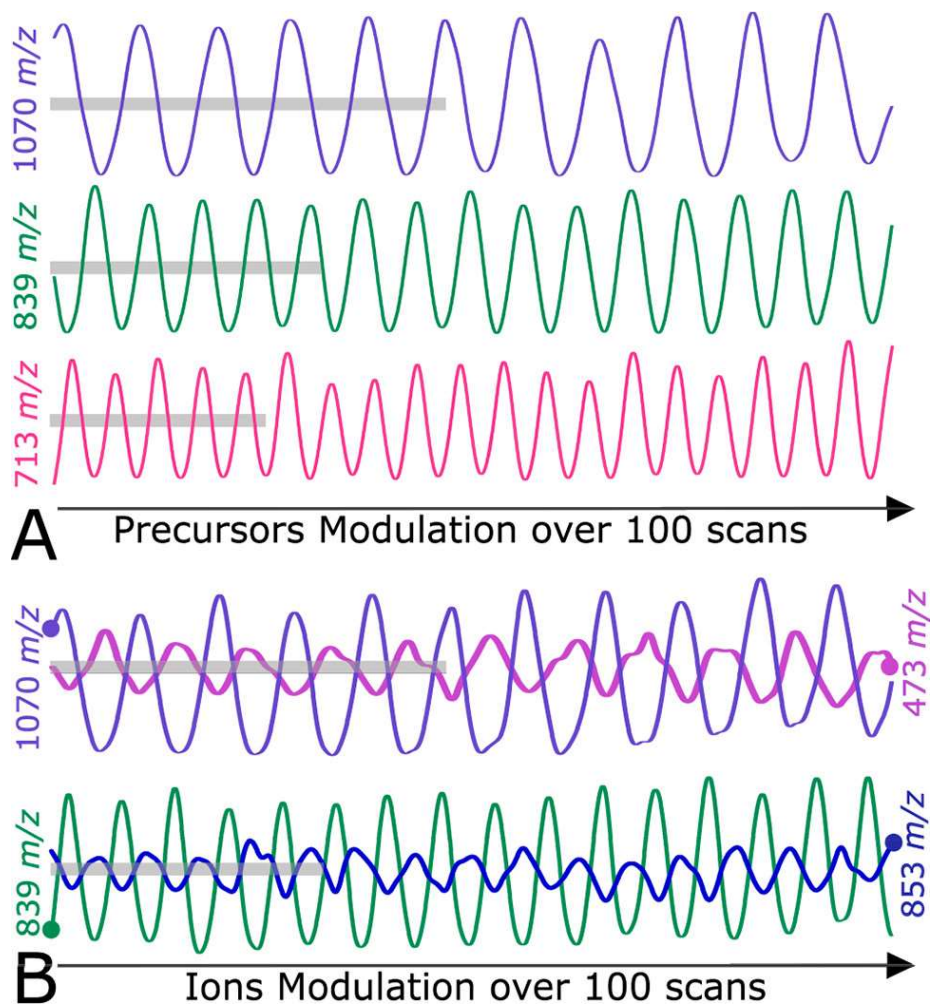


Figure 1. 48: Modulation of intensities during the IRMPD 2DMS experiment. (A) Modulation of precursors during the scans (B-spline smoothed). (B) Modulations of fragments and corresponding precursors (B-spline smoothed). Gray lines correspond to 5 periods. Reprinted with permission from Paris et al. Figure 2.¹⁸⁵ Copyright 2021 American Chemical Society.

Ions can be precursors and fragments of other precursors. Furthermore, secondary fragmentation can occur and increase the complexity of the experiment. The behavior of these ions was investigated (Figure 1.49) and their modulations revealed a combination of the fragment and precursor phase function which is still possible to compute.

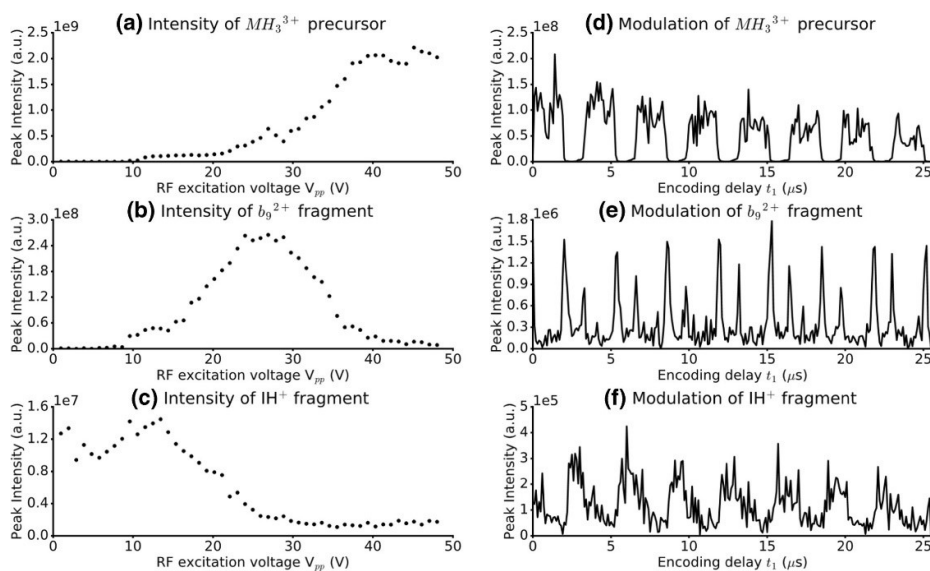


Figure 1. 49: IRMPD 2DMS experiment. Left side: Ion intensity vs. RF excitation voltage for (a) MH^{33+} of angiotensin, (b) the b_{92}^+ fragment, and (c) the IH^+ internal fragment. Right side: Ion intensity vs. encoding delay t_1 for (d) MH^{33+} of angiotensin, (e) the b_{92}^+ fragment, and (f) the IH^+ internal fragment. Reproduced from Van Agthoven et al¹⁸⁴ with permission from Copyright 2019 American Chemical Society.

1.3.5. 2DMS spectrum

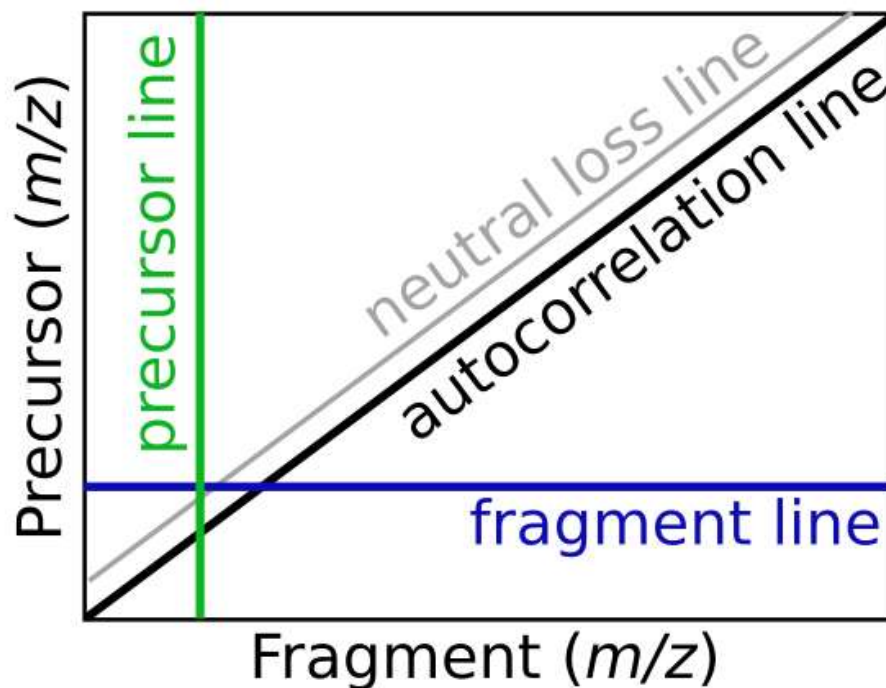


Figure 1. 50: Schematic of a 2DMS spectrum.

A 2DMS spectrum is a three-dimensional surface plot, which is normally represented as a contour plot (Figure 1.50). Each peak corresponds to an ion at an m/z (horizontal axis, fragment axis), linked to a precursor m/z (vertical axis), and an intensity.

The autocorrelation line ($x=y$ or $m/z(\text{precursor})=m/z(\text{fragment})$) corresponds to all the precursors that modulate during the 2DMS experiment. If the autocorrelation is sliced and projected along the m/z axis, it is similar of a 1D full MS mass spectrum however the intensity of the peaks depends on their modulations of intensity and therefore, includes their fragmentation efficiency. The neutral loss line corresponds to a diagonal line which, when extracted, shows all fragments from a particular neutral loss. The fragment line corresponds to all the fragments produced by one precursor. The precursor line corresponds to all the precursors which produced a particular fragment m/z .

1.3.6. Data processing of 2DMS data

For each 2DMS scan, a transient is acquired and saved into a 2DMS dataset $S(t_1, t_2)$. t_1 is the evolving incremental delay of the pulse sequence in the ICR cell. t_2 corresponds to the transient acquisition period (number of data points multiplied by the acquisition rate of the digitiser).¹⁸⁶

The FT of each transient according to t_2 is calculated, corresponding to the frequencies observed in each scan $S(t_1, w_2)$, then the FT of each frequency depending of t_1 is calculated, $S(w_1, w_2)$ giving the modulation of intensities of the observed frequencies.

As in 1D FT-ICR, the data can be optimized. Apodization occurs on each transient before the first FT, and on $S(t_1, w_2)$ before the second FT. All transients are zero-filled, which means the size of the dataset (typically 60 gigabytes) is multiply by at least 4 during the processing.

Nyquist frequencies correspond to the highest detected frequencies that can be accurately determined in an experiment. In 2DMS, there are two Nyquist frequencies, one for each dimension.¹⁸⁶ In the horizontal dimension (fragment axis), f_{N2} corresponds to the Nyquist frequency setup for each 1D scan and relates to the lowest m/z fragment. In the vertical dimension (precursor axis), f_{N1} corresponds to the lowest m/z precursor and is calculated with Δt_1 , the incremental delay between each scan.

$$f_{N1} = \frac{1}{2\Delta t_1}$$

Equation 1. 14

$$f_{N2} = \frac{1}{2\Delta t_2}$$

Equation 1. 15

Finally, in order to process and visualize the complex datasets, several different software suites were developed. First, a python library named SPIKE (spectrometry processing innovative kernel)¹⁸⁷, highly enhanced the use of 2DMS from 2016. Then a lab-view based software called T2D^{188, 189} allowed the extraction of the any horizontal, vertical, and diagonal lines of the 2DMS spectra into a format that Bruker DataAnalysis v4.3 software can read.

1.3.7. Noise and denoising of 2DMS spectra

Noise¹⁹⁰ in the second dimension is due to the random variations in the number of trapped ions from one 1D scan to another, the slow variation of trapped ions over the duration of the experiment due to an unstable ESI source, the relative abundance of trapped ions of different m/z values and the harmonics.

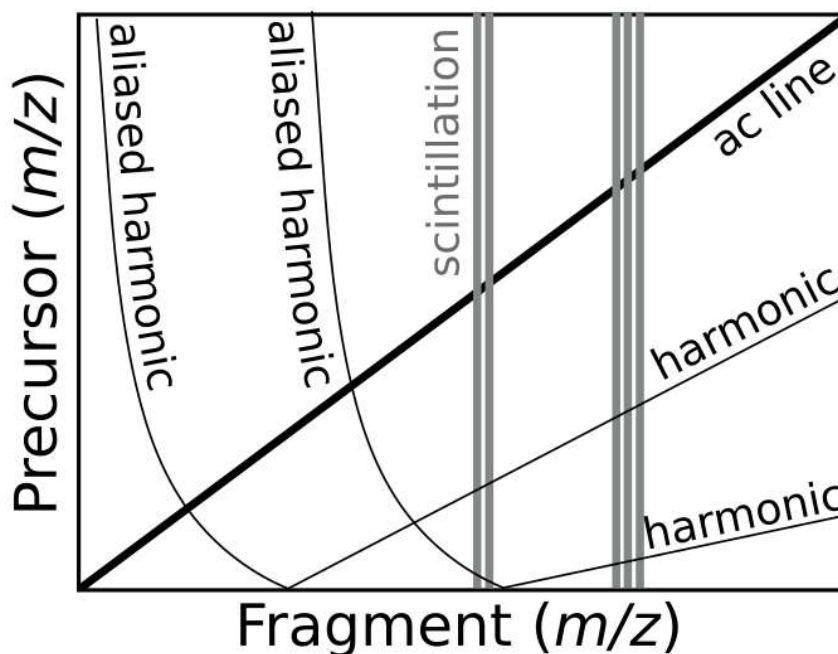


Figure 1. 51: Schematics of the main noises in 2DMS. ac: autocorrelation line.

The vertical stripes along frequencies are heteroscedastic scintillation noise and are proportional of the intensity of the ion peak. Scintillation noise is originally an astronomic term where the source of the noise is the brightness fluctuations of stars caused by atmospheric conditions.^{191,192} In 2D FT-ICR, it does affect the amplitude of low amplitude peaks (fragment peaks) and is mostly caused by fluctuations of the number of ions in the ICR cell due to random variation of signal intensity from scan to scan.

Fourier transform generates spectral artifact peaks corresponding to harmonics. In 2DMS, the nonlinearity of the fragmentation efficiency of the different species as a function of excitation magnitude induces an increase of unwanted harmonic frequencies intensities.¹⁹⁰ Harmonics are also generated because of the non-sinusoidal nature of the mirror current at the detection plates in the fragment dimension. By optimising the pulse sequence for an IRMPD experiment,¹⁹³ it was discovered that the shape and the size of

the fragmentation zone in the ICR cell was important. Moreover, if the ions were moving in space from scan to scan but staying in the beam of the IR laser, the fragmentation was nearly a sinusoidal function of t_1 and produces weaker harmonics. (The beam of the IR laser is thought to be gaussian because of the experimental imperfections.)

2DMS spectra also feature folded over signals which corresponds to signals of higher frequencies than the Nyquist frequency aliased into the spectrum.

Finally, the thermal noise also applied to the second dimension, for which the signal-to-noise ratio increases by the square root of the number of data points.

A few algorithms were developed for 2DMS denoising, without assuming the nature of the noise. First, the Cadzow algorithm was developed from the NMR denoising^{194,195} to 2D FT-ICR¹⁹⁶ in 2011, using data predictability on the transients without noise, but the processing was slow and not adapted for large signal. Then, using random projection theorem, Chiron et al¹⁹⁷ developed a de-noising approach called urQRd (uncoiled random QR denoising) for large data sets, reducing the computer memory footprint and the processing time by using data compressing and filtering methodologies. The algorithm was further developed into the SANE algorithm, which could achieve quicker processing and better noise rejection.¹⁹⁸

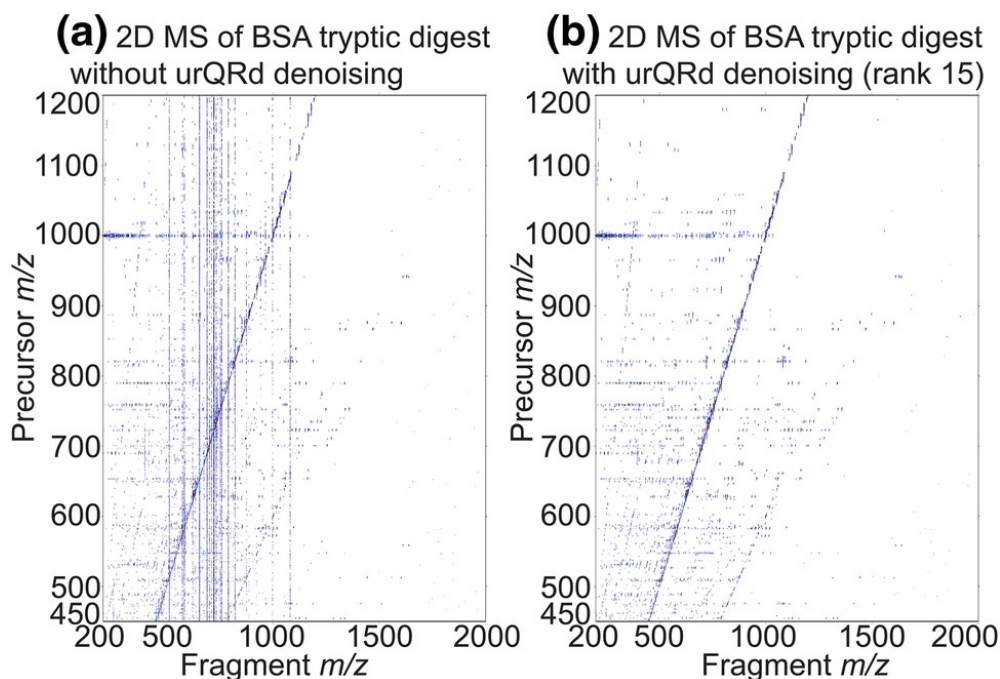


Figure 1.52: 2D IRMPD mass spectrum of bovine serum albumin without (a) and with (b) urQRd denoising. Reproduced with permission from Van Agthoven et al.¹⁸⁶

1.3.8. Resolution in the second dimension

In 1D FT-ICR, the resolution of peaks is dictated by the length of the transient, the pressure on the ICR cell, and the magnetic field. In 2DMS, because the peaks are 3-dimensional, each peak has a peak width and resolution in both the horizontal and vertical dimension which are very different. In 2D FT-ICR, the resolution in the vertical dimension is dictated by the number of acquired scans with different delays and the stability of the spray. In the fragment ion dimension (x-axis), the resolving power allows the separation of m/z ratios of fragment ions, and is identical to a 1D resolving power. In the precursor ion dimension (y-axis), the resolving power allows the accurate correlation between precursor and fragment ions. To increase the resolution in 2DMS, the length of the transient (horizontal resolution) and the number of acquired scans (vertical resolution) can be increased. However, due to the duration of such experiments and the size of the acquired file, there are practical limits on how far 2DMS resolution can be expanded. A few alternative strategies were developed.

A mathematical tool, the non-uniform sampling acquisition¹⁹⁹ allows the user to skip points in the 2D dimension, and then reconstructed them by data treatment. The

sampling distribution can either be uniform, Poisson or random. This technique permits to reach higher resolution without increasing the number of scans, albeit with an increase of signal to noise ratio.

An acquisition stratagem called narrowband 2DMS¹⁹⁸ was developed to increase the vertical resolution. By increasing the encoding time t_1 , with the same number of increments, the Nyquist frequency was reduced, and the vertical acquisition of the data had a narrow window of $\sim 150 m/z$. Sampling frequencies using the Shannon–Nyquist theorem, allow the aliasing of the signal which correspond to a folding of the signal into a narrow window of frequencies. The same number of data points are applied in the narrow window than in the usual window, giving higher resolution. The narrow band experiment is especially effective when the precursors are concentrated into a narrow m/z window (quadrupole isolation of the window removes interference of other m/z ions).

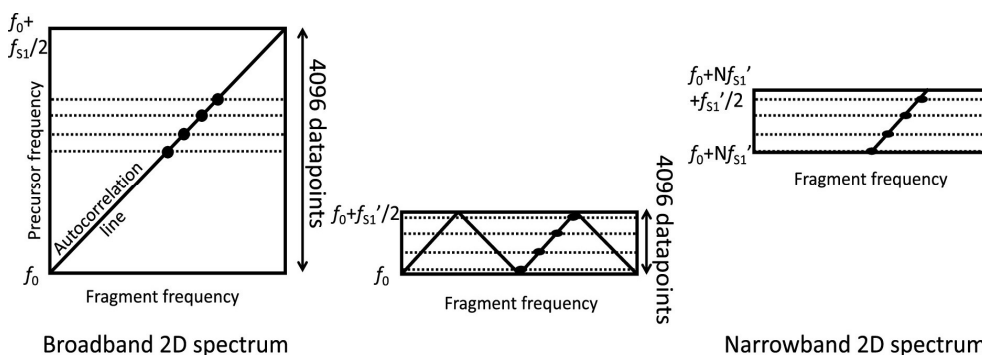


Figure 1. 53: Schematics of 2D mass spectra obtained in broadband (left) and narrowband mode (right). All precursors are concentrated in a small m/z window (big dots). The folding of the autocorrelation line (central diagram) does not mix the signals. Reproduced with permission from Halper et al.¹⁹⁸

A processing tool, called 3D peak picking,^{180, 185} calculate accurately the centre of the 3D peaks of the 2DMS experiment. In the precursor axis, there is a lower number of data points (number of scans) resulting in a lower vertical resolution and an overlap of species when extracting horizontal lines. However, the 2D Fourier transform process retains the information of the 3D shape of the peaks, and their resolution in 2DMS. The 3D data permits higher accuracy in the peak centroid determination in each dimension, which allows improved differentiation of fragments from precursors close in m/z , and reducing

chimeric peaks (spectral contamination) in the fragment lines. This processing tool will be further explained in chapter 4.

Finally, in 2021 was developed phase-corrected absorption mode in 2D mass spectrometry.^{184, 200} Chirp pulses are inducing a quadratic phase dependence to excite the large range of m/z fragments. By performing a quadratic phase correction in the fragment ion dimension and a linear phase correction in the precursor ion dimension, the signal-to-noise ratio and resolving power were improved by 2 in each dimension.

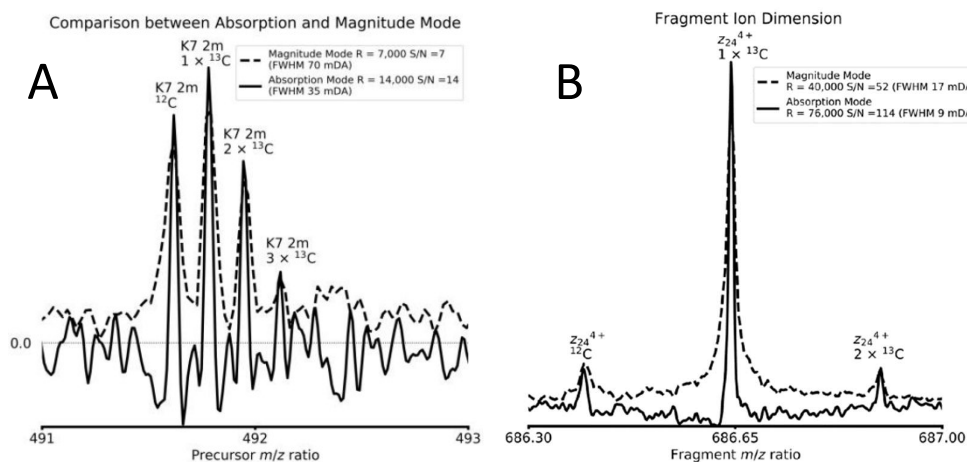


Figure 1. 54: Comparison between the absorption mode and magnitude mode in the precursor (A) and fragment (B) ion dimensions. Reproduced from Delsuc et al. Figures 2 and 3.¹⁹⁶

1.3.9. Applications of 2DMS

Usually, 2DMS FT-ICR is used with a nanoESI source or ESI source, but it was also coupled to an atmospheric pressure photoionization (APPI) for the analysis of cholesterol.²⁰¹

The 2DMS was first used for small molecules, in the analysis of six di-amino acids,¹⁹⁰ and then for the analysis of complex mixtures with an industrial interest, such as polyester oligomers and a 20-component sample from combinatorial synthesis.¹⁷⁵ After 2010, with the increase of computer abilities, the interest for 2DMS as an efficient analytical method

was renewed.²⁰² It was used for the single peptide analysis of Angiotensin I in 2011,¹⁷⁹ substance P, insulin and some glycopeptides in 2012.¹⁸¹

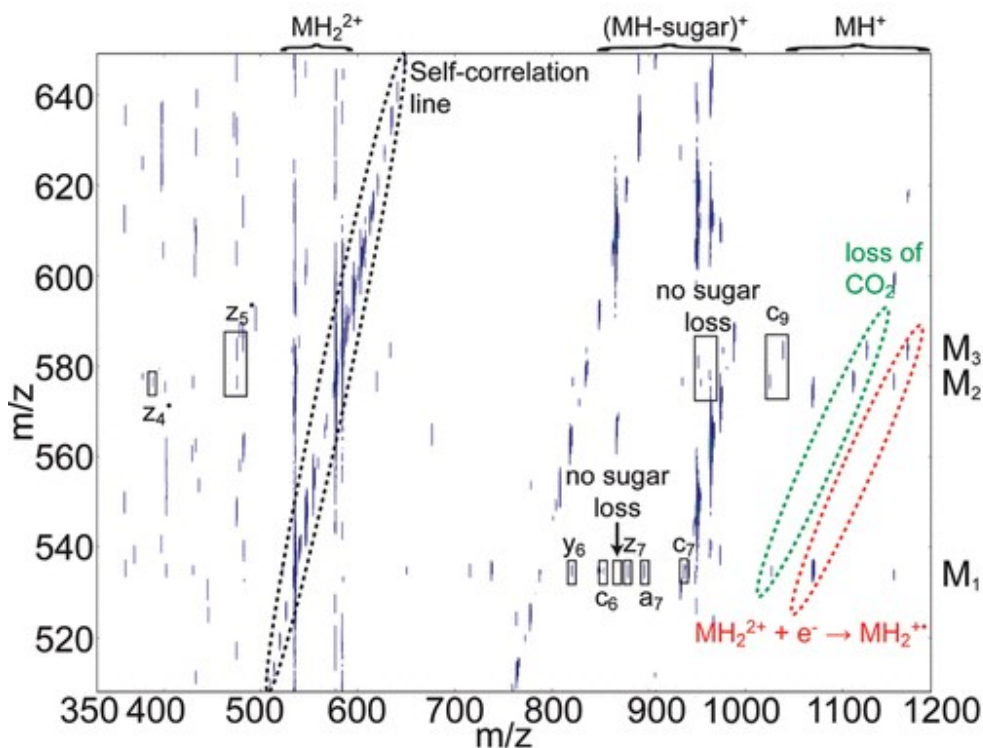


Figure 1. 55: ECD 2DMS mass spectrum of the mixture of custom synthetic glycopeptides (M1: YSPTS(β -O-GlcNAc)PSK-NH₂, M2: SVES(β -O-GlcNAc)GSADAK-NH₂, M3: SVET(β -O-GlcNAc)GSADAK-NH₂ at 1 pmol/ μ L in MeOH/water, 50:50, with 0.1% formic acid). Self-correlation line corresponds to the autocorrelation line. Reprinted with permission from Van Agthoven et al. Figure 4.¹⁸¹ Copyright 2012 American Chemical Society.

With the development of SPIKE in 2016, more complex samples could be analysed. First the analysis of the fragmentation pathway of cholesterol species²⁰¹ as an example of a small molecule analysis was investigated. Then 2DMS was used to study the protein digest mixtures of collagen²⁰³ (Figure 1.56), cytochrome c,⁸² and calmodulin.^{204,205} The chapters 3 and 4 will discuss 2DMS in the detection and analysis of post translational modifications such as phosphorylation in a complex mixture³⁵ or detection of PTMs in the trypsin digest of an antibody.¹⁸⁵

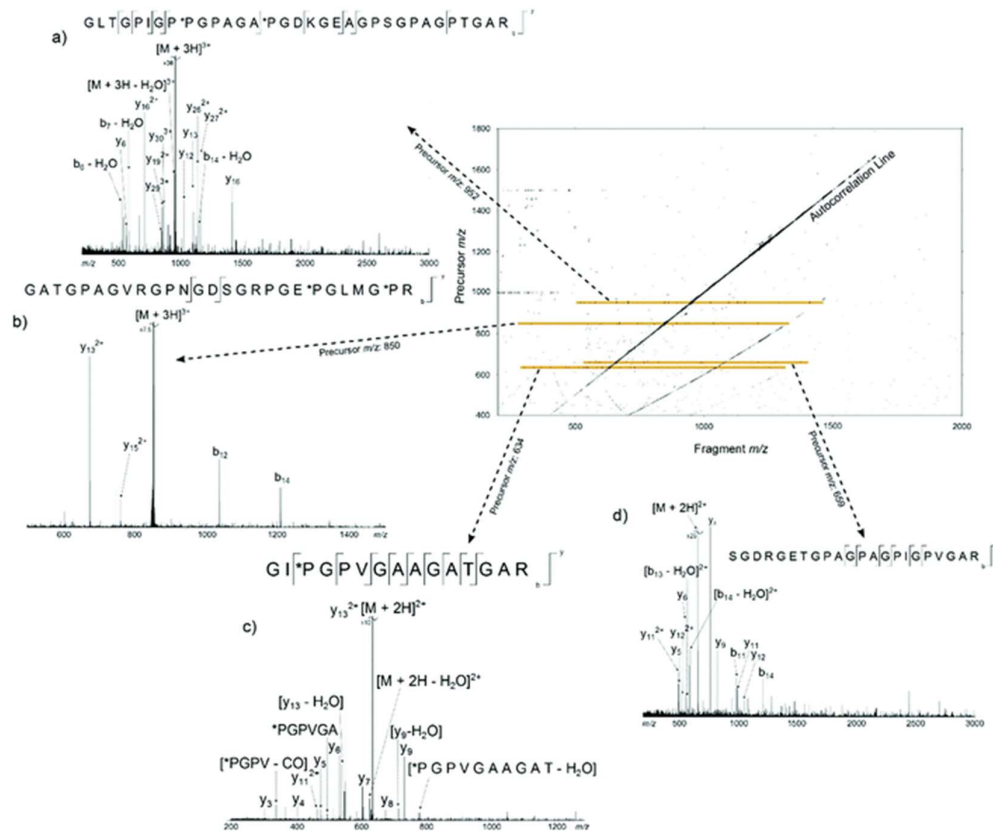


Figure 1. 56: 2D FT-ICR mass spectrum of the collagen tryptic digest mixture. Orange/yellow lines show the regions of the spectrum corresponding to the fragment ion scans in the four insets at precursor m/z (a) 951.81, (b) 850.41, (c) 634.34, and (d) 659.34. Reprinted from Simon et al. Figure 2.⁶ Copyright The Royal Society of Chemistry 2016.

Calmodulin was first analysed by top-down 2DMS in 2016,²⁰⁴ reaching 23% cleavage coverage. A new approach named MS/2DMS was developed in 2018 for the top down sequencing of the calmodulin²⁰⁶ reaching 42% cleavage coverage, and ubiquitin²⁰⁷, reaching 83% cleavage coverage (Figure 1.57). In MS/2DMS, the protein is analysed in a top-down approach. One charge state is isolated in the quadrupole and fragmented by either CAD or ETD before being send to the ICR cell. The 2DMS experiment corresponds to a MS3 experiment on each fragment ions of the isolated charge state, fragmented via IRMPD or ECD. This approach could lead to improvement in the top-down sequencing of proteins.

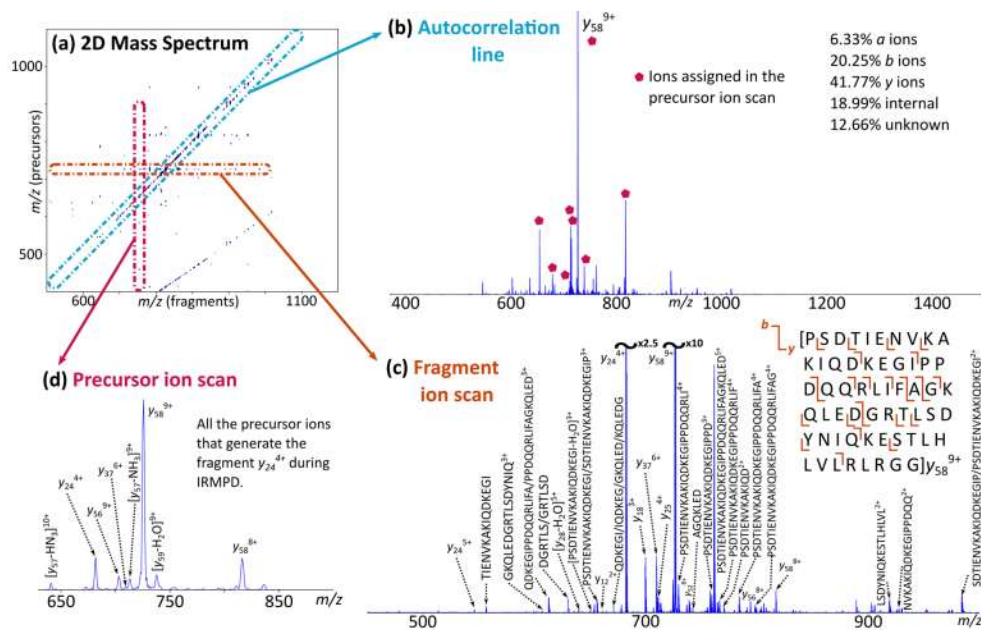


Figure 1. 57: CAD-MS/IRMPD-2DMS of ubiquitin in denaturing conditions. (a) Two-dimensional mass spectrum. (b) Extracted autocorrelation line. (c) Fragment ion scan of the ion y_{589}^{+} (m/z 726.2838) and respective cleavage coverage. (d) Precursor ion scan of the ion y_{244}^{+} (m/z 682.3820), constituting important information for the assignment of y ions on the autocorrelation line (b). Reprinted with permission from Floris et al. Figure 2.²⁰⁷ Copyright 2018 American Chemical Society.

2DMS allowed the analysis of polymers across their polydispersity. First in the analysis of D- α -tocopheryl polyethylene glycol 1000 succinate (TPSG), polysorbate80, and poly(methyl methacrylate) (PMMA)²⁰⁸ and then, after development of the method, in the analysis of various polyacrylamide polymers²⁰⁹ (Figure 1.58).

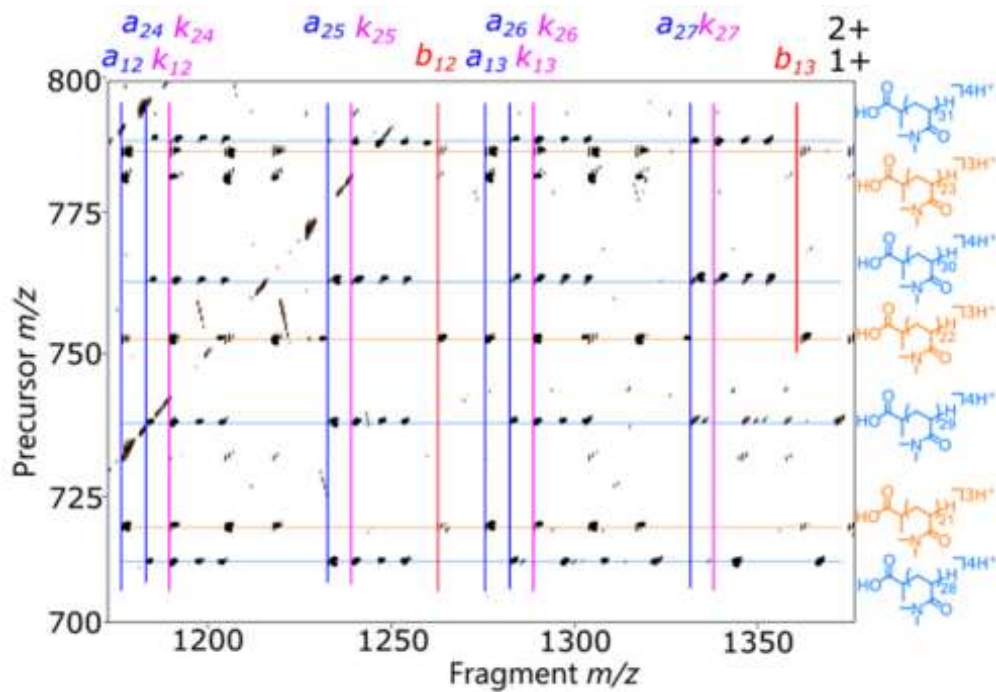


Figure 1. 58: Zoom of the 2DMS spectrum of the hydrogen-terminated polyacrylamide species showing the different fragment lines and the corresponding precursors to those species. Reprinted with permission from Morgan et al. Figure 4.b.²⁰⁹ Copyright 2021 American Chemical Society.

Implementation of new fragmentations techniques for the analysis of agrochemicals, lead to the first EID¹⁸² and UVPD¹⁸⁰ 2DMS spectrum (Figures 1.59 and 1.60).

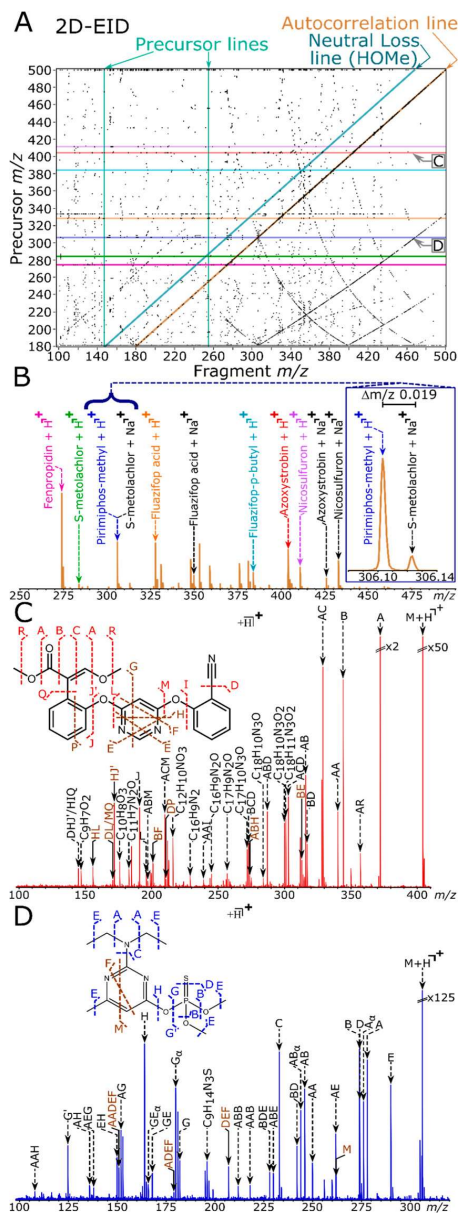


Figure 1.59: (A) The 2D-EID-MS of the 7 agrochemicals. (B) Extracted autocorrelation line. The extracted fragmentation line of the protonated (C) azoxystrobin and (D) pirimiphos-methyl species. Reprinted with permission from Marzullo et al. Figure 3.¹⁸² Copyright 2020 American Chemical Society.

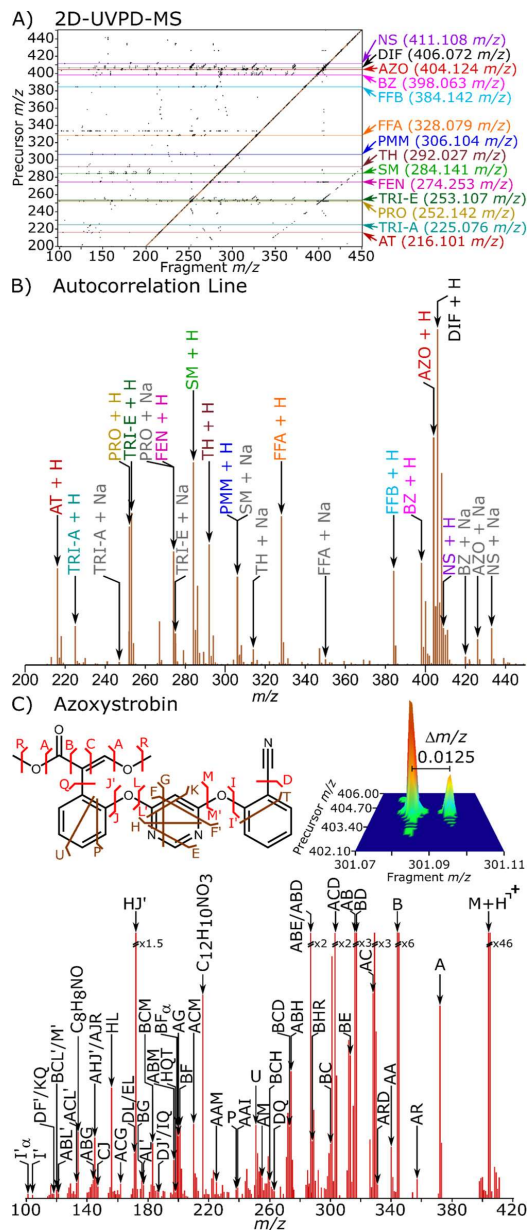


Figure 1.60: (A) 2D-UVPD-MS spectrum of the 14 agrochemical mixture. (B) Extracted autocorrelation line. (C) 2D-UVPD fragmentation spectrum of azoxystrobin with the cleavage diagram. Reprinted with permission from Marzullo et al. Figure 2.¹⁸⁰ Copyright 2021 American Chemical Society.

1.3.10. Alternative mass spectrometers for 2DMS

FT-ICR instruments are expensive mass spectrometers, the 2DMS experiment is also time-consuming. Few investigations have been made for implementing the 2D MS strategy on other ion trap mass analysers, which could be cheaper and quicker alternatives. 2DMS feasibility in a linear ion trap²¹⁰ was investigated using SIMON modelling software²¹¹. Instead of the Gaumann pulse sequence, stored waveform inverse Fourier transform techniques for radial excitation could be applied. In the model, the simulation of fragmentation with a laser at the centre of the linear ion trap showed that fragment abundance could be modulated according to the resonant frequency of their precursor, and therefore that the fragments can be associated with their precursors. The linear ion trap can be coupled to a time-of-flight, which would permit a quick acquisition of the 2DMS spectra and therefore the ability to do 2DMS with coupled liquid chromatography (LC/2DMS) for highly complex samples.

1.3.11. References

1. Cho, W. C. Proteomics technologies and challenges *Genomics Proteomics Bioinformatics* **2007**, *5*, 77-85.
2. Graves, P. R.; Haystead, T. A. Molecular biologist's guide to proteomics *Microbiol. Mol. Biol. Rev.* **2002**, *66*, 39-63.
3. O'Farrell, P. H. High resolution two-dimensional electrophoresis of proteins *J. Biol. Chem.* **1975**, *250*, 4007-4021.
4. Klose, J. Protein mapping by combined isoelectric focusing and electrophoresis of mouse tissues *Humangenetik* **1975**, *26*, 231-243.
5. Scheele, G. A. Two-dimensional gel analysis of soluble proteins. Characterization of guinea pig exocrine pancreatic proteins *J. Biol. Chem.* **1975**, *250*, 5375-5385.
6. Aebersold, R.; Mann, M. Mass spectrometry-based proteomics *Nature* **2003**, *422*, 198-207.
7. Chen, C.-H. W. Review of a current role of mass spectrometry for proteome research *Anal. Chim. Acta* **2008**, *624*, 16-36.

8. Edelman, G. M.; Cunningham, B. A.; Gall, W. E.; Gottlieb, P. D.; Rutishauser, U.; Waxdal, M. J. Pillars Article: The Covalent Structure of an Entire γ G Immunoglobulin Molecule. *Proc. Natl. Acad. Sci. USA*, 1969, 63: 78–85 *J Immunol* **2004**, 173, 5335-5342.
9. Silverton, E.; Navia, M. A.; Davies, D. R. Three-dimensional structure of an intact human immunoglobulin *PNAS* **1977**, 74, 5140-5144.
10. Ndassa, Y. M.; Orsi, C.; Marto, J. A.; Chen, S.; Ross, M. M. Improved immobilized metal affinity chromatography for large-scale phosphoproteomics applications *J. Proteome Res.* **2006**, 5, 2789-2799.
11. Isenman, D. E.; Painter, R. H.; Dorrington, K. J. The structure and function of immunoglobulin domains: studies with beta-2-microglobulin on the role of the intrachain disulfide bond *PNAS* **1975**, 72, 548-552.
12. Edmundson, A.; Ely, K.; Abola, E.; Schiffer, M.; Panagiotopoulos, N.; Deutsch, H. Conformational isomerism, rotational allomerism, and divergent evolution in immunoglobulin light chains *Fed Proc.* **1976**, 35, 2119-2123.
13. Jaton, J.; Riesen, W. The relationship between hypervariable regions, antigen-binding specificity and the three-dimensional structure of antibodies *Ann. Immunol.* **1976**, 127, 273-283.
14. Irani, V.; Guy, A. J.; Andrew, D.; Beeson, J. G.; Ramsland, P. A.; Richards, J. S. Molecular properties of human IgG subclasses and their implications for designing therapeutic monoclonal antibodies against infectious diseases *Mol. Immunol.* **2015**, 67, 171-182.
15. Smith, L. M.; Kelleher, N. L. Proteoform: a single term describing protein complexity *Nat. Methods* **2013**, 10, 186-187.
16. Hollas, M. A.; Robey, M. T.; Fellers, R. T.; LeDuc, R. D.; Thomas, P. M.; Kelleher, N. L. The Human Proteoform Atlas: a FAIR community resource for experimentally derived proteoforms *Nucleic Acids Res.* **2022**, 50, D526-D533.
17. Cohen, P. The origins of protein phosphorylation *Nat. Cell Biol.* **2002**, 4, E127-E130.
18. Pawson, T.; Scott, J. D. Protein phosphorylation in signaling—50 years and counting *Trends Biochem. Sci* **2005**, 30, 286-290.
19. Cohen, P. The regulation of protein function by multisite phosphorylation—a 25 year update *Trends Biochem. Sci* **2000**, 25, 596-601.

20. Zu, X.-L.; Besant, P.; Imhof, A.; Attwood, P. Mass spectrometric analysis of protein histidine phosphorylation *Amino acids* **2007**, *32*, 347-357.
21. Attwood, P.; Piggott, M.; Zu, X.; Besant, P. Focus on phosphohistidine *Amino acids* **2007**, *32*, 145-156.
22. Kleinnijenhuis, A. J.; Kjeldsen, F.; Kallipolitis, B.; Haselmann, K. F.; Jensen, O. N. Analysis of Histidine Phosphorylation Using Tandem MS and Ion– Electron Reactions *Anal. Chem.* **2007**, *79*, 7450-7456.
23. Cieśla, J.; Frączyk, T.; Rode, W. Phosphorylation of basic amino acid residues in proteins: important but easily missed *Acta Biochim. Pol.* **2011**, *58*, 137-148.
24. Hardman, G.; Perkins, S.; Brownridge, P. J.; Clarke, C. J.; Byrne, D. P.; Campbell, A. E.; Kalyuzhnyy, A.; Myall, A.; Evers, P. A.; Jones, A. R. Strong anion exchange-mediated phosphoproteomics reveals extensive human non-canonical phosphorylation *EMBO J.* **2019**, *38*, e100847.
25. Kim, D.; Pai, P.-J.; Creese, A. J.; Jones, A. W.; Russell, D. H.; Cooper, H. J. Probing the electron capture dissociation mass spectrometry of phosphopeptides with traveling wave ion mobility spectrometry and molecular dynamics simulations *JASMS* **2015**, *26*, 1004-1013.
26. Woods, A. S. The mighty arginine, the stable quaternary amines, the powerful aromatics, and the aggressive phosphate: their role in the noncovalent minuet *J. Proteome Res.* **2004**, *3*, 478-484.
27. Kumar, S.; Nussinov, R. Close-range electrostatic interactions in proteins *ChemBioChem* **2002**, *3*, 604-617.
28. Iakoucheva, L. M.; Radivojac, P.; Brown, C. J.; O'Connor, T. R.; Sikes, J. G.; Obradovic, Z.; Dunker, A. K. The importance of intrinsic disorder for protein phosphorylation *Nucleic Acids Res.* **2004**, *32*, 1037-1049.
29. Medzihradszky, K.; Darula, Z.; Perlson, E.; Fainzilber, M.; Chalkley, R.; Ball, H.; Greenbaum, D.; Bogyo, M.; Tyson, D.; Bradshaw, R. O-sulfonation of serine and threonine: mass spectrometric detection and characterization of a new posttranslational modification in diverse proteins throughout the eukaryotes *Mol. Cell Proteomics* **2004**, *3*, 429-440.
30. Wilm, M.; Neubauer, G.; Mann, M. Parent ion scans of unseparated peptide mixtures *Anal. Chem.* **1996**, *68*, 527-533.

31. Olsen, J. V.; Macek, B.; Lange, O.; Makarov, A.; Horning, S.; Mann, M. Higher-energy C-trap dissociation for peptide modification analysis *Nat. Methods* **2007**, *4*, 709-712.
32. Huddleston, M. J.; Annan, R. S.; Bean, M. F.; Carr, S. A. Selective detection of phosphopeptides in complex mixtures by electrospray liquid chromatography/mass spectrometry *JASMS* **1993**, *4*, 710-717.
33. Qin, J.; Chait, B. T. Identification and characterization of posttranslational modifications of proteins by MALDI ion trap mass spectrometry *Anal. Chem.* **1997**, *69*, 4002-4009.
34. Schlosser, A.; Pipkorn, R.; Bossemeyer, D.; Lehmann, W. D. Analysis of protein phosphorylation by a combination of elastase digestion and neutral loss tandem mass spectrometry *Anal. Chem.* **2001**, *73*, 170-176.
35. Paris, J.; Morgan, T. E.; Wootton, C. A.; Barrow, M. P.; O'Hara, J.; O'Connor, P. B. Facile determination of phosphorylation sites in peptides using two-dimensional mass spectrometry *Anal. Chem.* **2020**.
36. Mao, Y.; Zamdborg, L.; Kelleher, N. L.; Hendrickson, C. L.; Marshall, A. G. Identification of phosphorylated human peptides by accurate mass measurement alone *Int. J. Mass spectrom.* **2011**, *308*, 357-361.
37. Wind, M.; Wesch, H.; Lehmann, W. D. Protein phosphorylation degree: determination by capillary liquid chromatography and inductively coupled plasma mass spectrometry *Anal. Chem.* **2001**, *73*, 3006-3010.
38. Chen, M.; Su, X.; Yang, J.; Jenkins, C. M.; Cedars, A. M.; Gross, R. W. Facile identification and quantitation of protein phosphorylation via β -elimination and Michael addition with natural abundance and stable isotope labeled thiocholine *Anal. Chem.* **2010**, *82*, 163-171.
39. DeGnore, J. P.; Qin, J. Fragmentation of phosphopeptides in an ion trap mass spectrometer *JASMS* **1998**, *9*, 1175-1188.
40. Rožman, M. Modelling of the gas-phase phosphate group loss and rearrangement in phosphorylated peptides *J. Mass Spectrom.* **2011**, *46*, 949-955.
41. Beck, A.; Wagner-Rousset, E.; Ayoub, D.; Van Dorsselaer, A.; Sanglier-Cianferani, S. Characterization of therapeutic antibodies and related products *Anal. Chem.* **2013**, *85*, 715-736.

42. Li, F.; Vijayasankaran, N.; Shen, A.; Kiss, R.; Amanullah, A. Cell culture processes for monoclonal antibody production *MABs* **2010**, *2*, 466-479.
43. Yang, B.; Li, W.; Zhao, H.; Wang, A.; Lei, Y.; Xie, Q.; Xiong, S. Discovery and characterization of CHO host cell protease-induced fragmentation of a recombinant monoclonal antibody during production process development *J. Chromatogr. B* **2019**, *1112*, 1-10.
44. Dashivets, T.; Stracke, J.; Dengl, S.; Knaupp, A.; Pollmann, J.; Buchner, J.; Schlothauer, T. Oxidation in the complementarity-determining regions differentially influences the properties of therapeutic antibodies *MABs* **2016**, *8*, 1525-1535.
45. Szigeti, M.; Chapman, J.; Borza, B.; Guttman, A. Quantitative assessment of mAb Fc glycosylation of CQA importance by capillary electrophoresis *Electrophoresis* **2018**, *39*, 2340-2343.
46. Jefferis, R. Posttranslational modifications and the immunogenicity of biotherapeutics *J. Immunol. Res.* **2016**, 5358272.
47. Luo, Q.; Joubert, M. K.; Stevenson, R.; Ketchum, R. R.; Narhi, L. O.; Wypych, J. Chemical modifications in therapeutic protein aggregates generated under different stress conditions *J. Biol. Chem.* **2011**, *286*, 25134-25144.
48. Bertolotti-Ciarlet, A.; Wang, W.; Lownes, R.; Pristatsky, P.; Fang, Y.; McKelvey, T.; Li, Y.; Li, Y.; Drummond, J.; Prueksaritanont, T. Impact of methionine oxidation on the binding of human IgG1 to FcRn and Fcγ receptors *Mol. Immunol.* **2009**, *46*, 1878-1882.
49. Stracke, J.; Emrich, T.; Rueger, P.; Schlothauer, T.; Kling, L.; Knaupp, A.; Hertenberger, H.; Wolfert, A.; Spick, C.; Lau, W. A novel approach to investigate the effect of methionine oxidation on pharmacokinetic properties of therapeutic antibodies *MABs* **2014**, *6*, 1229-1242.
50. Wang, W.; Vlasak, J.; Li, Y.; Pristatsky, P.; Fang, Y.; Pittman, T.; Roman, J.; Wang, Y.; Prueksaritanont, T.; Ionescu, R. Impact of methionine oxidation in human IgG1 Fc on serum half-life of monoclonal antibodies *Mol. Immunol.* **2011**, *48*, 860-866.
51. Liu, H.; Nowak, C.; Andrien, B.; Shao, M.; Ponniah, G.; Neill, A. Impact of IgG Fc-Oligosaccharides on Recombinant Monoclonal Antibody Structure, Stability, Safety, and Efficacy *Biotechnol. Progr.* **2017**, *33*, 1173-1181.
52. Liu, L. Antibody glycosylation and its impact on the pharmacokinetics and pharmacodynamics of monoclonal antibodies and Fc-fusion proteins *J. Pharm. Sci.* **2015**, *104*, 1866-1884.

53. Chumsae, C.; Gaza-Bulseco, G.; Sun, J.; Liu, H. Comparison of methionine oxidation in thermal stability and chemically stressed samples of a fully human monoclonal antibody *J. Chromatogr. B* **2007**, *850*, 285-294.
54. Jacobitz, A. W.; Liu, Q.; Suravajjala, S.; Agrawal, N. J. Tryptophan oxidation of a monoclonal antibody under diverse oxidative stress conditions: distinct oxidative pathways favor specific tryptophan residues *J. Pharm. Sci.* **2021**, *110*, 719-726.
55. Reddie, K. G.; Carroll, K. S. Expanding the functional diversity of proteins through cysteine oxidation *Curr. Opin. Chem. Biol.* **2008**, *12*, 746-754.
56. Amano, M.; Kobayashi, N.; Yabuta, M.; Uchiyama, S.; Fukui, K. Detection of histidine oxidation in a monoclonal immunoglobulin gamma (IgG) 1 antibody *Anal. Chem.* **2014**, *86*, 7536-7543.
57. Pace, A. L.; Wong, R. L.; Zhang, Y. T.; Kao, Y.-H.; Wang, Y. J. Asparagine deamidation dependence on buffer type, pH, and temperature *J. Pharm. Sci.* **2013**, *102*, 1712-1723.
58. Alam, M. E.; Barnett, G. V.; Slaney, T. R.; Starr, C. G.; Das, T. K.; Tessier, P. M. Deamidation can compromise antibody colloidal stability and enhance aggregation in a pH-dependent manner *Mol. Pharm.* **2019**, *16*, 1939-1949.
59. Vlasak, J.; Bussat, M. C.; Wang, S.; Wagner-Rousset, E.; Schaefer, M.; Klinguer-Hamour, C.; Kirchmeier, M.; Corvaia, N.; Ionescu, R.; Beck, A. Identification and characterization of asparagine deamidation in the light chain CDR1 of a humanized IgG1 antibody *Anal. Biochem.* **2009**, *392*, 145-154.
60. Lima, M.; Baynes, J. Glycation *Encyclopedia of Biological Chemistry* **2013**, 405-411.
61. Yang, J.; Primack, R.; Frohn, M.; Wang, W.; Luan, P.; Retter, M. W.; Flynn, G. C. Impact of glycation on antibody clearance *AAPS J* **2015**, *17*, 237-244.
62. Brorson, K.; Jia, A. Y. Therapeutic monoclonal antibodies and consistent ends: terminal heterogeneity, detection, and impact on quality *Curr. Opin. Biotechnol.* **2014**, *30*, 140-146.
63. Faid, V.; Leblanc, Y.; Berger, M.; Seifert, A.; Bihoreau, N.; Chevreux, G. C-terminal lysine clipping of IgG1: impact on binding to human FcγRIIIa and neonatal Fc receptors *Eur J Pharm Sci* **2021**, *159*, 105730.
64. Thomson, J. J. In, Ed. [^]Eds.; The British Institute of Radiology, 1914, p[^]pp.
65. Aston, F. Isotopes and atomic weights *Nature* **1920**, *105*, 617-619.

66. Loo, J. A.; Loo, R. R. O.; Light, K. J.; Edmonds, C. G.; Smith, R. D. Multiply charged negative ions by electrospray ionization of polypeptides and proteins *Anal. Chem.* **1992**, *64*, 81-88.
67. Karas, M.; Hillenkamp, F. Laser desorption ionization of proteins with molecular masses exceeding 10,000 daltons *Anal. Chem.* **1988**, *60*, 2299-2301.
68. Karas, M.; Bachmann, D.; Bahr, U.; Hillenkamp, F. Matrix-assisted ultraviolet laser desorption of non-volatile compounds *Int. J. Mass Spectrom. Ion Processes* **1987**, *78*, 53-68.
69. Karas, M.; Bachmann, D.; Hillenkamp, F. Influence of the wavelength in high-irradiance ultraviolet laser desorption mass spectrometry of organic molecules *Anal. Chem.* **1985**, *57*, 2935-2939.
70. Tanaka, K.; Waki, H.; Ido, Y.; Akita, S.; Yoshida, Y.; Yoshida, T.; Matsuo, T. Protein and polymer analyses up to m/z 100 000 by laser ionization time-of-flight mass spectrometry *Rapid Commun. Mass Spectrom.* **1988**, *2*, 151-153.
71. Dreisewerd, K. The desorption process in MALDI *Chem. Rev.* **2003**, *103*, 395-426.
72. Hillenkamp, F.; Karas, M. The MALDI process and method *Maldi Ms* **2007**, *2*, 1-40.
73. Meng, C.; Mann, M.; Fenn, J. Of protons or proteins *Z. Phys. D: At., Mol. Clusters* **1988**, *10*, 361-368.
74. Mann, M.; Meng, C. K.; Fenn, J. B. Interpreting mass spectra of multiply charged ions *Anal. Chem.* **1989**, *61*, 1702-1708.
75. Fenn, J. B.; Mann, M.; Meng, C. K.; Wong, S. F.; Whitehouse, C. M. Electrospray ionization for mass spectrometry of large biomolecules *Science* **1989**, *246*, 64-71.
76. Johnson, T. H. Intensities of Molecular Beams *Nature* **1927**, *119*, 745-746.
77. Kebarle, P.; Tang, L. From ions in solution to ions in the gas phase-the mechanism of electrospray mass spectrometry *Anal. Chem.* **1993**, *65*, 972A-986A.
78. Konermann, L.; Ahadi, E.; Rodriguez, A. D.; Vahidi, S. In, Ed.^Eds.; ACS Publications, 2013, p^pp.
79. Jebanathirajah, J. A.; Pittman, J. L.; Thomson, B. A.; Budnik, B. A.; Kaur, P.; Rape, M.; Kirschner, M.; Costello, C. E.; O'Connor, P. B. Characterization of a new qQq-FTICR mass spectrometer for post-translational modification analysis and top-down tandem mass spectrometry of whole proteins *JASMS* **2005**, *16*, 1985-1999.
80. O'connor, P. B.; Pittman, J. L.; Thomson, B. A.; Budnik, B. A.; Cournoyer, J. C.; Jebanathirajah, J.; Lin, C.; Moyer, S.; Zhao, C. A new hybrid electrospray Fourier transform

mass spectrometer: design and performance characteristics *Rapid Communications in Mass Spectrometry: An International Journal Devoted to the Rapid Dissemination of Up-to-the-Minute Research in Mass Spectrometry* **2006**, *20*, 259-266.

81. Marshall, A. G.; Hendrickson, C. L.; Jackson, G. S. Fourier transform ion cyclotron resonance mass spectrometry: a primer *Mass Spectrom. Rev.* **1998**, *17*, 1-35.

82. Amster, I. J. Fourier transform mass spectrometry *J. Mass Spectrom.* **1996**, *31*, 1325-1337.

83. Comisarow, M. B.; Marshall, A. G. Selective-phase ion cyclotron resonance spectroscopy *Can. J. Chem.* **1974**, *52*, 1997-1999.

84. Comisarow, M. B.; Marshall, A. G. Fourier transform ion cyclotron resonance spectroscopy *Chem. Phys. Lett.* **1974**, *25*, 282-283.

85. Comisarow, M. B.; Marshall, A. G. Frequency-sweep Fourier transform ion cyclotron resonance spectroscopy *Chem. Phys. Lett.* **1974**, *26*, 489-490.

86. Marshall, A. G.; Grosshans, P. B. Fourier transform ion cyclotron resonance mass spectrometry: the teenage years *Anal. Chem.* **1991**, *63*, 215A-229A.

87. Qi, Y.; O'Connor, P. B. Data processing in Fourier transform ion cyclotron resonance mass spectrometry *Mass Spectrom. Rev.* **2014**, *33*, 333-352.

88. Nikolaev, E. N.; Kostyukevich, Y. I.; Vladimirov, G. N. Fourier transform ion cyclotron resonance (FT ICR) mass spectrometry: Theory and simulations *Mass Spectrom. Rev.* **2016**, *35*, 219-258.

89. Madeira, P. J. A.; Alves, P. A.; Borges, C. M. High resolution mass spectrometry using FTICR and orbitrap instruments *Fourier Transform–Materials Analysis* **2012**.

90. Marshall, A. G.; Roe, D. C. Theory of Fourier transform ion cyclotron resonance mass spectroscopy: Response to frequency-sweep excitation *J. Chem. Phys.* **1980**, *73*, 1581-1590.

91. Marshall, A. G.; Wang, T. C. L.; Ricca, T. L. Tailored excitation for Fourier transform ion cyclotron mass spectrometry *JACS* **1985**, *107*, 7893-7897.

92. Guan, S.; Marshall, A. G. Stored waveform inverse Fourier transform (SWIFT) ion excitation in trapped-ion mass spectrometry: Theory and applications *Int. J. Mass Spectrom. Ion Processes* **1996**, *157*, 5-37.

93. Comisarow, M. B. Signal modeling for ion cyclotron resonance *J. Chem. Phys.* **1978**, *69*, 4097-4104.

94. Zhang, L. K.; Rempel, D.; Pramanik, B. N.; Gross, M. L. Accurate mass measurements by Fourier transform mass spectrometry *Mass Spectrom. Rev.* **2005**, *24*, 286-309.
95. Shi, S. D.-H.; Hendrickson, C. L.; Marshall, A. G. Counting individual sulfur atoms in a protein by ultrahigh-resolution Fourier transform ion cyclotron resonance mass spectrometry: experimental resolution of isotopic fine structure in proteins *PNAS* **1998**, *95*, 11532-11537.
96. Nikolaev, E. N.; Boldin, I. A.; Jertz, R.; Baykut, G. Initial experimental characterization of a new ultra-high resolution FTICR cell with dynamic harmonization *JASMS* **2011**, *22*, 1125-1133.
97. Qi, Y.; Witt, M.; Jertz, R.; Baykut, G.; Barrow, M. P.; Nikolaev, E. N.; O'Connor, P. B. Absorption-mode spectra on the dynamically harmonized Fourier transform ion cyclotron resonance cell *Rapid Commun. Mass Spectrom.* **2012**, *26*, 2021-2026.
98. Marshall, A. G.; Rodgers, R. P. Petroleomics: Chemistry of the underworld *PNAS* **2008**, *105*, 18090-18095.
99. Barrow, M. P.; Witt, M.; Headley, J. V.; Peru, K. M. Athabasca oil sands process water: Characterization by atmospheric pressure photoionization and electrospray ionization Fourier transform ion cyclotron resonance mass spectrometry *Anal. Chem.* **2010**, *82*, 3727-3735.
100. Schaub, T. M.; Hendrickson, C. L.; Horning, S.; Quinn, J. P.; Senko, M. W.; Marshall, A. G. High-performance mass spectrometry: Fourier transform ion cyclotron resonance at 14.5 Tesla *Anal. Chem.* **2008**, *80*, 3985-3990.
101. Brenna, J.; Creasy, W. R. Experimental evaluation of apodization functions for quantitative Fourier transform mass spectrometry *Int. J. Mass Spectrom. Ion Processes* **1989**, *90*, 151-166.
102. Lutz, N. W.; Sweedler, J. V.; Wevers, R. A. Methodologies for metabolomics: experimental strategies and techniques, ed.; Cambridge University Press, 2013; Vol., p.
103. Tsybin, Y. O.; Witt, M.; Baykut, G.; Kjeldsen, F.; Håkansson, P. Combined infrared multiphoton dissociation and electron capture dissociation with a hollow electron beam in Fourier transform ion cyclotron resonance mass spectrometry *Rapid Commun. Mass Spectrom.* **2003**, *17*, 1759-1768.
104. Roepstorff, P.; Fohlman, J. Proposal for a common nomenclature for sequence ions in mass spectra of peptides *Biomed.* **1984**, *11*, 601-601.

105. Johnson, R. S.; Martin, S. A.; Biemann, K.; Stults, J. T.; Watson, J. T. Novel fragmentation process of peptides by collision-induced decomposition in a tandem mass spectrometer: differentiation of leucine and isoleucine *Anal. Chem.* **1987**, *59*, 2621-2625.
106. Papayannopoulos, I. A. The interpretation of collision-induced dissociation tandem mass spectra of peptides *Mass Spectrom. Rev.* **1995**, *14*, 49-73.
107. Jennings, K. R. The changing impact of the collision-induced decomposition of ions on mass spectrometry *Int. J. Mass spectrom.* **2000**, *200*, 479-493.
108. Shukla, A. K.; Futrell, J. H. Tandem mass spectrometry: dissociation of ions by collisional activation *J. Mass Spectrom.* **2000**, *35*, 1069-1090.
109. Wysocki, V. H. Internal energy effects in mass spectrometry. Purdue University, 1987.
110. Dongré, A. R.; Jones, J. L.; Somogyi, Á.; Wysocki, V. H. Influence of peptide composition, gas-phase basicity, and chemical modification on fragmentation efficiency: Evidence for the mobile proton model *JACS* **1996**, *118*, 8365-8374.
111. Loo, J. A.; Edmonds, C. G.; Smith, R. D. Tandem mass spectrometry of very large molecules. 2. Dissociation of multiply charged proline-containing proteins from electrospray ionization *Anal. Chem.* **1993**, *65*, 425-438.
112. Gu, C.; Tsapralis, G.; Brecci, L.; Wysocki, V. H. Selective gas-phase cleavage at the peptide bond C-terminal to aspartic acid in fixed-charge derivatives of Asp-containing peptides *Anal. Chem.* **2000**, *72*, 5804-5813.
113. Tsapralis, G.; Somogyi, Á.; Nikolaev, E. N.; Wysocki, V. H. Refining the model for selective cleavage at acidic residues in arginine-containing protonated peptides *Int. J. Mass spectrom.* **2000**, *195*, 467-479.
114. Gauthier, J.; Trautman, T.; Jacobson, D. Sustained off-resonance irradiation for collision-activated dissociation involving Fourier transform mass spectrometry. Collision-activated dissociation technique that emulates infrared multiphoton dissociation *Anal. Chim. Acta* **1991**, *246*, 211-225.
115. Zubarev, R. A.; Kelleher, N. L.; McLafferty, F. W. Electron capture dissociation of multiply charged protein cations. A nonergodic process *JACS* **1998**, *120*, 3265-3266.
116. Zhurov, K. O.; Fornelli, L.; Wodrich, M. D.; Laskay, Ü. A.; Tsybin, Y. O. Principles of electron capture and transfer dissociation mass spectrometry applied to peptide and protein structure analysis *Chem. Soc. Rev.* **2013**, *42*, 5014-5030.

117. Stensballe, A.; Jensen, O. N.; Olsen, J. V.; Haselmann, K. F.; Zubarev, R. A. Electron capture dissociation of singly and multiply phosphorylated peptides *Rapid Commun. Mass Spectrom.* **2000**, *14*, 1793-1800.
118. Qi, Y.; Volmer, D. A. Electron-based fragmentation methods in mass spectrometry: an overview *Mass Spectrom. Rev.* **2017**, *36*, 4-15.
119. Breuker, K.; Oh, H.; Horn, D. M.; Cerda, B. A.; McLafferty, F. W. Detailed unfolding and folding of gaseous ubiquitin ions characterized by electron capture dissociation *JACS* **2002**, *124*, 6407-6420.
120. Lin, C.; Cournoyer, J. J.; O'Connor, P. B. Probing the gas-phase folding kinetics of peptide ions by IR activated DR-ECD *JASMS* **2008**, *19*, 780-789.
121. Turecek, F. N C α Bond Dissociation Energies and Kinetics in Amide and Peptide Radicals. Is the Dissociation a Non-ergodic Process? *JACS* **2003**, *125*, 5954-5963.
122. Syka, J. E.; Coon, J. J.; Schroeder, M. J.; Shabanowitz, J.; Hunt, D. F. Peptide and protein sequence analysis by electron transfer dissociation mass spectrometry *PNAS* **2004**, *101*, 9528-9533.
123. Budnik, B. A.; Haselmann, K. F.; Zubarev, R. A. Electron detachment dissociation of peptide di-anions: an electron-hole recombination phenomenon *Chem. Phys. Lett.* **2001**, *342*, 299-302.
124. Anusiewicz, I.; Jasionowski, M.; Skurski, P.; Simons, J. Backbone and side-chain cleavages in electron detachment dissociation (EDD) *J. Phys. Chem. A* **2005**, *109*, 11332-11337.
125. Kjeldsen, F.; Silivra, O. A.; Ivonin, I. A.; Haselmann, K. F.; Gorshkov, M.; Zubarev, R. A. C α -C Backbone Fragmentation Dominates in Electron Detachment Dissociation of Gas-Phase Polypeptide Polyanions *Chem. Eur. J.* **2005**, *11*, 1803-1812.
126. Brodbelt, J. S. Photodissociation mass spectrometry: new tools for characterization of biological molecules *Chem. Soc. Rev.* **2014**, *43*, 2757-2783.
127. Brodbelt, J. S.; Wilson, J. J. Infrared multiphoton dissociation in quadrupole ion traps *Mass Spectrom. Rev.* **2009**, *28*, 390-424.
128. Little, D. P.; Speir, J. P.; Senko, M. W.; O'Connor, P. B.; McLafferty, F. W. Infrared multiphoton dissociation of large multiply charged ions for biomolecule sequencing *Anal. Chem.* **1994**, *66*, 2809-2815.

129. Talebpour, A.; Bandrauk, A.; Yang, J.; Chin, S. Multiphoton ionization of inner-valence electrons and fragmentation of ethylene in an intense Ti: sapphire laser pulse *Chem. Phys. Lett.* **1999**, *313*, 789-794.
130. Maitre, P.; Scuderi, D.; Corinti, D.; Chiavarino, B.; Crestoni, M. E.; Fornarini, S. Applications of Infrared Multiple Photon Dissociation (IRMPD) to the Detection of Posttranslational Modifications *Chem. Rev.* **2019**.
131. McCormack, A. L.; Somogyi, A.; Dongre, A. R.; Wysocki, V. H. Fragmentation of protonated peptides: surface-induced dissociation in conjunction with a quantum mechanical approach *Anal. Chem.* **1993**, *65*, 2859-2872.
132. Tsaprailis, G.; Nair, H.; Somogyi, Á.; Wysocki, V. H.; Zhong, W.; Futrell, J. H.; Summerfield, S. G.; Gaskell, S. J. Influence of secondary structure on the fragmentation of protonated peptides *JACS* **1999**, *121*, 5142-5154.
133. Ly, T.; Julian, R. R. Ultraviolet photodissociation: developments towards applications for mass-spectrometry-based proteomics *Angew. Chem. Int. Ed.* **2009**, *48*, 7130-7137.
134. Modzel, M.; Wollenberg, D. T. W.; Trelle, M. B.; Larsen, M. R.; Jørgensen, T. J. Ultraviolet Photodissociation of Protonated Peptides and Proteins Can Proceed with H/D Scrambling *Anal. Chem.* **2020**, *93*, 691-696.
135. Shaw, J. B.; Li, W.; Holden, D. D.; Zhang, Y.; Griep-Raming, J.; Fellers, R. T.; Early, B. P.; Thomas, P. M.; Kelleher, N. L.; Brodbelt, J. S. Complete protein characterization using top-down mass spectrometry and ultraviolet photodissociation *JACS* **2013**, *135*, 12646-12651.
136. Wong, S.; Meng, C.; Fenn, J. Multiple charging in electrospray ionization of poly(ethylene glycols) *J. Phys. Chem.* **1988**, *92*, 546-550.
137. Bogdanov, B.; Smith, R. D. Proteomics by FTICR mass spectrometry: top down and bottom up *Mass Spectrom. Rev.* **2005**, *24*, 168-200.
138. Mao, Y.; Valeja, S. G.; Rouse, J. C.; Hendrickson, C. L.; Marshall, A. G. Top-down structural analysis of an intact monoclonal antibody by electron capture dissociation-Fourier transform ion cyclotron resonance-mass spectrometry *Anal. Chem.* **2013**, *85*, 4239-4246.
139. Courchesne, P. L.; Jones, M. D.; Robinson, J. H.; Spahr, C. S.; McCracken, S.; Bentley, D. L.; Luethy, R.; Patterson, S. D. Optimization of capillary chromatography ion

- trap-mass spectrometry for identification of gel-separated proteins *Electrophoresis* **1998**, *19*, 956-967.
140. Masselon, C.; Anderson, G. A.; Harkewicz, R.; Bruce, J. E.; Pasa-Tolic, L.; Smith, R. D. Accurate mass multiplexed tandem mass spectrometry for high-throughput polypeptide identification from mixtures *Anal. Chem.* **2000**, *72*, 1918-1924.
141. Chapman, J. D.; Goodlett, D. R.; Masselon, C. D. Multiplexed and data-independent tandem mass spectrometry for global proteome profiling *Mass Spectrom. Rev.* **2014**, *33*, 452-470.
142. Hondius, D. C.; van Nierop, P.; Li, K. W.; Hoozemans, J. J.; van der Schors, R. C.; van Haastert, E. S.; van der Vies, S. M.; Rozemuller, A. J.; Smit, A. B. Profiling the human hippocampal proteome at all pathologic stages of Alzheimer's disease *Alzheimer's & dementia* **2016**, *12*, 654-668.
143. Domon, B.; Aebersold, R. Options and considerations when selecting a quantitative proteomics strategy *Nat. Biotechnol.* **2010**, *28*, 710.
144. Liu, H.; Sadygov, R. G.; Yates, J. R. A model for random sampling and estimation of relative protein abundance in shotgun proteomics *Anal. Chem.* **2004**, *76*, 4193-4201.
145. De Godoy, L. M.; Olsen, J. V.; Cox, J.; Nielsen, M. L.; Hubner, N. C.; Fröhlich, F.; Walther, T. C.; Mann, M. Comprehensive mass-spectrometry-based proteome quantification of haploid versus diploid yeast *Nature* **2008**, *455*, 1251-1254.
146. Hebert, A. S.; Richards, A. L.; Bailey, D. J.; Ulbrich, A.; Coughlin, E. E.; Westphall, M. S.; Coon, J. J. The one hour yeast proteome *Mol. Cell Proteomics* **2014**, *13*, 339-347.
147. Bekker-Jensen, D. B.; Kelstrup, C. D.; Batth, T. S.; Larsen, S. C.; Haldrup, C.; Bramsen, J. B.; Sørensen, K. D.; Høyer, S.; Ørntoft, T. F.; Andersen, C. L. An optimized shotgun strategy for the rapid generation of comprehensive human proteomes *Cell systems* **2017**, *4*, 587-599. e584.
148. Lange, V.; Picotti, P.; Domon, B.; Aebersold, R. Selected reaction monitoring for quantitative proteomics: a tutorial *Mol. Syst. Biol.* **2008**, *4*.
149. Doerr, A. Mass spectrometry-based targeted proteomics *Nat. Methods* **2013**, *10*, 23-23.
150. Cima, I.; Schiess, R.; Wild, P.; Kaelin, M.; Schüffler, P.; Lange, V.; Picotti, P.; Ossola, R.; Templeton, A.; Schubert, O. Cancer genetics-guided discovery of serum biomarker signatures for diagnosis and prognosis of prostate cancer *PNAS* **2011**, *108*, 3342-3347.

151. Addona, T. A.; Abbatiello, S. E.; Schilling, B.; Skates, S. J.; Mani, D.; Bunk, D. M.; Spiegelman, C. H.; Zimmerman, L. J.; Ham, A.-J. L.; Keshishian, H. Multi-site assessment of the precision and reproducibility of multiple reaction monitoring-based measurements of proteins in plasma *Nat. Biotechnol.* **2009**, *27*, 633.
152. Picotti, P.; Bodenmiller, B.; Mueller, L. N.; Domon, B.; Aebersold, R. Full dynamic range proteome analysis of *S. cerevisiae* by targeted proteomics *Cell* **2009**, *138*, 795-806.
153. Gorshkov, M. V.; Tolic, P.; Tolić, L. P.; Udseth, H. R.; Anderson, G. A.; Huang, B. M.; Bruce, J. E.; Prior, D. C.; Hofstadler, S. A.; Tang, L. Electrospray ionization—Fourier transform ion cyclotron resonance mass spectrometry at 11.5 tesla: Instrument design and initial results *JASMS* **1998**, *9*, 692-700.
154. Li, L.; Masselon, C. D.; Anderson, G. A.; Paša-Tolić, L.; Lee, S.-W.; Shen, Y.; Zhao, R.; Lipton, M. S.; Conrads, T. P.; Tolić, N. High-throughput peptide identification from protein digests using data-dependent multiplexed tandem FTICR mass spectrometry coupled with capillary liquid chromatography *Anal. Chem.* **2001**, *73*, 3312-3322.
155. McLafferty, F. W.; Stauffer, D. B.; Loh, S. Y.; Williams, E. R. Hadamard transform and "no-peak" enhancement in measurement of tandem Fourier transform mass spectra *Anal. Chem.* **1987**, *59*, 2212-2213.
156. Williams, E. R.; Loh, S. Y.; McLafferty, F. W.; Cody, R. B. Hadamard transform measurement of tandem Fourier-transform mass spectra *Anal. Chem.* **1990**, *62*, 698-703.
157. Haebel, S.; Gäumann, T. Difference measurements and shaped waveforms applied to Hadamard transform FT/ICR *Int. J. Mass Spectrom. Ion Process.* **1995**, *144*, 139-166.
158. Purvine, S.; Eppel*, J. T.; Yi, E. C.; Goodlett, D. R. Shotgun collision-induced dissociation of peptides using a time of flight mass analyzer *Proteomics* **2003**, *3*, 847-850.
159. Silva, J. C.; Gorenstein, M. V.; Li, G.-Z.; Vissers, J. P.; Geromanos, S. J. Absolute Quantification of Proteins by LCMSE: A Virtue of Parallel ms Acquisition* *S Mol. Cell Proteomics* **2006**, *5*, 144-156.
160. Gillet, L. C.; Navarro, P.; Tate, S.; Röst, H.; Selevsek, N.; Reiter, L.; Bonner, R.; Aebersold, R. Targeted data extraction of the MS/MS spectra generated by data-independent acquisition: a new concept for consistent and accurate proteome analysis *Mol. Cell Proteomics* **2012**, *11*.

161. Kang, Y.; Burton, L.; Lau, A.; Tate, S. SWATH-ID: An instrument method which combines identification and quantification in a single analysis *Proteomics* **2017**, *17*, 1500522.
162. Koopmans, F.; Ho, J. T.; Smit, A. B.; Li, K. W. Comparative analyses of data independent acquisition mass spectrometric approaches: DIA, WiSIM-DIA, and untargeted DIA *Proteomics* **2018**, *18*, 1700304.
163. Kiyonami, R.; Patel, B.; Senko, M.; Zabrouskov, V.; Egertson, J.; Ting, S.; MacCoss, M.; Rogers, J.; Hühmer, A. F. Large scale targeted protein quantification using WiSIM-DIA workflow on a orbitrap fusion tribrid mass spectrometer *Thermo Scientific Application Note 600* **2014**.
164. Panchaud, A.; Scherl, A.; Shaffer, S. A.; von Haller, P. D.; Kulasekara, H. D.; Miller, S. I.; Goodlett, D. R. Precursor acquisition independent from ion count: how to dive deeper into the proteomics ocean *Anal. Chem.* **2009**, *81*, 6481-6488.
165. Pfändler, P.; Bodenhausen, G.; Rapin, J.; Houriet, R.; Gäumann, T. Two-dimensional Fourier transform ion cyclotron resonance mass spectrometry *Chem. Phys. Lett.* **1987**, *138*, 195-200.
166. Marshall, A. G.; Wang, T.-C. L.; Ricca, T. L. Ion cyclotron resonance excitation/de-excitation: A basis for Stochastic fourier transform ion cyclotron mass spectrometry *Chem. Phys. Lett.* **1984**, *105*, 233-236.
167. Bax, A. Two-dimensional nuclear magnetic resonance in liquids **1981**.
168. Ernst, R. R.; Bodenhausen, G.; Wokaun, A. Principles of nuclear magnetic resonance in one and two dimensions, ed.; Clarendon Press Oxford, 1987; Vol. 14, p.
169. Gorcester, J.; Freed, J. H. Two-dimensional Fourier transform ESR spectroscopy *J. Chem. Phys.* **1986**, *85*, 5375-5377.
170. Meier, B.; Ernst, R. Elucidation of chemical exchange networks by two-dimensional NMR spectroscopy: the heptamethylbenzenonium ion *JACS* **1979**, *101*, 6441-6442.
171. Jeener, J.; Meier, B.; Bachmann, P.; Ernst, R. Investigation of exchange processes by two-dimensional NMR spectroscopy *J. Chem. Phys.* **1979**, *71*, 4546-4553.
172. Pfändler, P.; Bodenhausen, G.; Rapin, J.; Walser, M. E.; Gaeumann, T. Broad-band two-dimensional Fourier transform ion cyclotron resonance *JACS* **1988**, *110*, 5625-5628.

173. Bensimon, M.; Zhao, G.; Gäumann, T. A method to generate phase continuity in two-dimensional Fourier transform ion cyclotron resonance mass spectrometry *Chem. Phys. Lett.* **1989**, *157*, 97-100.
174. Ross III, C. W.; Guan, S.; Grosshans, P. B.; Ricca, T. L.; Marshall, A. G. Two-dimensional Fourier transform ion cyclotron resonance mass spectrometry/mass spectrometry with stored-waveform ion radius modulation *JACS* **1993**, *115*, 7854-7861.
175. Ross, C. W.; Simonsick, W. J.; Aaserud, D. J. Application of stored waveform ion modulation 2D-FTICR MS/MS to the analysis of complex mixtures *Anal. Chem.* **2002**, *74*, 4625-4633.
176. Sehgal, A. A.; Pelupessy, P.; Rolando, C.; Bodenhausen, G. Theory for spiralling ions for 2D FT-ICR and comparison with precessing magnetization vectors in 2D NMR *Phys. Chem. Chem. Phys.* **2016**, *18*, 9167-9175.
177. Guan, S.; Jones, P. R. A theory for two-dimensional Fourier-transform ion cyclotron resonance mass spectrometry *J. Chem. Phys.* **1989**, *91*, 5291-5295.
178. Cody, R.; Freiser, B. Collision-induced dissociation in a Fourier-transform mass spectrometer *Int. J. Mass Spectrom. Ion Processes* **1982**, *41*, 199-204.
179. van Agthoven, M. A.; Delsuc, M.-A.; Rolando, C. Two-dimensional FT-ICR/MS with IRMPD as fragmentation mode *Int. J. Mass spectrom.* **2011**, *306*, 196-203.
180. Marzullo, B. P.; Morgan, T. E.; Theisen, A.; Haris, A.; Wootton, C. A.; Perry, S. J.; Saeed, M.; Barrow, M. P.; O'Connor, P. B. Combining Ultraviolet Photodissociation and Two-Dimensional Mass Spectrometry: A Contemporary Approach for Characterizing Singly Charged Agrochemicals *Anal. Chem.* **2021**, *93*, 9462-9470.
181. van Agthoven, M. A.; Chiron, L.; Coutouly, M.-A.; Delsuc, M.-A.; Rolando, C. Two-dimensional ECD FT-ICR mass spectrometry of peptides and glycopeptides *Anal. Chem.* **2012**, *84*, 5589-5595.
182. Marzullo, B. P.; Morgan, T. E.; Wootton, C. A.; Perry, S. J.; Saeed, M.; Barrow, M. P.; O'Connor, P. B. Advantages of two-dimensional electron-induced dissociation and infrared multiphoton dissociation mass spectrometry for the analysis of agrochemicals *Anal. Chem.* **2020**, *92*, 11687-11695.
183. van Agthoven, M. A.; Lynch, A. M.; Morgan, T. E.; Wootton, C. A.; Lam, Y. P.; Chiron, L.; Barrow, M. P.; Delsuc, M.-A.; O'Connor, P. B. Can Two-Dimensional IR-ECD Mass Spectrometry Improve Peptide de Novo Sequencing? *Anal. Chem.* **2018**, *90*, 3496-3504.

184. van Agthoven, M. A.; Kilgour, D. P.; Lynch, A. M.; Barrow, M. P.; Morgan, T. E.; Wootton, C. A.; Chiron, L.; Delsuc, M.-A.; O'Connor, P. B. Phase relationships in two-dimensional mass spectrometry *JASMS* **2019**, *30*, 2594-2607.
185. Paris, J.; Morgan, T. E.; Marzullo, B. P.; Wootton, C. A.; Barrow, M. P.; O'Hara, J.; O'Connor, P. B. Two-Dimensional Mass Spectrometry Analysis of IgG1 Antibodies *JASMS* **2021**.
186. van Agthoven, M. A.; Lam, Y. P.; O'Connor, P. B.; Rolando, C.; Delsuc, M.-A. Two-dimensional mass spectrometry: new perspectives for tandem mass spectrometry *Eur. Biophys. J.* **2019**, 1-17.
187. Chiron, L.; Coutouly, M.-A.; Starck, J.-P.; Rolando, C.; Delsuc, M.-A. SPIKE a Processing Software dedicated to Fourier Spectroscopies *arXiv:1608.06777 [physics.comp-ph]* **2016**.
188. *Ultra-high resolution 2D-FTMS for truly DIA analysis of challenging systems*, Wootton, C. A.; Morgan, T. E.; Marzullo, B. P.; Lam, Y. P. Y.; Lozano, D. C. P.; Theisen, A.; Haris, A.; Barrow, M. P.; O'Connor, P. B., 298156, Proceedings of the 67th ASMS Conference on Mass Spectrometry and Allied Topics, Atlanta, Georgia, June 2-6, 2019;
189. Paris, J.; Morgan, T. E.; Wootton, C. A.; Barrow, M. P.; O'Hara, J.; O'Connor, P. B. Facile determination of phosphorylation sites in peptides using two-dimensional mass spectrometry *Anal. Chem.* **2020**, *92*, 6817-6821.
190. van der Rest, G.; Marshall, A. G. Noise analysis for 2D tandem Fourier transform ion cyclotron resonance mass spectrometry *Int. J. Mass spectrom.* **2001**, *210*, 101-111.
191. Reiger, S. Starlight scintillation and atmospheric turbulence *The Astronomical Journal* **1963**, *68*, 395.
192. Young, A. T. *The Astronomical Journal* **1967**, *72*, 747.
193. van Agthoven, M. A.; Chiron, L.; Coutouly, M.-A.; Sehgal, A. A.; Peluopessy, P.; Delsuc, M.-A.; Rolando, C. Optimization of the discrete pulse sequence for two-dimensional FT-ICR mass spectrometry using infrared multiphoton dissociation *Int. J. Mass spectrom.* **2014**, *370*, 114-124.
194. Diop, A.; Briguët, A.; Graveron-Demilly, D. Automatic in vivo NMR data processing based on an enhancement procedure and linear prediction method *Magn Reson Med* **1992**, *27*, 318-328.

195. Diop, A.; Zaimwadghiri, Y.; Briguet, A.; Graverondemilly, D. Improvements of quantitation by using the Cadzow enhancement procedure prior to any linear-prediction methods *J. Magn. Reson., Ser B* **1994**, *105*, 17-24.
196. van Agthoven, M. A.; Coutouly, M. A.; Rolando, C.; Delsuc, M. A. Two-dimensional Fourier transform ion cyclotron resonance mass spectrometry: reduction of scintillation noise using Cadzow data processing *Rapid Commun. Mass Spectrom.* **2011**, *25*, 1609-1616.
197. Chiron, L.; van Agthoven, M. A.; Kieffer, B.; Rolando, C.; Delsuc, M.-A. Efficient denoising algorithms for large experimental datasets and their applications in Fourier transform ion cyclotron resonance mass spectrometry *PNAS* **2014**, *111*, 1385-1390.
198. Halper, M.; Delsuc, M.-A.; Breuker, K.; van Agthoven, M. A. Narrowband Modulation Two-Dimensional Mass Spectrometry and Label-Free Relative Quantification of Histone Peptides *Anal. Chem.* **2020**, *92*, 13945-13952.
199. Bray, F.; Bouclon, J.; Chiron, L.; Witt, M.; Delsuc, M.-A.; Rolando, C. Nonuniform Sampling Acquisition of Two-Dimensional Fourier Transform Ion Cyclotron Resonance Mass Spectrometry for Increased Mass Resolution of Tandem Mass Spectrometry Precursor Ions *Anal. Chem.* **2017**, *89*, 8589-8593.
200. Delsuc, M.-A.; Breuker, K.; van Agthoven, M. A. Phase Correction for Absorption Mode Two-Dimensional Mass Spectrometry *Molecules* **2021**, *26*, 3388.
201. van Agthoven, M. A.; Barrow, M. P.; Chiron, L.; Coutouly, M.-A.; Kilgour, D.; Wootton, C. A.; Wei, J.; Soulby, A.; Delsuc, M.-A.; Rolando, C. Differentiating fragmentation pathways of cholesterol by two-dimensional Fourier transform ion cyclotron resonance mass spectrometry *JASMS* **2015**, *26*, 2105-2114.
202. Van Agthoven, M. A.; Delsuc, M.-A.; Bodenhausen, G.; Rolando, C. Towards analytically useful two-dimensional Fourier transform ion cyclotron resonance mass spectrometry *Anal. Bioanal. Chem.* **2013**, *405*, 51-61.
203. Simon, H.; van Agthoven, M.; Lam, P.; Floris, F.; Chiron, L.; Delsuc, M.-A.; Rolando, C.; Barrow, M.; O'Connor, P. Uncoiling collagen: a multidimensional mass spectrometry study *Analyst* **2016**, *141*, 157-165.
204. Floris, F.; van Agthoven, M.; Chiron, L.; Soulby, A. J.; Wootton, C. A.; Lam, Y. P.; Barrow, M. P.; Delsuc, M.-A.; O'Connor, P. B. 2D FT-ICR MS of calmodulin: a top-down and bottom-up approach *JASMS* **2016**, *27*, 1531-1538.

205. Floris, F.; van Agthoven, M. A.; Chiron, L.; Wootton, C. A.; Lam, P. Y. Y.; Barrow, M. P.; Delsuc, M.-A.; O'Connor, P. B. Bottom-up two-dimensional electron-capture dissociation mass spectrometry of calmodulin *JASMS* **2018**, *29*, 207-210.
206. Floris, F.; Chiron, L.; Lynch, A. M.; Barrow, M. P.; Delsuc, M.-A.; O'Connor, P. B. Application of Tandem Two-Dimensional Mass Spectrometry for Top-Down Deep Sequencing of Calmodulin *JASMS* **2018**, 1-6.
207. Floris, F.; Chiron, L.; Lynch, A. M.; Barrow, M. P.; Delsuc, M.-A.; O'Connor, P. B. Top-Down Deep Sequencing of Ubiquitin using two-dimensional mass spectrometry *Anal. Chem.* **2018**, *90*, 7302-7309.
208. Floris, F.; Vallotto, C.; Chiron, L.; Lynch, A. M.; Barrow, M. P.; Delsuc, M.-A.; O'Connor, P. B. Polymer analysis in the second dimension: preliminary studies for the characterization of polymers with 2D MS *Anal. Chem.* **2017**, *89*, 9892-9899.
209. Morgan, T. E.; Wootton, C. A.; Marzullo, B.; Paris, J.; Kerr, A.; Ellacott, S. H.; van Agthoven, M. A.; Barrow, M. P.; Bristow, A. W.; Perrier, S. Characterization across a dispersity: polymer mass spectrometry in the second dimension *JASMS* **2021**, *32*, 2153-2161.
210. Douglas, D. J.; Frank, A. J.; Mao, D. Linear ion traps in mass spectrometry *Mass Spectrom. Rev.* **2005**, *24*, 1-29.
211. van Agthoven, M. A.; O'Connor, P. B. Two-dimensional mass spectrometry in a linear ion trap, an in silico model *Rapid Commun. Mass Spectrom.* **2017**, *31*, 674-684.

CHAPTER 2.

Multimodal tandem mass spectrometry techniques for the
analysis of phosphopeptides

3.1. Declaration

This chapter consist of one published research article:

Paris, J.; Theisen, A.; Marzullo, B., P.; Haris, A.; Morgan, T. E.; Barrow, M. P.; O'Hara, J.; O'Connor, P. B. Multimodal tandem mass spectrometry techniques for the analysis of phosphopeptides. *J. Am. Soc. Mass. Spectrom.* 2022.

Except for minor adjustments to aid incorporation into this thesis and extra Figures, the article has been reproduced unchanged. The tables of assignments are at the end of the chapter.

As a first author I carried out all experiments, analysed all data, and prepared all Figures as well as the manuscript. AT trained me on UVPD, BPM trained me on EDD. AT and AH installed the UVPD laser. MPB, JOH and PBOC were involved in project management and editing the final manuscript.

Multimodal tandem mass spectrometry techniques for the analysis of phosphopeptides

JASMS, 2022, doi: 10.1021/jasms.1c00353

Johanna Parist, Alina Theisent, Bryan P. Marzullo†, Anisha Harist, Tomos E. Morgant, Mark P. Barrow†, John O'Hara‡, Peter B. O'Connor†*

†University of Warwick, Department of Chemistry, Coventry, CV4 7AL, United Kingdom

‡UCB, 216 Bath Road, Slough, SL1 3WE, United Kingdom

*Corresponding author email address: p.oconnor@warwick.ac.uk

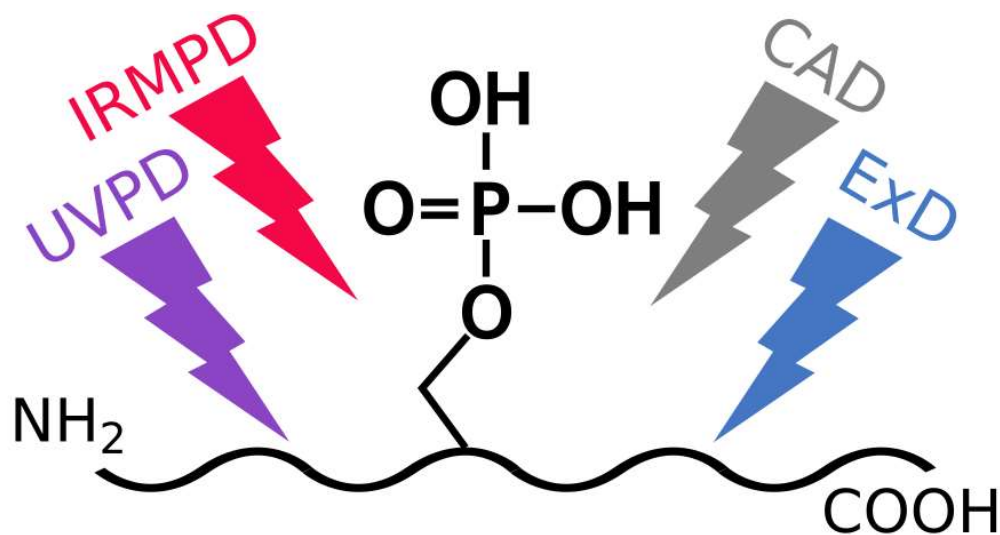


Figure 2. 1: Graphical Abstract

3.2. Abstract

Collisionally-activated dissociation (CAD), infrared multiphoton dissociation (IRMPD), ultraviolet photodissociation (UVPD), electron capture dissociation (ECD) and electron detachment dissociation (EDD) experiments were conducted on a set of phosphopeptides, in a Fourier transform ion cyclotron resonance (FT-ICR) mass spectrometer. The fragmentation patterns were compared and varied according to the fragmentation mechanisms and the composition of the peptides. CAD and IRMPD produced similar fragmentation profiles of the phosphopeptides, while UVPD produced a large number of complementary fragments. Electron-based dissociation (ExD) techniques displayed lower fragmentation efficiencies, despite retaining the labile phosphate group, and drastically different fragmentation profiles. EDD produced complex spectra whose interpretation proved challenging.

3.3. Introduction

Phosphorylation is a posttranslational modification which occurs predominantly on serine, threonine, and tyrosine amino acid residues. Non-canonical phosphorylation may occur on other residues such as histidine, lysine, and arginine through phosphoramidate bonds, and on aspartic acid and glutamic acid through anhydride linkages.¹⁻⁵ The phosphoryl group is a labile modification that can be lost during the mass spectrometry experiment, either by the hydrolysis of the phosphoramidate group by acidic additives frequently added to aid protonation of the analyte molecules during electrospray, or by the dissociation technique itself. Loss of phosphoric acid (H_3PO_4) or metaphosphoric acid (HPO_3) can be observed in positive mode and loss of phosphite (PO_3) in negative mode. When the loss is induced by the fragmentation techniques, the phosphopeptides can be identified by immonium ions,⁶⁻⁸ or the neutral losses can be used as a signature.⁹⁻¹¹ Other strategies also allow the identification of phosphopeptides by accurate mass alone, using the mass defect of the phosphorus-31 isotope, ^{31}P (-0.0262 Da)¹², or with the specific detection of ^{31}P by ICP-MS,¹³ or by tagging the phosphate groups.¹⁴ However, the loss of the phosphate from the sequence ions makes phosphorylation site assignment difficult. The loss depends on the fragmentation techniques, the charge states of the precursor, the residue the phosphate is linked to, and the neighboring amino acids.^{15, 16}

During collisionally-activated dissociation, the ions undergo multiple collisions with inert gas atoms such as argon, increasing the internal energy of the precursor ion until reaching a threshold for dissociation.¹⁷ The fragmentation occurs via a low energy proton rearrangement resulting in the destabilization and cleavage of an amide bond (b and y type fragments). The phosphoryl group is favored as a site for protonation, resulting in the cleavage of the labile group and a domination of the spectra by the loss of phosphoric acid (H₃PO₄). In-beam CAD in a collision cell, such as CAD in a triple quadrupole or an FT-ICR instrument, or higher-energy collisional dissociation (HCD),^{7,18} the collisions are more energetic than resonant-excitation CAD used in radio frequency quadrupole ion traps,¹⁹ resulting in greater intensities of sequence-informative b, y ions, compared to the phosphate neutral loss intensities. Evidence of rearrangement reactions in the gas-phase has been exhibited in a broad range of peptides, under resonant CAD conditions.²⁰ Furthermore, rearrangement of the phosphoryl group to an alternate hydroxyl-containing peptide has also been observed.¹⁹ The timescale of the activation could also allow the transfer of the phosphate group to another residue in resonant CAD experiments.¹⁵

Electron based fragmentation techniques are radical-driven dissociation methods, where the labile groups are often retained,²¹⁻²³ allowing identification and localization of the phosphorylation. Electron capture dissociation (ECD) involves the capture of a low-energy electron by a multiply-charged precursor cation.²⁴ Fragmentation of the N-C α bond of the peptide backbone produces predominantly c- and z-type product ions. Electron detachment dissociation (EDD) consists of the use of electrons with kinetic energies above 10 eV to detach electrons from a negatively-charged precursor in negative mode analysis.²⁵ The negative charges are located at the amide nitrogen bond along the backbone, and therefore produce a•/x fragments, or at the amino acid side chain, producing neutral losses.^{26, 27} Fragmentation efficiency and sequence coverage with electron based techniques are lower when a peptide is phosphorylated.^{28, 29} On phosphopeptides with basic residues, the phosphate group can exist in a deprotonated form and can form salt-bridges with protonated side chains.^{30, 31} Salt-bridges are electrostatic interactions between amino acids of different charges.³² These strong noncovalent bonds stabilize the phosphopeptide ion, additional electron energy is therefore necessary to dissociate it.³³⁻³⁵ Basic residues are common around phosphorylation sites suggesting that salt-bridges could be part of their formation.³⁶

Different lasers can be used to dissociate ions. In infrared multiphoton dissociation (IRMPD),³⁷⁻³⁹ ions are irradiated using a CO₂ laser. The sequential absorption of 10.6 μm photons increases the internal energy of ions (0.117 eV per photon) until dissociation occurs. It is a slow heating method, similar to CAD, and the energy is distributed throughout the peptide, resulting in bond cleavage at the weakest points (b and y fragments, labile post translational modifications).^{40, 41} Infrared (IR) radiation is resonant with the phosphate vibrational modes of the phosphorylated peptide,^{42, 43} leading to enhanced fragmentation of phosphopeptides.⁴⁴⁻⁴⁷ Ultraviolet photodissociation (UVPD) at 193 nm deposits the required energy for dissociation within the absorption of a single photon⁴⁸ (6.4 eV per photon) emitted through a nanosecond-scale laser pulse.⁴⁹ The peptide absorbs the high-energy photon at the chromophore and the protein backbone amide group,⁵⁰ accessing many dissociation pathways, leading to the generation of a/x, b/y, and c/z complementary ion pairs.^{51, 52} The fast fragmentation of the peptide reduces the frequency of phosphate group loss.⁵³

The 12 T solariX FT-ICR mass spectrometer is a versatile instrument. CAD fragmentation is possible in the front-end. The addition of lasers allows fragmentation via IRMPD and UVPD in the ICR cell.^{54, 55} Finally, the hollow beam electrode allows ExD fragmentation. CAD, IRMPD, UVPD, ECD, and EDD fragmentation of a phosphoserine, a phosphothreonine and a phosphotyrosine peptide were conducted and compared in this chapter.

3.4. Experimental section

2.4.1. Material

MS Phosphomix 1 and 2 Light were obtained from Sigma Aldrich (MSP1L-1VL and MSP2L-1VL). Water was purified by a Millipore Direct-Q purification system (Merck Millipore, MA, USA). Acetonitrile was obtained from VWR chemicals (CAS: 75-05-8). Formic acid (FA) was obtained from Sigma-Aldrich (CAS: 64-18-6). The Phosphomix were diluted into 80:20 water:ACN + 0.1 % FA, the final concentration of the peptides was 0.2 μM.

2.4.2. Ionisation

The samples were ionized using a custom nano electrospray ionization source (nESI). 10-20 μL of sample were loaded into a pulled glass capillary tip with several μm open orifice⁵⁶ and analysed with a 12 T Bruker solariX FTICR mass spectrometer (Bruker Daltonik GmbH, Bremen, Germany). The applied capillary voltage was 500 V.

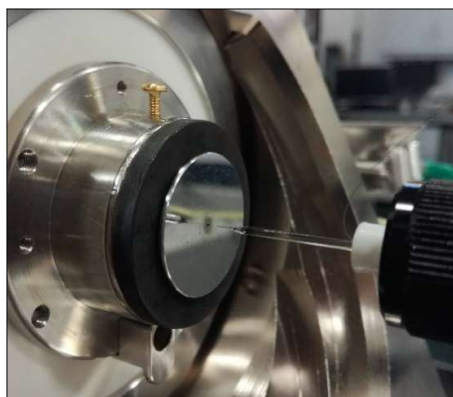


Figure 2. 2: NanoESI setup.

2.4.3. Tandem MS parameters

For CAD, argon was used as the neutral collision gas ($\sim 7 \times 10^{-6}$ mbar). Ions were isolated in the quadrupole, accumulated and fragmented in the collision cell with an optimized collision potential, and then analyzed in the infinity cell.⁵⁵

For ECD, IRMPD, and UVPD, the peptides were isolated in the quadrupole, accumulated in the collision cell, and transferred into the ICR cell where the ions were fragmented, excited, and detected.

For ECD, ions were irradiated with electrons from a 1.5 A indirectly heated hollow cathode by applying a bias voltage of 1.2V. Below 1.2V, no fragmentation was observed. Various pulse lengths were applied, the best spectra are shown in the Figures. Higher and lower pulse lengths than the optimized ones, shown lower number of sequence ions. IRMPD fragmentation was achieved using a continuous wave, 25 W, CO_2 laser (Synrad Inc., Mulkiteo, Washington, USA). UVPD was performed using a 193 nm excimer laser (ExciStar XS Coherent, 500 Hz). Ions were irradiated with a varying number of shots with a pulse energy of 5 mJ (measured at laser output).

RDSLGPtYSSR was quadrupole isolated at m/z 612.5 ± 4 , and the acquired mass-to-charge ratio range was m/z 147.4-3000. EVQAEQPSSpSSPR was quadrupole isolated at m/z 741.0 ± 4 , and the acquired mass-to-charge ratio range was m/z 98.3-3000. VIEDNEpYTAR was quadrupole isolated at m/z 647.0 ± 10 , and the acquired mass-to-charge ratio range was m/z 98.3-1300. The mass spectrometer was tuned to get the best signal for each spectrum and data was acquired at different fragmentation parameters. The spectra with the best fragmentation efficiency, with a high number of sequence ions, low internal fragmentation, and phosphate loss, are shown in this chapter and compared. 4M (222, 22-bit) data points were acquired for each spectrum. For CAD, IRMPD and UVPD 100 scans were averaged, for ECD 200 scans, and for EDD 500 scans, to achieve a desirable signal-to-noise ratio. The data was internally calibrated using known fragment peaks with a quadratic calibration function in the Bruker DataAnalysis v4.3 software (Bruker Daltonics GmbH, Bremen, Germany).

3.5. Results and discussion

The three phosphopeptides were quadrupole isolated, fragmented and characterized. In the spectra, only fragments without neutral losses are shown on the cleavage diagrams. On the fragmentation intensity profiles, black and grey represent the summed percentages of abc and xyz, respectively.

2.5.1. RDSLGPtYSSR – Phosphothreonine peptide

CAD and IRMPD fragmentation spectra of doubly-charged RDSLGPtYSSR are shown in Figure 2.3 and 2.4. The slow heating dissociation techniques spectra show high similarities and have similar fragmentation profiles. Both fragmentation techniques localized the phosphorylation site at the threonine. The highest intensity sequence ions were b2 for IRMPD and y4 for both fragmentation techniques, demonstrating preferential cleavage at DS and pTY linkages. RDSLGPtYSSR is composed of two basic arginine residues, which sequestered the two ionizing protons. Therefore, no mobile proton and no charge delocalization occurred, making the charge-remote dissociation channels competitive. The peptide dissociates selectively at the C-terminus of the two acidic residues (aspartic acid and phosphothreonine) as shown in previous fragmentation studies.^{41, 57, 58}

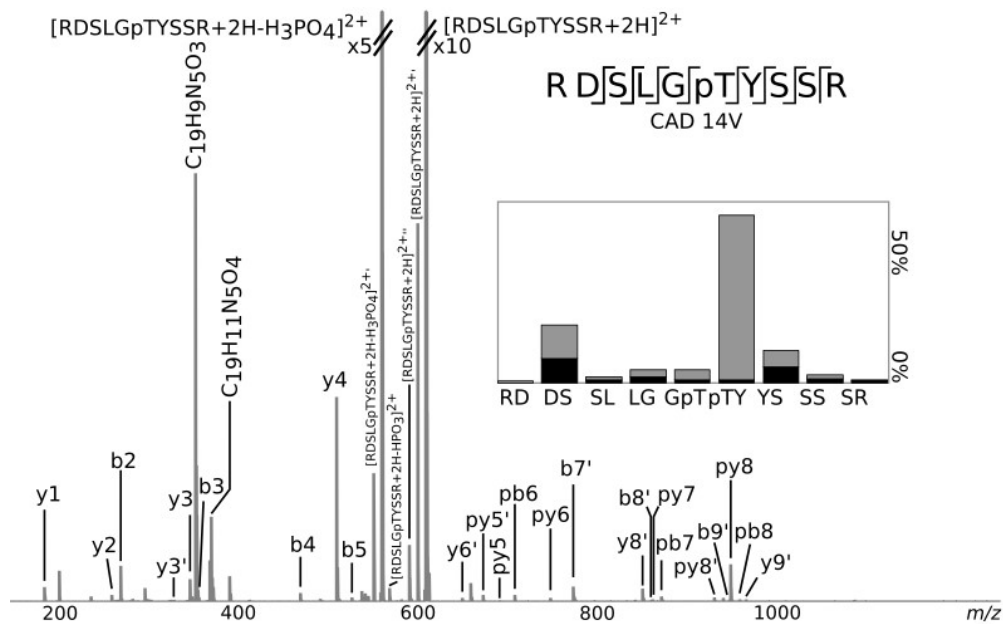


Figure 2. 3: CAD fragmentation of RDSLGPpTYSSR. p: fragment with phosphate attached. ' loss of water.

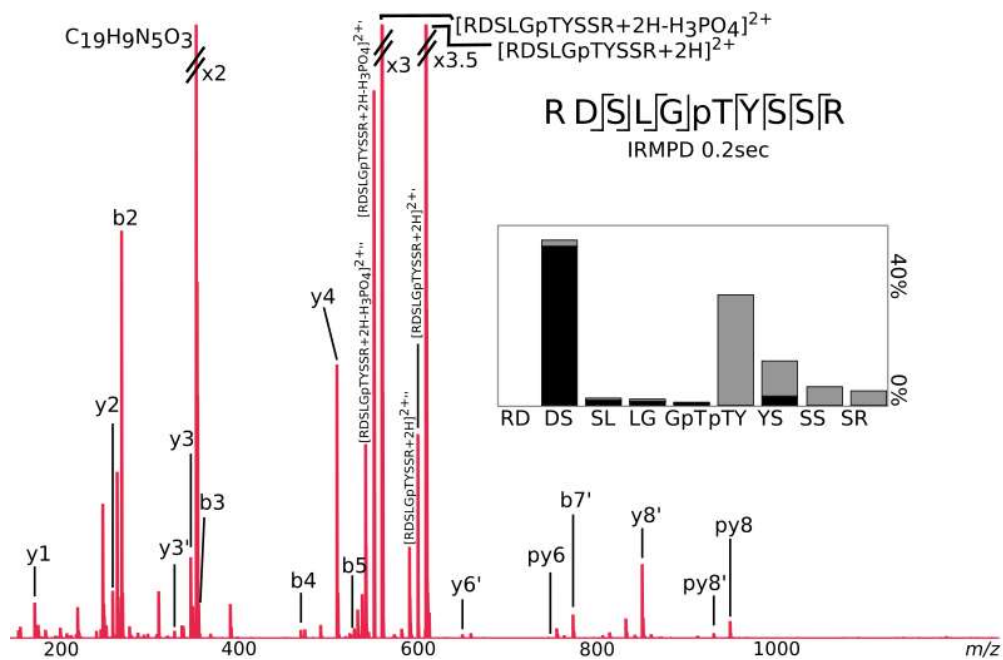


Figure 2. 4: IRMPD fragmentation of RDSLGPpTYSSR. p: fragment with phosphate attached. ' loss of water.

Cleavage between the R and D residue was not observed. Neutral loss of H_3PO_4 was prominent with CAD and IRMPD (27.4% and 83.7% respectively, in the $[M+2H-H_3PO_4]^{2+}/[M+2H]^{2+}$ ratio) and CAD also produced loss of HPO_3 (0.2% $[M+2H-HPO_3]^{2+}/[M+2H]^{2+}$). Fragments with water losses (' refers to loss of water) were observed: y_5-9' , b_7-9' for CAD, y_5-7' and b_7' for IRMPD, representing 10.0% and 3.8% respectively of the identified sequence ion intensities. However, the fragments have their phosphorylated counterpart, and the phosphorylation site is easily identified on the threonine. Both fragmentation techniques produced internal fragments identified as $C_{19}H_9N_5O_3^+$ for CAD and IRMPD (~ -0.17 ppm for both), and $C_{19}H_{11}N_5O_4^+$ for CAD (-0.07 ppm). The percentage of internal fragments and rearrangements (the percentage of unknown peaks and internal fragments compared to the total ion intensity) was 3.5% for CAD, and 25.6% for IRMPD with the prominence of $C_{19}H_9N_5O_3$ in the IRMPD spectrum.

For peptides with no mobile proton, it has been shown that the hydrogen bond between the phosphate group and the protonated arginine residue can lead to the gas-phase rearrangement of the phosphate to a different residue.¹⁹ However, no ions resulting from such rearrangement were observed in the spectra (y_2 , y_3 , and y_4 with phosphate).

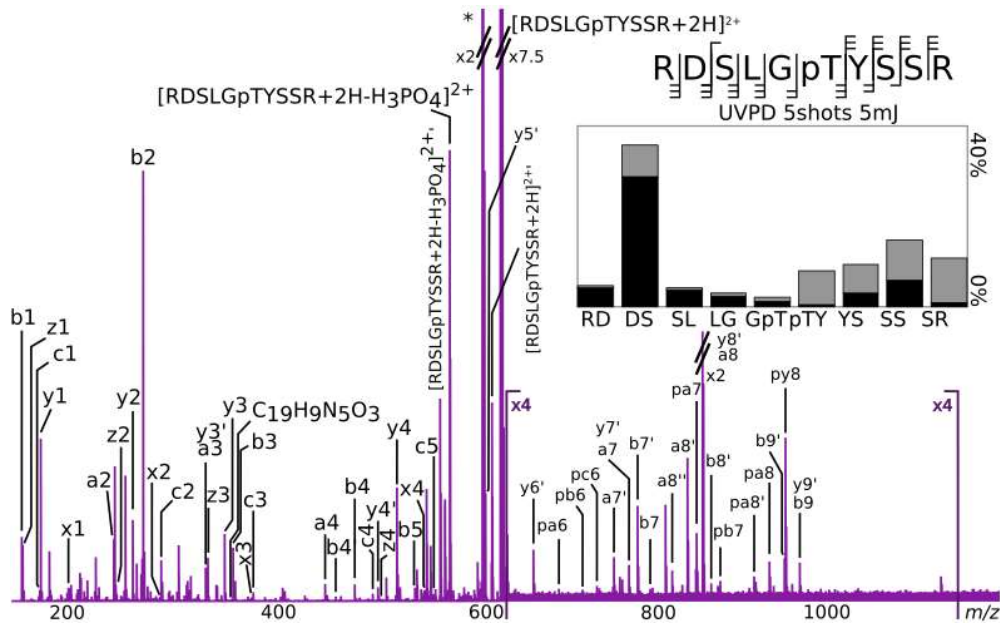


Figure 2. 5: UVPD fragmentation of RDSLGPpTYSSR. p: fragment with phosphate attached. ' loss of water. " loss of two water molecules.

UVPD (Figure 2.5) produced a large number of complementary fragments, leading to 100% cleavage coverage. The fragmentation profile shows high intensity fragments originating from the DS linkage. UVPD did not dissociate selectively at the pTY linkage compared to the slow heating techniques.

UVPD produced an internal fragment assigned as $C_{19}H_{19}N_5O_3$ (-0.17 ppm), and 28.3% of the intensity of the peaks observed were due to internal fragmentation (the high percentage is due to the unidentified high intensity m/z 593.15759). UVPD lost less of the phosphate group from the precursor (9.0%) than the slow heating methods, but more of the identified fragments were dephosphorylated (17.5%). However, phosphorylated sequence ions allowed the identification of the phosphorylated site at the threonine.

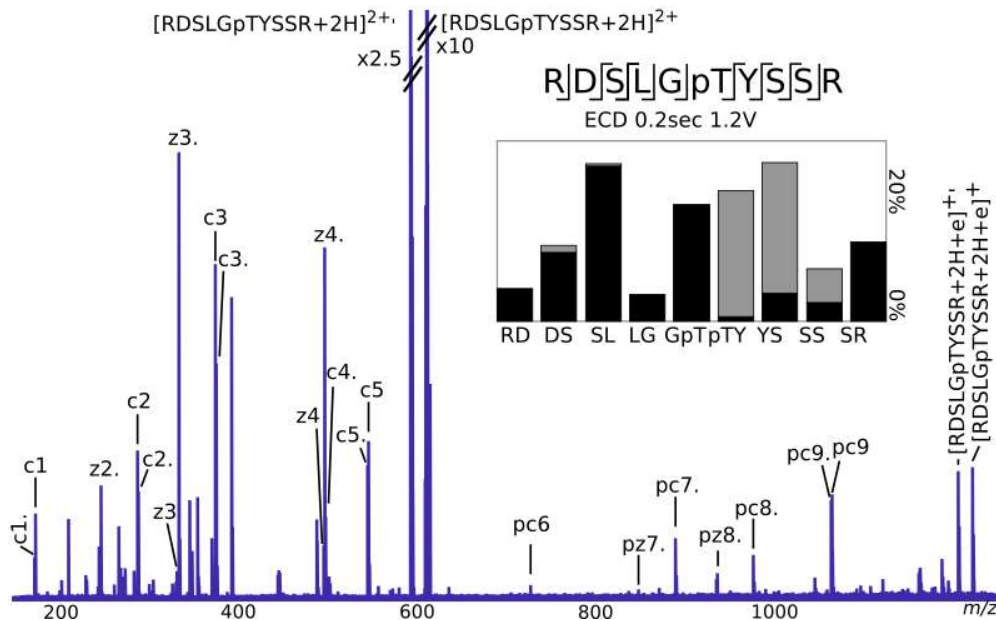


Figure 2. 6: ECD fragmentation of RDSLGLpTYSSR. p: fragment with phosphate attached.

The ECD fragmentation profiles show more homogenous fragmentation through the backbone of the peptide, leading to 100% cleavage coverage. No selective cleavage was observed compared to the other techniques. There was no loss of phosphate from the precursor or the fragments, permitting the identification of the phosphorylation site at the threonine. Starting from a similar precursor intensity, prior to fragmentation, ECD required the accumulation of more scans than the other fragmentation techniques due to fragment peaks being observed with lower intensities (~ between 2 to 5 times lower). This phenomenon is expected with ECD fragmentation, but is also possibly enhanced by the phosphorylation.

2.5.2. EVQAEQPSSpSSPR – Phosphoserine peptide

Fragmentation spectra of the doubly-charged EVQAEQPSSpSSPR are shown in Figure 2.7, 2.8, 2.9 and 2.10. CAD and IRMPD techniques produced similar fragmentation profiles, with high abundance complementary fragments arising from the EQ (py8/b5) and QP (py7/b6) cleavages. The glutamic acid residue has been shown to produce similar selective fragmentation to asparagine.⁵⁹ With slow heating methods, the high gas-phase basicity of the proline compared to the other residues with alkyl sidechains enhances the dissociation of the amide bond at the N-terminus side.⁶⁰ As expected, the dominant fragment ion in the CAD and IRMPD spectra was the γ fragment between the Q and P residues (denoted py7 because it is a phosphorylated γ ion).

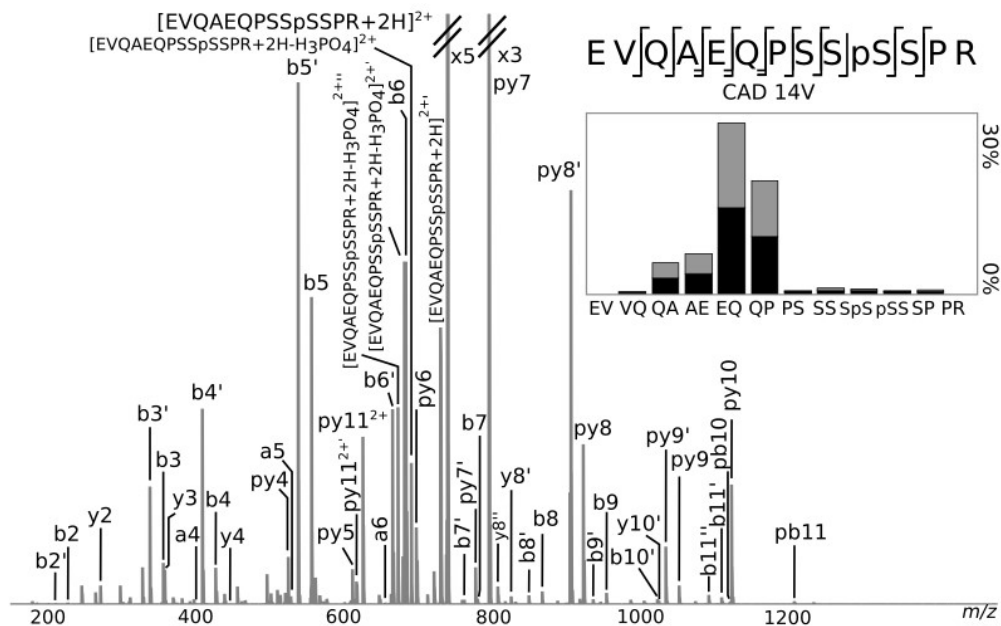


Figure 2. 7: CAD fragmentation of EVQAEQPSSpSSPR. p: fragment with phosphate attached. ' loss of water. '' loss of two waters.

The slow heating techniques produced limited fragments at QA and AE linkage and very low fragmentation with PSSpSSEPR. Fragment with EV cleavages were not identified. With both fragmentation techniques, H₃PO₄ losses were identified at the precursor, as well as loss of one, two or three H₂O. Fragments with phosphate losses are observed: y5-9', b7-9' for CAD, y5-7' and b7' for IRMPD, representing 10.0% and 3.8% respectively of the identified sequence ion intensities. However, the fragments have their

(7.0%), and UVPD (19.3%). MS/MS of EVQAEQPSSpSSPR with ECD gave low intensity fragments suggesting an inner stabilization of the peptide.

Despite its mobile proton, and the proline residue at the C-terminus of the peptide, the doubly charged EVQAEQPSSpSSPR has low fragmentation efficiency at PSSpSSPR, around the site of the phosphorylation, in all spectra, with all dissociation techniques. Also, the neutral loss of H_3PO_4 from the precursor was low with all techniques (respectively 4.7%, 1.7%, 0%, and 0.4% for CAD, IRMPD, ECD and UVPD in the $[M+2H-H_3PO_4]^{2+}/[M+2H]^{2+}$ ratio), compared to the loss in the two other model peptides, and there was no loss of HPO_3 with any of the fragmentation techniques. These two observations, and the ECD fragmentation behavior, suggest an inner stabilization, which could be due to a strong hydrogen bonding interaction between the phosphoserine and the protonated arginine residue.^{33, 35} The use of activated ion ECD, with the simultaneous irradiation of the IR laser, could potentially separate the ECD ions which are held together by a hydrogen bond, testing this hypothesis.^{54, 62}

EVQAEQPSSpSSPR was fragmented in negative mode via electron detachment dissociation (EDD). Low intensity a• and x fragments were observed in the spectra (Figure 2.11), as well as neutral losses (CO_2 , C_2H_5O , CH_2O). The labile phosphate was not cleaved from the precursor or the fragments. Despite the low fragmentation efficiency, the ions gave sequence information localizing the phosphorylation between the third and fourth serine.

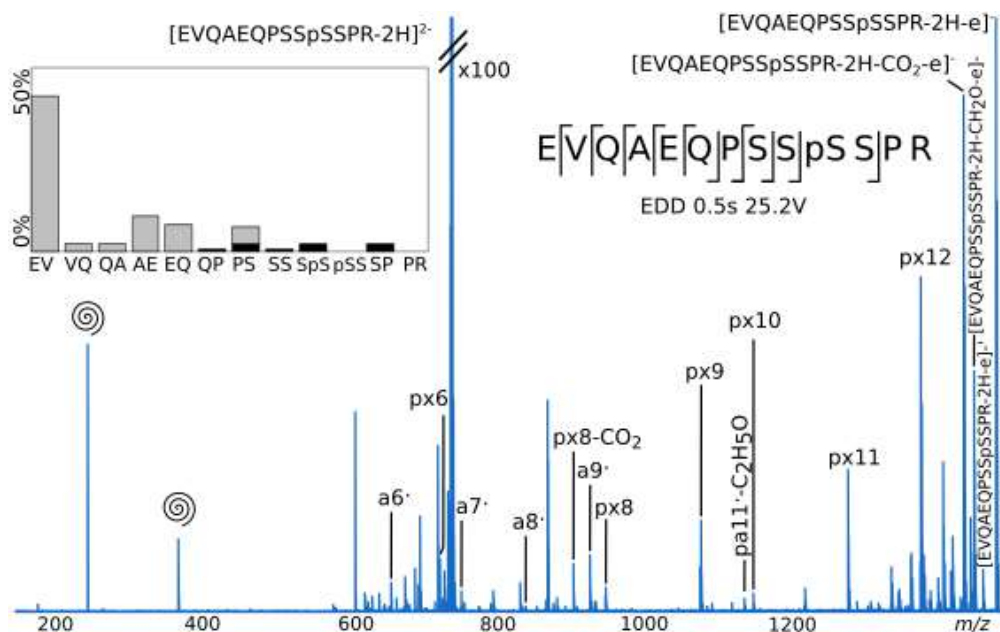


Figure 2. 11: EDD fragmentation of EVQAEQPSSpSSPR. p: fragment with phosphate attached. ‘: loss of water. Swirl: harmonics.

The fragmentation profile shows a high intensity fragment arising from the EV cleavage (px12). This data is consistent with the electron-hole recombination phenomenon,²⁵ where the loss of the electron produces a radical with a positive charge, mobile via coulombic attraction on the backbone, and neutralized at a negative amino acid such as the glutamic acid (E). The tuning for EDD was more challenging than for the other fragmentation techniques. With CAD, IRMPD, ECD and UVPD, most of the acquired spectra showed the same product ions and fragmentation profiles, with different results when reaching extreme parameters. For EDD, optimal data was obtained for EVQAEQPSSpSSPR using a bias voltage of 25.2 V and pulse length of 0.5 s. Some fragments were not observed at 25 V and 25.4 V bias, or at 25.2 V with pulse lengths of 0.3 or 0.4 s. This narrow tuning window demonstrates the difficulty of the fragmentation tuning but also the complexity of the EDD mechanism.⁶³ EDD required more averaged scans to get good signal to noise ratio (500 scans). Furthermore, the fragmentation of RDSLGPITYSSR and VIEDNEpYTAR led to complex spectra with mostly unidentified fragments. Only px9, px8 and px7 were identified for RDSLGPITYSSR (data not shown).

2.5.3. VIEDNEpYTAR – Phosphotyrosine peptide

Fragmentation spectra of doubly-charged VIEDNEpYTAR are shown in Figure 2.12, 2.13, 2.14, and 2.15. CAD, IRMPD and UVPD displayed similar fragmentation profiles with selective dissociation at the IE linkage. a2, b2, py8, and/or py8' fragments were detected at high intensities in the three spectra. The dominant fragment ions are observed to arise from cleavage reactions at the N-terminus of the glutamic acid. The peptide contains three acidic residues (2xE and D), and surprisingly the selective fragmentation was detected at the glutamic acid residue only.

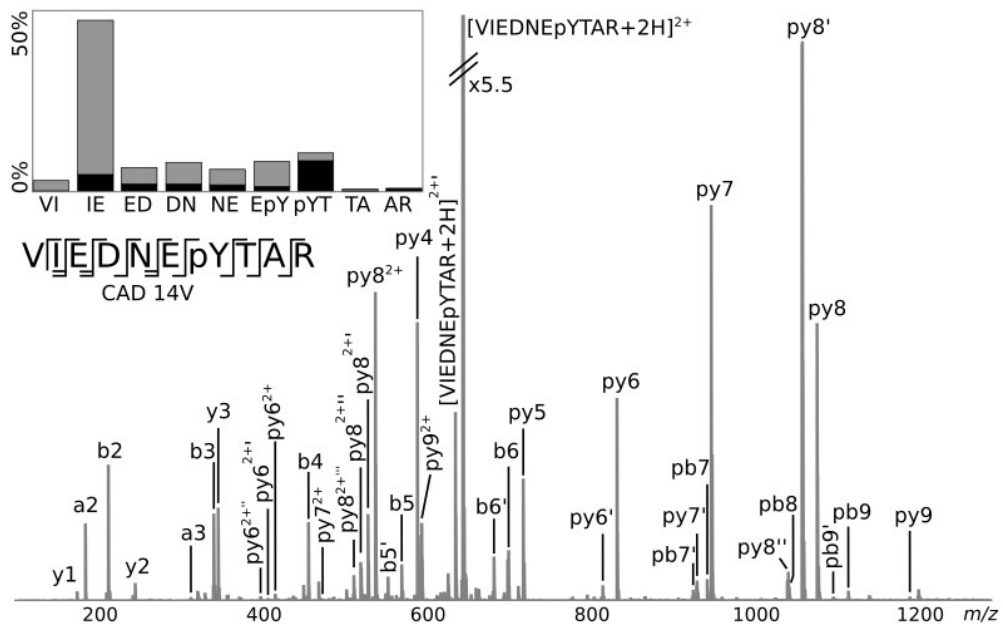


Figure 2. 12: CAD fragmentation of VIEDNEpYTAR. p: fragment with phosphate attached. ′: loss of water.

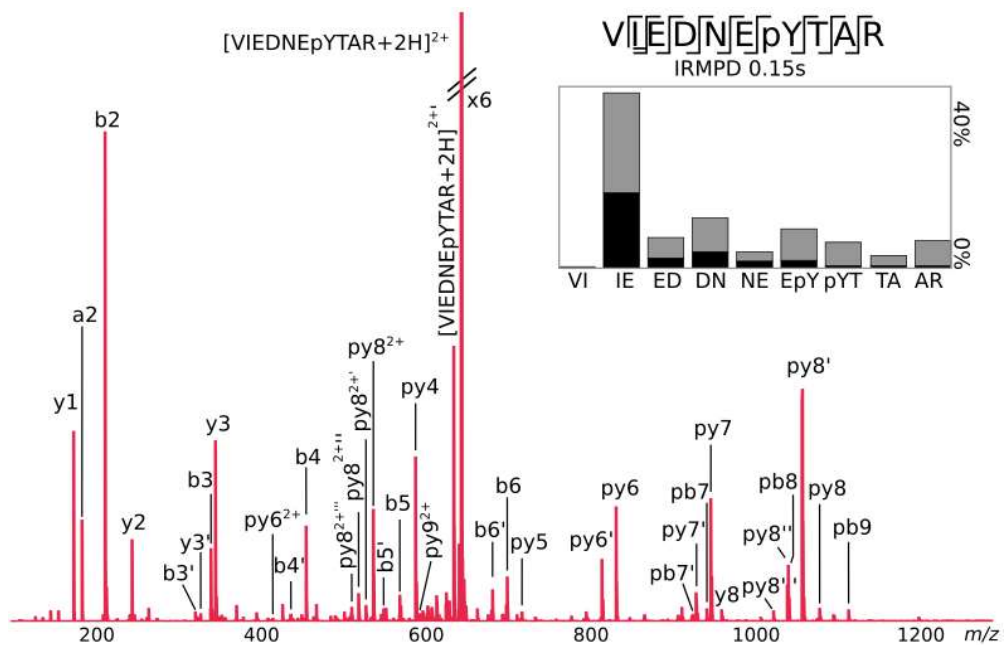


Figure 2. 13: IRMPD fragmentation of VIEDNEpYTAR. p: fragment with phosphate attached. ‘: loss of water.

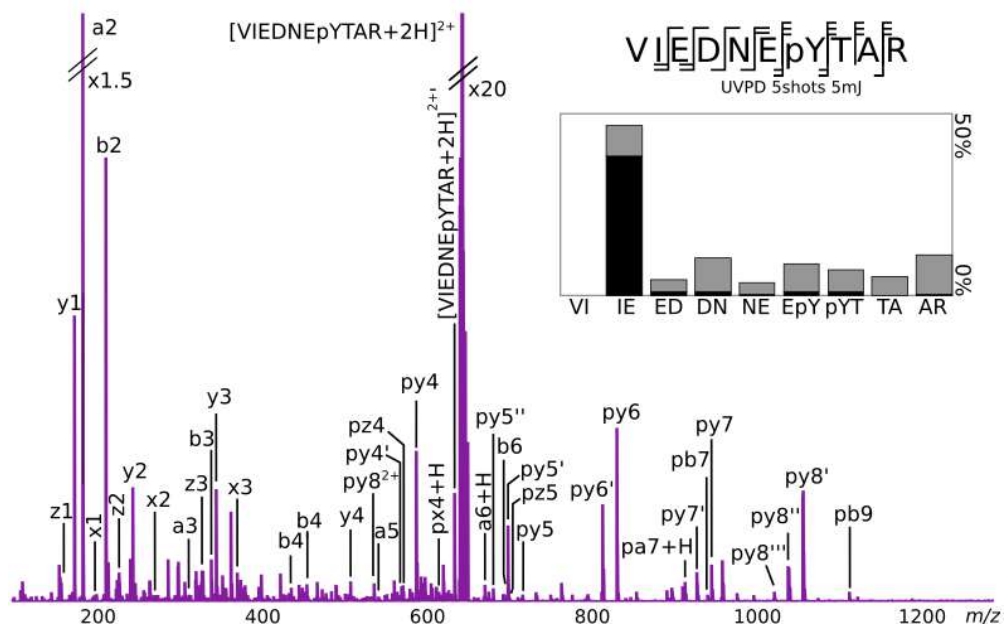


Figure 2. 14: UVPD fragmentation of VIEDNEpYTAR. p: fragment with phosphate attached. ‘: loss of water. ‘’: loss of two water molecules.

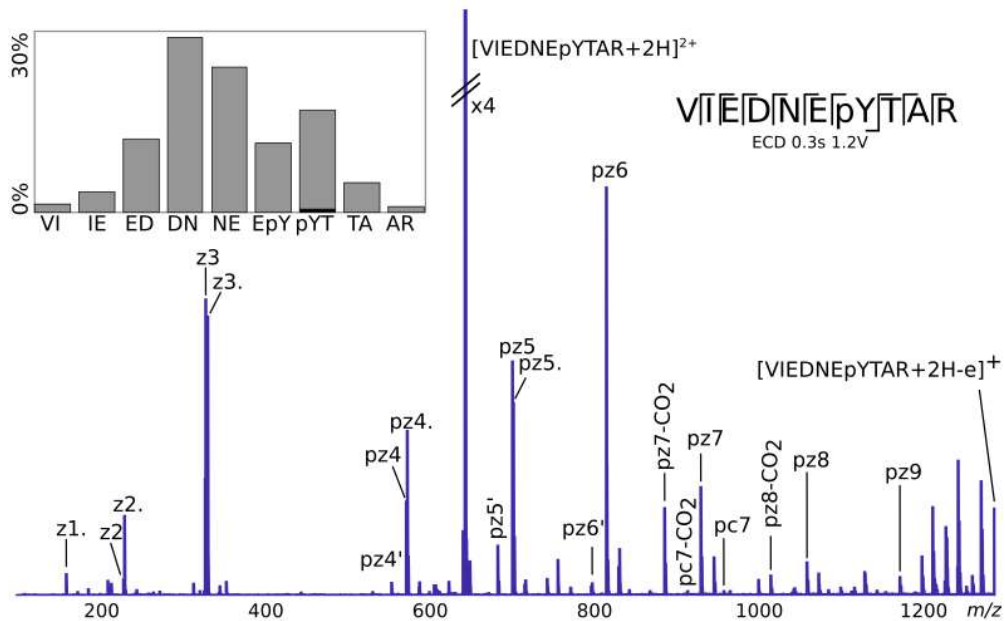


Figure 2. 15: ECD fragmentation of VIEDNEpYTAR. p: fragment with phosphate attached.

The C-terminus arginine sequestered one of the protons, the electron was captured by the proton, resulting in most of the ECD fragments containing the C-terminus. The central part of the peptide, where all the acidic residues were located, was more prone to fragmentation than the extremities of the peptide. Neutral losses from the electron-capture species such as CO₂ were detected.

Phosphotyrosine cannot undergo the direct loss of H₃PO₄ or HPO₃ from the precursor, via β-elimination reaction. VIEDNEpYTAR spectra displayed no loss of the phosphate group from the precursor, and there is no fragment suggesting the transfer of the phosphate. CAD and ECD spectra contain no fragment that would indicate a loss of phosphate. Laser fragmentation techniques produced low intensity fragments with a loss of phosphate: 0.4% for IRMPD and 2.2% for UVPD of the intensity of the identified fragments: y₄, y_{4'}, y_{6'}, y_{6''}, and y_{8'} for IRMPD, and y₄, y_{4'}, y₆, and y_{6'} for UVPD, which is lower than for the other peptides. Phosphotyrosine peptides are known to lose less phosphate group than phosphoserine and phosphothreonine peptides.¹⁵

The percentages of internal fragments or rearrangements are 3.1%, 5.7%, and 11.5% for CAD, IRMPD, and UVPD, which are lower than for RDSLGPtYSSR and EVQAEQPSSpSSPR. RDSLGPtYSSR shown the higher internal fragmentation percentages due to the high intensities of its two main internal fragments, and EVQAEQPSSpSSPR

shown higher neutral and side chain losses than the two other peptides. CAD, IRMPD and ECD produced 100% cleavage coverage, while the UVPD did not cleave at the VI linkage.

3.6. Conclusion and outlook

FT-ICR mass spectrometers are versatile instruments, where multiple fragmentations techniques can be implemented and compared. For the characterization of the three selected phosphopeptides, the two slow heating methods (CAD and IRMPD) produced similar fragmentation profiles with very little variation between the spectra. With the IRMPD technique, the fragments remain in the laser beam during the irradiation time and can be further fragmented; therefore, higher percentages of internal fragments are detected in the IRMPD spectra than the CAD spectra of the three peptides. These two fragmentation techniques can be distinguished by different characteristics. First, in the design of the instrument, the CAD fragmentation occurs in the collision cell at the front end of the mass spectrometer, and the IRMPD fragmentation occurs in the ICR cell. Second, it has been shown that the phosphopeptides fragment via IRMPD dissociation at a much lower threshold than their unphosphorylated counterparts.^{46, 47} These two characteristics of IRMPD fragmentation compared to CAD can be useful, for example, IRMPD can be used to perform a two-dimensional mass spectrometry (2DMS) analysis of a phosphoproteomic sample as shown in chapter 3.¹¹ It is also possible to perform sustained off-resonance irradiation Collisionally-activated dissociation (SORI-CAD) in the ICR cell, however in-cell fragmentation requires an increase in pressure and therefore reduces the resolving power of the experiment.

UVPD fragmentation produced a lot of complementary fragments. No significant variation of fragmentation efficiency was detected between the phosphoserine, phosphothreonine and the phosphotyrosine peptides. Selective fragmentation at the N-terminus of proline, and around the acidic amino acid residues were observed in the CAD, IRMPD and UVPD spectra, especially when the protons were immobilized. In these cases, competing fragmentation channels are discriminated against. Selective cleavages were observed with UVPD in peptides 1 and 3. A high energy photon can cause dissociation via three pathways: the absorption leads to an electron shifting to an electronic excited state, breaking a bond into two radicals, one hot, one cold. The hot radical is beyond the threshold of dissociation resulting in direct cleavage. The cold radical under-goes radical

rearrangements similar to ECD, and internal conversion of the electronic energy to vibrational modes results in even-electron fragmentation similar to CAD. These latter even-electron fragmentations lead to selective cleavages. The phosphotyrosine peptide had a UVPD fragmentation profile similar to the slow heating profiles, while the UVPD fragmentation profiles of the phosphoserine and phosphothreonine peptides had patterns of all the ECD, CAD, and IRMPD profiles. This difference is likely due to the nature of the phosphorylated amino acid, which is a UV chromophore. The use of electron-based fragmentation techniques did not show selective dissociation, as expected, but was less effective in the fragmentation of the phosphopeptides. Despite the more homogeneous fragmentation profile, and the ability to retain the labile phosphorylation, ECD produced lower intensity fragments, and rearrangements, due to an inner stabilization caused by the phosphorylation. EDD fragmentation in negative mode produced unidentified fragments and difficult spectra to interpret, leading to low sequence information.

CAD, IRMPD, ECD, and UVPD produced complementary sequence information, and permitted the localization of the phosphate group. No phosphate transfer between the phosphoamino acid residue and another amino acid residue of the peptide were detected. The cleavage coverage was around 100% for all spectra with exceptions relating to the composition of the peptides more than the ability of the fragmentation techniques.

3.7. Acknowledgement

The authors would like to thank all the ICR lab for their support. Johanna Paris thanks EPSRC for a PhD studentship through the EPSRC Centre for Doctoral Training in Molecular Analytical Science, grant number EP/L015307/1, UCB, and BB/R022399/1, BB/P021879/1, EP/N033191/1, and Horizon 2020 EU FTICR MS network (731077) for funding.

3.8. References

1. Zu, X.-L.; Besant, P.; Imhof, A.; Attwood, P. Mass spectrometric analysis of protein histidine phosphorylation *Amino acids* **2007**, *32*, 347-357.
2. Attwood, P.; Piggott, M.; Zu, X.; Besant, P. Focus on phosphohistidine *Amino acids* **2007**, *32*, 145-156.
3. Kleinnijenhuis, A. J.; Kjeldsen, F.; Kallipolitis, B.; Haselmann, K. F.; Jensen, O. N. Analysis of Histidine Phosphorylation Using Tandem MS and Ion– Electron Reactions *Anal. Chem.* **2007**, *79*, 7450-7456.
4. Cieśla, J.; Frączyk, T.; Rode, W. Phosphorylation of basic amino acid residues in proteins: important but easily missed *Acta Biochim. Pol.* **2011**, *58*, 137-148.
5. Hardman, G.; Perkins, S.; Brownridge, P. J.; Clarke, C. J.; Byrne, D. P.; Campbell, A. E.; Kalyuzhnyy, A.; Myall, A.; Evers, P. A.; Jones, A. R. Strong anion exchange-mediated phosphoproteomics reveals extensive human non-canonical phosphorylation *EMBO J.* **2019**, *38*, e100847.
6. Wilm, M.; Neubauer, G.; Mann, M. Parent ion scans of unseparated peptide mixtures *Anal. Chem.* **1996**, *68*, 527-533.
7. Olsen, J. V.; Macek, B.; Lange, O.; Makarov, A.; Horning, S.; Mann, M. Higher-energy C-trap dissociation for peptide modification analysis *Nat. Methods* **2007**, *4*, 709-712.
8. Huddleston, M. J.; Annan, R. S.; Bean, M. F.; Carr, S. A. Selective detection of phosphopeptides in complex mixtures by electrospray liquid chromatography/mass spectrometry *JASMS* **1993**, *4*, 710-717.
9. Qin, J.; Chait, B. T. Identification and characterization of posttranslational modifications of proteins by MALDI ion trap mass spectrometry *Anal. Chem.* **1997**, *69*, 4002-4009.
10. Schlosser, A.; Pipkorn, R.; Bossemeyer, D.; Lehmann, W. D. Analysis of protein phosphorylation by a combination of elastase digestion and neutral loss tandem mass spectrometry *Anal. Chem.* **2001**, *73*, 170-176.
11. Paris, J.; Morgan, T. E.; Wootton, C. A.; Barrow, M. P.; O'Hara, J.; O'Connor, P. B. Facile determination of phosphorylation sites in peptides using two-dimensional mass spectrometry *Anal. Chem.* **2020**.

12. Mao, Y.; Zamdborg, L.; Kelleher, N. L.; Hendrickson, C. L.; Marshall, A. G. Identification of phosphorylated human peptides by accurate mass measurement alone *Int. J. Mass spectrom.* **2011**, *308*, 357-361.
13. Wind, M.; Wesch, H.; Lehmann, W. D. Protein phosphorylation degree: determination by capillary liquid chromatography and inductively coupled plasma mass spectrometry *Anal. Chem.* **2001**, *73*, 3006-3010.
14. Chen, M.; Su, X.; Yang, J.; Jenkins, C. M.; Cedars, A. M.; Gross, R. W. Facile identification and quantitation of protein phosphorylation via β -elimination and Michael addition with natural abundance and stable isotope labeled thiocholine *Anal. Chem.* **2010**, *82*, 163-171.
15. DeGnore, J. P.; Qin, J. Fragmentation of phosphopeptides in an ion trap mass spectrometer *JASMS* **1998**, *9*, 1175-1188.
16. Rožman, M. Modelling of the gas-phase phosphate group loss and rearrangement in phosphorylated peptides *J. Mass Spectrom.* **2011**, *46*, 949-955.
17. Wysocki, V. H. Internal energy effects in mass spectrometry. Purdue University, 1987.
18. Zhang, Y.; Ficarro, S. B.; Li, S.; Marto, J. A. Optimized Orbitrap HCD for quantitative analysis of phosphopeptides *JASMS* **2009**, *20*, 1425-1434.
19. Palumbo, A. M.; Reid, G. E. Evaluation of gas-phase rearrangement and competing fragmentation reactions on protein phosphorylation site assignment using collision induced dissociation-MS/MS and MS3 *Anal. Chem.* **2008**, *80*, 9735-9747.
20. Mous, L.; Aubagnac, J.-L.; Martinez, J.; Enjalbal, C. Low energy peptide fragmentations in an ESI-Q-ToF type mass spectrometer *J. Proteome Res.* **2007**, *6*, 1378-1391.
21. Stensballe, A.; Jensen, O. N.; Olsen, J. V.; Haselmann, K. F.; Zubarev, R. A. Electron capture dissociation of singly and multiply phosphorylated peptides *Rapid Commun. Mass Spectrom.* **2000**, *14*, 1793-1800.
22. Kowalewska, K.; Stefanowicz, P.; Ruman, T.; Frączyk, T.; Rode, W.; Szewczuk, Z. Electron capture dissociation mass spectrometric analysis of lysine-phosphorylated peptides *Biosci. Rep.* **2010**, *30*, 433-443.
23. Voinov, V. G.; Bennett, S. E.; Beckman, J. S.; Barofsky, D. F. ECD of tyrosine phosphorylation in a triple quadrupole mass spectrometer with a radio-frequency-free electromagnetostatic cell *JASMS* **2014**, *25*, 1730-1738.

24. Zubarev, R. A.; Kelleher, N. L.; McLafferty, F. W. Electron capture dissociation of multiply charged protein cations. A nonergodic process *JACS* **1998**, *120*, 3265-3266.
25. Budnik, B. A.; Haselmann, K. F.; Zubarev, R. A. Electron detachment dissociation of peptide di-anions: an electron-hole recombination phenomenon *Chem. Phys. Lett.* **2001**, *342*, 299-302.
26. Anusiewicz, I.; Jasionowski, M.; Skurski, P.; Simons, J. Backbone and side-chain cleavages in electron detachment dissociation (EDD) *J. Phys. Chem. A* **2005**, *109*, 11332-11337.
27. Kjeldsen, F.; Silivra, O. A.; Ivonin, I. A.; Haselmann, K. F.; Gorshkov, M.; Zubarev, R. A. C α -C Backbone Fragmentation Dominates in Electron Detachment Dissociation of Gas-Phase Polypeptide Polyanions *Chem. Eur. J.* **2005**, *11*, 1803-1812.
28. Creese, A. J.; Cooper, H. J. The effect of phosphorylation on the electron capture dissociation of peptide ions *JASMS* **2008**, *19*, 1263-1274.
29. Moss, C. L.; Chung, T. W.; Wyer, J. A.; Nielsen, S. B.; Hvelplund, P.; Tureček, F. Dipole-guided electron capture causes abnormal dissociations of phosphorylated pentapeptides *JASMS* **2011**, *22*, 731-751.
30. Kim, D.; Pai, P.-J.; Creese, A. J.; Jones, A. W.; Russell, D. H.; Cooper, H. J. Probing the electron capture dissociation mass spectrometry of phosphopeptides with traveling wave ion mobility spectrometry and molecular dynamics simulations *JASMS* **2015**, *26*, 1004-1013.
31. Woods, A. S. The mighty arginine, the stable quaternary amines, the powerful aromatics, and the aggressive phosphate: their role in the noncovalent minuet *J. Proteome Res.* **2004**, *3*, 478-484.
32. Kumar, S.; Nussinov, R. Close-range electrostatic interactions in proteins *ChemBioChem* **2002**, *3*, 604-617.
33. Jackson, S. N.; Wang, H.-Y. J.; Woods, A. S. Study of the fragmentation patterns of the phosphate-arginine noncovalent bond *J. Proteome Res.* **2005**, *4*, 2360-2363.
34. Jackson, S. N.; Wang, H.-Y. J.; Yergey, A.; Woods, A. S. Phosphate stabilization of intermolecular interactions *J. Proteome Res.* **2006**, *5*, 122-126.
35. Woods, A. S.; Ferré, S. Amazing stability of the arginine-phosphate electrostatic interaction *J. Proteome Res.* **2005**, *4*, 1397-1402.

36. Iakoucheva, L. M.; Radivojac, P.; Brown, C. J.; O'Connor, T. R.; Sikes, J. G.; Obradovic, Z.; Dunker, A. K. The importance of intrinsic disorder for protein phosphorylation *Nucleic Acids Res.* **2004**, *32*, 1037-1049.
37. Little, D. P.; Speir, J. P.; Senko, M. W.; O'Connor, P. B.; McLafferty, F. W. Infrared multiphoton dissociation of large multiply charged ions for biomolecule sequencing *Anal. Chem.* **1994**, *66*, 2809-2815.
38. Talebpour, A.; Bandrauk, A.; Yang, J.; Chin, S. Multiphoton ionization of inner-valence electrons and fragmentation of ethylene in an intense Ti: sapphire laser pulse *Chem. Phys. Lett.* **1999**, *313*, 789-794.
39. Maitre, P.; Scuderi, D.; Corinti, D.; Chiavarino, B.; Crestoni, M. E.; Fornarini, S. Applications of Infrared Multiple Photon Dissociation (IRMPD) to the Detection of Posttranslational Modifications *Chem. Rev.* **2019**.
40. McCormack, A. L.; Somogyi, A.; Dongre, A. R.; Wysocki, V. H. Fragmentation of protonated peptides: surface-induced dissociation in conjunction with a quantum mechanical approach *Anal. Chem.* **1993**, *65*, 2859-2872.
41. Tsaprailis, G.; Nair, H.; Somogyi, Á.; Wysocki, V. H.; Zhong, W.; Futrell, J. H.; Summerfield, S. G.; Gaskell, S. J. Influence of secondary structure on the fragmentation of protonated peptides *JACS* **1999**, *121*, 5142-5154.
42. Correia, C. F.; Balaj, P. O.; Scuderi, D.; Maitre, P.; Ohanessian, G. Vibrational signatures of protonated, phosphorylated amino acids in the gas phase *JACS* **2008**, *130*, 3359-3370.
43. Stedwell, C. N.; Patrick, A. L.; Gulyuz, K.; Polfer, N. C. Screening for phosphorylated and nonphosphorylated peptides by infrared photodissociation spectroscopy *Anal. Chem.* **2012**, *84*, 9907-9912.
44. Flora, J. W.; Muddiman, D. C. Gas-phase ion unimolecular dissociation for rapid phosphopeptide mapping by IRMPD in a penning ion trap: An energetically favored process *JACS* **2002**, *124*, 6546-6547.
45. Flora, J. W.; Muddiman, D. C. Determination of the relative energies of activation for the dissociation of aromatic versus aliphatic phosphopeptides by ESI-FTICR-MS and IRMPD *JASMS* **2004**, *15*, 121-127.
46. Crowe, M. C.; Brodbelt, J. S. Infrared multiphoton dissociation (IRMPD) and collisionally activated dissociation of peptides in a quadrupole ion trap with selective IRMPD of phosphopeptides *JASMS* **2004**, *15*, 1581-1592.

47. Crowe, M. C.; Brodbelt, J. S. Differentiation of phosphorylated and unphosphorylated peptides by high-performance liquid chromatography-electrospray ionization-infrared multiphoton dissociation in a quadrupole ion trap *Anal. Chem.* **2005**, *77*, 5726-5734.
48. Ly, T.; Julian, R. R. Ultraviolet photodissociation: developments towards applications for mass-spectrometry-based proteomics *Angew. Chem. Int. Ed.* **2009**, *48*, 7130-7137.
49. Madsen, J. A.; Kaoud, T. S.; Dalby, K. N.; Brodbelt, J. S. 193-nm photodissociation of singly and multiply charged peptide anions for acidic proteome characterization *Proteomics* **2011**, *11*, 1329-1334.
50. Shaw, J. B.; Li, W.; Holden, D. D.; Zhang, Y.; Griep-Raming, J.; Fellers, R. T.; Early, B. P.; Thomas, P. M.; Kelleher, N. L.; Brodbelt, J. S. Complete protein characterization using top-down mass spectrometry and ultraviolet photodissociation *JACS* **2013**, *135*, 12646-12651.
51. Brodbelt, J. S. Photodissociation mass spectrometry: new tools for characterization of biological molecules *Chem. Soc. Rev.* **2014**, *43*, 2757-2783.
52. Modzel, M.; Wollenberg, D. T. W.; Trelle, M. B.; Larsen, M. R.; Jørgensen, T. J. Ultraviolet Photodissociation of Protonated Peptides and Proteins Can Proceed with H/D Scrambling *Anal. Chem.* **2020**, *93*, 691-696.
53. Fort, K. L.; Dyachenko, A.; Potel, C. M.; Corradini, E.; Marino, F.; Barendregt, A.; Makarov, A. A.; Scheltema, R. A.; Heck, A. J. Implementation of ultraviolet photodissociation on a benchtop Q exactive mass spectrometer and its application to phosphoproteomics *Anal. Chem.* **2016**, *88*, 2303-2310.
54. Tsybin, Y. O.; Witt, M.; Baykut, G.; Kjeldsen, F.; Håkansson, P. Combined infrared multiphoton dissociation and electron capture dissociation with a hollow electron beam in Fourier transform ion cyclotron resonance mass spectrometry *Rapid Commun. Mass Spectrom.* **2003**, *17*, 1759-1768.
55. Caravatti, P.; Allemann, M. The 'infinity cell': A new trapped-ion cell with radiofrequency covered trapping electrodes for Fourier transform ion cyclotron resonance mass spectrometry *Org. Mass Spectrom.* **1991**, *26*, 514-518.
56. Wilm, M.; Mann, M. Analytical properties of the nano-electrospray ion source *Anal. Chem.* **1996**, *68*, 1-8.

57. Gu, C.; Tsapralis, G.; Brechi, L.; Wysocki, V. H. Selective gas-phase cleavage at the peptide bond C-terminal to aspartic acid in fixed-charge derivatives of Asp-containing peptides *Anal. Chem.* **2000**, *72*, 5804-5813.
58. Paizs, B.; Suhai, S. Fragmentation pathways of protonated peptides *Mass Spectrom. Rev.* **2005**, *24*, 508-548.
59. Qin, J.; Chait, B. T. Preferential fragmentation of protonated gas-phase peptide ions adjacent to acidic amino acid residues *JACS* **1995**, *117*, 5411-5412.
60. Schwartz, B. L.; Bursey, M. M. Some proline substituent effects in the tandem mass spectrum of protonated pentaalanine *Biol. Mass Spectrom.* **1992**, *21*, 92-96.
61. Cooper, H. J.; Hudgins, R. R.; Håkansson, K.; Marshall, A. G. Secondary fragmentation of linear peptides in electron capture dissociation *Int. J. Mass spectrom.* **2003**, *228*, 723-728.
62. Lin, C.; Cournoyer, J. J.; O'Connor, P. B. Probing the gas-phase folding kinetics of peptide ions by IR activated DR-ECD *JASMS* **2011**, *19*, 780-789.
63. Yang, J.; Håkansson, K. Characterization and optimization of electron detachment dissociation Fourier transform ion cyclotron resonance mass spectrometry *Int. J. Mass spectrom.* **2008**, *276*, 144-148.

3.9. Assignment tables

Absolute error is calculated as the average of the absolute ppm errors of all the assigned peaks. Absolute standard deviation is calculated as the standard deviation of the absolute ppm errors of all the assigned peaks.

RDSLGPtYSSR		CAD (14 V)		
Species	Theoretical m/z	Observed m/z	Intensity	ppm
$[M+2H]^{2+}$	611.26662	611.26582	1.7E+10	-1.303
$[M+2H-H_2O]^{2+}$	602.26133	602.26091	1.1E+09	-0.705
$[M+2H-HPO_3]^{2+}$	571.28345	571.28342	3.7E+07	-0.055
$[M+2H-H_3PO_4]^{2+}$	562.27817	562.27782	4.7E+09	-0.621
b2	272.13533	272.13533	6.5E+07	-0.002
b3	359.16736	359.16736	8.4E+06	0.003
b4	472.25142	472.25144	1.6E+07	0.036
b5	529.27289	529.27295	8.3E+06	0.120
y4	512.24634	512.24626	4.4E+08	-0.151
y3	349.18301	349.18301	4.1E+07	0.003
y2	262.15098	262.15099	1.3E+07	0.036
y1	175.11895	175.11895	1.7E+06	-0.012
pb6	710.28690	710.28686	7.6E+06	-0.051
pb7	873.35022	873.35043	1.5E+07	0.235
pb8	960.38225	960.38226	5.3E+06	0.007
py8	950.39790	950.39724	6.8E+07	-0.698
py7	863.36587	863.36609	4.8E+06	0.250
py6	750.28181	750.28190	9.8E+06	0.119
py5	693.26035	693.26035	2.0E+07	0.005
b7'	775.37333	775.37280	2.8E+07	-0.682
b8'	862.40536	862.40541	4.0E+06	0.061
b9'	949.43739	949.43673	4.8E+06	-0.691
y9'	967.44795	967.44704	4.9E+06	-0.941
y8'	852.42101	852.42042	2.4E+07	-0.689
y7'	765.38898	765.38922	2.0E+06	0.315
y6'	652.30492	652.30456	7.9E+06	-0.544
y5'	595.28345	595.28322	6.0E+06	-0.389
y4'	494.23577	494.23585	6.0E+06	0.156
y3'	331.17244	331.17246	3.9E+06	0.047
$C_{19}H_{11}N_5O_4^+$	373.08056	373.08053	1.5E+08	-0.068
$C_{19}H_9N_5O_3^+$	355.06999	355.06993	7.7E+08	-0.171
Average of absolute errors (ppm)			0.296	
Standard deviation (ppm)			0.334	

Table 2. 1: Peaks assignment for RDSLGPtYSSR CAD spectrum. ': loss of water. p: fragment with phosphate.

RDSLGP TYSSR		IRMPD (0.2 s)		
Species	Theoretical m/z	Observed m/z	Intensity	ppm
$[M+2H]^{2+}$	611.26662	611.26622	6.4E+09	-0.649
$[M+2H-H_2O]^{2+}$	602.26133	602.26119	5.6E+08	-0.240
$[M+2H-H_3PO_4]^{2+}$	562.27817	562.27804	5.4E+09	-0.229
b2	272.13533	272.13533	7.0E+08	-0.002
b3	359.16736	359.16741	8.4E+06	0.142
b4	472.25142	472.25158	1.5E+07	0.333
b5	529.27289	529.27324	7.4E+06	0.668
y4	512.24634	512.24633	4.7E+08	-0.015
y3	349.18301	349.18304	1.4E+08	0.089
y2	262.15098	262.15100	8.3E+07	0.074
y1	175.11895	175.11895	6.2E+07	-0.012
py8	950.39790	950.39792	3.0E+07	0.018
py6	750.28181	750.28154	2.4E+06	-0.361
a2	244.14042	244.14044	1.4E+07	0.099
a3	331.17244	331.17252	1.4E+07	0.229
b7'	775.37333	775.37267	4.2E+07	-0.850
y8'	852.42101	852.42040	2.5E+07	-0.713
y7'	765.38898	765.38793	6.0E+06	-1.371
y6'	652.30492	652.30454	8.3E+06	-0.575
y5'	595.28345	595.28373	6.5E+06	0.468
y4'	494.23577	494.23588	2.4E+07	0.217
y3'	331.17244	331.17252	1.4E+07	0.229
$C_{19}H_{19}N_5O_3^+$	355.06999	355.06993	1.8E+09	-0.171
Average of absolute errors (ppm)			0.337	
Standard deviation (ppm)			0.329	

Table 2. 2: Peaks assignment for RDSLGP TYSSR IRMPD spectrum. '': loss of water. p: fragment with phosphate.

RDSLGPtYSSR		UVPD (5 shots 5 mJ)		
Species	Theoretical <i>m/z</i>	Observed <i>m/z</i>	Intensity	ppm
[M+2H] ²⁺	611.26662	611.26632	1.9E+10	-0.485
[M+2H-H ₂ O] ²⁺	602.26133	602.26134	4.5E+08	0.009
[M+2H-HPO ₃] ²⁺	571.28345	571.28352	1.2E+07	0.120
[M+2H-H ₃ PO ₄] ²⁺	562.27817	562.27817	1.0E+09	0.002
b1	157.10839	157.10839	8.8E+07	0.016
b2	272.13533	272.13533	5.8E+08	-0.002
b3	359.16736	359.16736	2.9E+07	0.003
b4	472.25142	472.25145	2.4E+07	0.057
b5	529.27289	529.27297	2.0E+07	0.158
b9	967.44795	967.44790	1.1E+07	-0.052
y4	512.24634	512.24638	1.5E+08	0.083
y3	349.18301	349.18302	9.1E+07	0.032
y2	262.15098	262.15098	1.1E+08	-0.002
y1	175.11895	175.11895	2.2E+08	-0.012
pb6	710.28690	710.28663	3.2E+06	-0.374
pb7	873.35022	873.35041	5.6E+06	0.212
py8	950.39790	950.39790	4.4E+07	-0.003
c1	174.13494	174.13494	1.6E+07	0.020
c2	289.16188	289.16188	5.7E+07	0.001
c3	376.19391	376.19393	1.4E+07	0.058
c4	489.27797	489.27803	1.2E+07	0.119
c5	546.29944	546.29944	1.1E+07	0.008
c2.	288.15405	288.15406	2.8E+06	0.019
c3.	375.18608	375.18610	4.4E+06	0.045
z4	496.22761	496.22777	4.2E+06	0.316
z3	333.16428	333.16429	6.0E+07	0.015
z2	246.13226	246.13225	2.3E+07	-0.026
z1	159.10023	159.10024	1.6E+07	0.075
z4.	497.23544	497.23542	4.5E+06	-0.037
z3.	334.17211	334.17213	5.0E+06	0.060
pc6	727.31345	727.31353	4.4E+06	0.117
a2	244.14042	244.14041	8.5E+07	-0.024
a3	331.17244	331.17244	4.7E+07	-0.013
a4	444.25651	444.25654	2.5E+07	0.071
a7	765.38898	765.38904	1.0E+07	0.080
a8	852.42101	852.42105	1.4E+08	0.050
x4	538.22560	538.22574	5.5E+06	0.256
x3	375.16227	375.16231	7.0E+06	0.097
x2	288.13025	288.13025	7.7E+06	0.017

x1	201.09822	201.09822	1.3E+07	0.016
pa6	682.29198	682.29215	3.5E+06	0.247
pa7	845.35531	845.35539	1.8E+07	0.095
pa8	932.38734	932.38803	6.8E+06	0.742
b7'	775.37333	775.37327	2.6E+07	-0.076
a7'	747.37841	747.37838	1.2E+07	-0.046
b8'	862.40536	862.40541	5.0E+06	0.061
b9'	949.43739	949.43724	1.2E+07	-0.153
y9'	967.44795	967.44790	1.1E+07	-0.052
y8'	852.42101	852.42105	1.4E+08	0.050
y7'	765.38898	765.38904	1.0E+07	0.080
y6'	652.30492	652.30482	1.4E+07	-0.146
y5'	595.28345	595.28353	2.3E+07	0.132
y4'	494.23577	494.23582	2.0E+07	0.095
y3'	331.17244	331.17240	4.3E+06	-0.134
y2'	244.14042	244.14041	8.5E+07	-0.024
C ₁₉ H ₉ N ₅ O ₃ ⁺	355.06999	355.06993	4.6E+06	-0.171
Average of absolute errors (ppm)			0.098	
Standard deviation (ppm)			0.129	

Table 2. 3: Peaks assignment for RDSLGPtYSSR UVPD spectrum. ': loss of water. p: fragment with phosphate.

RDSLGPtYSSR		ECD (0.2 s 1.2 V)		
Species	Theoretical m/z	Observed m/z	Intensity	ppm
[M+2H] ²⁺	611.26662	611.26674	2.4E+09	0.202
b2	272.13533	272.13532	2.9E+06	-0.039
y3	349.18301	349.18302	1.4E+07	0.032
y2	262.15098	262.15099	5.0E+06	0.036
c1	174.13494	174.13494	2.4E+07	0.020
c2	289.16188	289.16188	2.9E+07	0.001
c3	376.19391	376.19392	6.2E+07	0.032
c4	489.27797	489.27796	5.0E+06	-0.024
c5	546.29944	546.29944	4.5E+07	0.008
c1.	173.12711	173.12711	1.2E+07	-0.009
c2.	288.15405	288.15406	4.5E+07	0.019
c3.	375.18608	375.18608	1.1E+08	-0.008
c4.	488.27015	488.27015	2.4E+07	0.006
c5.	545.29161	545.29161	8.5E+07	-0.001
z4	496.22761	496.22757	1.6E+07	-0.088
z3	333.16428	333.16427	8.1E+06	-0.045
z4.	497.23544	497.23543	1.3E+08	-0.017
z3.	334.17211	334.17211	1.2E+08	0.000

z2.	247.14008	247.14008	3.4E+07	-0.006
pc6	727.31345	727.31317	4.4E+06	-0.378
pc9	1064.44083	1064.44142	5.5E+07	0.554
pc7.	889.36895	889.36893	3.1E+07	-0.021
pc8.	976.40098	976.40106	2.0E+07	0.085
pc9.	1063.43301	1063.43303	3.3E+07	0.023
pz8.	935.38700	935.38687	7.8E+06	-0.143
pz7.	848.35498	848.35458	2.5E+06	-0.466
Average of absolute errors (ppm)			0.087	
Standard deviation (ppm)			0.146	

Table 2. 4: Peaks assignment for RDSLGPITYSSR ECD spectrum. p: fragment with phosphate.

EVQAEQPSSpSSPR		CAD (14 V)		
Species	Theoretical m/z	Observed m/z	Intensity	ppm
$[M+2H]^{2+}$	741.31703	741.31633	2.1E+10	-0.951
$[M+2H-H_2O]^{2+}$	732.31175	732.31167	2.1E+09	-0.113
$[M+2H-H_3PO_4]^{2+}$	692.32859	692.32849	9.9E+08	-0.140
b2	229.11828	229.11828	2.5E+06	-0.015
b3	357.17686	357.17683	1.7E+08	-0.087
b4	428.21397	428.21397	1.5E+08	-0.011
b5	557.25657	557.25644	1.3E+09	-0.229
b6	685.31515	685.31496	1.5E+09	-0.270
b7	782.36791	782.36759	3.0E+07	-0.408
b8	869.39994	869.39981	6.6E+07	-0.147
b9	956.43197	956.43209	6.1E+07	0.130
y4	446.23577	446.23577	3.4E+06	-0.006
y3	359.20374	359.20369	1.4E+08	-0.151
y2	272.17172	272.17167	7.4E+07	-0.169
pb10	1123.43033	1123.43030	1.5E+07	-0.022
pb11	1210.46235	1210.46293	2.0E+07	0.476
py10	1125.45721	1125.45715	5.9E+08	-0.052
py9	1054.42010	1054.41977	1.0E+08	-0.308
py8	925.37750	925.37755	7.4E+08	0.052
py7	797.31892	797.31821	8.6E+09	-0.896
py6	700.26616	700.26615	1.8E+08	-0.015
py5	613.23413	613.23413	1.5E+08	-0.003
py4	526.20210	526.20207	1.9E+08	-0.064
a4	400.21906	400.21903	7.5E+06	-0.075

a5	529.26165	529.26152	3.7E+07	-0.252
a6	657.32023	657.32017	9.1E+06	-0.092
y10'	1027.48031	1027.48020	1.9E+07	-0.110
y8'	827.40061	827.40053	3.9E+07	-0.092
y7'	699.34203	699.34173	3.3E+08	-0.427
y6'	602.28926	602.28913	1.1E+07	-0.224
y5'	515.25724	515.25711	4.3E+07	-0.246
y4'	428.22521	428.22519	4.2E+07	-0.042
y10''	1009.46975	1009.46954	1.1E+07	-0.207
y9''	938.43263	938.43277	2.4E+07	0.144
y8''	809.39004	809.38958	8.5E+07	-0.570
y7''	681.33146	681.33138	2.1E+08	-0.123
y6''	584.27870	584.27872	6.2E+06	0.034
y5''	497.24667	497.24657	1.3E+08	-0.205
b2'	211.10772	211.10773	6.0E+06	0.053
b3'	339.16630	339.16620	4.7E+08	-0.284
b4'	410.20341	410.20330	6.9E+08	-0.268
b5'	539.24600	539.24579	2.3E+09	-0.395
b6'	667.30458	667.30442	8.7E+08	-0.241
b7'	764.35734	764.35715	2.5E+07	-0.254
b8'	851.38937	851.38927	4.6E+07	-0.121
b9'	938.42140	938.42146	2.6E+07	0.063
b10'	1025.45343	1025.45380	2.6E+07	0.361
b11'	1112.48546	1112.48491	4.4E+07	-0.493
py11 ²⁺	627.26153	627.26144	9.3E+08	-0.146
py11 ²⁺⁺	618.25625	618.25618	1.3E+08	-0.112
py9'	1036.40953	1036.40964	2.8E+08	0.106
py8'	907.36694	907.36668	2.3E+09	-0.283
py7'	779.30836	779.30790	1.7E+08	-0.590
Average of absolute errors (ppm)			0.209	
Standard deviation (ppm)			0.205	

Table 2. 5: Peaks assignment for EVQAEQPSSpSSPR CAD spectrum. ': loss of water. '': loss of two waters. p: fragment with phosphate.

EVQAEQPSSpSSPR		IRMPD (0.2 s)		
Species	Theoretical m/z	Observed m/z	Intensity	ppm
$[M+2H]^{2+}$	741.31703	741.31663	3.4E+09	-0.546
$[M+2H-H_2O]^{2+}$	732.31175	732.31195	6.9E+07	0.270
$[M+2H-H_3PO_4]^{2+}$	692.32859	692.32854	5.8E+07	-0.068
b2	229.11828	229.11825	5.2E+06	-0.146

b3	357.17686	357.17680	3.7E+07	-0.171
b4	428.21397	428.21397	1.2E+07	-0.011
b5	557.25657	557.25657	1.6E+08	0.004
b6	685.31515	685.31520	6.1E+07	0.080
b8	869.39994	869.39934	7.5E+06	-0.687
b9	956.43197	956.43272	8.9E+06	0.788
y3	359.20374	359.20369	1.1E+08	-0.151
y2	272.17172	272.17165	2.0E+06	-0.242
y1	175.11895	175.11895	1.1E+07	-0.013
py10	1125.45721	1125.45720	9.3E+07	-0.008
py8	925.37750	925.37751	1.6E+07	0.009
py7	797.31892	797.31900	9.6E+08	0.095
py6	700.26616	700.26646	2.7E+07	0.428
py5	613.23413	613.23412	1.4E+07	-0.020
py4	526.20210	526.20214	3.5E+07	0.069
y7'	699.34203	699.34214	7.2E+07	0.159
y6'	602.28926	602.28932	2.8E+06	0.091
y5'	515.25724	515.25730	1.7E+07	0.123
y4'	428.22521	428.22520	3.6E+07	-0.019
y3'	341.19318	341.19318	1.5E+06	0.001
y8''	809.39004	809.38999	2.9E+07	-0.064
y7''	681.33146	681.33162	5.9E+07	0.229
y5''	497.24667	497.24670	6.7E+07	0.057
b2'	211.10772	211.10770	1.9E+07	-0.089
b3'	339.16630	339.16622	3.0E+08	-0.225
b4'	410.20341	410.20332	4.2E+08	-0.220
b5'	539.24600	539.24589	6.5E+08	-0.210
b6'	667.30458	667.30459	7.8E+07	0.014
b7'	764.35734	764.35741	4.2E+06	0.086
b11'	1112.48546	1112.48547	4.0E+06	0.011
py11 ²⁺	627.26153	627.26138	6.1E+07	-0.241
py11 ²⁺	618.25625	618.25625	7.6E+07	0.002
py9'	1036.40953	1036.40973	6.3E+07	0.193
py8'	907.36694	907.36693	5.7E+08	-0.008
py7'	779.30836	779.30838	5.5E+07	0.026
Average of absolute errors (ppm)			0.161	
Standard deviation (ppm)			0.190	

Table 2. 6: Peaks assignment for EVQAEQPSSSPR IRMPD spectrum. '': loss of water. '': loss of two waters. p: fragment with phosphate.

EVQAEQPSSpSSPR		ECD (0.2 s 1.2 V)		
Species	Theoretical <i>m/z</i>	Observed <i>m/z</i>	Intensity	ppm
[M+2H] ²⁺	741.31703	741.31657	1.3E+10	-0.627
[M+2H-H ₂ O] ²⁺	732.31175	732.31212	1.3E+07	0.502
y3	359.20374	359.20379	2.0E+06	0.127
py11	1253.51579	1253.51657	3.3E+07	0.625
py10	1125.45721	1125.45717	2.2E+07	-0.035
py8	925.37750	925.37780	1.2E+07	0.322
py7	797.31892	797.31897	1.7E+07	0.057
z3	343.18502	343.18501	1.1E+07	-0.030
z3.	344.19285	344.19285	1.2E+08	0.013
pz12	1336.56548	1336.56585	7.7E+07	0.280
pz11	1237.49706	1237.49708	5.1E+07	0.015
pz10	1109.43849	1109.43854	4.3E+07	0.050
pz9	1038.40137	1038.40136	1.4E+08	-0.011
pz8	909.35878	909.35876	1.1E+08	-0.020
pz4	510.18338	510.18352	4.2E+07	0.275
pz8.	910.36660	910.36673	1.9E+08	0.140
pz6.	685.25526	685.25512	2.3E+07	-0.206
pz5.	598.22323	598.22324	1.7E+07	0.012
pz4.	511.19120	511.19118	4.4E+07	-0.048
z12'	1238.58858	1238.58887	5.1E+07	0.234
z11'	1139.52017	1139.52038	6.2E+07	0.187
z10'	1011.46159	1011.46148	1.7E+08	-0.108
z9'	940.42448	940.42476	7.8E+06	0.303
z8'	811.38188	811.38183	3.5E+07	-0.064
pz8'	891.34821	891.34807	2.0E+07	-0.161
pw13	1394.57096	1394.57115	9.6E+07	0.140
pw12	1265.52836	1265.52820	4.0E+07	-0.128
pw11	1166.45995	1166.46052	2.4E+07	0.490
pw9	967.36426	967.36435	1.9E+07	0.096
Average of absolute errors (ppm)			0.183	
Standard deviation (ppm)			0.178	

Table 2. 7: Peaks assignment for EVQAEQPSSpSSPR ECD spectrum. ': loss of water. p: fragment with phosphate. w: z-C₃H₅NO

EVQAEQPSSpSSPR		UVPD (5 shots 5 mJ)		
Species	Theoretical <i>m/z</i>	Observed <i>m/z</i>	Intensity	ppm
[M+2H] ²⁺	741.31703	741.31638	7.1E+09	-0.088
[M+2H-H ₂ O] ²⁺	732.31175	732.31162	2.5E+08	-0.018
[M+2H-H ₃ PO ₄] ²⁺	692.32859	692.32849	2.5E+07	-0.014
[M+2H-CO] ²⁺	727.31958	727.31949	2.8E+07	-0.012
a1	102.05495	102.05495	4.0E+06	-0.005
b1	130.04987	130.04987	2.3E+06	0.000
c1	147.07642	147.07642	5.2E+06	0.001
y1'	157.10839	157.10839	5.7E+06	0.002
z1	159.10023	159.10022	5.9E+06	-0.005
y1	175.11895	175.11895	4.1E+07	-0.001
x1	201.09822	201.09822	6.0E+06	0.002
a2	201.12337	201.12337	1.6E+07	0.001
b2'	211.10772	211.10772	7.0E+07	0.001
b2	229.11828	229.11829	1.1E+07	0.003
y2'	254.16115	254.16115	8.1E+06	-0.001
y2	272.17172	272.17171	1.0E+08	-0.002
y3''	323.18262	323.18256	4.4E+06	-0.017
a3	329.18195	329.18197	1.1E+08	0.007
b3'	339.16630	339.16629	2.4E+08	-0.002
y3'	341.19318	341.19319	5.1E+06	0.003
z3	343.18502	343.18504	6.0E+06	0.006
b3	357.17686	357.17685	2.9E+07	-0.003
y3	359.20374	359.20375	5.8E+07	0.002
b4'-CO	382.20850	382.20851	2.1E+07	0.004
x3	385.18301	385.18298	2.9E+06	-0.008
a4	400.21906	400.21904	1.9E+06	-0.005
b4'	410.20341	410.20341	1.9E+08	0.000
y4''	410.21464	410.21461	6.5E+06	-0.008
b4	428.21397	428.21401	1.0E+07	0.008
y4'	428.22521	428.22522	3.8E+07	0.003
z4.	431.22487	431.22482	2.7E+06	-0.012
y5''	497.24667	497.24669	5.8E+07	0.004
y5'	515.25724	515.25725	1.9E+07	0.003
b5'-CO	511.25109	511.25117	7.2E+06	0.016
y6''	584.27870	584.27869	4.4E+06	-0.002
b5''	521.23544	521.23544	1.7E+07	0.000
a5	529.26165	529.26173	4.1E+06	0.015
b5'	539.24600	539.24601	1.1E+08	0.001
b5	557.25657	557.25658	5.1E+07	0.002
y6'	602.28926	602.28931	1.7E+06	0.007

c5	574.28312	574.28309	1.3E+07	-0.005
y7'''	663.32090	663.32102	9.8E+06	0.018
y7''	681.33146	681.33146	5.0E+07	-0.001
y7'	699.34203	699.34204	1.1E+08	0.002
y8'''	791.37948	791.37928	2.9E+07	-0.025
y8''	809.39004	809.39002	5.0E+07	-0.003
b6'	667.30458	667.30464	3.2E+07	0.009
y9'''	920.42207	920.42242	7.4E+06	0.038
y9''	938.43263	938.43268	1.8E+07	0.005
b6	685.31515	685.31519	1.9E+07	0.007
y10''	1009.46975	1009.46944	6.2E+06	-0.031
y10'	1027.48031	1027.48032	1.9E+07	0.001
py8 ²⁺	463.19239	463.19228	1.8E+06	-0.024
py4	526.20210	526.20213	1.9E+07	0.005
a7	754.37299	754.37371	1.9E+06	0.095
py10 ²⁺	563.23224	563.23203	1.9E+06	-0.038
b7'	764.35734	764.35728	2.0E+06	-0.008
py5	613.23413	613.23406	5.8E+06	-0.012
py11 ²⁺	627.26153	627.26159	5.2E+06	0.009
pz6	684.24744	684.24740	3.2E+06	-0.005
py6	700.26616	700.26624	2.0E+07	0.011
b8'	851.38937	851.39008	2.5E+06	0.083
b8	869.39994	869.39893	2.7E+06	-0.116
py7''	761.29780	761.29774	1.4E+07	-0.007
py7'	779.30836	779.30838	8.3E+07	0.003
py7	797.31892	797.31896	1.8E+08	0.004
pz8-H-H ₂ O	890.34039	890.34064	4.6E+06	0.028
pz8-H	908.35095	908.35107	4.7E+07	0.013
pz8	909.35878	909.35437	1.9E+07	-0.485
pz8.	910.36660	910.35763	4.3E+06	-0.986
py8	925.37750	925.37764	2.5E+07	0.015
py10	1125.45721	1125.45711	1.7E+07	-0.009
pc10	1140.45687	1140.45661	2.9E+06	-0.023
b3-C ₂ H ₆ O	311.13500	311.13499	1.8E+07	-0.002
Average of absolute errors (ppm)			0.033	
Standard deviation (ppm)			0.126	

Table 2. 8: Peaks assignment for EVQAEQPSSpSSPR UVPD spectrum. '': loss of water. ''': loss of two water. p: fragment with phosphate.

VIEDNEpYTAR		CAD (14 V)		
Species	Theoretical <i>m/z</i>	Observed <i>m/z</i>	Intensity	ppm
[M+2H] ²⁺	645.27411	645.27390	4.2E+09	-0.321

[M+2H]'	636.26883	636.26871	4.7E+08	-0.181
[M+2H]''	627.26354	627.26336	5.3E+07	-0.291
a2	185.16484	185.16484	6.7E+07	0.001
a3	314.20743	314.20752	3.2E+06	0.277
a5	543.27730	543.27732	2.1E+06	0.031
b2	213.15975	213.15977	1.2E+08	0.073
b3	342.20235	342.20238	7.7E+07	0.095
b4	457.22929	457.22932	7.4E+07	0.065
b5	571.27222	571.27220	3.6E+07	-0.031
b5'	553.26165	553.26175	2.7E+07	0.175
b6	700.31481	700.31471	4.3E+07	-0.144
b6'	682.30425	682.30412	8.1E+06	-0.185
pb7	943.34447	943.34398	3.3E+08	-0.520
pb7'	925.33391	925.33349	1.6E+07	-0.449
pb8	1044.39215	1044.39212	5.0E+06	-0.031
pb9	1115.42926	1115.42939	1.2E+07	0.114
py4	590.23340	590.23335	2.8E+08	-0.091
py5	719.27600	719.27574	1.3E+08	-0.357
py5'	701.26543	701.26523	5.0E+07	-0.288
py6	833.31892	833.31873	2.2E+08	-0.233
py6'	815.30836	815.30839	1.9E+07	0.037
py6 ²⁺	417.16310	417.16316	5.9E+06	0.143
py6 ²⁺ '	408.15782	408.15774	2.6E+06	-0.191
py6 ²⁺ ''	399.15254	399.15255	3.9E+06	0.036
py7	948.34587	948.34575	1.4E+08	-0.124
py7 ²⁺	474.67657	474.67654	2.2E+06	-0.067
py8	1077.38846	1077.38798	3.5E+08	-0.446
py8'	1059.37790	1059.37744	7.2E+08	-0.430
py8 ²⁺	539.19787	539.19784	3.8E+08	-0.053
py8 ²⁺ '	530.19259	530.19256	1.2E+08	-0.049
py8 ²⁺ ''	521.18730	521.18725	9.1E+07	-0.103
py8 ²⁺ '''	512.18202	512.18191	4.1E+07	-0.218
py9	1190.47252	1190.47173	3.6E+06	-0.667
py9 ²⁺	586.73462	586.73464	1.5E+07	0.037
py9 ²⁺ '	595.73990	595.73980	1.0E+08	-0.169
y1	175.11895	175.11896	7.6E+06	0.045
y2	246.15607	246.15609	1.6E+07	0.098
y3	347.20374	347.20377	8.4E+07	0.074
Average of absolute errors (ppm)			0.174	
Standard deviation (ppm)			0.156	

Table 2. 9: Peaks assignment for VIEDNEpYTAR CAD spectrum. '': loss of water. ''': loss of two waters. ''': loss of three water. p: fragment with phosphate.

VIEDNEpYTAR		IRMPD (0.15 s)		
Species	Theoretical <i>m/z</i>	Observed <i>m/z</i>	Intensity	ppm
[M+2H] ²⁺	645.27411	645.27384	7.2E+09	-0.414
[M+2H] ²⁺	636.26883	636.26868	8.5E+08	-0.228
[M+2H] ²⁺	627.26354	627.26347	8.8E+07	-0.116
a2	185.16484	185.16484	1.2E+08	0.001
a4'	411.22381	411.22367	2.1E+06	-0.343
b2	213.15975	213.15975	5.2E+08	-0.020
b3	342.20235	342.20235	7.8E+07	0.007
b3'	324.19178	324.19177	6.5E+06	-0.039
b4	457.22929	457.22929	1.3E+08	-0.001
b4'	439.21873	439.21873	1.4E+07	0.010
b4 ²⁺	229.11828	229.11831	1.6E+06	0.116
b5	571.27222	571.27224	3.7E+07	0.039
b5'	553.26165	553.26161	2.6E+07	-0.078
b6	700.31481	700.31482	1.9E+07	0.013
b6'	682.30425	682.30431	3.0E+07	0.093
b6''	664.29368	664.29352	2.1E+07	-0.243
pb7	943.34447	943.34428	1.9E+07	-0.202
pb8	1044.39215	1044.39177	3.0E+06	-0.363
pb9	1115.42926	1115.42927	2.2E+07	0.007
py4	590.23340	590.23339	2.3E+08	-0.023
py4'	572.22284	572.22278	2.1E+07	-0.103
py5	719.27600	719.27599	1.5E+07	-0.010
py5'	701.26543	701.26541	6.3E+07	-0.032
py6	833.31892	833.31896	1.7E+08	0.043
py6'	815.30836	815.30842	9.9E+07	0.074
py6 ²⁺	417.16310	417.16302	4.1E+06	-0.193
py7	948.34587	948.34583	1.3E+08	-0.039
py7'	930.33530	930.33518	4.4E+07	-0.132
py8	1077.38846	1077.38876	4.0E+06	0.278
py8'	1059.37790	1059.37795	3.9E+08	0.051
py8''	1041.36733	1041.36724	1.3E+08	-0.087
py8'''	1023.35677	1023.35643	2.1E+07	-0.329
py8 ²⁺	539.19787	539.19781	1.8E+08	-0.108
py8 ²⁺	530.19259	530.19253	2.7E+07	-0.106
py8 ²⁺	521.18730	521.18727	4.1E+07	-0.065
py8 ²⁺	512.18202	512.18204	3.7E+07	0.036
y8'	961.40100	961.40128	2.0E+07	0.291
py9 ²⁺	595.73990	595.73982	1.2E+07	-0.135
y1	175.11895	175.11895	2.2E+08	-0.012

y2	246.15607	246.15607	8.8E+07	0.016
y2'	228.14550	228.14549	4.0E+06	-0.049
y3	347.20374	347.20374	1.9E+08	-0.013
y3'	329.19318	329.19317	1.1E+07	-0.030
y4	510.26707	510.26715	6.2E+06	0.151
y4'	492.25651	492.25656	9.0E+06	0.105
y6'	735.34203	735.34221	9.6E+06	0.246
y6''	717.33146	717.33151	4.1E+06	0.064
Average of absolute errors (ppm)			0.110	
Standard deviation (ppm)			0.109	

Table 2. 10: Peaks assignment for VIEDNEpYTAR IRMPD spectrum. ': loss of water. '':
loss of two waters. ''': loss of three water. p: fragment with phosphate.

VIEDNEpYTAR		ECD (0.3 s 1.2 V)		
Species	Theoretical <i>m/z</i>	Observed <i>m/z</i>	Intensity	ppm
[M+2H] ²⁺	645.27411	645.27406	3.3E+09	-0.073
z1.	160.10805	160.10805	1.7E+07	-0.020
z2	230.13734	230.13735	7.0E+07	0.035
z2.	231.14517	231.14518	8.2E+07	0.057
z3	331.18502	331.18503	4.3E+07	0.029
z3.	332.19285	332.19285	2.4E+08	0.014
pz4'	556.20412	556.20414	6.3E+06	0.045
pz4	574.21468	574.21468	6.8E+07	0.000
pz4.	575.22250	575.22251	1.2E+08	0.009
pz5'	685.24671	685.24668	4.7E+07	-0.041
pz5	703.25727	703.25727	1.7E+08	-0.004
pz5.	704.26510	704.26508	1.9E+08	-0.025
pz6'	799.28964	799.28954	2.3E+07	-0.120
pz6	817.30020	817.30021	3.9E+08	0.012
pz6.	818.30803	818.30867	7.7E+07	0.788
pz7-CO ₂	888.33731	888.33735	9.2E+07	0.040
pz7	932.32714	932.32716	1.1E+08	0.018
pc7	960.37102	960.37129	4.2E+06	0.282
pz8-CO ₂	1017.37991	1017.37992	2.2E+07	0.013
pz8	1061.36974	1061.36965	3.6E+07	-0.081
pz9	1174.45380	1174.45332	2.2E+07	-0.409
[M+2H+e] ⁺	1289.53984	1289.54041	1.6E+08	0.441
Average of absolute errors (ppm)			0.116	
Standard deviation (ppm)			0.191	

Table 2. 11: Peaks assignment for VIEDNEpYTAR ECD spectrum. ': loss of water. p:
fragment with phosphate.

VIEDNEpYTAR		UVPD (5 shots 5mJ)		
Species	Theoretical <i>m/z</i>	Observed <i>m/z</i>	Intensity	ppm
[M+2H] ²⁺	645.27411	645.27353	7.0E+09	-0.895
[M+2H-H ₂ O] ²⁺	636.26883	636.26874	7.0E+07	-0.134
z1	159.10023	159.10023	3.4E+06	0.012
y1	175.11895	175.11895	9.0E+07	-0.012
a2	185.16484	185.16483	2.0E+08	-0.053
x1	201.09822	201.09822	2.3E+06	0.016
x1+H	202.10604	202.10605	1.5E+06	0.041
b2	213.15975	213.15975	1.4E+08	-0.020
b4 ²⁺	229.11828	229.11828	1.8E+06	-0.015
z2	230.13734	230.13735	5.1E+06	0.035
y2-2H	244.14042	244.14039	1.0E+06	-0.106
y2	246.15607	246.15607	3.6E+07	0.016
x2	272.13533	272.13530	2.0E+06	-0.112
x2+H	273.14316	273.14315	2.0E+06	-0.020
a3	314.20743	314.20745	2.0E+06	0.055
z3	331.18502	331.18503	9.4E+06	0.029
b3	342.20235	342.20235	6.6E+06	0.007
y3-H	346.19592	346.19605	1.0E+06	0.377
y3	347.20374	347.20375	3.4E+07	0.016
x3+H	374.19083	374.19089	1.8E+06	0.150
b4'	439.21873	439.21873	1.4E+06	0.010
b4	457.22929	457.22929	4.5E+06	-0.001
y4'	492.25651	492.25656	4.9E+06	0.105
y4	510.26707	510.26706	7.6E+06	-0.025
py8 ²⁺	539.19787	539.19778	6.4E+06	-0.164
a5+H	544.28513	544.28513	1.3E+06	0.003
pz4	574.21468	574.21466	2.6E+06	-0.034
py4	590.23340	590.23338	4.7E+07	-0.040
px4+H	617.22049	617.22042	2.9E+06	-0.119
a6+H	673.32772	673.32755	5.7E+06	-0.255
py5''	683.25487	683.25473	3.4E+06	-0.201
b6	700.31481	700.31492	2.2E+06	0.156
py5'	701.26543	701.26532	2.4E+07	-0.160
py5	719.27600	719.27573	2.2E+06	-0.371
y6'	735.34203	735.34203	4.9E+06	0.002
y6	753.35259	753.35201	2.1E+06	-0.775
py6'	815.30836	815.30765	3.6E+07	-0.870
py6	833.31892	833.31882	4.3E+07	-0.125
pa7+H	916.35738	916.35744	7.0E+06	0.065
py7'	930.33530	930.33493	1.7E+07	-0.401

pb7	943.34447	943.34450	1.8E+06	0.031
py7	948.34587	948.34561	1.2E+07	-0.271
py8''	1041.36733	1041.36661	2.5E+07	-0.692
py8'	1059.37790	1059.37732	4.2E+07	-0.544
pb9	1115.42926	1115.42926	2.4E+06	-0.002
Average of absolute errors (ppm)			0.152	
Standard deviation (ppm)			0.213	

Table 2. 12: Peaks assignment for VIEDNEpYTAR UVPD spectrum. ': loss of water. '': loss of two waters. ''': loss of three water. p: fragment with phosphate.

CHAPTER 3.

Facile determination of phosphorylation sites in peptides
using two-dimensional mass spectrometry

4.1. Declaration

This chapter consist of one published research article:

Paris, J.; Morgan, T. E.; Wootton, C. A.; Barrow, M. P.; O'Hara, J.; O'Connor, P. B. Facile determination of phosphorylation sites in peptides using two-dimensional mass spectrometry. *Anal Chem* 2020.

Except for minor adjustments to aid incorporation into this thesis and extra Figures, the article has been reproduced unchanged. The tables of assignments are at the end of the chapter.

As a first author I carried out all experiments, analysed all data, and prepared all Figures as well as the manuscript. TEM trained me on 2DMS. TEM and CAW developed the 2DMS homemade software. MPB, JOH and PBOC were involved in project management and editing the final manuscript.

Facile determination of phosphorylation sites in peptides using two-dimensional mass spectrometry

Anal Chem. 2020, 92, 10, 6817–6821

Johanna Parist, Tomos E. Morgan†, Christopher A. Wootton†, Mark P. Barrow†, John O’Hara‡, Peter B. O’Connor*†

†University of Warwick, Department of Chemistry, Coventry, CV4 7AL, United Kingdom

‡UCB, 216 Bath Road, Slough, SL1 3WE, United Kingdom

*Corresponding author email address: p.oconnor@warwick.ac.uk

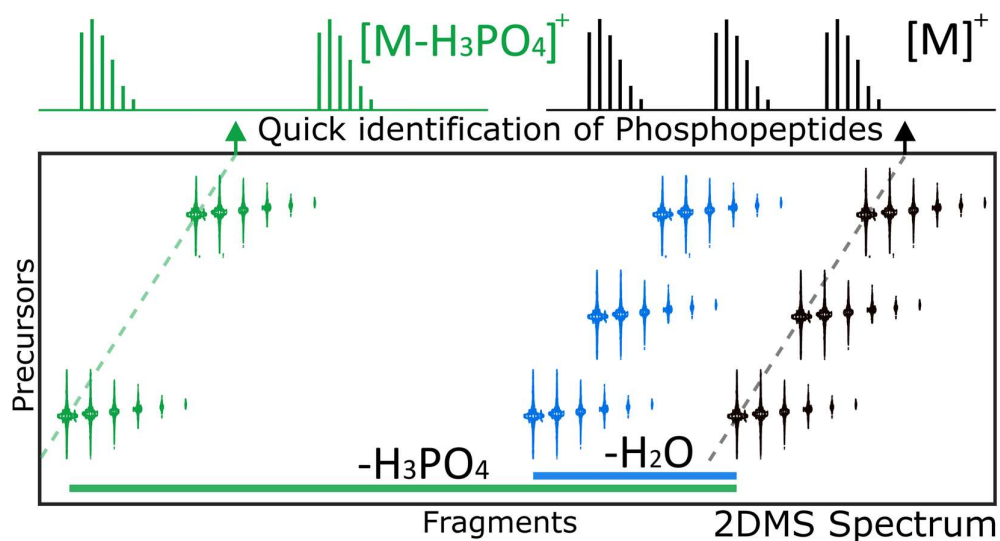


Figure 3. 1: Graphical Abstract

4.2. Abstract

Detection and characterization of phosphopeptides by infrared multiphoton dissociation two-dimensional mass spectrometry is shown to be particularly effective. A mixture of phosphopeptides was analyzed by 2DMS without any prior separation. 2DMS enables the data independent analysis of the mixture, and the correlation of the fragments to their precursor ions. The extraction of neutral loss lines corresponding to the loss of phosphate under IRMPD fragmentation allows the selective identification of phosphopeptides. Resonance of the 10.6 μm infrared radiation with the vibrational modes of the phosphate functional group produced efficient absorption and high cleavage coverage of the phosphopeptides at much lower irradiation fluence than for non-phosphorylated peptides improving discrimination. Additionally, the localization of the phosphate group was determined.

4.3. Introduction

Thousands of proteins are expressed in mammalian cells; a third of them are thought to be phosphorylated.¹ Protein phosphorylation is one of the major known signal transduction mechanisms for controlling and regulating intercellular processes.² Phosphorylation also alters protein activity, subcellular location, degradation, and interactions with other proteins.³ Phosphorylation predominantly occurs on serine, threonine, or tyrosine, through the formation of a phosphoester linkage between the amino acid and the phosphate group at the side-chain hydroxyl oxygen. However, it has also been shown on histidine, lysine, and arginine through phosphoamidate bonds, and on aspartic acid and glutamic acid through anhydride linkages.^{4,5}

Infrared multiphoton dissociation⁶⁻⁸ (IRMPD) is a fragmentation technique typically using a CO_2 laser. The sequential absorption of 10.6 μm photons increases the internal energy of ions (0.117 eV per photon) until dissociation occurs. IRMPD is a slow heating method leading to similar fragmentation to collision-induced dissociation (CID) for peptides and proteins. For these species, fragmentation occurs via a low energy proton rearrangement leading to destabilisation and cleavage of an amide bond.^{9,10} Additionally, labile post translational modifications (PTMs) can also be cleaved. In non-phosphorylated peptides, the IR photons are broadly absorbed, particularly into NH and OH bonds, but rapidly redistributes via vibrational coupling. The infrared (IR) radiation is resonant with

one or more phosphate vibrational modes,^{11, 12} and therefore, with IRMPD, phosphopeptides fragment at a much lower threshold than their unphosphorylated counterpart, in both negative^{13, 14} and in positive^{15, 16} ionisation mode. Correia et al compared the fragmentation efficiencies between phosphopeptides and their unphosphorylated counterparts and found that phosphopeptides fragment at a lower threshold (Figure 3.2).

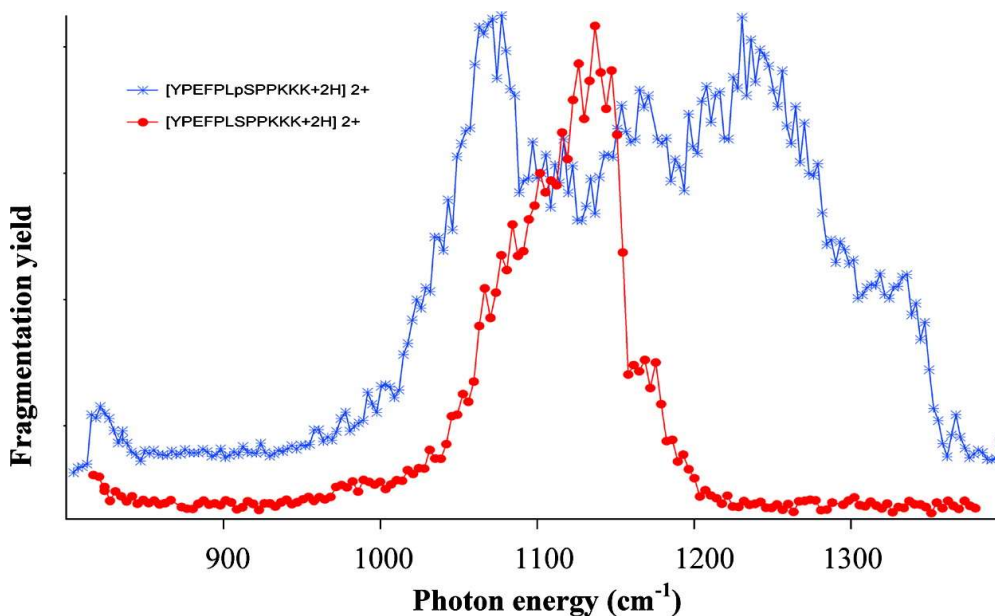


Figure 3. 2: Fragmentation efficiency defined as $-\ln(P/F + P)$, with F being the sum of fragment abundances and P the abundance of the intact precursor. Reprinted (adapted) with permission from Correia et al.¹¹ Copyright 2007 American Chemical Society.

Phosphates are considered labile groups in mass spectrometry and produce diagnostic ions under CID or IRMPD fragmentation. Depending on the charge state of the peptide and the amino acid the phosphate is linked to, the fragmentation pathway is different^{17, 18} and leads to the loss of phosphoric acid (H_3PO_4) or metaphosphoric acid (HPO_3) in positive mode, and phosphite (PO_3) in negative mode. Phosphorylated peptides are selectively detected in complex mixtures, by diagnostic ions^{19, 20} or neutral loss from the precursor.^{21, 22} Radical-mediated techniques such as ECD and ETD fragment selectively at the peptide backbone and, therefore, allow the sequencing of the phosphopeptide without the loss of the phosphate group allowing localisation.^{23, 24}

Usually, complex samples are analysed by liquid chromatography tandem mass spectrometry (LC-MS/MS), the compounds are separated by liquid chromatography and then fragmented and detected in the mass analyser. Two-dimensional mass spectrometry (2DMS) is an alternative technique that enables the direct infusion of the sample, without the need for liquid chromatography separation or quadrupole isolation of the species, and retains the information of which fragment ions are formed from which precursors. The 2DMS sequence pulse has been previously optimised for IRMPD.²⁵ IRMPD 2DMS was carried out in the analysis of Angiotensin I,²⁶ cytochrome C,²⁷ and calmodulin,²⁸ but also in the analysis of polymers.²⁹ To date, for posttranslational modification, only glycosylation has been analysed by 2DMS.³⁰

One of the limitations of phosphoproteomics is the phosphopeptide loss because of its increase hydrophilicity during the sample preparation or subsequent liquid chromatography in reverse phase column. In the 2DMS workflow, the direct infusion strategy allows avoidance of these losses. The nanoelectrospray ion source³¹ also allows the detection of low concentration phosphopeptides.³² The extraction of neutral loss lines in 2DMS selectively identifies phosphopeptides.

4.4. Experimental section

2.4.1. Material

MS Phosphomix 1 Light was obtained from Sigma (MSP1L-1VL) and contained 10 phosphopeptides: Ph01: VLHSGpSR, Ph02: RSpYpSRSR, Ph03: RDSLGPpTYSSR, Ph04: pTKLIpTQLRDAK, Ph05: EVQAEQPSSpSSPR, Ph06: ADEPpSSEESDLEIDK, Ph07: ADEPpSSEEpSDLEIDK, Ph08: FEDEGAGFEESpSETGDYEK, Ph09: ELSNpSPLRENSFGpSPLFR and Ph10: SPTEYHEPVpYANPFYRPTpTPQR. Water was purified by a Millipore Direct-Q purification system (Merck Millipore, MA, USA). Acetonitrile was obtained from VWR chemicals (CAS: 75-05-8). Formic acid was obtained from Sigma-Aldrich (CAS: 64-18-6).

2.4.2. Ionisation

MS Phosphomix 1 was dissolved into 80:20 Water:ACN + 0.1% FA (0.2 μM) and was ionised using a custom nano electrospray ionisation source (nESI) using a pulled glass capillary with several μm open orifice. For 2DMS, longer tips were produced however only 30 μL of sample was sprayed during the experiment.

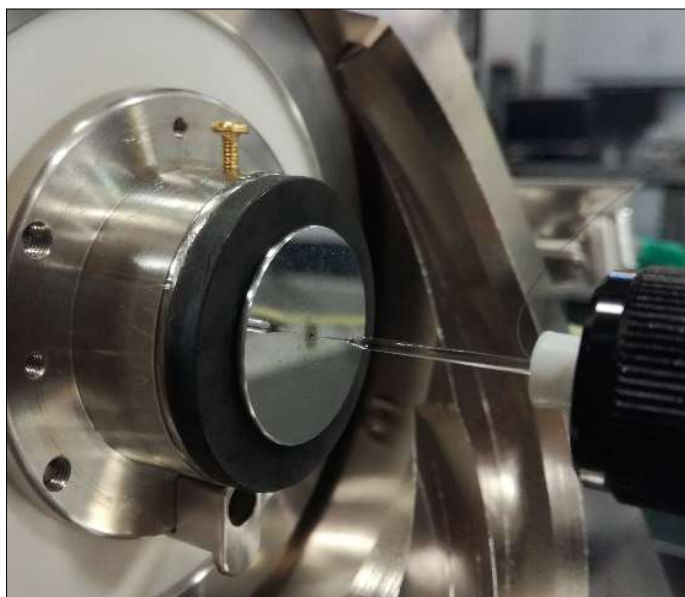


Figure 3. 3: NanoESI set-up.

2.4.3. 2DMS Sequence

In a FT-ICR instrument,^{33, 34} 2DMS uses a non-standard pulse sequence,^{35, 36} shown Figure 3.4. Before excite/detect, ions are modulated radially in the ICR cell before the in-cell fragmentation event, using a first excitation (P1), then delay, followed by a second excitation (P1) sequence. The pulse sequence separates ions in space depending on their m/z . Spatially resolved in-cell fragmentation methods such as IRMPD may be used for 2DMS. Scans are accumulated with an incremental delay, thereby the ions modulate in and out of the central fragmentation zone of the cell over successive scans. In each scan, the ions are at a different radius in the ICR cell and undergo different extents of fragmentation. The modulation of intensities of the precursor and its fragments with each scan is the same but opposite phase. Computing the intensities permits the creation of a 2DMS spectrum where all the fragments are correlated to their precursors.

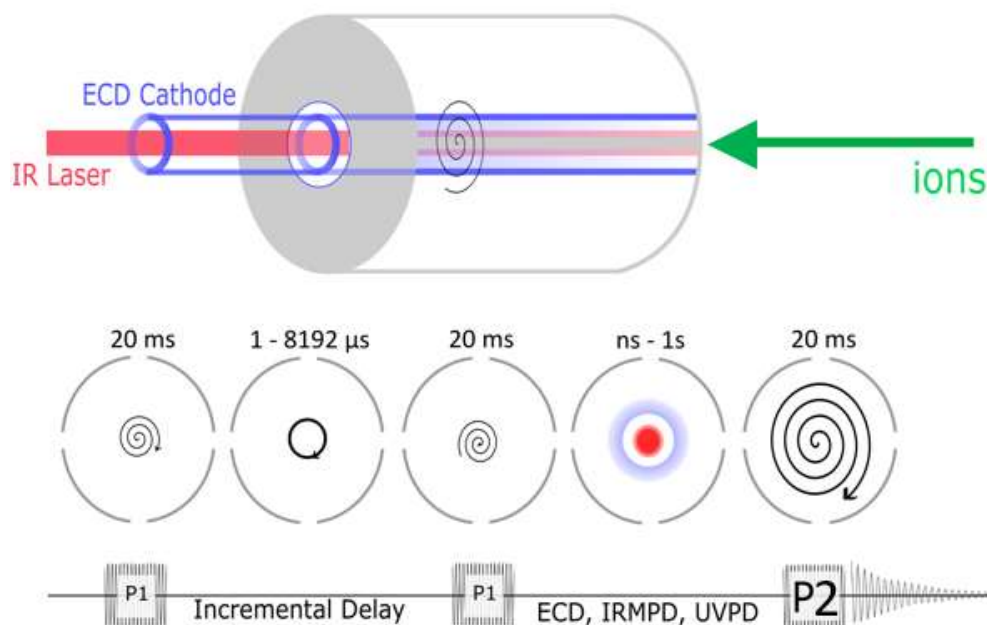


Figure 3. 4: Fundamentals of 2DMS. Illustration of the ICR Cell,³⁷ 2DMS pulse sequence and corresponding ion motions within the ICR cell.³⁵

2.4.4. 2DMS Workflow

Mass spectrometry was conducted using a 12 T Bruker solarix FT-ICR mass spectrometer (Bruker Daltonik GmbH, Bremen, Germany), and IRMPD fragmentation was achieved using a continuous wave, 25 W, CO₂ laser (Synrad Inc., Washington, USA) for 0.135 seconds at a laser power of 40%. 8192 scans of 1M (16-bit) data points were acquired over a mass range of m/z 328-3000 on the vertical (precursor) axis and m/z 147-3000 on the horizontal (fragment) axis. The 2DMS experiment was acquired over 170 min. (1.25 second per scan). The data was processed with SPIKE,³⁷ using urQRd³⁸ with rank 15. Spectra were extracted using T2D³⁹ and they were internally calibrated using known fragment peaks with a quadratic calibration function in the Bruker DataAnalysis v4.3 software (Bruker Daltonics GmbH, Bremen, Germany).

4.5. Results and discussion

2.5.1. Modulation of intensities

During the 2DMS pulse sequence, ions are separated radially before fragmentation. For each scan, the precursor is at a different radius at the time of fragmentation. Therefore, the precursor ion intensity oscillates over the various scans depending on its own cyclotron frequency and magnitude of fragmentation. With phosphopeptides, using IRMPD, the most intense fragment is usually the loss of the phosphate. The intensity of the fragment ions have the same modulation frequency as of the precursor, but opposite phase (Figure 3.5).

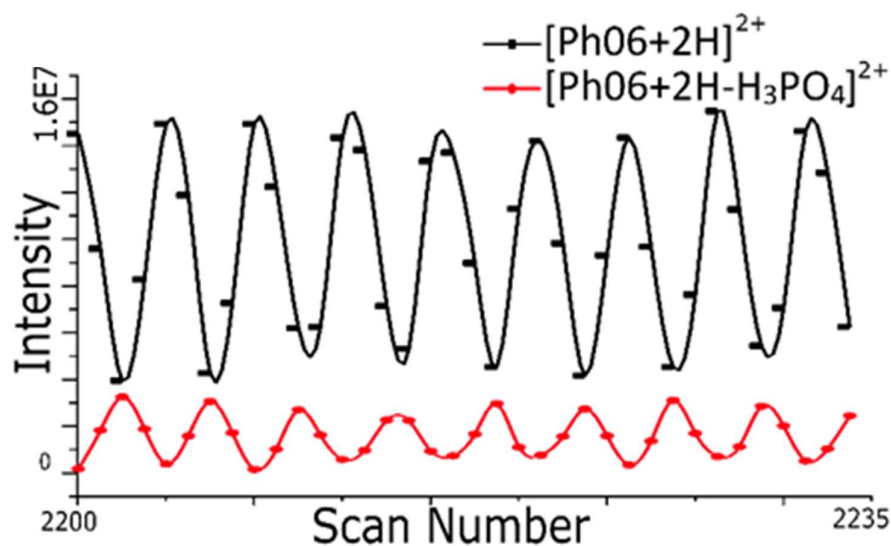


Figure 3. 5: Modulation of intensities of the precursor Ph06 in black and in red the fragment of Ph06 corresponding to the loss of phosphate. (B-spline).

All observed precursors had different m/z values and therefore different cyclotron frequencies in the ion cyclotron cell. The frequency of modulation of the intensities over the scan enables the differentiation of which fragments are derived from which precursors in a complex mixture.

2.5.2. A 2DMS spectrum

All phosphopeptides were analysed simultaneously without prior liquid chromatography separation or quadrupole isolation. The 2DMS spectrum is a three dimensional plot of precursor m/z , fragment m/z , and intensity, usually shown as a contour plot.⁴⁰ Figure 3.6 shows the complete 2D spectrum of the phosphopeptides mixture as a contour plot. Any line of the 2DMS spectrum may be extracted and analyzed in Bruker's DataAnalysis software using an in-house generated T2D software, which rewrites the 2DMS scan lines into a format that DataAnalysis can read. Horizontal lines are fragment ion scan lines, discussed below, and correlate the fragments of a given precursor.

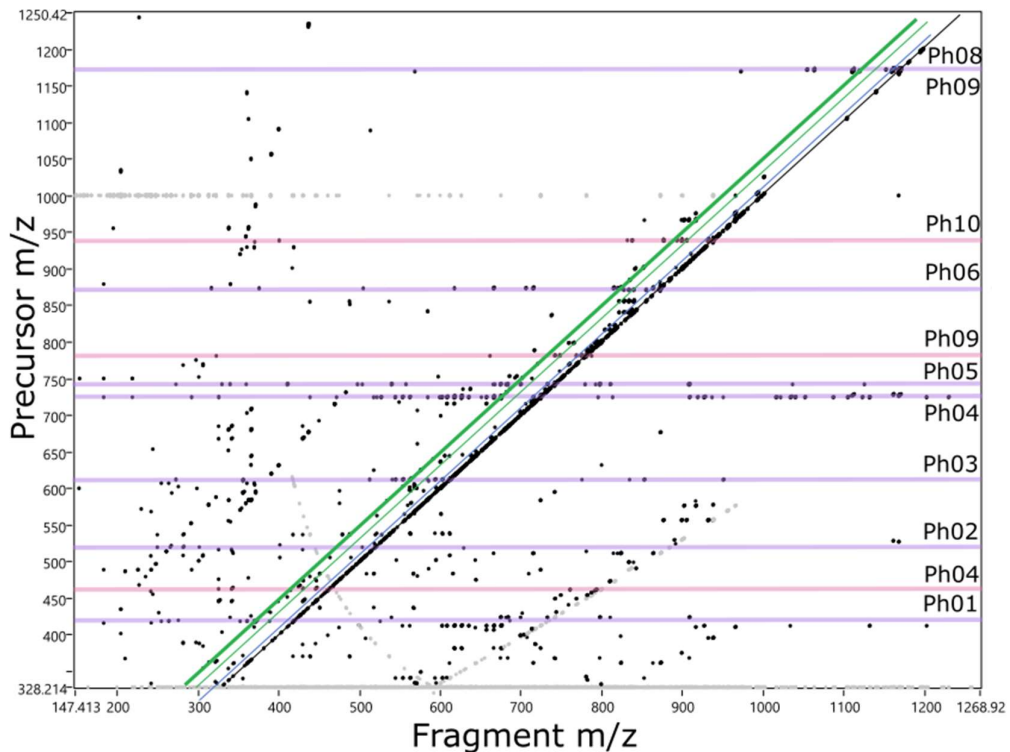


Figure 3. 6: 2DMS spectrum of the phosphopeptides mixture. In pink and purple, precursor lines respectively at 3+ and 2+. In black, auto-correlation line. In blue and green, neutral loss lines.

It is possible to zoom in the 2DMS spectrum and extract information. Figure 3.7 shows two zooms of a 2+ Ph04 and 3+ Ph09 precursors. The isotope envelopes are retained in the 2DMS experiment, and it is possible to quickly identify the charge states of the ions.

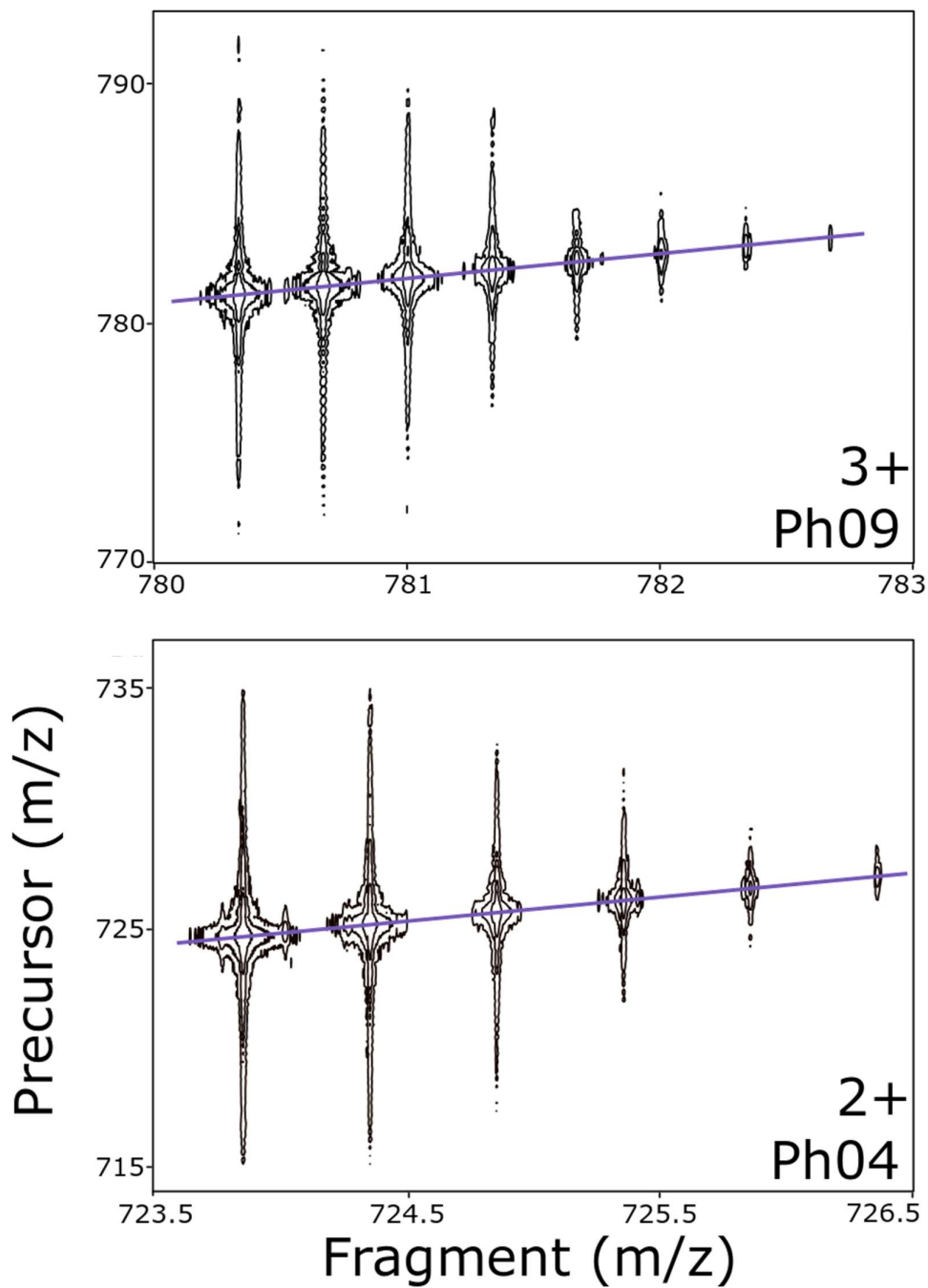


Figure 3. 7: Extracted zooms of the 2DMS spectrum of $[\text{Ph09}+3\text{H}]^{3+}$ and $[\text{Ph04}+2\text{H}]^{2+}$

The autocorrelation line corresponds to the diagonal line $x=y$ and can be extracted from the 2DMS spectrum (Figure 3.8.B). It contains all the fragmented precursors and is similar to a standard MS spectrum (Figure 3.8.A).

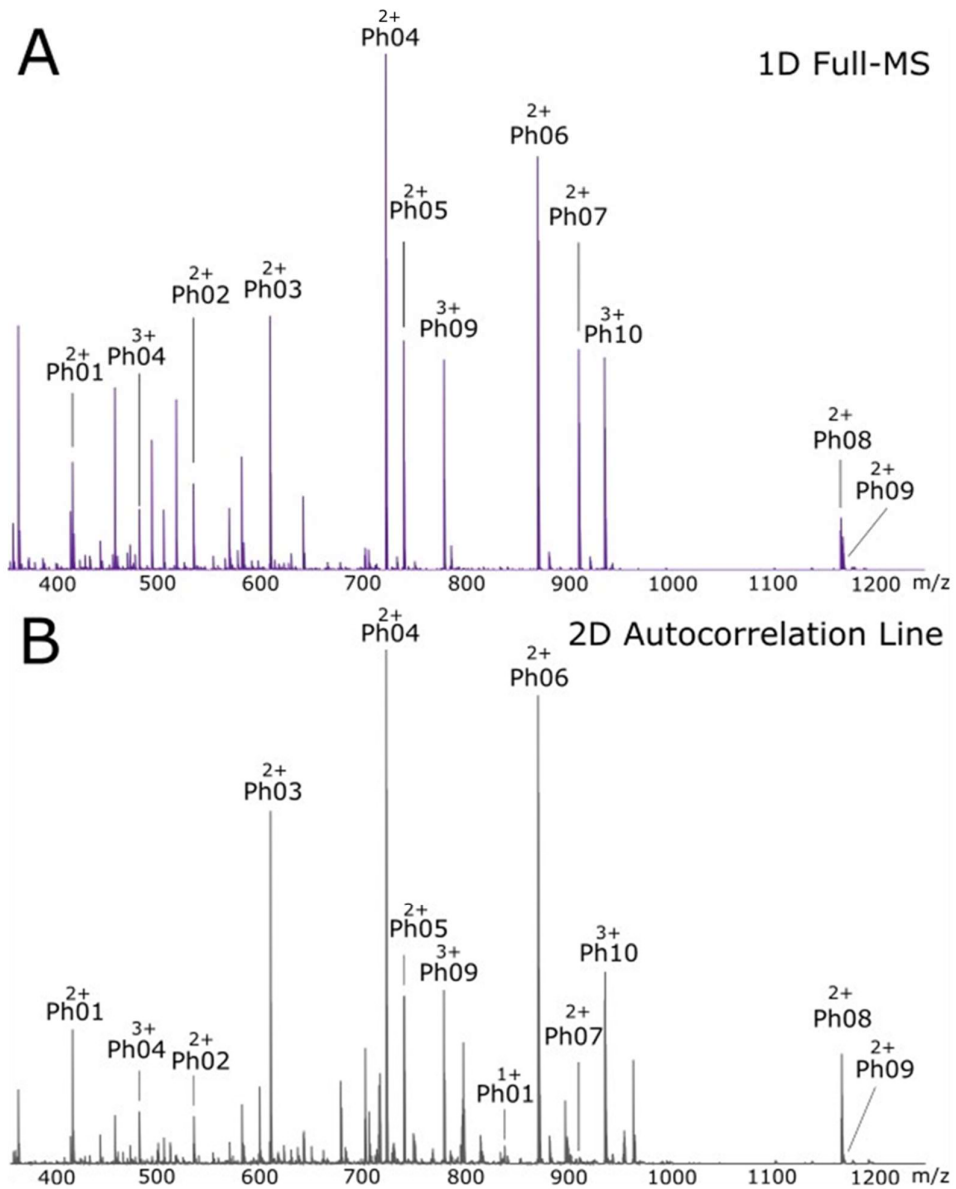


Figure 3. 8: Precursors of the MS Phosphomix 1 Light Sample (A) 1D standard MS scan. (B) Extracted 2D autocorrelation line.

Variations in intensities are seen between the two spectra due to the variability of fragmentation of the species which impact the precursor intensity in 2DMS. Therefore, some low intensity species are at higher intensity in 2DMS such as peptides from the matrice, by-products or $[\text{Ph01}+\text{H}]^+$. The main difference in the two spectra which is critical for the experiment, is the lower intensity of $[\text{Ph07}+2\text{H}]^{2+}$.

To understand why Ph07 was not observed at higher intensities in the 2DMS spectrum, a chromatography mode experiment was run, without any fragmentation, showing the direct infusion of the mixtures within a stable spray. After further investigation (Figure 3.9) it has been found that Ph07 was only detected for a brief amount of time in a chromatography mode experiment. The loss of Ph07 was, therefore, not due to the 2DMS experiment. Ph07 is a hydrophobic peptide; it undergoes adsorption at the glass surface of the pulled glass capillary used in the direct infusion experiment.

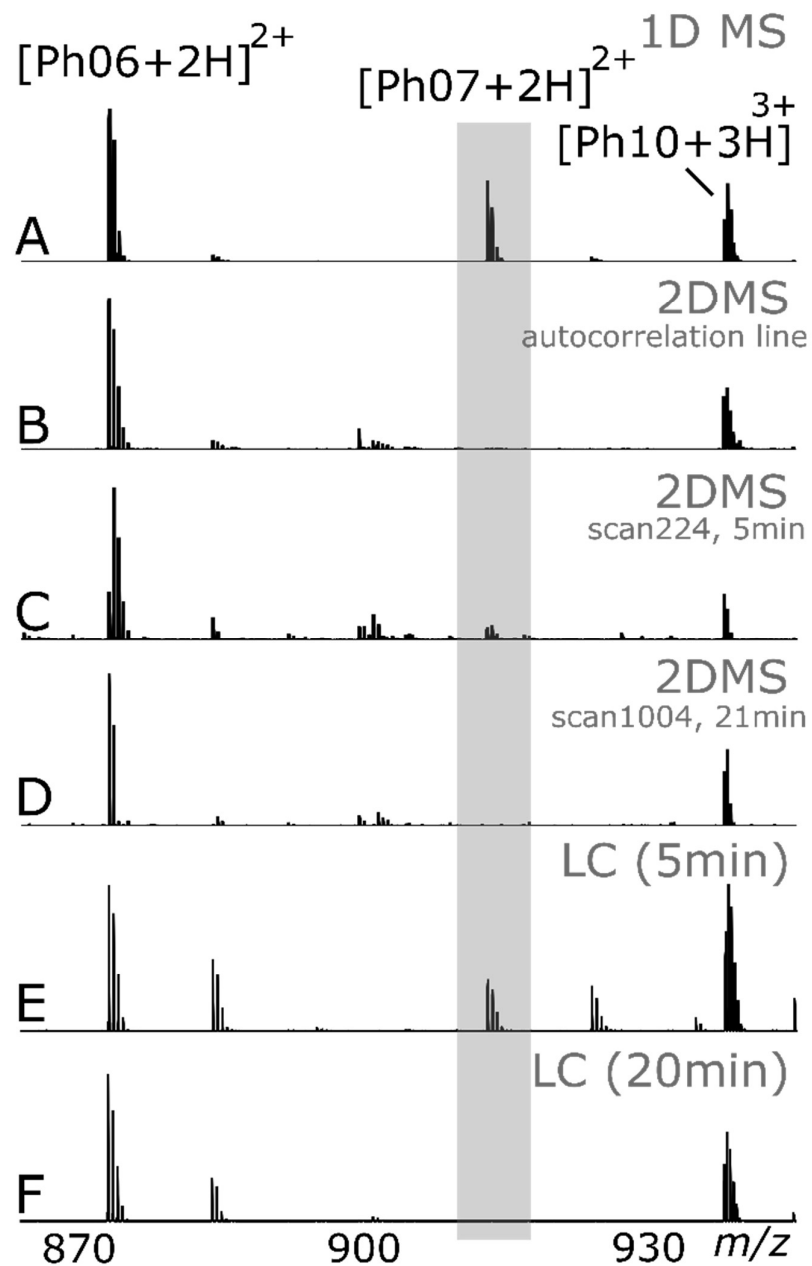


Figure 3. 9: Loss of Ph07 (A) 1D standard MS scan. (B) Extracted 2D autocorrelation line. (C) Extracted 1D scan of the 2DMS experiment (scan #224 at 4.75min). (D) Extracted 1D scan of the 2DMS experiment (scan #1004 at 21min). (E) Extracted 1D scan of the LCMS experiment (at 5min). (F) Extracted 1D scan of the LCMS experiment (at 20min).

2.5.3. Resolution of the experiment

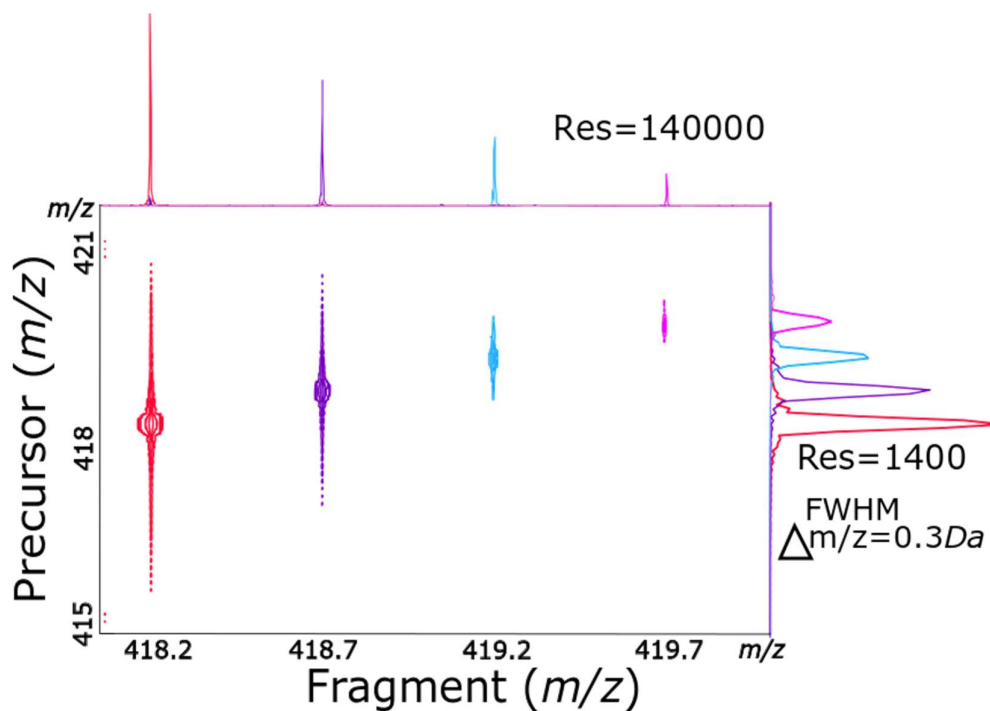


Figure 3. 10: Resolution of the 2DMS experiment, zoom on $[Ph01+2h]^{2+}$ and extracted lines in the two dimensions.

In Figure 3.10, the phosphopeptide Ph01 is shown at charge state 2+. The resolution in the horizontal dimension is around 140 000 at m/z 420 which is consistent with a 0.4194 second transient (1 MW) at 12 T. The resolution in the vertical axis is around 1400 at m/z 420, which is consistent with the collection of the 8192 data points (scans) in the second dimension.

2.5.4. Extraction of the neutral loss lines

Diagonal lines in 2DMS correspond to the autocorrelation line ($x=y$) and the neutral loss lines.

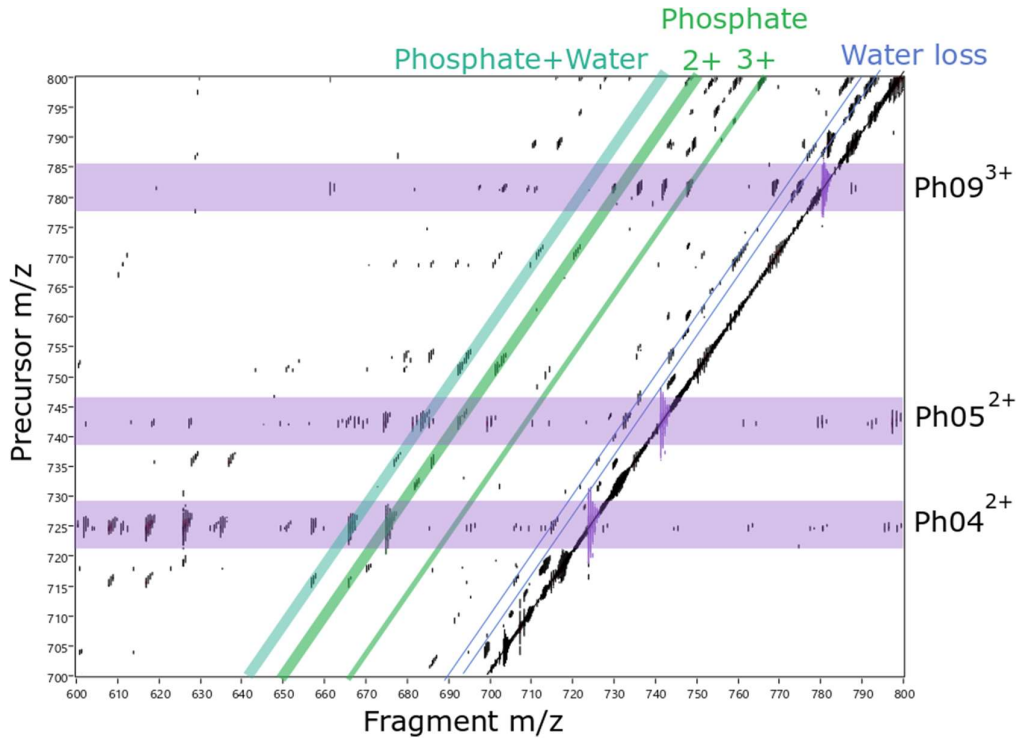


Figure 3. 11: Zoom of the 2DMS spectrum, showing in purple the fragment lines of three precursors, in blue the water loss lines, and in green the phosphate loss lines.

The neutral loss lines can be extracted and analyzed in the DataAnalysis Bruker software. Figure 3.12 show the extracted neutral loss lines of a loss of 49 Da and 32.5 Da which correspond to the loss of H_3PO_4 (98 Da) in 2+ and 3+ charge states respectively. The extraction of the neutral loss lines quickly reveals the phosphopeptides in the mixture.

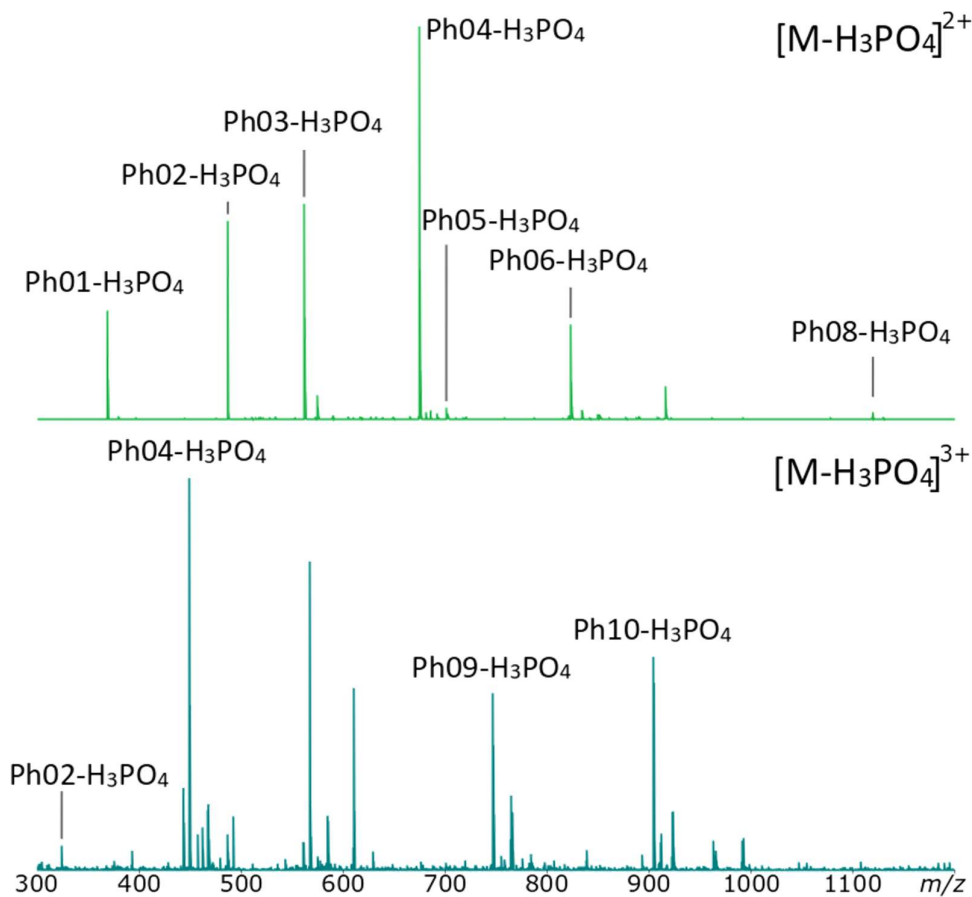


Figure 3. 12: Extracted H_3PO_4 loss lines, at 2+ and 3+.

Except Ph07, all phosphopeptides in the mixture were found in the extracted phosphate loss lines. Other phosphopeptides were detected, they are expected to be synthetic by-products. No phosphate migration was detected. The focus will be on the ten major compounds.

The intensity of the phosphate loss fragment of Ph05 is low. Low intensity phosphate loss fragments have been seen in the literature when the phosphopeptide undergoes a different fragmentation pathway, especially with phosphothreonine and phosphotyrosine containing peptides.¹⁷ However, the phosphate on Ph05 is on the serine, so an alternate mechanism was not expected. Ph05 has few amino acids (arginine, serine, and glutamic acid) with the potential of having hydrogen bonds with the phosphate group, which could lead to a stabilisation of the phosphorylation and explain why there are less phosphate loss fragments.

2.5.5. Cleavage coverage of the phosphopeptides

For each detected precursor, it is possible to extract a horizontal line containing the fragments of that precursor. Figure 3.13. shows the fragment line of Ph06 (ADEPpSSEESDLEID).

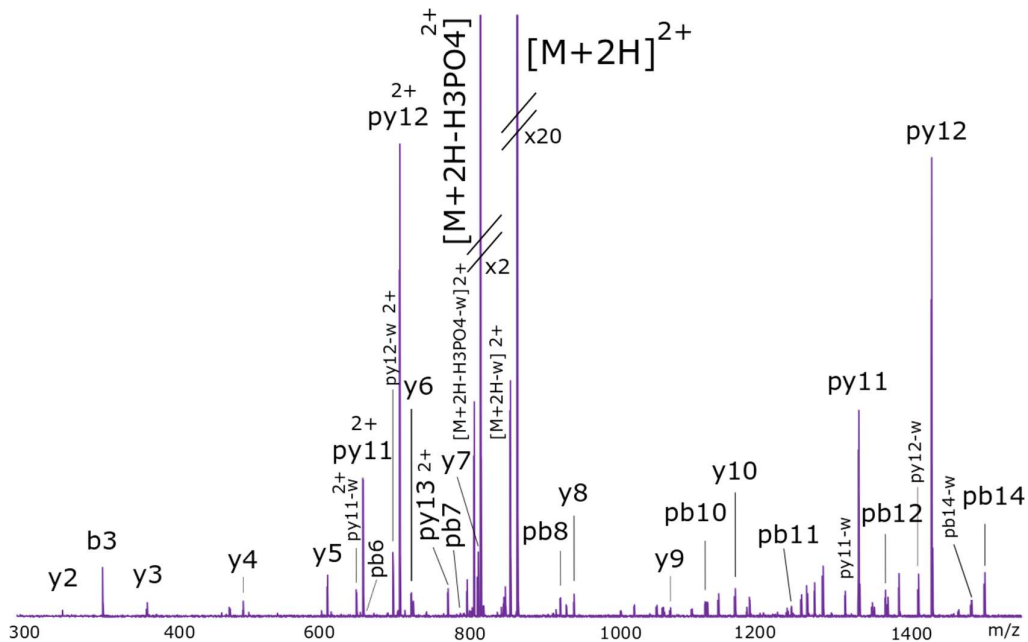


Figure 3. 13: Extracted fragment line of Ph06. -w: loss of water. p: fragment containing the phosphorylation. M: ADEPpSSEESDLEID (precursor Ph06).



Diagram 3. 1: Cleavage diagram for Ph06. In green and bold: fragments with phosphorylation. In red: fragments without phosphate group.

Cleavage coverage of Ph06 is 92%. The phosphorylation was retained on the sequence ion, allowing the localization of the PTM on the first serine.

Table 3.1. contains all the information on the phosphopeptides extracted from the 2DMS spectra with cleavages marked and the region of the phosphate localization highlighted in green. In most of the phosphopeptides, no fragments with the loss of the phosphate group were detected along with the fragment containing the phosphate. Therefore, the localization of the phosphate group was assigned using all fragments.

Species	Cleavage Coverage	Phosphate sites & comments
Ph01	V L H S G p S R	50% GSR
Ph02	R S p Y p S R S R	50% S. Loss of the phosphate at Y in b3, pb4 and pb5
Ph03	R D S L G p T Y S S R	67% GT
Ph04	p T K L I p T Q L R D A K	70% TK & TQ Loss of phosphate at b4
Ph05	E V Q A E Q P S S p S S P R	75% S
Ph06	A D E P p S S E E S D L E I D	92% S
Ph08	F E D E G A G F E E S p S E T G D Y E E K	63% SSE
Ph09	E L S N p S P L R E N S F G p S P L E F R	22% ELSNSPLRENF & GS
Ph10	S P T E Y H E P V p Y A N P F Y R P T p T P Q R	24% PVYANPFY & T

Table 3. 1: Observed cleavage coverage of the detected phosphopeptides by 2DMS. Green, bold: b/y fragment containing a single phosphate, Green, double lined: b/y fragment containing two phosphates, red: b/y fragment without a phosphate group, green box: localisation of the phosphate group.

The IRMPD pulse length was optimized beforehand in a 1DMS experiment for the fragmentation of medium sized phosphopeptides. Ph06 was quadrupole isolated and fragmented at different IRMPD pulse length. 0.135 seconds IRMPD pulse length gave the best cleavage coverage for the peptide and was selected for the analysis of the complex mixture.

Therefore, Ph03, Ph04, Ph05, Ph06, Ph08 have high cleavage coverage (~75%). The smaller peptide Ph01 and Ph02 are over fragmented. The phosphate group on the tyrosine on Ph02 is cleaved in the fragments b3, pb4 and pb5. Therefore, the localisation of the phosphate group on the tyrosine is lost; the localisation of the phosphate group on serine is retained for Ph02. Ph09, and Ph10 showed lower cleavage coverage (~25%) due

to their longer length. The site of the phosphate was determined in eleven out of the thirteen phosphorylation sites.

4.6. Conclusion and outlook

Two-dimensional mass spectrometry enabled the characterisation of a mixture of phosphopeptides. The extraction of neutral loss lines enabled their selective identification. 90% of the phosphopeptides were assigned in a single direct infusion experiment without the need for liquid chromatography separation or quadrupole isolation. High cleavage coverage was achieved, and the localisation of the phosphate was not lost during the fragmentation.

The obtained resolving power was sufficient for confident assignment of the precursors and the fragments in this experiment. However, to increase the resolution of the 2DMS spectra, it is possible to acquire a longer transient for each scan to increase the horizontal resolution power or to increase the number of scans to increase the vertical resolving power. In both cases, more acquisition time and more processing time are required due to the size of the resulting data file.

The method presented shows a data independent approach for phosphopeptide analysis and fragmentation analysis independent of liquid chromatography.

To investigate a full phosphoproteome, the 2DMS experiment would be done on 200 m/z quadrupole isolated windows. Each of the windows would have their own optimized IRMPD pulse length, depending on the size of the precursors in the mass-to-charge ratio window.

4.7. Acknowledgement

The authors would like to thank Bryan Marzullo, Yuko Lam, and Maria van Agthoven for their help. As well as all the ICR lab for their support. Johanna Paris thanks EPSRC for a PhD studentship through the EPSRC Centre for Doctoral Training in Molecular Analytical Science, grant number EP/L015307/1, UCB, and BB/R022399/1, BB/P021879/1, EP/N033191/1, and Horizon 2020 EU FTICR MS network (731077) for funding.

4.8. References

1. Cohen, P. The origins of protein phosphorylation *Nature cell biology* **2002**, *4*, E127-E130.
2. Pawson, T.; Scott, J. D. Protein phosphorylation in signaling—50 years and counting *Trends Biochem. Sci* **2005**, *30*, 286-290.
3. Cohen, P. The regulation of protein function by multisite phosphorylation—a 25 year update *Trends Biochem. Sci* **2000**, *25*, 596-601.
4. Cieśla, J.; Frączyk, T.; Rode, W. Phosphorylation of basic amino acid residues in proteins: important but easily missed *Acta Biochim. Pol.* **2011**, *58*, 137-148.
5. Hardman, G.; Perkins, S.; Ruan, Z.; Kannan, N.; Brownridge, P.; Byrne, D. P.; Eyers, P. A.; Jones, A. R.; Eyers, C. E. Extensive non-canonical phosphorylation in human cells revealed using strong-anion exchange-mediated phosphoproteomics *BioRxiv* **2017**, 202820.
6. Little, D. P.; Speir, J. P.; Senko, M. W.; O'Connor, P. B.; McLafferty, F. W. Infrared multiphoton dissociation of large multiply charged ions for biomolecule sequencing *Anal. Chem.* **1994**, *66*, 2809-2815.
7. Talebpour, A.; Bandrauk, A.; Yang, J.; Chin, S. Multiphoton ionization of inner-valence electrons and fragmentation of ethylene in an intense Ti: sapphire laser pulse *Chem. Phys. Lett.* **1999**, *313*, 789-794.
8. Maitre, P.; Scuderi, D.; Corinti, D.; Chiavarino, B.; Crestoni, M. E.; Fornarini, S. Applications of Infrared Multiple Photon Dissociation (IRMPD) to the Detection of Posttranslational Modifications *Chem. Rev.* **2019**.
9. McCormack, A. L.; Somogyi, A.; Dongre, A. R.; Wysocki, V. H. Fragmentation of protonated peptides: surface-induced dissociation in conjunction with a quantum mechanical approach *Anal. Chem.* **1993**, *65*, 2859-2872.
10. Tsaprailis, G.; Nair, H.; Somogyi, Á.; Wysocki, V. H.; Zhong, W.; Futrell, J. H.; Summerfield, S. G.; Gaskell, S. J. Influence of secondary structure on the fragmentation of protonated peptides *JACS* **1999**, *121*, 5142-5154.
11. Correia, C. F.; Balaj, P. O.; Scuderi, D.; Maitre, P.; Ohanessian, G. Vibrational signatures of protonated, phosphorylated amino acids in the gas phase *JACS* **2008**, *130*, 3359-3370.

12. Stedwell, C. N.; Patrick, A. L.; Gulyuz, K.; Polfer, N. C. Screening for phosphorylated and nonphosphorylated peptides by infrared photodissociation spectroscopy *Anal. Chem.* **2012**, *84*, 9907-9912.
13. Flora, J. W.; Muddiman, D. C. Gas-phase ion unimolecular dissociation for rapid phosphopeptide mapping by IRMPD in a penning ion trap: An energetically favored process *JACS* **2002**, *124*, 6546-6547.
14. Flora, J. W.; Muddiman, D. C. Determination of the relative energies of activation for the dissociation of aromatic versus aliphatic phosphopeptides by ESI-FTICR-MS and IRMPD *JASMS* **2004**, *15*, 121-127.
15. Crowe, M. C.; Brodbelt, J. S. Infrared multiphoton dissociation (IRMPD) and collisionally activated dissociation of peptides in a quadrupole ion trap with selective IRMPD of phosphopeptides *JASMS* **2004**, *15*, 1581-1592.
16. Crowe, M. C.; Brodbelt, J. S. Differentiation of phosphorylated and unphosphorylated peptides by high-performance liquid chromatography-electrospray ionization-infrared multiphoton dissociation in a quadrupole ion trap *Anal. Chem.* **2005**, *77*, 5726-5734.
17. DeGnore, J. P.; Qin, J. Fragmentation of phosphopeptides in an ion trap mass spectrometer *JASMS* **1998**, *9*, 1175-1188.
18. Rožman, M. Modelling of the gas-phase phosphate group loss and rearrangement in phosphorylated peptides *J. Mass Spectrom.* **2011**, *46*, 949-955.
19. Huddleston, M. J.; Annan, R. S.; Bean, M. F.; Carr, S. A. Selective detection of phosphopeptides in complex mixtures by electrospray liquid chromatography/mass spectrometry *JASMS* **1993**, *4*, 710-717.
20. Flora, J. W.; Muddiman, D. C. Selective, sensitive, and rapid phosphopeptide identification in enzymatic digests using ESI-FTICR-MS with infrared multiphoton dissociation *Anal. Chem.* **2001**, *73*, 3305-3311.
21. Carr, S. A.; Huddleston, M. J.; Annan, R. S. Selective detection and sequencing of phosphopeptides at the femtomole level by mass spectrometry *Anal. Biochem.* **1996**, *239*, 180-192.
22. Chang, E. J.; Archambault, V.; McLachlin, D. T.; Krutchinsky, A. N.; Chait, B. T. Analysis of protein phosphorylation by hypothesis-driven multiple-stage mass spectrometry *Anal. Chem.* **2004**, *76*, 4472-4483.

23. Stensballe, A.; Jensen, O. N.; Olsen, J. V.; Haselmann, K. F.; Zubarev, R. A. Electron capture dissociation of singly and multiply phosphorylated peptides *Rapid Commun. Mass Spectrom.* **2000**, *14*, 1793-1800.
24. Song, H.; Håkansson, K. Electron detachment dissociation and negative ion infrared multiphoton dissociation of electrosprayed intact proteins *Anal. Chem.* **2011**, *84*, 871-876.
25. van Agthoven, M. A.; Chiron, L.; Coutouly, M.-A.; Sehgal, A. A.; Pelupessy, P.; Delsuc, M.-A.; Rolando, C. Optimization of the discrete pulse sequence for two-dimensional FT-ICR mass spectrometry using infrared multiphoton dissociation *Int. J. Mass spectrom.* **2014**, *370*, 114-124.
26. van Agthoven, M. A.; Delsuc, M.-A.; Rolando, C. Two-dimensional FT-ICR/MS with IRMPD as fragmentation mode *Int. J. Mass spectrom.* **2011**, *306*, 196-203.
27. van Agthoven, M. A.; Wootton, C. A.; Chiron, L.; Coutouly, M.-A.; Soulby, A.; Wei, J.; Barrow, M. P.; Delsuc, M.-A.; Rolando, C.; O'Connor, P. B. Two-dimensional mass spectrometry for proteomics, a comparative study with cytochrome c *Anal. Chem.* **2016**, *88*, 4409-4417.
28. Floris, F.; van Agthoven, M.; Chiron, L.; Soulby, A. J.; Wootton, C. A.; Lam, Y. P.; Barrow, M. P.; Delsuc, M.-A.; O'Connor, P. B. 2D FT-ICR MS of calmodulin: a top-down and bottom-up approach *JASMS* **2016**, *27*, 1531-1538.
29. Floris, F.; Vallotto, C.; Chiron, L.; Lynch, A. M.; Barrow, M. P.; Delsuc, M.-A.; O'Connor, P. B. Polymer analysis in the second dimension: preliminary studies for the characterization of polymers with 2D MS *Anal. Chem.* **2017**, *89*, 9892-9899.
30. van Agthoven, M. A.; Chiron, L.; Coutouly, M.-A.; Delsuc, M.-A.; Rolando, C. Two-dimensional ECD FT-ICR mass spectrometry of peptides and glycopeptides *Anal. Chem.* **2012**, *84*, 5589-5595.
31. Wilm, M.; Mann, M. Analytical properties of the nanoelectrospray ion source *Anal. Chem.* **1996**, *68*, 1-8.
32. Wilm, M.; Neubauer, G.; Mann, M. Parent ion scans of unseparated peptide mixtures *Anal. Chem.* **1996**, *68*, 527-533.
33. Amster, I. J. Fourier transform mass spectrometry *J. Mass Spectrom.* **1996**, *31*, 1325-1337.
34. Marshall, A. G.; Hendrickson, C. L.; Jackson, G. S. Fourier transform ion cyclotron resonance mass spectrometry: a primer *Mass Spectrom. Rev.* **1998**, *17*, 1-35.

35. Pfändler, P.; Bodenhausen, G.; Rapin, J.; Houriet, R.; Gäumann, T. Two-dimensional Fourier transform ion cyclotron resonance mass spectrometry *Chem. Phys. Lett.* **1987**, *138*, 195-200.
36. Pfändler, P.; Bodenhausen, G.; Rapin, J.; Walser, M. E.; Gaeumann, T. Broad-band two-dimensional Fourier transform ion cyclotron resonance *JACS* **1988**, *110*, 5625-5628.
37. Chiron, L.; Coutouly, M.-A.; Starck, J.-P.; Rolando, C.; Delsuc, M.-A. SPIKE a Processing Software dedicated to Fourier Spectroscopies *arXiv:1608.06777 [physics.comp-ph]* **2016**.
38. Chiron, L.; van Agthoven, M. A.; Kieffer, B.; Rolando, C.; Delsuc, M.-A. Efficient denoising algorithms for large experimental datasets and their applications in Fourier transform ion cyclotron resonance mass spectrometry *PNAS* **2014**, *111*, 1385-1390.
39. *Ultra-high resolution 2D-FTMS for truly DIA analysis of challenging systems*, Wootton, C. A.; Morgan, T. E.; Marzullo, B. P.; Lam, Y. P. Y.; Lozano, D. C. P.; Theisen, A.; Haris, A.; Barrow, M. P.; O'Connor, P. B., 298156, Proceedings of the 67th ASMS Conference on Mass Spectrometry and Allied Topics, Atlanta, Georgia, June 2-6, 2019;
40. van Agthoven, M. A.; Kilgour, D. P.; Lynch, A. M.; Barrow, M. P.; Morgan, T. E.; Wootton, C. A.; Chiron, L.; Delsuc, M.-A.; O'Connor, P. B. Phase relationships in two-dimensional mass spectrometry *JASMS* **2019**, *30*, 2594-2607.

4.9. Assignment tables

Absolute error is calculated as the average of the absolute ppm errors of all the assigned peaks. Absolute standard deviation is calculated as the standard deviation of the absolute ppm errors of all the assigned peaks.

Species	Theoretical m/z	Observed m/z	ppm
[Ph01+2H] ²⁺	418.19473	418.19493	0.467
[Ph02+2H]²⁺	536.21026	536.21026	-0.006
[Ph03+2H] ²⁺	611.26662	611.26651	-0.175
[Ph04+2H] ²⁺	723.85950	723.85951	0.014
[Ph05+2H]²⁺	741.31703	741.31703	-0.007
[Ph06+2H] ²⁺	872.34585	872.34632	0.537
[Ph07+2H] ²⁺	912.32902	912.32926	0.266
[Ph08+2H]²⁺	1167.92592	1167.92594	0.015
[Ph09+2H] ²⁺	1170.00888	1170.00892	0.034
[Ph09+3H] ³⁺	780.34168	780.34156	-0.152
[Ph10+3H]³⁺	937.40523	937.40521	-0.022

Table 3. 2: Peaks assignment of the 1D Standard MS Scan. Internal calibration points are in bold. Absolute error is 0.154 ppm, absolute standard deviation is 0.184 ppm.

Species	Theoretical m/z	Observed m/z	ppm
[Ph01+H] ¹⁺	835.38219	835.38205	-0.172
[Ph01+2H]²⁺	418.19473	418.19473	-0.012
[Ph02+2H] ²⁺	536.21026	536.21168	2.642
[Ph03+2H]²⁺	611.26662	611.26663	0.022
[Ph03+3H] ³⁺	407.84684	407.84663	-0.507
[Ph04+2H] ²⁺	723.85950	723.85961	0.152
[Ph04+3H] ³⁺	482.90876	482.90879	0.065
[Ph05+2H] ²⁺	741.31703	741.31739	0.479
[Ph06+2H] ²⁺	872.34585	872.34567	-0.208
[Ph07+2H] ²⁺	912.32902	912.32889	-0.140
[Ph08+2H] ²⁺	1167.92592	1167.92205	-3.316
[Ph09+2H] ²⁺	1170.00888	1170.00827	-0.522
[Ph09+3H]³⁺	780.34168	780.34164	-0.050
[Ph10+3H]³⁺	937.40523	937.40526	0.032

Table 3. 3: Peaks assignment of the extracted autocorrelation line of the 2DMS spectrum. Internal calibration points are in bold. Absolute error is 0.594 ppm, absolute standard deviation is 0.997 ppm.

Species	Theoretical m/z	Observed m/z	ppm
[Ph01+2H-H₃PO₄]²⁺	369.20629	369.20629	0.008
[Ph02+2H-H ₃ PO ₄] ²⁺	487.22182	487.22221	0.810
[Ph03+2H-H ₃ PO ₄] ²⁺	562.27817	562.27793	-0.425
[Ph04+2H-H ₃ PO ₄] ²⁺	674.87105	674.87065	-0.596
[Ph05+2H-H₃PO₄]²⁺	692.32859	692.32854	-0.068
[Ph06+2H-H₃PO₄]²⁺	823.35740	823.35744	0.044
[Ph08+2H-H₃PO₄]²⁺	1118.93748	1118.93751	0.031

Table 3. 4: Peaks assignment of the extracted 2+ phosphate neutral loss (H₃PO₄). Internal calibration points are in bold. Absolute error is 0.283 ppm; absolute standard deviation is 0.301 ppm.

Species	Theoretical m/z	Observed m/z	ppm
[Ph02+3H-H₃PO₄]³⁺	325.15030	325.15030	-0.007
[Ph04+3H-H₃PO₄]³⁺	450.24979	450.24980	0.017
[Ph09+3H-H₃PO₄]³⁺	747.68271	747.68267	-0.059
[Ph10+3H-H₃PO₄]³⁺	904.74627	904.74631	0.050

Table 3. 5: Peaks assignment of the extracted 3+ phosphate neutral loss (H₃PO₄). Internal calibration points are in bold. Absolute error is 0.033 ppm; absolute standard deviation is 0.021 ppm.

Species	Theoretical m/z	Observed m/z	ppm
[Ph01+2H]²⁺	418.19473	418.19462	-0.275
[Ph01+2H-H ₂ O] ²⁺	409.18945	409.18938	-0.177
[Ph01+2H-H ₃ PO ₄] ²⁺	369.20629	369.20634	0.143
b2	213.15975	213.15975	-0.020
b3	350.21867	350.21873	0.182
b4	437.25069	437.25111	0.950
py5	623.22972	623.22979	0.120

Table 3. 6: Peaks assignment of the extracted [Ph01+2H]²⁺ precursor line. Ph01: VLHSGpSR. Internal calibration points are in bold. Absolute error is 0.267 ppm; absolute standard deviation is 0.288 ppm.

Species	Theoretical m/z	Observed m/z	ppm
[Ph02+2H]²⁺	536.21026	536.21035	0.162
[Ph02+2H-H ₂ O] ²⁺	527.20498	527.20508	0.188
[Ph02+2H-H ₃ PO ₄] ²⁺	487.22182	487.22192	0.215
b3	407.20374	407.20373	-0.035
pb5	730.30321	730.30298	-0.321
pb6	817.33524	817.33544	0.241

Table 3. 7: Peaks assignment of the extracted [Ph02+2H]²⁺ precursor line. Ph02: RSpYpSRSR. Internal calibration points are in bold. Absolute error is 0.194 ppm; absolute standard deviation is 0.087 ppm.

Species	Theoretical m/z	Observed m/z	ppm
[Ph03+2H]²⁺	611.26662	611.26653	-0.142
[Ph03+2H-H ₂ O] ²⁺	602.26133	602.26167	0.557
[Ph03+2H-H ₃ PO ₄] ²⁺	562.27817	562.27845	0.500
b2	272.13533	272.13525	-0.296
b3	359.16736	359.16694	-1.166
b4	472.25142	472.25146	0.079
pb8	960.38225	960.38566	3.548
y2	262.15098	262.15098	-0.002
y3	349.18301	349.18313	0.347
y4	512.24634	512.24665	0.610
py6	750.28181	750.28237	0.746
py7	863.36587	863.36522	-0.758
py8	950.39790	950.39797	0.070

Table 3. 8: Peaks assignment of the extracted [Ph03+2H]²⁺ precursor line. Ph03: RDSLGPtYSSR. Internal calibration points are in bold. Absolute error is 0.678 ppm; absolute standard deviation is 0.889 ppm.

Species	Theoretical m/z	Observed m/z	ppm
[Ph04+2H-H ₃ PO ₄ -HPO ₃] ²⁺	634.88789	634.88792	0.053
[Ph04+2H-2H ₃ PO ₄] ²⁺	625.88260	625.88262	0.025
[Ph04+2H-H ₃ PO ₄] ²⁺	674.87105	674.87096	-0.136
[Ph04+2H-H ₂ O] ²⁺	714.85422	714.85416	-0.080
[Ph04+2H]²⁺	723.85950	723.85954	0.056
b4	456.31805	456.31832	0.601
ppb7	958.44103	958.44203	1.046
ppb8	1114.54214	1114.54497	2.540
ppb9	1229.56908	1229.56903	-0.042
ppb10	1300.60620	1300.60556	-0.489
y2	218.14992	218.14992	0.009
y3	333.17686	333.17681	-0.153
y4	489.27797	489.27796	-0.024
y5	602.36204	602.36204	0.007
py7	911.43462	911.43290	-1.890
py9	1137.60275	1137.60253	-0.194

Table 3. 9: Peaks assignment of the extracted [Ph04+2H]²⁺ precursor line. Ph04: pTKLlpTQLRDAK. Internal calibration points are in bold. Absolute error is 0.459 ppm; absolute standard deviation is 0.726 ppm.

Species	Theoretical m/z	Observed m/z	ppm
[Ph05+2H] ²⁺	741.31703	741.31680	-0.317
[Ph05+2H-H ₂ O] ²⁺	732.31175	732.31162	-0.181
[Ph05+2H-H ₃ PO ₄] ²⁺	692.32859	692.32841	-0.256
b3	357.17686	357.17681	-0.143
b4	428.21397	428.21435	0.876
b5	557.25657	557.25670	0.237
b6	685.31515	685.31619	1.524
b9	956.43197	956.43092	-1.094
y2	272.17172	272.17172	0.015
y3	359.20374	359.20373	-0.040
py4	526.20210	526.20216	0.107
py5	613.23413	613.23302	-1.813
py6	700.26616	700.26604	-0.172
py7	797.31892	797.31939	0.584
py10	1125.45721	1125.45732	0.099

Table 3. 10: Peaks assignment of the extracted [Ph05+2H]²⁺ precursor line. Ph05: EVQAEQPSSpSSPR. Internal calibration points are in bold. Absolute error is 0.497 ppm; absolute standard deviation is 0.550 ppm.

Species	Theoretical m/z	Observed m/z	ppm
[Ph08+2H] ²⁺	1167.92592	1167.92646	0.460
[Ph08+2H-H ₂ O] ²⁺	1158.92064	1158.92141	0.664
[Ph08+2H-H₃PO₄]²⁺	1118.93748	1118.93760	0.112
b3	392.14523	392.14502	-0.527
b4	521.18782	521.18844	1.190
b8	853.33627	853.33639	0.135
pb16	1767.59053	1767.59037	-0.089
y2	276.15540	276.15540	0.010
y3	405.19799	405.19791	-0.198
y4	568.26132	568.26123	-0.156
y5	683.28826	683.28658	-2.461
y6	740.30973	740.30970	-0.035
y7	841.35740	841.35701	-0.468
py10	1224.43039	1224.43227	1.539
py14	1686.60545	1686.60456	-0.527
py16	1814.66403	1814.66177	-1.243
py17 ²⁺	972.35695	972.35730	0.362
py18 ²⁺	1029.87042	1029.87137	0.923

Table 3. 11: Peaks assignment of the extracted [Ph08+2H]²⁺ precursor line. Ph08: FEDEGAGFEESpSETGDYEEK. Internal calibration points are in bold. Absolute error is 0.617 ppm; absolute standard deviation is 0.626 ppm.

Species	Theoretical m/z	Observed m/z	ppm
[Ph06+2H]²⁺	872.34585	872.34577	-0.094
[Ph06+2H-H ₂ O] ²⁺	863.34057	863.34079	0.255
[Ph06+2H-H ₃ PO ₄] ²⁺	823.35740	823.35756	0.189
b2	187.07133	187.07133	-0.018
b3	316.11393	316.11398	0.170
pb6	667.19708	667.19731	0.348
pb7	796.23967	796.24088	1.518
pb8	925.28226	925.28132	-1.020
pb10	1127.34124	1127.34253	1.148
pb11	1240.42530	1240.42449	-0.652
pb12	1369.46789	1369.46866	0.560
pb14	1597.57890	1597.57916	0.163
y2	262.13975	262.13974	-0.027
y3	375.22381	375.22341	-1.069
y4	504.26640	504.26576	-1.277
y4'	486.25584	486.25586	0.042
y5	617.35047	617.35043	-0.062
y6	732.37741	732.37771	0.408
y7	819.40944	819.40935	-0.109
y7'	801.39888	801.39894	0.081
y8	948.45203	948.45166	-0.393
y8'	930.44147	930.44109	-0.406
y9	1077.49463	1077.49366	-0.897
y9'	1059.48406	1059.48406	-0.001
y10	1164.52665	1164.52659	-0.055
py11	1331.52501	1331.52603	0.763
py12	1428.57778	1428.57614	-1.146
py13 ²⁺	779.31382	779.31334	-0.620

Table 3. 12: Peaks assignment of the extracted [Ph06+2H]²⁺ precursor line. Ph06: ADEPsSEESDLEIDK. Internal calibration points are in bold. ' : water loss. Absolute error is 0.482 ppm; absolute standard deviation is 0.446 ppm.

Species	Theoretical m/z	Observed m/z	ppm
[Ph09+3H]³⁺	780.34168	780.34143	-0.319
[Ph09+3H-H ₂ O] ³⁺	774.33816	774.33767	-0.629
[Ph09+3H-H ₃ PO ₄] ³⁺	747.68271	747.68227	-0.593
ppb17 ²⁺	1009.41884	1009.42166	2.798
y3	451.22996	451.22996	0.002
y5	661.36679	661.36688	0.141
py7	885.38661	885.38678	0.192

Table 3. 13: Peaks assignment of the extracted [Ph09+3H]³⁺ precursor line. Ph09: ELSNpSPLRENSFGpSPLEFR. Internal calibration points are in bold. Absolute error is 0.668 ppm; absolute standard deviation is 0.896 ppm.

Species	Theoretical m/z	Observed m/z	ppm
[Ph10+3H]³⁺	937.40523	937.40577	0.576
[Ph10+3H-H ₂ O] ³⁺	931.40171	931.40246	0.807
[Ph10+3H-H ₃ PO ₄] ³⁺	904.74627	904.74693	0.735
b7	844.34717	844.34840	1.452
pb16-2+	1016.43547	1016.43099	-4.410
pb18-2+	1115.48569	1115.48939	3.313
y3	400.23029	400.23029	-0.009
py6	779.34475	779.34509	0.442
py7	935.44586	935.44575	-0.114
ppy15²⁺	983.93426	983.93323	-1.045

Table 3. 14: Peaks assignment of the extracted [Ph10+3H]³⁺ precursor line. Ph10: SPTEYHEPVpYANPFYRPTpTPQR. Internal calibration points are in bold. Absolute error is 1.290 ppm; absolute standard deviation is 1.368 ppm.

CHAPTER 4.

Two-dimensional mass spectrometry analysis
of IgG1 antibodies

4.1. Declaration

This chapter consist of one published research article:

Paris, J.; Morgan, T. E.; Marzullo, B. P.; Wootton, C. A.; Barrow, M. P.; O'Hara, J.; O'Connor, P. B. Two-Dimensional Mass Spectrometry Analysis of IgG1 Antibodies J. Am. Soc. Mass. Spectrom. 2021.

Except for minor adjustments to aid incorporation into this thesis and extra Figures, the article has been reproduced unchanged. The tables of assignments are at the end of the chapter.

As a first author I carried out all experiments, analysed all data, and prepared all Figures as well as the manuscript. TEM trained me on 2DMS. TEM, BPM, and CAW developed the 2DMS homemade software. MPB, JOH and PBOC were involved in project management and editing the final manuscript.

Two-Dimensional Mass Spectrometry Analysis of IgG1 Antibodies

J. Am. Soc. Mass Spectrom. 2021, 32, 7, 1716–1724

Johanna Paris[†], Tomos E. Morgan[†], Bryan P. Marzullo[†], Christopher A. Wootton[†], Mark P. Barrow[†], John O’Hara[‡], and Peter B. O’Connor^{†*}

[†]University of Warwick, Department of Chemistry, Coventry, CV4 7AL, United Kingdom

[‡]UCB, 216 Bath Road, Slough, SL1 3WE, United Kingdom

*Corresponding author email address: p.oconnor@warwick.ac.uk

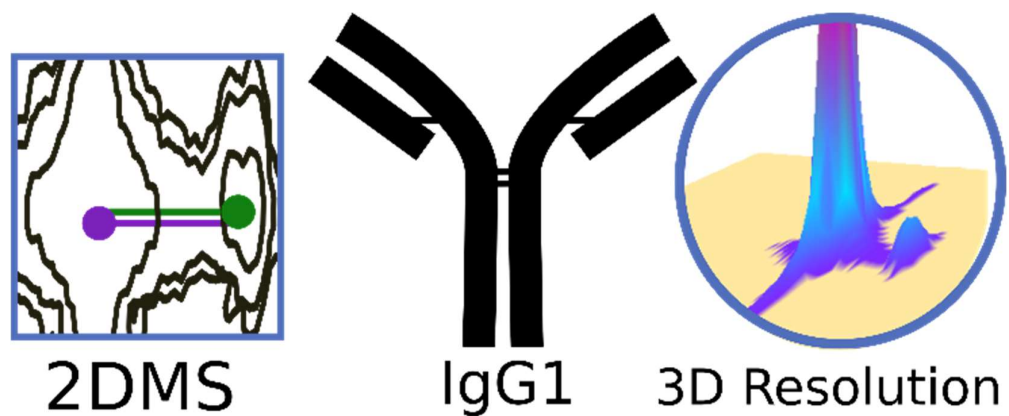


Figure 4. 1: Graphical Abstract

4.2. Abstract

Two-dimensional mass spectrometry (2DMS) is a new, and theoretically ideal, data independent analysis tool, which allows the characterisation of a complex mixture, and was used in the bottom-up analysis of IgG1 for the identification of PTMs. The new peak picking algorithm allows the distinction between chimeric peaks in proteomics. In this application, the processing of 2DMS data correlates fragments to their corresponding precursors, with fragments from precursors which are $<0.1 m/z$ at m/z 840 easily resolved, without the need for quadrupole or chromatographic separation.

4.3. Introduction

Since the approval of the first therapeutic monoclonal antibody (mAb), Orthoclone OKT3,¹ for the prevention of kidney transplant rejection, mAbs and antibody-related products have become a highly successful class of biotherapeutics. Over 90 antibodies are on the market and a further 79 are undergoing late-stage clinical studies in 2020.^{2,3} The success of antibodies as drug candidates is due to their long serum life, low side effects, high specificity, and stability.

Due to their complexity, structure and N-linked glycosylation, mAbs are typically produced in mammalian tissue cell cultures.⁴ Despite their natural stability, antibodies display a wide variety of minor changes, called micro-heterogeneities⁵ or posttranslational modifications (PTMs), which are caused by the manufacturing process, formulation, and storage.⁶ Common antibody PTMs are glycosylation, oxidation, deamidation, glycation, N-terminal pyroglutamic acid formation, and C-terminal lysine clipping. Some modifications affect the efficacy,^{7,8} immunogenicity,⁹ stability,¹⁰ and clearance of the antibody.¹¹⁻¹⁴ These attributes are called critical quality attributes (CQAs) and need to be controlled during production and storage.¹⁵ The process parameters that affect the CQAs must be identified, characterized, and controlled.^{16,17}

Anti-A33 is an IgG1, developed by UCB and is intellectual property (IP) free for the use in collaboration within different academia laboratories. IgG1 antibodies are composed of two heavy chains (HC) of ~50kDa and two light chains (LC) of ~25kDa, linked together by 4 inter-chain disulphides bonds and 12 intra-chain disulphides bonds.^{18,19} Antibodies are composed of homology regions (2 in the LC, 4 in the HC), called immunoglobulin domains,

forming β -barrel structures bridged via an intra-chain disulphide bond.²⁰ Most of the sequence of IgG1 is constant within a species. However, there are three hypervariable regions in the antibody, composed of six complementarity-determining regions (CDRs) near the N-terminus of the light and heavy chains.²¹ The regions are brought into spatial proximity by the immunoglobulin fold, and form unique and highly specific epitope-binding paratopes.²² The fragment crystallisable (Fc) region interacts with activating and inhibitory Fc γ R receptors to mediate cellular and complement response for efficient pathogen clearance, and the neonatal receptor for IgG (FcRN) which impacts the drug half-life.²³

Chemical degradation in the constant region of antibodies can affect their function. Oxidation of methionine residues is the most common post-translational modification of antibodies during storage. IgG1 contains five methionine residues in each pair of light and heavy chain, and is prone to oxidation at M256 and M428, which can cause conformational change of the backbone. Therefore, methionine oxidation can affect the binding of IgG1 to FcRN and Fc γ receptors,¹¹ reducing the serum circulation half-life.¹³ Methionine oxidation can be analysed by peptide mapping²⁴ and its impact on the conformation of the Fc region can be analysed by FcRN affinity chromatography.¹² It is possible to oxidize methionine in vitro with the use of hydrogen peroxide (H₂O₂).²⁵

Peptide mapping by liquid chromatography mass spectrometry (LC-MS/MS) is a key method for the characterisation of antibodies, confirming primary sequence and localising PTMs.²⁶⁻²⁸ LC-MS/MS peptide mapping includes an enzymatic digestion of the antibody into peptides after reduction of the disulphides bonds and alkylation of the now free cysteine residues.²⁹ The peptides are separated through a reversed phase column and then identified by tandem mass spectrometry analysis.³⁰ During peptide mapping analysis, labile modifications can be lost.

With the identification of the CQAs for antibodies, multiple data dependant approaches have been developed including the multi-attribute method (MAM)³¹ using a quadrupole mass analyser as a quality control (QC) friendly monitoring method.³² The MAM strategy allows the simultaneous analysis of the different CQAs.³³ However, in the analysis of new therapeutics, or degraded samples, PTM that are not expected can be missed. A data independent approach is more likely to fully characterize the antibody of interest and its variations.

Sequential window acquisition of all theoretical mass spectra (SWATH-MS) presented as a data independent analysis approach, fragments peptides within a narrow mass-to-charge ratio window simultaneously.³⁴ The fragments are allocated to their respective precursors using the elution time of the precursor and data search spectral libraries. The acquisition is repeated in successively stepped windows in order to cover the m/z range of the mixture. However, SWATH-MS produces chimeric spectra (spectra with fragments from multiple precursors) that are difficult to interpret. Two-dimensional mass spectrometry (2DMS) can be used as an alternative to SWATH as a data independent analysis method which is not based on quadrupole isolation windows. In addition, 2DMS does not require chromatographic separation or the use of spectral database libraries for the analysis of the inherent chimeric spectra produced by SWATH or other DIA approaches.

In a Fourier transform ion cyclotron resonance (FT-ICR) instrument,^{35, 36} 2DMS uses a non-standard pulse sequence (Figure 4.2).^{37, 38} Ions are trapped by applying a potential on the trapping plates of the Infinity ICR cell³⁹ and can be modulated in space inside the cell. If the ions' radial positions are modulated before a radius-dependent fragmentation method is applied, they are subject to modulation of the fragmentation efficiencies and the fragments will be formed with intensities varying according to the modulation frequency of the precursor. Multiple in-cell fragmentations methods which are radially defined are available. Laser dissociation methods such as infrared multiphoton dissociation (IRMPD) and ultra-violet photodissociation (UVPD),⁴⁰ create a fragmentation zone at the centre of the ICR cell, when, with electron capture dissociation (ECD),⁴¹ the hollow cathode⁴² produces a spatially defined hollow electron beam.

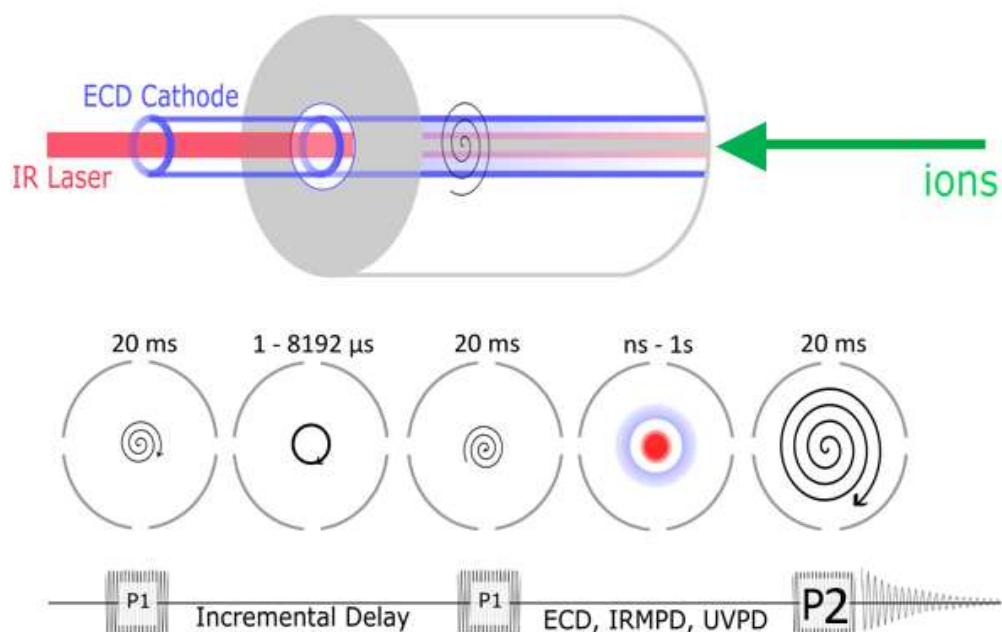


Figure 4. 2: Fundamentals of 2DMS. Illustration of the ICR Cell,⁴² and 2DMS pulse sequence and corresponding ion motions within the ICR cell.³⁷

In 2DMS, during the first pulse, delay, pulse event, the ions acquire different radii in the cell (Figure 4.2) which varies according to the incrementing delay.⁴³ In-cell fragmentation methods (IRMPD, UVPD or ECD) fragment the ions differently depending on where they are radially located within the cell. The incremental delay during the encoding sequence⁴⁴ leads to a variation of the spatial modulation of the ions and therefore, a variation of fragmentation efficiency. Each precursor is modulated at its reduced cyclotron frequency, which varies according to the mass-to-charge ratio. Each fragment shows the same modulation of intensity as its precursor, but with inverse phase, and the Fourier transform can extract these modulation frequencies to correlate fragments to their precursors. Thus, the 2DMS approach⁴⁴ allows the identification of which fragments were produced from which precursor(s) via the modulation frequencies of their fragment ion intensities when analysing all the precursors simultaneously, with complex mixtures of precursors.

A 2DMS spectrum is a three-dimensional surface plot of precursor m/z , fragment m/z , and intensity, usually shown as a contour plot for simplicity.⁴⁵ The 2DMS pulse sequence has been previously optimised for IRMPD.⁴⁶

IRMPD⁴⁷⁻⁴⁹ is a fragmentation technique using a CO₂ laser, a slow heating method leading to similar fragmentation to collision-induced dissociation (CID) for peptides and proteins. The sequential absorption of 10.6 μm photons slowly increases the internal energy of the ions (0.117 eV per photon), and low energy proton rearrangements lead to the destabilisation and dissociation of amide bonds.^{50, 51} IRMPD 2DMS has been successful in the analysis of phosphopeptides,⁵² angiotensin I,⁵³ cytochrome C,⁵⁴ and calmodulin.⁵⁵ ECD 2DMS was effective in the analysis of glycopeptides,⁵⁶ calmodulin,⁵⁷ and histones,⁵⁸ and EID 2DMS in the analysis of agrochemicals.⁵⁹ Combined IR-ECD 2DMS has been shown to improve peptide de novo sequencing.⁶⁰

In this study, 2DMS was used to characterise the tryptic digested sample of an oxidised IgG1 and, especially, demonstrated as a useful tool for the identification of IgG1 PTMs.

4.4. Experimental section

2.4.1. Material

The IgG1 was produced by UCB Pharma Ltd. 208 Bath Road, Slough, Berkshire, SL1 3WE. Water was purified by a Millipore Direct-Q purification system (Merck Millipore, MA, USA). Acetonitrile was obtained from VWR chemicals (34851). Formic acid (FA) (F0507), calcium chloride (CaCl₂) dihydrate (C3881-500g), dithiothreitol (DTT) (D-9779-5g), iodoacetamide (I1149-5g), guanidine hydrochloride (G9284) were obtained from Sigma-Aldrich. The zeba spin columns (89882) were purchased from Thermo Fisher. Tris (A18494) was obtained from Alfa Aesar. Trypsin (V5111) was obtained from Promega.

2.4.2. Protein Oxidation

Oxidised IgG1 was obtained by adding 1% of H₂O₂ to IgG1 (10 g/L) and incubated at 5°C for 48 hours.

2.4.3. Protein reduction, alkylation, and digestion

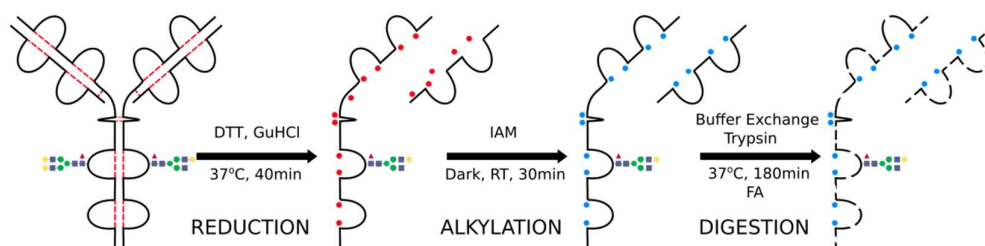


Figure 4. 3: Protocol of Digestion. Red dot line: disulphide bond. Red dot: free cysteine. Blue dot: alkylated cysteine.

2 μL of 500 mM DTT into 750 mM tris(hydroxymethyl) aminomethane (tris) 150 mM CaCl_2 pH 7.9 and 60 μL of 8M guanidine hydrochloride was added to 80 μg (20 μL) of IgG1. The sample was mixed and incubated at 37°C for 40 min. 6 μL of 500 mM iodoacetamide into 750 mM tris 150 mM CaCl_2 pH 7.9 was added. The sample was mixed and incubated in the dark for 30 min. The sample was buffer exchanged into 7.5 mM tris 1.5 CaCl_2 mM pH 7.9 using zeba spin desalting columns with a cut-off of 7kDa. 3.5 μL of trypsin (1 g/L into 7.5 mM tris 1.5 mM CaCl_2 pH 7.9) was added to the mixture. The sample was mixed and incubated at 37°C for 180 minutes. 5 μL of 3.6% formic acid was added to quench the digestion.

2.4.4. Mass spectrometry analysis

The sample (50 μL , 70:30 Water:ACN + 0.1% FA, 0.2 μM analyte) was ionised in a custom nano electrospray ionisation source (nESI) using a pulled glass capillary with several μm open orifice.⁶¹ Mass spectrometry was conducted on a 12 T Bruker solariX FTICR mass spectrometer (Bruker Daltonik GmbH, Bremen, Germany), and IRMPD fragmentation was achieved using a continuous wave, 25 W, CO_2 laser (Synrad Inc., Washington, USA) for 0.4 seconds at a laser power of 40%. 8192 scans of 1 M (16-bit) data points were acquired over a mass range of m/z 328-3000 on the vertical (precursor) axis and m/z 147-3000 on the horizontal (fragment) axis. The 2DMS experiment was acquired over 212 min (1.55 second per scan).

2.4.5. Data analysis

The data was processed with hardware and SPIKE,⁶² using urQRd denoising with rank 15.⁴⁵ Spectra were either extracted using an inhouse T2D⁶³ software and they were internally calibrated using known fragment peaks with a quadratic calibration function in the Bruker DataAnalysis v4.3 software (Bruker Daltonik GmbH, Bremen, Germany). Or the data was processed in the T2D software with a 3D peak picking algorithm which analyses the geometry and shape of all the 2DMS peaks and assigns a peak centre with x-y-z coordinates. Precursor View allowed the grouping of the 3D peaks and a display of the results.

4.5. Results and discussion

2.5.1. Raw Data Modulation of intensities

The frequency of intensity modulation in 2DMS allows the distinction of which fragments were produced from which precursors, without isolation, in a broadband fashion.⁶⁴ Figure 4.4 shows the modulation of three precursors, during one hundred consecutive scans. The intensity of the precursors depends on the radius modulation of the precursor in the fragmentation zone after the first pulse, delay, pulse event within the 2DMS sequence.

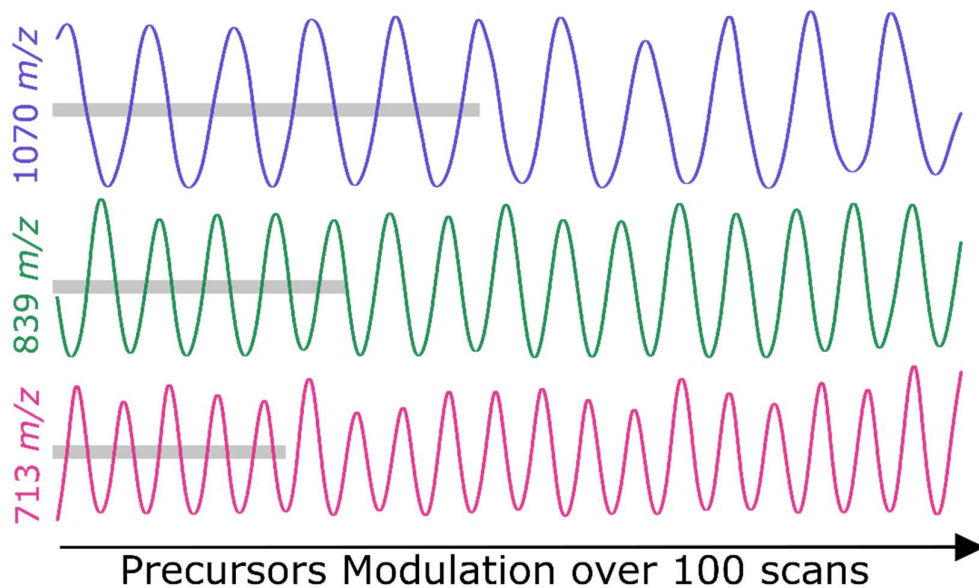


Figure 4. 4: Modulation of intensity of three different precursors during the 2DMS scans (B-spline smoothed). Grey lines correspond to 5 periods.

In FTICR, after excitation, all ions are at approximately the same radius, with different angular velocity depending on their mass-to-charge ratio.³⁵ During the delay, the difference in angular velocities causes each precursor to acquire a different phase.⁶⁴ The scan-to-scan intensity of the precursor depends on the timing of the second excitation pulse, which will modulate the ions radially, in and out of the fragmentation zone depending on their phase (Figure 4.2). The fragments have the same frequencies of modulation of their respective precursors but 180° out of phase (Figure 4.5).

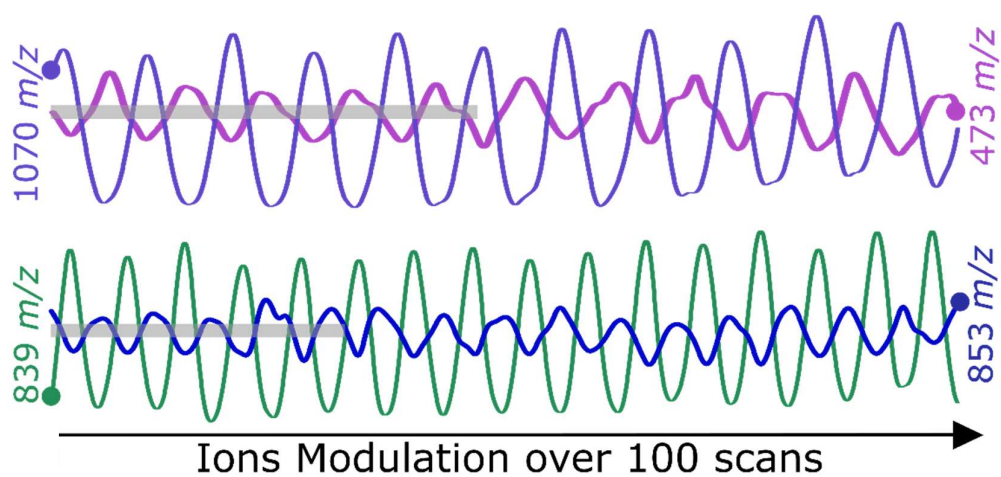
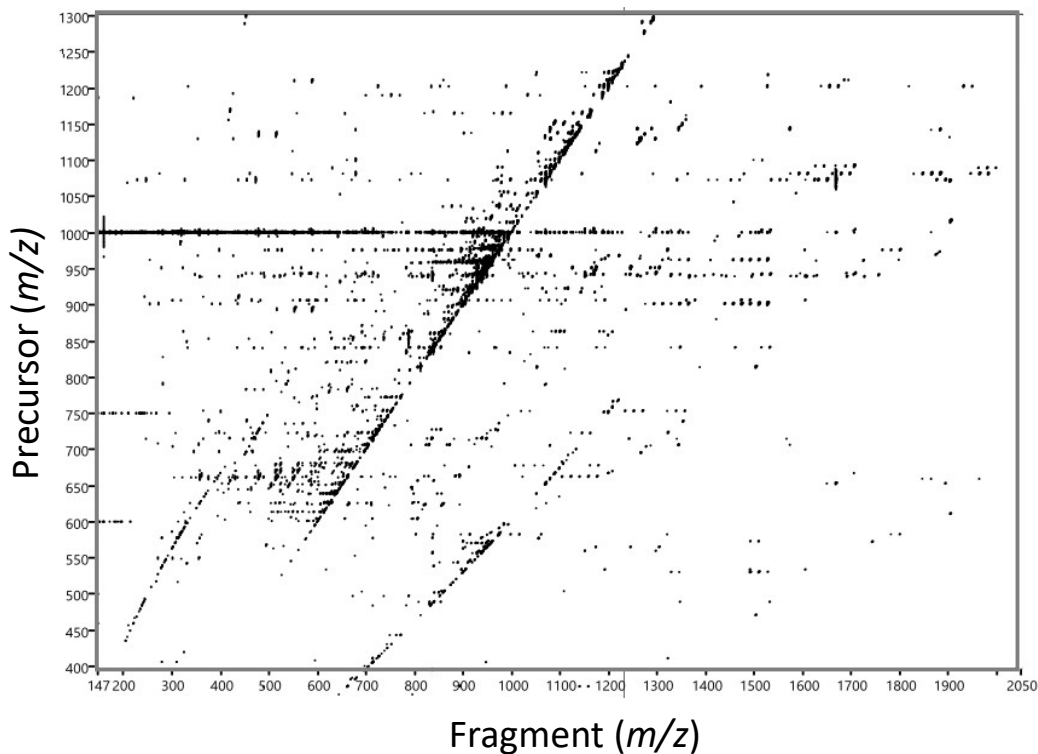


Figure 4. 5: Modulations of intensity of fragments (right) and corresponding precursors (left) during the 2DMS experiment. (B-spline smoothed). Grey lines correspond to 5 periods.

2.5.2. A 2DMS spectrum

A 2DMS spectrum is a 3-dimensional surface plot, which is normally represented as a contour plot. Each data point corresponds to an ion at an m/z (horizontal axis, fragment axis), linked to a precursor m/z (vertical axis), and an intensity. Unlike usual DIA approaches with isolation windows,^{34, 65-68} 2DMS produces a three dimensional spectrum wherein the vertical axis shows the precursor m/z in a continuum. Approximately 1.5 μg of IgG1 was sprayed to produce this spectrum, during a 212 minutes 2DMS experiment. The sample and the spray were stable. Instability in the sample could cause a loss of data, and instability in the spray could cause noise in the 2DMS spectrum. The representation in Figure 4.6 is a two dimensional contour plot, but the information of intensities is retained entirely and it is possible to 3D plot the observed peaks.



2.5.3. Sequence coverage

Any line (horizontal, vertical, and diagonal) can be extracted from the 2DMS spectrum using T2D, and either analysed as is with internal functions or exported to be analysed using downstream software such as the Bruker DataAnalysis software to take advantage of additional functionalities. The diagonal line ($y=x$) is the autocorrelation line (Figure 4.7). It corresponds to all the detected precursors of the complex mixture and is similar to a standard 1D direct infusion mass spectrum.

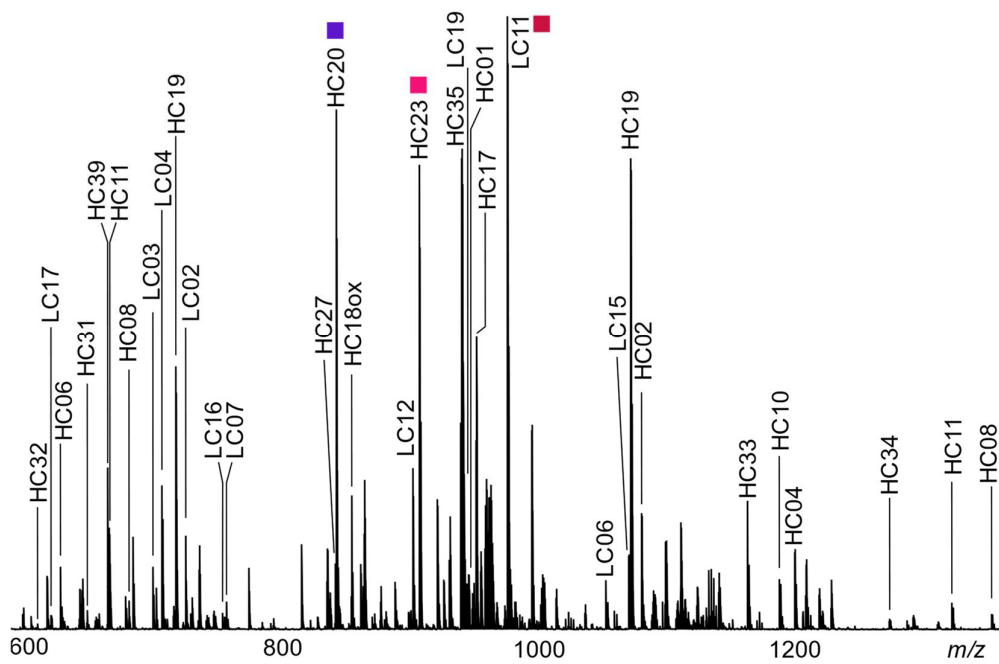


Figure 4. 7: Extracted autocorrelation line from the 2DMS spectrum (Figure 4.6) showing all detected precursors

The sequence coverage (Figure 4.7) is calculated from the autocorrelation line and correspond to all the peptides observed during the experiment. CDR1 (LC: KASQNVRTVVA and HC: TYDMSV) and CDR2 (LC: YLASNRHT and HC: TISSGGSYTYLDSVKG) were observed (as defined by Kabat et al).⁶⁹ All the tryptic peptides containing methionine residues were observed. The sequence coverage was 75%. The strength of 2DMS is the ability to analyse all the peptides and their fragments simultaneously.

LIGHT CHAIN

N-term
1 DIQMTQSPSSLSASVGDRVTITCKA 25
26 SQNVRTVVAWYQQKPKAPKTLIYL 50
51 ASNRHTGVPSRFSGSGSGTDFTLTI 75
76 SSLQPEDFATYFCLQHWSYPLTFGQ 100
101 GTKVEIKRTVAAPSVFIFPPSDEQL 125
126 KSGTASVVCLLNFPREAKVQWKV 150
151 DNALQSGNSQESVTEQDSK DSTYSL 175
176 SSTLTLSKADYEKHKVYACEVTHQG 200
201 LSSPVTKSFNRGEC 214 C-term

HEAVY CHAIN

N-term
1 EVQLVESGGGLVQPGGSLRLSCAA 25
26 SGFAFSTYDMSWVRQAPGKGLEWVAT 50
51 ISSGGSYTYYLDSVKGRFTISR DSS 75
76 KNTLYLQMNSLRAEDTAVYYCAPTT 100
101 VVPFAYWGQGTLVTVSSASTKGPSV 125
126 FPLAPSSKSTSGGTAALGCLVKDYF 150
151 PEPVTVSWNSGALTSGVHTFPAVLQ 175
176 SSGLYSLSSVVTVPSSSLGTQTYIC 200
201 NVNHKPSNTKVDKKVEPKSCDKTHT 225
226 CPPCPAPELLGGPSVFLFPPKPKDT 250
251 LMISRTPEVTCVVVDVSHEDPEVKF 275
276 NWYVDGVEVHNAKTKPREEQYNSTY 300
301 RVVSVLTVLHQDWLNGKEYCKVSN 325
326 KALPAPIEKTISKAKGQPREPQVYT 350
351 LPPSRDELTKNQVSLTCLVKGFYPS 375
376 DIAVEWESNGQPENNYKTTPPVLD 400
401 DGSFFLYSKLTVDKSRWQQGNVFSC 425
426 SVMHEALHNYHTQKSLSLSPGK C-term

Figure 4. 8: Sequence of the IgG1. Sequence coverage in blue, from the peptides observed on the autocorrelation line. Cysteine in bold. Square is the site of the N-glycosylation.

All peptides observed in the standard 1D MS mode were also observed and fragmented in the 2DMS experiment. Transmission was optimized for 500-2500 m/z . Therefore, some peptides of five or fewer amino acids were not observed. Furthermore, some particularly large peptides with few basic residues were also not observed: HC09 (AEDTA...), LC08 (FSGSG...) and HC12 (DYFPE...). All the missing peptides are also missing in the 1D mass spectrum. With direct infusion, competition of ionisation can cause ion suppression. While sequence coverage with LC-MS/MS can reach 90 to 100%, MS/MS spectrum of many of these peptides are difficult to obtain because their low signal intensity. It is possible to change the digestion enzyme to have complementary data on those regions of the antibody.⁷⁰

2.5.4. Fragmentation efficiency

Horizontal lines corresponding to the squares in the autocorrelation line were extracted from the 2DMS spectrum (Figure 4.6). The horizontal lines are called fragment ion lines and correspond to all the fragments from a precursor; these lines are the 2DMS equivalent of individual MS/MS spectra. The precursor lines of HC20 (FNWYVDGVEVHNAK), HC23 (VSVLTVLHQDWLNGK), and LC11 (TVAAPSVFIFPPSDEQLK) are shown in Figure 4.9, 4.10, and 4.11, along with their peak assignments and cleavage maps.

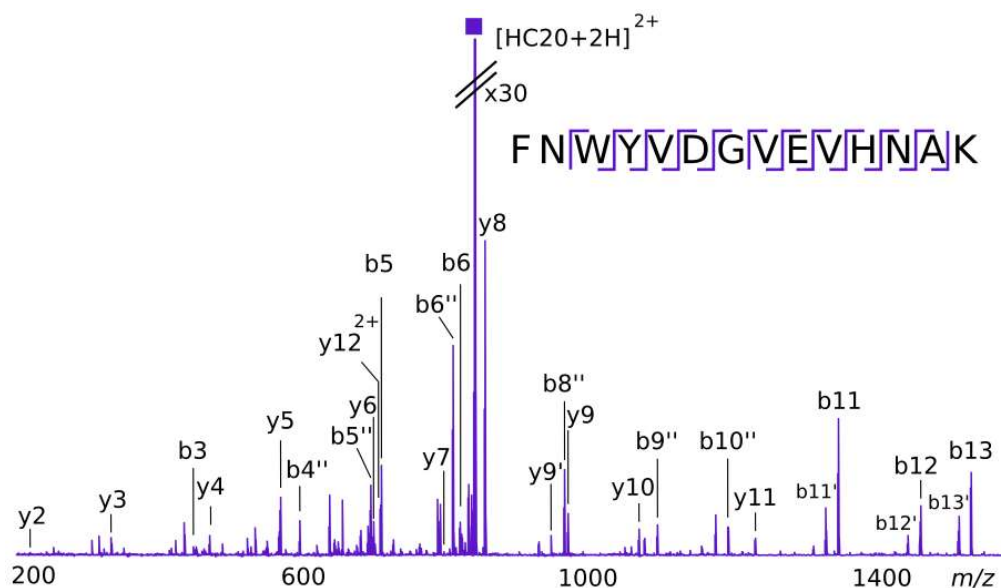


Figure 4.8: Extracted m/z 839 fragment line from the 2DMS Spectrum showing the b/y fragments of HC20. ' : loss of water. '' : loss of NH3. 2' : loss of two water molecules.

HC20 shows a fragmentation efficiency of 29% and cleavage coverage of 92%, and the average absolute error is 1.14 +/- 1.07 ppm.

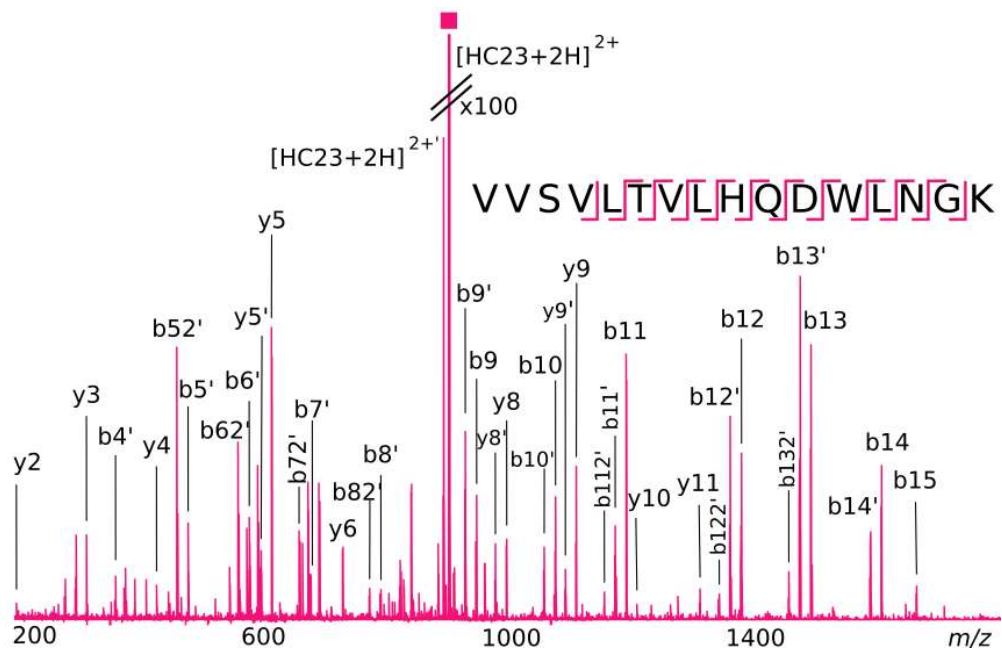


Figure 4.9: Extracted m/z 904 fragment line from the 2DMS Spectrum showing the b/y fragments of HC23. ' : loss of water. '' : loss of NH3. 2' : loss of two water molecules.

HC23 has a fragmentation efficiency of 32%, a cleavage coverage of 80%, and an average absolute error of 1.03 +/- 0.93 ppm.

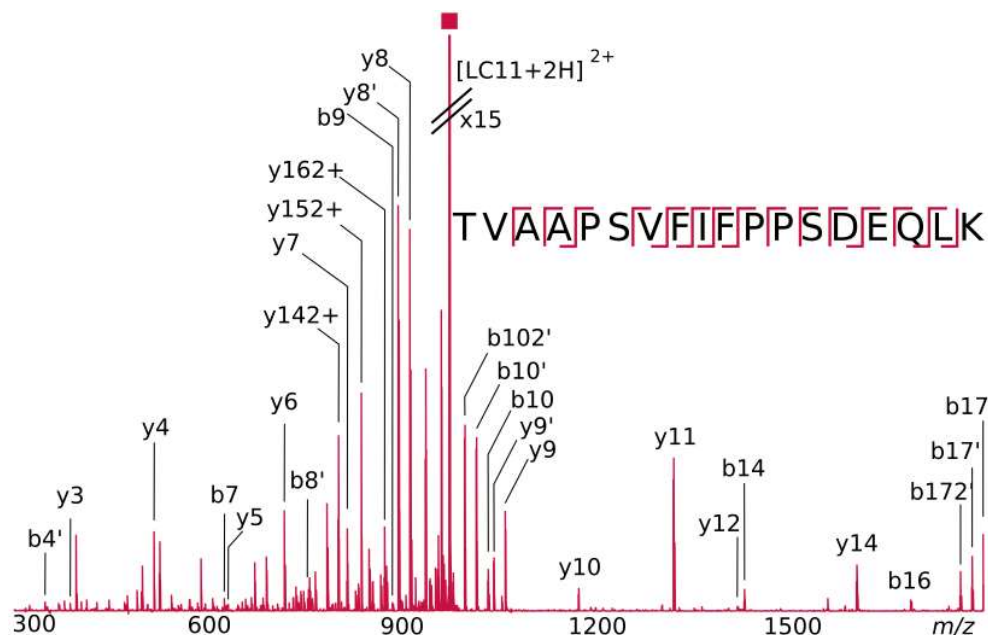


Figure 4. 10: Extracted m/z 973 fragment line from the 2DMS Spectrum showing the b/y fragments of LC11. ‘: loss of water. “: loss of NH3. 2’: loss of two water molecules.

LC11 has a fragmentation efficiency of 44%, a cleavage coverage of 88%, and an average absolute error of 1.34 +/- 1.03 ppm.

In a previous experiment, the IRMPD beam at 50% power (25 W at the laser) and 0.4 seconds displayed the best fragmentation efficiency for HC20, and was therefore used for the 2DMS experiment. This way, the laser set-up was tuned for the fragmentation of middle size peptides and the analysis shows high cleavage coverage for most of the peptides. However, some small peptides were over fragmented and some high mass peptides were under fragmented. The overall cleavage coverage on the observed peptides was 57.5% (Figure 4.12).

LIGHT CHAIN

N-term
 1 D I Q M T Q S P S S L S A S V G D R V T I T C K A 25
 26 S Q N V R T V V A W Y Q Q K P G K A P K T L I Y L 50
 51 A S N R H T G V P S R F S G S G S G T D F T L T I 75
 76 S S L Q P E D F A T Y F C L Q H W S Y P L T F G Q 100
 101 G T K V E I K R T V A A P S V F I F P P S D E Q L 125
 126 K S G T A S V V C L L N N F Y P R E A K V Q W K V 150
 151 D N A L Q S G N S Q E S V T E Q D S K D S T Y S L 175
 176 S S T L T L S K A D Y E K H K V Y A C E V T H Q G 200
 201 L S S P V T K S F N R G E C 214 C-term

HEAVY CHAIN

N-term
 1 E V Q L V E S G G G L V Q P G G S L R L S C A A 25
 26 S G F A F S T Y D M S W V R Q A P G K G L E W V A T 50
 51 I S S G G S Y T Y Y L D S V K G R F T I S R D S S 75
 76 K N T L Y L Q M N S L R A E D T A V Y Y C A P T T 100
 101 V V P F A Y W G Q G T L V T V S S A S T K G P S V 125
 126 F P L A P S S K S T S G G T A A L G C L V K D Y F 150
 151 P E P V T V S W N S G A L T S G V H T F P A V L Q 175
 176 S S G L Y S L S S V V T V P S S S L G T Q T Y I C 200
 201 N V N H K P S N T K V D K K V E P K S C D K T H T 225
 226 C P P C P A P E L L G G P S V F L F P P K P K D T 250
 251 L M I S R T P E V T C V V V D V S H E D P E V K F 275
 276 N W Y V D G V E V H N A K T K P R E E Q Y N S T Y 300
 301 R V V S V L T V L H Q D W L N G K E Y K C K V S N 325
 326 K A L P A P I E K T I S K A K G Q P R E P Q V Y T 350
 351 L P P S R D E L T K N Q V S L T C L V K G F Y P S 375
 376 D I A V E W E S N G Q P E N N Y K T T P P V L D S 400
 401 D G S F F L Y S K L T V D K S R W Q Q G N V F S C 425
 426 S V M H E A L H N H Y T Q K S L S L S P G K C-term

Figure 4. 11: Sequence of the IgG1. Sequence coverage in blue, obtained from the autocorrelation line. Cleavage of the b/y ions in black obtained from the fragment lines analysis. Cysteine in bold. Square is the site of the N-glycosylation.

2.5.5. PTM identification

Modifications between two samples can be noticed on the extracted autocorrelation line or on the 2DMS spectrum, when comparing contour plots. In Figure 4.13, two samples were compared: IgG1 and IgG1 after oxidative stress.

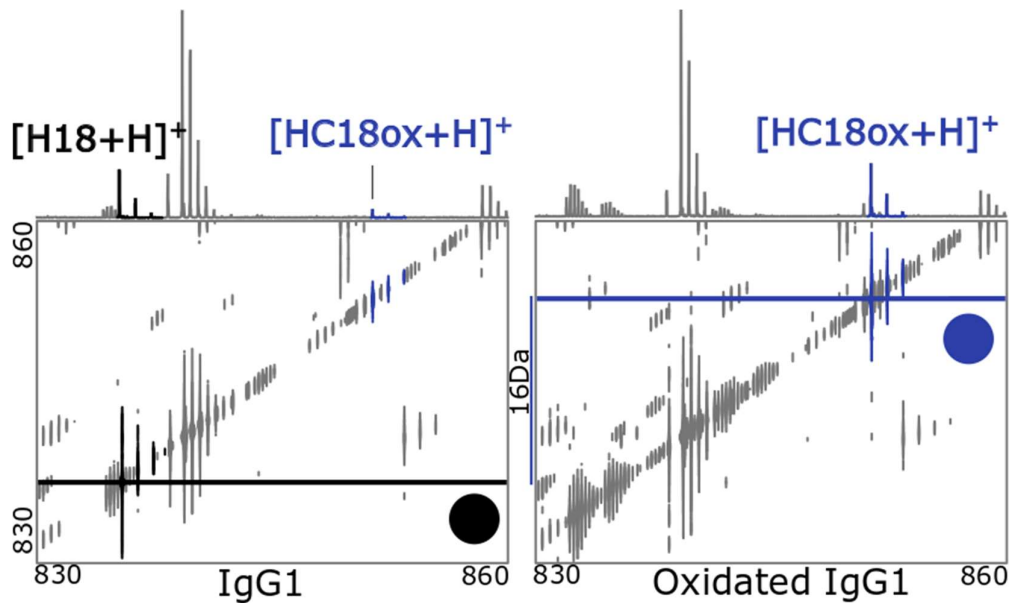


Figure 4. 12: Detection and Identification of posttranslational modifications. Extracted autocorrelation lines of the IgG1 sample and the IgG1 sample after oxidative stress, between m/z 830 and 860. 2DMS zoom into m/z 830-860. In black HC18, in blue oxidised HC18.

From a difference between the two 2DMS spectra, fragments lines were extracted and compared (Figure 4.13). The fragments allowed the identification of the peptide DTLMISR and DTLMoxISR, identifying and locating the oxidation point to Met252 on the heavy chain.

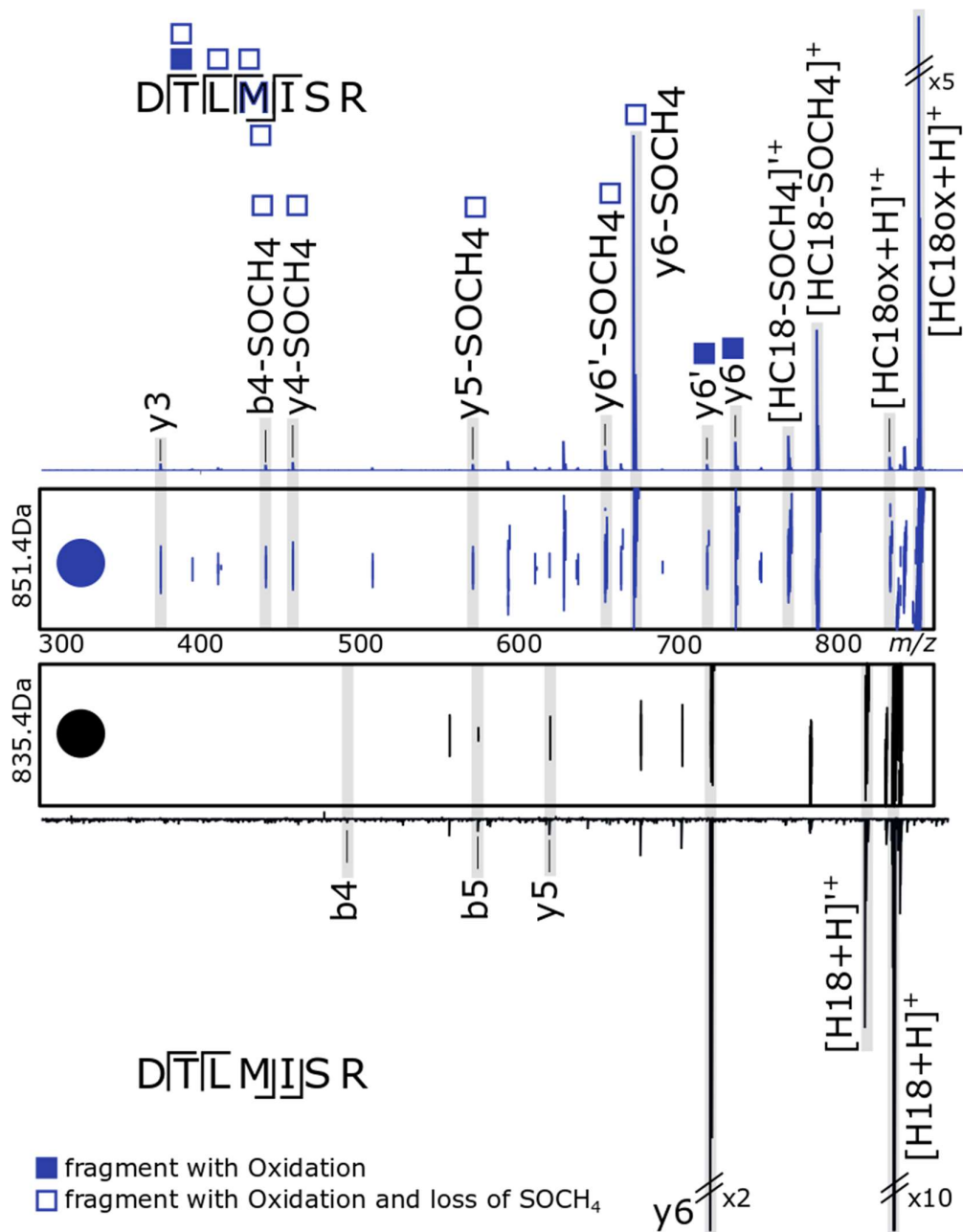


Figure 4. 13: Detection and Identification of posttranslational modifications. Extracted fragments lines at m/z 851.4 for the oxidative sample, and m/z 835.4 for the IgG1 sample, compared to extracted 2DMS contour plot related to the species.

2.5.6. Resolution in 2DMS

1.5.6.1. 2DMS zoom

Figure 4.14 is a zoom into the 2DMS spectrum (Figure 4.6) on the autocorrelation line at m/z 840 showing two overlapping precursor ion isotopic distributions with vertical projections along the right and horizontal projections along the top. HC20 (in purple) is the FNWYVDGVEVHNAK peptide (with the modulation of intensity shown in Figure 4.4 and 4.5, and the extracted precursor line shown in Figure 4.9). Resolution was calculated on the $[\text{HC20}+2\text{H}]^{2+}$ first isotope peak (m/z 839.40594).

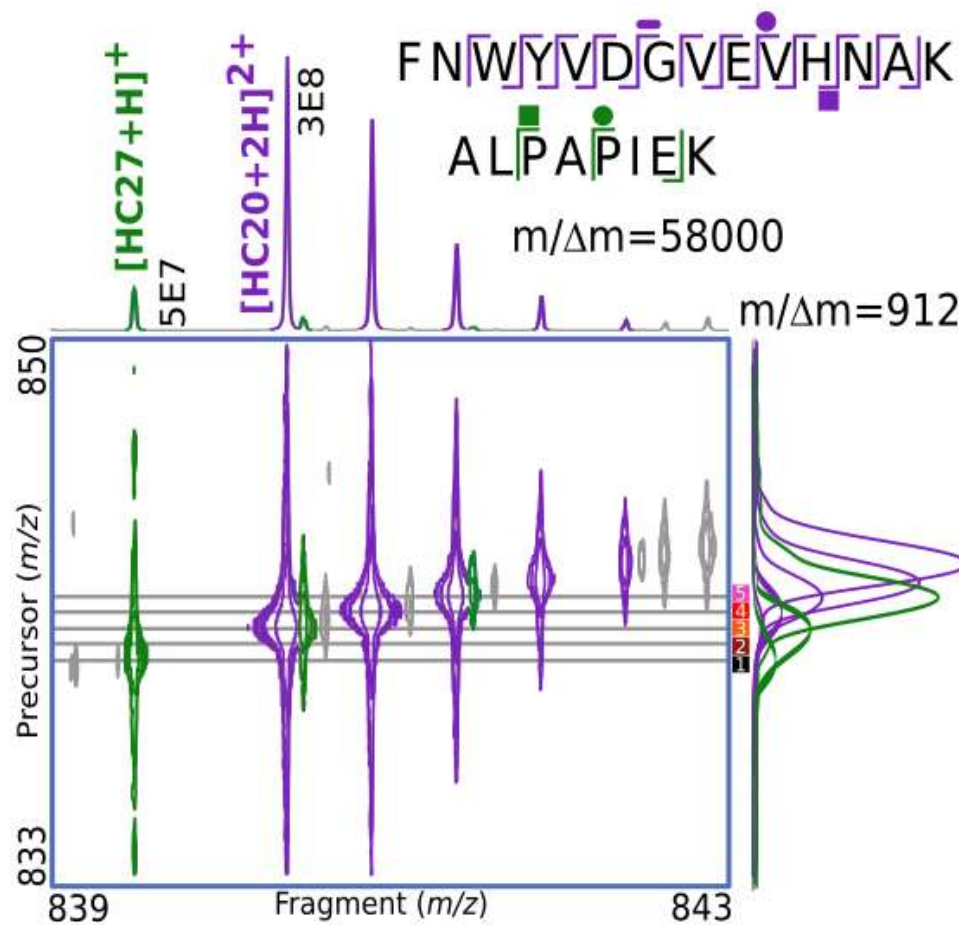


Figure 4. 14: Zoom of the m/z 839-843, m/z 833-847 region on the 2DMS spectrum, and extracted horizontal and vertical lines. HC20: purple. HC27: green. The horizontal lines on the 2DMS spectrum are every two datapoint lines and correspond to: 1, black: m/z 840.059692, 2, brown: m/z 840.527520, 3, orange: m/z 840.995870, 4, red: m/z 841.464741, and 5, pink: m/z 841.934136.

HC27 (in green) is the peptide ALPAPIEK with a singly-charged mass-to-charge ratio of 838.49927. The second isotope of HC27 has a mass-to-charge ratio of 839.50186.

Extracting lines via T2D allows the analysis of sections of the 2DMS data through Bruker Data Analysis software, or other third party software. Horizontal and vertical lines were extracted to calculate the resolving power in the two dimensions. The resolution was calculated on the first isotope of HC20. At m/z 840, the resolution was 58000 in the horizontal dimension, with a transient length of 0.4194 seconds, and 912 in the vertical dimension (122000 in the horizontal dimension and 1900 in the vertical dimension at m/z 400). The resolution in the horizontal dimension is due to the length of the transient of each scan (0.4 seconds). The resolution in the vertical dimension is due to the number of scans (8192). To increase the overall resolution, more scans can be acquired or a longer transient can be recorded. In the vertical dimension, the resolution can be improved by non-uniform sampling of the scans, increasing the processing time of the data, but not the acquisition time of the experiment,⁷¹ or the resolution can be increased by decreasing the sampling frequency in a narrow band experiment as shown with a m/z 30 precursor window.⁵⁸

The first isotope of HC20 and second isotope of HC27 ($\Delta m/z = 0.09592$) are not resolved in the vertical dimension and only just resolved in the horizontal dimension.

1.5.6.2. Extraction of lines

In previous studies, the method of data extraction involved extracting all the data points in a horizontal line from a vertical data point position. Since each horizontal line is a slice through a 3D surface, each data point is not truly representative of the peak centre. Thus, when extracting horizontal lines, as shown in Figure 4.15.A, the precursor ions were identified on five consecutive horizontal lines, with a higher intensity at the lines closer to the m/z of the precursor. Moreover, the fragments ions from two different species were identified on the five lines (Figure 4.15.B-G). Overall, extracting lines using discrete data points can lead to spectral contamination (chimeric spectra) from closely spaced precursors and their fragments.

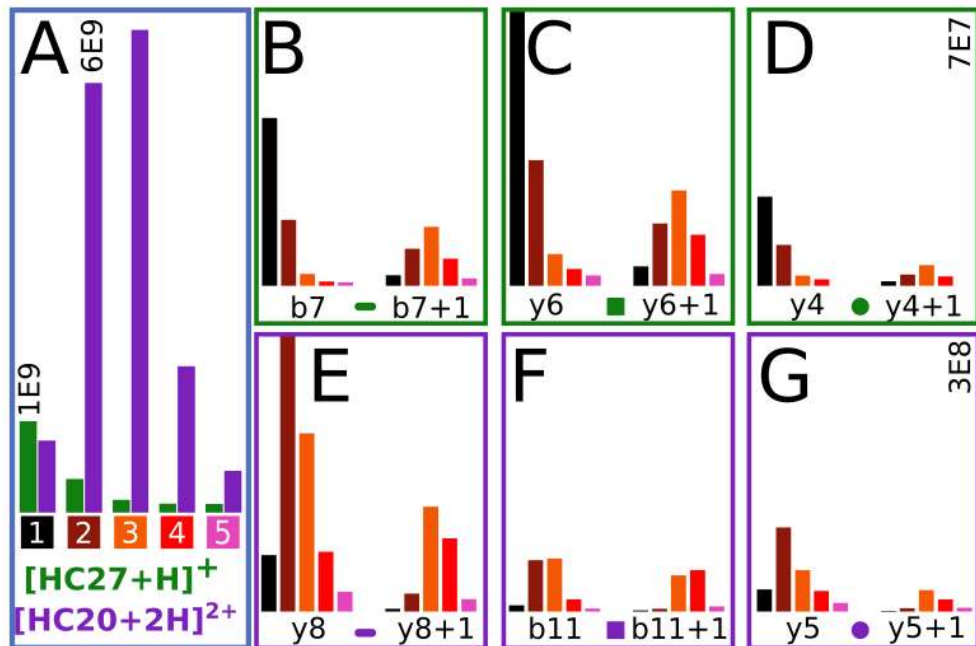


Figure 4. 15: Extracted intensities of precursors (A) b7, y6, and y4 fragments of HC27. (B-D) y8, b11, and y5 fragments of HC20. (E-G) on the 5 lines marked on Figure 4.14. (+1 is the second isotope peak).

Furthermore, isotopes from the different fragments (a and a+1 for example) were at different intensities depending on the extracted lines; Figure 4.16.A shows a 2DMS zoom of the b11 species and Figure 4.16.B shows the corresponding change in peak intensity across the isotopic envelope from line to line. The building of a true picture of the isotopic envelope is therefore very challenging using the line extraction method.

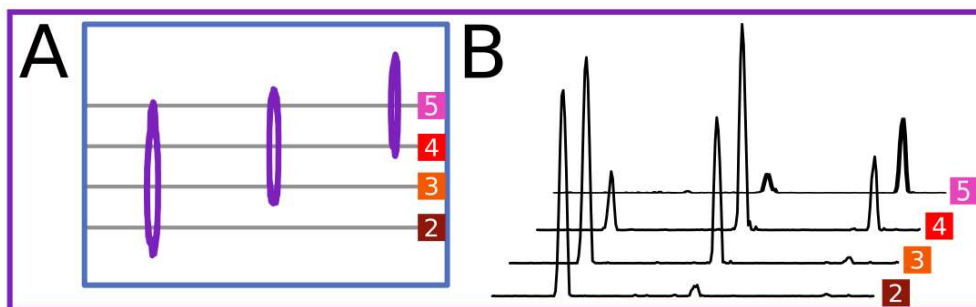


Figure 4. 16: Isotope envelope of b11 (A) Zoom of the 2DMS spectrum (m/z 1346-1349, m/z 840-843) showing the b11 fragment of HC20. (B) Extracted scans of the b11 fragment, across the marked lines from Figure 4.14.

1.5.6.3. 3D visualization

In the 2DMS spectrum, it is possible to determine the charge state of the precursor for each species from the 3D plot. Furthermore, it is possible to resolve the first isotope of HC20 and the second isotope of HC27, despite the low intensity of the HC27 peak, and the mass difference of m/z 0.09592, because they are separated in three dimensions. Figure 4.17 show the 3D views and demonstrate the resolution of the two peaks. 2DMS results in higher 'real' resolution than is possible in either dimension alone.

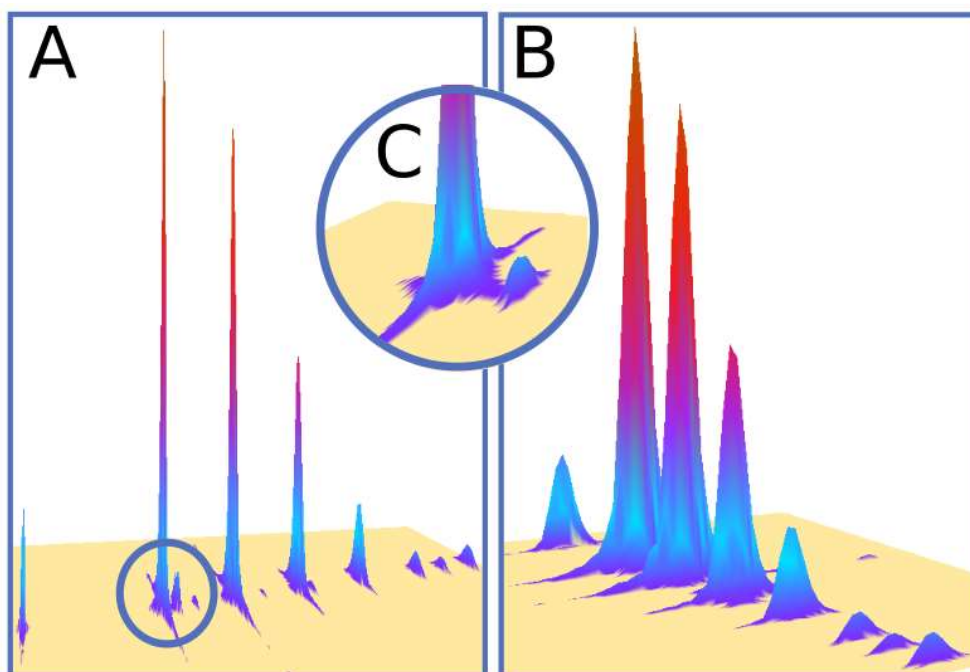


Figure 4. 17: 3D visualisation. (A, B) 3D plot of the two precursors. (C) Zoom showing the 2DMS resolution between the first isotope of HC20 and the second isotope of HC27.

1.5.6.4. Peak picking algorithm

3D peak picking can be carried out, producing a true 3-dimensional peak centre for each peak in the 2DMS spectrum. Figure 4.18 shows the peak centres generated through peak centroiding in 3D space for the two isotope species of HC27 and HC20. The difference between the two peak centres is m/z 0.0944 in the horizontal (fragment) axis, and m/z 0.0885 in the vertical (precursor) axis.

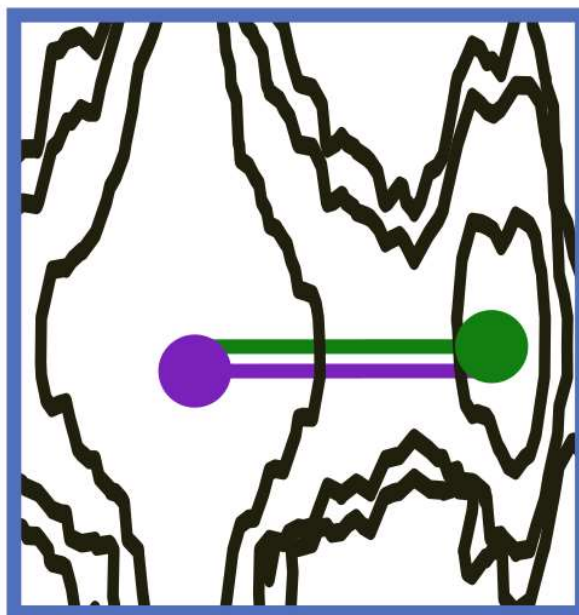


Figure 4. 18: Zoom on the 2DMS spectra. Dots represent result of the 3D peak picking algorithm. HC20 in purple. HC27 in green.

1.5.6.5. Precursor view of two peptides

After 3D peak picking, fragment ions with similar vertical (precursor) m/z values can be clustered and the corresponding horizontal fragment spectrum is much more accurately correlated to the m/z of the precursor.

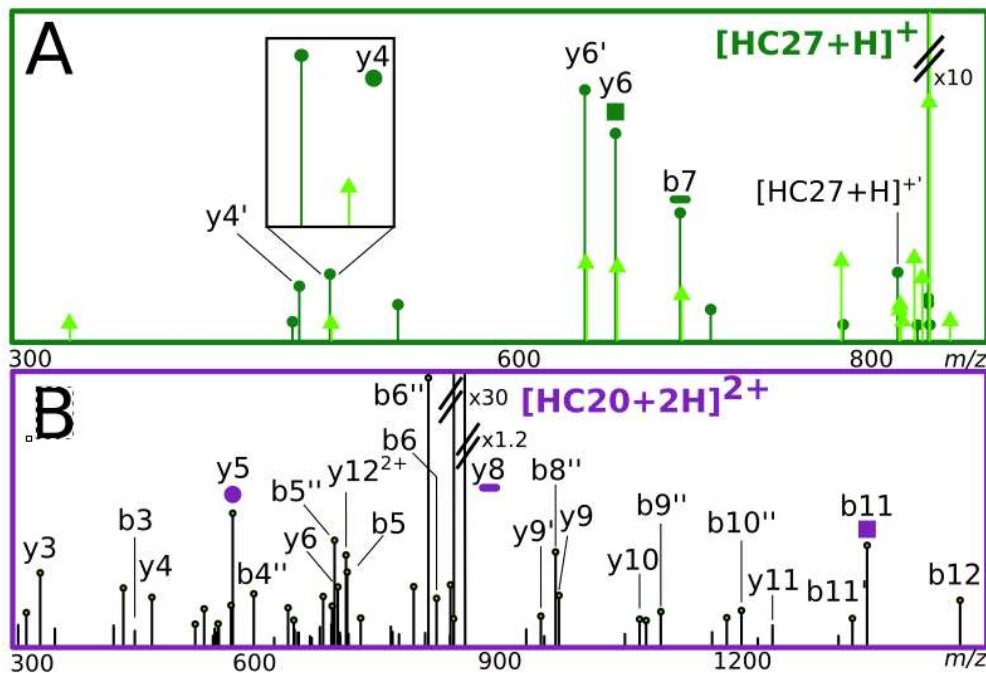


Figure 4. 19: Fragment ion spectra extracted from Precursor View from the two peak picked points in Figure 4.18. (A) Fragment ion spectrum from the peak picked first isotope of HC27 (dark green, circle) and from the peak picked second isotope of HC27 (light green, triangle). (B) Fragment ion spectrum from the peak picked first isotope of HC20.

Figure 4.19.B shows the fragments related to the first isotope of HC20, and Figure 4.19.A shows the first two isotopes of all fragments and precursors with the first isotope in dark green, circle, the second isotope in light green, triangle. Figure 4.19.A shows the isotope resolution of the analysis. No peaks are overlapping between the 4.19.A and 4.19.B spectra, highlighting the resolution advantage of 2DMS. The corresponding fragment spectra are much more accurately correlated, greatly increasing analytical power. Despite the m/z 0.1 difference and the difference of intensities between the precursor peaks (22 fold), the fragments from each precursor are resolved at m/z 840.

Resolution of fragments between precursors of m/z 0.1 at m/z 840 is much higher than quadrupole isolation can achieve and challenging to achieve on FTICR,⁷²⁻⁷⁵ showcasing the power of 2DMS.

4.6. Conclusion and Outlook

Two-dimensional mass spectrometry is an ideal tool for the data independent analysis of complex mixtures. The technique was applied to the analysis of a bottom up sample of IgG1 yielding 75% sequence coverage with a total cleavage coverage of 57.5%, allowing the identification of the majority of the unique peptides. The high resolution of 2DMS allowed the differentiation of which fragments come from which precursors even with very close mass-to-charge ratios between the precursor ions which were less than 0.1 m/z apart. This distinction cannot be done by a quadrupole isolation only and is challenging with any other isolation method. In proteomics, complex biological analysis often have chimeric spectra. This paper is a proof of principle showing the power of the 2DMS technique in resolving chimeric spectra with the use of the 3D peak picking algorithm.

Antibodies are prone to be modified during production, storage, or under stress conditions. To access and control their CQAs, multiple data independent approaches have been developed. 2DMS is a complementary data independent tool which can be integrated to the workflow, especially in forced degradation studies. 2DMS was demonstrated for the comparison of two complex proteomics mixtures, an antibody digest and a modified variant. Any discrepancies between two contour plots can be extracted, and the fragments lines can be analysed in order to identify the peptides and localize PTMs for reaction monitoring or biological process applications.

4.7. Acknowledgement

The authors would like to thank Yuko Lam, and Maria van Agthoven for their help. As well as all the ICR lab for their support. Johanna Paris thanks EPSRC for a PhD studentship through the EPSRC Centre for Doctoral Training in Molecular Analytical Science, grant number EP/L015307/1, UCB, and BB/R022399/1, BB/P021879/1, EP/N033191/1, and Horizon 2020 EU FTICR MS network (731077) for funding.

4.8. References

1. Van Wauwe, J. P.; De Mey, J.; Goossens, J. OKT3: a monoclonal anti-human T lymphocyte antibody with potent mitogenic properties *J Immunol* **1980**, *124*, 2708-2713.
2. Kaplon, H.; Muralidharan, M.; Schneider, Z.; Reichert, J. M. Antibodies to watch in 2020 *mAbs* **2020**, *12*.
3. Ecker, D. M.; Jones, S. D.; Levine, H. L. The therapeutic monoclonal antibody market *MABs* **2015**, *7*, 9-14.
4. Li, F.; Shen, A.; Amanullah, A. Cell culture processes in monoclonal antibody production *Pharmaceutical Sciences Encyclopedia: Drug Discovery, Development, Manufacturing* **2010**, 1-38.
5. Liu, H.; Gaza-Bulseco, G.; Faldu, D.; Chumsae, C.; Sun, J. Heterogeneity of monoclonal antibodies *J. Pharm. Sci.* **2008**, *97*, 2426-2447.
6. Yang, B.; Li, W.; Zhao, H.; Wang, A.; Lei, Y.; Xie, Q.; Xiong, S. Discovery and characterization of CHO host cell protease-induced fragmentation of a recombinant monoclonal antibody during production process development *Journal of Chromatography B* **2019**, *1112*, 1-10.
7. Dashivets, T.; Stracke, J.; Dengl, S.; Knaupp, A.; Pollmann, J.; Buchner, J.; Schlothauer, T. Oxidation in the complementarity-determining regions differentially influences the properties of therapeutic antibodies *MABs* **2016**, *8*, 1525-1535.
8. Szigeti, M.; Chapman, J.; Borza, B.; Guttman, A. Quantitative assessment of mAb Fc glycosylation of CQA importance by capillary electrophoresis *Electrophoresis* **2018**, *39*, 2340-2343.
9. Jefferis, R. Posttranslational modifications and the immunogenicity of biotherapeutics *Journal of immunology research* **2016**, 5358272.
10. Luo, Q.; Joubert, M. K.; Stevenson, R.; Ketchum, R. R.; Narhi, L. O.; Wypych, J. Chemical modifications in therapeutic protein aggregates generated under different stress conditions *J. Biol. Chem.* **2011**, *286*, 25134-25144.
11. Bertolotti-Ciarlet, A.; Wang, W.; Lownes, R.; Pristatsky, P.; Fang, Y.; McKelvey, T.; Li, Y.; Li, Y.; Drummond, J.; Prueksaritanont, T. Impact of methionine oxidation on the binding of human IgG1 to FcRn and Fcγ receptors *Mol. Immunol.* **2009**, *46*, 1878-1882.
12. Stracke, J.; Emrich, T.; Rueger, P.; Schlothauer, T.; Kling, L.; Knaupp, A.; Hertenberger, H.; Wolfert, A.; Spick, C.; Lau, W. A novel approach to investigate the effect

of methionine oxidation on pharmacokinetic properties of therapeutic antibodies *MAbs* **2014**, *6*, 1229-1242.

13. Wang, W.; Vlasak, J.; Li, Y.; Pristatsky, P.; Fang, Y.; Pittman, T.; Roman, J.; Wang, Y.; Prueksaritanont, T.; Ionescu, R. Impact of methionine oxidation in human IgG1 Fc on serum half-life of monoclonal antibodies *Mol. Immunol.* **2011**, *48*, 860-866.

14. Liu, H.; Nowak, C.; Andrien, B.; Shao, M.; Ponniah, G.; Neill, A. Impact of IgG Fc-Oligosaccharides on Recombinant Monoclonal Antibody Structure, Stability, Safety, and Efficacy *Biotechnol. Progr.* **2017**, *33*, 1173-1181.

15. Goetze, A. M.; Schenauer, M. R.; Flynn, G. C. Assessing monoclonal antibody product quality attribute criticality through clinical studies *MAbs* **2010**, *2*, 500-507.

16. Guerra, A.; von Stosch, M.; Glassey, J. Toward biotherapeutic product real-time quality monitoring *Crit. Rev. Biotechnol.* **2019**, *39*, 289-305.

17. Goyon, A.; Dai, L.; Chen, T.; Wei, B.; Yang, F.; Andersen, N.; Kopf, R.; Leiss, M.; Mølhøj, M.; Guilleme, D. From proof of concept to the routine use of an automated and robust multi-dimensional liquid chromatography mass spectrometry workflow applied for the charge variant characterization of therapeutic antibodies *J. Chromatogr. A* **2020**, *1615*, 460740.

18. Edelman, G. M.; Cunningham, B. A.; Gall, W. E.; Gottlieb, P. D.; Rutishauser, U.; Waxdal, M. J. Pillars Article: The Covalent Structure of an Entire γ G Immunoglobulin Molecule. *Proc. Natl. Acad. Sci. USA*, 1969, *63*: 78–85 *J Immunol* **2004**, *173*, 5335-5342.

19. Silverton, E.; Navia, M. A.; Davies, D. R. Three-dimensional structure of an intact human immunoglobulin *PNAS* **1977**, *74*, 5140-5144.

20. Isenman, D. E.; Painter, R. H.; Dorrington, K. J. The structure and function of immunoglobulin domains: studies with beta-2-microglobulin on the role of the intrachain disulfide bond *PNAS* **1975**, *72*, 548-552.

21. Edmundson, A.; Ely, K.; Abola, E.; Schiffer, M.; Panagiotopoulos, N.; Deutsch, H. Conformational isomerism, rotational allomerism, and divergent evolution in immunoglobulin light chains *Fed Proc.* **1976**, *35*, 2119-2123.

22. Jaton, J.; Riesen, W. The relationship between hypervariable regions, antigen-binding specificity and the three-dimensional structure of antibodies *Ann. Immunol.* **1976**, *127*, 273-283.

23. Irani, V.; Guy, A. J.; Andrew, D.; Beeson, J. G.; Ramsland, P. A.; Richards, J. S. Molecular properties of human IgG subclasses and their implications for designing

therapeutic monoclonal antibodies against infectious diseases *Mol. Immunol.* **2015**, *67*, 171-182.

24. Chen, Y.; Doud, E.; Stone, T.; Xin, L.; Hong, W.; Li, Y. Rapid global characterization of immunoglobulin G1 following oxidative stress *mAbs* **2019**, *11*, 1089-1100.

25. Vogt, W. Oxidation of methionyl residues in proteins: tools, targets, and reversal *Free Radic Biol Med* **1995**, *18*, 93-105.

26. Aebersold, R.; Mann, M. Mass spectrometry-based proteomics *Nature* **2003**, *422*, 198-207.

27. Kaur, P.; Tomechko, S.; Kiselar, J.; Shi, W.; Deperalta, G.; Weckslar, A. T.; Gokulrangan, G.; Ling, V.; Chance, M. R. Characterizing monoclonal antibody structure by carbodiimide/GEE footprinting *Mabs* **2014**, *6*, 1486-1499.

28. Srzentić, K.; Fornelli, L.; Laskay, U. n. A.; Monod, M.; Beck, A.; Ayoub, D.; Tsybin, Y. O. Advantages of extended bottom-up proteomics using Sap9 for analysis of monoclonal antibodies *Anal. Chem.* **2014**, *86*, 9945-9953.

29. Bobaly, B.; D'Atri, V.; Goyon, A.; Colas, O.; Beck, A.; Fekete, S.; Guillarme, D. Protocols for the analytical characterization of therapeutic monoclonal antibodies. II—enzymatic and chemical sample preparation *Journal of Chromatography B* **2017**, *1060*, 325-335.

30. D'Atri, V.; Goyon, A.; Bobaly, B.; Beck, A.; Fekete, S.; Guillarme, D. Protocols for the analytical characterization of therapeutic monoclonal antibodies. III—Denaturing chromatographic techniques hyphenated to mass spectrometry *Journal of Chromatography B* **2018**, *1096*, 95-106.

31. Rogers, R. S.; Abernathy, M.; Richardson, D. D.; Rouse, J. C.; Sperry, J. B.; Swann, P.; Wypych, J.; Yu, C.; Zang, L.; Deshpande, R. A view on the importance of “multi-attribute method” for measuring purity of biopharmaceuticals and improving overall control strategy *AAPS J* **2018**, *20*, 7.

32. Xu, W.; Jimenez, R. B.; Mowery, R.; Luo, H.; Cao, M.; Agarwal, N.; Ramos, I.; Wang, X.; Wang, J. A Quadrupole Dalton-based multi-attribute method for product characterization, process development, and quality control of therapeutic proteins *MABs* **2017**, *9*, 1186-1196.

33. Wang, Y.; Li, X.; Liu, Y.-H.; Richardson, D.; Li, H.; Shameem, M.; Yang, X. Simultaneous monitoring of oxidation, deamidation, isomerization, and glycosylation of

monoclonal antibodies by liquid chromatography-mass spectrometry method with ultrafast tryptic digestion *MABs* **2016**, *8*, 1477-1486.

34. Gillet, L. C.; Navarro, P.; Tate, S.; Röst, H.; Selevsek, N.; Reiter, L.; Bonner, R.; Aebersold, R. Targeted data extraction of the MS/MS spectra generated by data-independent acquisition: a new concept for consistent and accurate proteome analysis *Mol. Cell Proteomics* **2012**, *11*.

35. Amster, I. J. Fourier transform mass spectrometry *J. Mass Spectrom.* **1996**, *31*, 1325-1337.

36. Marshall, A. G.; Hendrickson, C. L.; Jackson, G. S. Fourier transform ion cyclotron resonance mass spectrometry: a primer *Mass Spectrom. Rev.* **1998**, *17*, 1-35.

37. Pfändler, P.; Bodenhausen, G.; Rapin, J.; Houriet, R.; Gäumann, T. Two-dimensional Fourier transform ion cyclotron resonance mass spectrometry *Chem. Phys. Lett.* **1987**, *138*, 195-200.

38. Pfändler, P.; Bodenhausen, G.; Rapin, J.; Walser, M. E.; Gaeumann, T. Broad-band two-dimensional Fourier transform ion cyclotron resonance *JACS* **1988**, *110*, 5625-5628.

39. Caravatti, P.; Allemann, M. The 'infinity cell': A new trapped-ion cell with radiofrequency covered trapping electrodes for fourier transform ion cyclotron resonance mass spectrometry *Org. Mass Spectrom.* **1991**, *26*, 514-518.

40. Brodbelt, J. S. Photodissociation mass spectrometry: new tools for characterization of biological molecules *Chem. Soc. Rev.* **2014**, *43*, 2757-2783.

41. Zubarev, R. A.; Kelleher, N. L.; McLafferty, F. W. Electron capture dissociation of multiply charged protein cations. A nonergodic process *JACS* **1998**, *120*, 3265-3266.

42. Tsybin, Y. O.; Witt, M.; Baykut, G.; Kjeldsen, F.; Håkansson, P. Combined infrared multiphoton dissociation and electron capture dissociation with a hollow electron beam in Fourier transform ion cyclotron resonance mass spectrometry *Rapid Commun. Mass Spectrom.* **2003**, *17*, 1759-1768.

43. Van Agthoven, M. A.; Delsuc, M.-A.; Bodenhausen, G.; Rolando, C. Towards analytically useful two-dimensional Fourier transform ion cyclotron resonance mass spectrometry *Anal. Bioanal. Chem.* **2013**, *405*, 51-61.

44. van Agthoven, M. A.; Lam, Y. P.; O'Connor, P. B.; Rolando, C.; Delsuc, M.-A. Two-dimensional mass spectrometry: new perspectives for tandem mass spectrometry *European Biophysics Journal* **2019**, *48*, 213-229.

45. Chiron, L.; van Agthoven, M. A.; Kieffer, B.; Rolando, C.; Delsuc, M.-A. Efficient denoising algorithms for large experimental datasets and their applications in Fourier transform ion cyclotron resonance mass spectrometry *PNAS* **2014**, *111*, 1385-1390.
46. van Agthoven, M. A.; Chiron, L.; Coutouly, M.-A.; Sehgal, A. A.; Pelupessy, P.; Delsuc, M.-A.; Rolando, C. Optimization of the discrete pulse sequence for two-dimensional FT-ICR mass spectrometry using infrared multiphoton dissociation *Int. J. Mass spectrom.* **2014**, *370*, 114-124.
47. Little, D. P.; Speir, J. P.; Senko, M. W.; O'Connor, P. B.; McLafferty, F. W. Infrared multiphoton dissociation of large multiply charged ions for biomolecule sequencing *Anal. Chem.* **1994**, *66*, 2809-2815.
48. Talebpour, A.; Bandrauk, A.; Yang, J.; Chin, S. Multiphoton ionization of inner-valence electrons and fragmentation of ethylene in an intense Ti: sapphire laser pulse *Chem. Phys. Lett.* **1999**, *313*, 789-794.
49. Maitre, P.; Scuderi, D.; Corinti, D.; Chiavarino, B.; Crestoni, M. E.; Fornarini, S. Applications of Infrared Multiple Photon Dissociation (IRMPD) to the Detection of Posttranslational Modifications *Chem. Rev.* **2019**.
50. McCormack, A. L.; Somogyi, A.; Dongre, A. R.; Wysocki, V. H. Fragmentation of protonated peptides: surface-induced dissociation in conjunction with a quantum mechanical approach *Anal. Chem.* **1993**, *65*, 2859-2872.
51. Tsaprailis, G.; Nair, H.; Somogyi, Á.; Wysocki, V. H.; Zhong, W.; Futrell, J. H.; Summerfield, S. G.; Gaskell, S. J. Influence of secondary structure on the fragmentation of protonated peptides *JACS* **1999**, *121*, 5142-5154.
52. Paris, J.; Morgan, T. E.; Wootton, C. A.; Barrow, M. P.; O'Hara, J.; O'Connor, P. B. Facile determination of phosphorylation sites in peptides using two-dimensional mass spectrometry *Anal. Chem.* **2020**.
53. van Agthoven, M. A.; Delsuc, M.-A.; Rolando, C. Two-dimensional FT-ICR/MS with IRMPD as fragmentation mode *Int. J. Mass spectrom.* **2011**, *306*, 196-203.
54. van Agthoven, M. A.; Wootton, C. A.; Chiron, L.; Coutouly, M.-A.; Soulby, A.; Wei, J.; Barrow, M. P.; Delsuc, M.-A.; Rolando, C.; O'Connor, P. B. Two-dimensional mass spectrometry for proteomics, a comparative study with cytochrome c *Anal. Chem.* **2016**, *88*, 4409-4417.

55. Floris, F.; van Agthoven, M.; Chiron, L.; Soulby, A. J.; Wootton, C. A.; Lam, Y. P.; Barrow, M. P.; Delsuc, M.-A.; O'Connor, P. B. 2D FT-ICR MS of calmodulin: a top-down and bottom-up approach *J. Am. Soc. Mass. Spectrom.* **2016**, *27*, 1531-1538.
56. van Agthoven, M. A.; Chiron, L.; Coutouly, M.-A.; Delsuc, M.-A.; Rolando, C. Two-dimensional ECD FT-ICR mass spectrometry of peptides and glycopeptides *Anal. Chem.* **2012**, *84*, 5589-5595.
57. Floris, F.; van Agthoven, M. A.; Chiron, L.; Wootton, C. A.; Lam, P. Y. Y.; Barrow, M. P.; Delsuc, M.-A.; O'Connor, P. B. Bottom-up two-dimensional electron-capture dissociation mass spectrometry of calmodulin *J. Am. Soc. Mass. Spectrom.* **2018**, *29*, 207-210.
58. Halper, M.; Delsuc, M.-A.; Breuker, K.; van Agthoven, M. A. Narrowband Modulation Two-Dimensional Mass Spectrometry and Label-Free Relative Quantification of Histone Peptides *Anal. Chem.* **2020**, *92*, 13945-13952.
59. Marzullo, B. P.; Morgan, T. E.; Wootton, C. A.; Perry, S. J.; Saeed, M.; Barrow, M. P.; O'Connor, P. B. Advantages of Two-Dimensional Electron-Induced Dissociation and Infrared Multiphoton Dissociation Mass Spectrometry for the Analysis of Agrochemicals *Anal. Chem.* **2020**, *92*, 11687-11695.
60. van Agthoven, M. A.; Lynch, A. M.; Morgan, T. E.; Wootton, C. A.; Lam, Y. P.; Chiron, L.; Barrow, M. P.; Delsuc, M.-A.; O'Connor, P. B. Can Two-Dimensional IR-ECD Mass Spectrometry Improve Peptide de Novo Sequencing? *Anal. Chem.* **2018**, *90*, 3496-3504.
61. Wilm, M.; Mann, M. Analytical properties of the nanoelectrospray ion source *Anal. Chem.* **1996**, *68*, 1-8.
62. Chiron, L.; Coutouly, M.-A.; Starck, J.-P.; Rolando, C.; Delsuc, M.-A. SPIKE a Processing Software dedicated to Fourier Spectroscopies *arXiv:1608.06777 [physics.comp-ph]* **2016**.
63. *Ultra-high resolution 2D-FTMS for truly DIA analysis of challenging systems*, Wootton, C. A.; Morgan, T. E.; Marzullo, B. P.; Lam, Y. P. Y.; Lozano, D. C. P.; Theisen, A.; Haris, A.; Barrow, M. P.; O'Connor, P. B., 298156, Proceedings of the 67th ASMS Conference on Mass Spectrometry and Allied Topics, Atlanta, Georgia, June 2-6, 2019;
64. van Agthoven, M. A.; Kilgour, D. P.; Lynch, A. M.; Barrow, M. P.; Morgan, T. E.; Wootton, C. A.; Chiron, L.; Delsuc, M.-A.; O'Connor, P. B. Phase relationships in two-dimensional mass spectrometry *J. Am. Soc. Mass. Spectrom.* **2019**, *30*, 2594-2607.

65. Panchaud, A.; Scherl, A.; Shaffer, S. A.; von Haller, P. D.; Kulasekara, H. D.; Miller, S. I.; Goodlett, D. R. Precursor acquisition independent from ion count: how to dive deeper into the proteomics ocean *Anal. Chem.* **2009**, *81*, 6481-6488.
66. Bekker-Jensen, D. B.; Bernhardt, O.; Hogrebe, A.; del Val, A. M.; Verbeke, L.; Gandhi, T.; Kelstrup, C. D.; Reiter, L.; Olsen, J. V. Rapid and site-specific deep phosphoproteome profiling by data-independent acquisition (DIA) without the need for spectral libraries *bioRxiv* **2019**, 657858.
67. Moseley, M. A.; Hughes, C. J.; Juvvadi, P. R.; Soderblom, E. J.; Lennon, S.; Perkins, S. R.; Thompson, J. W.; Steinbach, W. J.; Geromanos, S. J.; Wildgoose, J. Scanning quadrupole data-independent acquisition, Part A: Qualitative and quantitative characterization *J. Proteome Res.* **2018**, *17*, 770-779.
68. Meier, F.; Brunner, A.-D.; Koch, S.; Koch, H.; Lubeck, M.; Krause, M.; Goedecke, N.; Decker, J.; Kosinski, T.; Park, M. A. Online parallel accumulation–serial fragmentation (PASEF) with a novel trapped ion mobility mass spectrometer *Mol. Cell Proteomics* **2018**, *17*, 2534-2545.
69. Kabat, E. A.; Te Wu, T.; Perry, H. M.; Foeller, C.; Gottesman, K. S. Sequences of proteins of immunological interest, ed.; DIANE publishing, 1992; Vol., p.
70. Schweiger-Hufnagel, U.; Hufnagel, P.; Hebel, R.; Witt, M.; Schmit, P.; Macht, M.; Asperger, A. Towards 100% Sequence Coverage in Protein QC: In-depth Sequence Characterization of Monoclonal Antibodies *J. Biomol. Tech.* **2010**, *21*, S63.
71. Bray, F.; Bouclon, J.; Chiron, L.; Witt, M.; Delsuc, M.-A.; Rolando, C. Nonuniform Sampling Acquisition of Two-Dimensional Fourier Transform Ion Cyclotron Resonance Mass Spectrometry for Increased Mass Resolution of Tandem Mass Spectrometry Precursor Ions *Anal. Chem.* **2017**, *89*, 8589-8593.
72. O'Connor, P. B.; McLafferty, F. W. High-resolution ion isolation with the ion cyclotron resonance capacitively coupled open cell *J. Am. Soc. Mass. Spectrom.* **1995**, *6*, 533-535.
73. O'Connor, P. B.; Little, D. P.; McLafferty, F. W. Isotopic assignment in large-molecule mass spectra by fragmentation of a selected isotopic peak *Anal. Chem.* **1996**, *68*, 542-545.
74. Heck, A. J.; Derrick, P. J. Selective fragmentation of single isotopic ions of proteins up to 17 kDa using 9.4 Tesla Fourier transform ion cyclotron resonance *Eur. Mass Spectrom.* **1998**, *4*, 181-188.

75. Smith, D. F.; Blakney, G. T.; Beu, S. C.; Anderson, L. C.; Weisbrod, C. R.; Hendrickson, C. L. Ultrahigh Resolution Ion Isolation by Stored Waveform Inverse Fourier Transform 21 T Fourier Transform Ion Cyclotron Resonance Mass Spectrometry *Anal. Chem.* **2020**, *92*, 3213-3219.

4.9. Nomenclature of the IgG1 peptides

HCXX means peptide from the heavy chain protein, number XX, starting from the N-term.

LCXX means peptide from the light chain protein, number XX, starting from the N-term.

Peptide Name	Amino Acid Sequence	Mass (Da)
LC01	DIQMTQSPSSLSASVGDR	1877.87891
LC02	VTITCK	720.38401
LC03	ASQNVK	673.35074
LC04	TVVAWYQQKPGK	1403.75613
LC05	APK	314.19541
LC06	TLIYLASNR	1049.58694
LC07	HTGVPSR	752.39294
LC08	FSGSGSGTDFTLTISLQPEDFATYFCLQHWSYPLTFGQGTK	4679.17114
LC09	VEIK	487.30060
LC10	R	174.11168
LC11	TVAAPSVFIFPPSDEQLK	1945.01968
LC12	SGTASVVCLLNNFYPR	1796.88795
LC13	EAK	346.18523
LC14	VQWK	559.31183
LC15	VDNALQSGNSQESVTEQDSK	2134.96145
LC16	DSTYLSSTLTLSK	1501.75117
LC17	ADYEK	624.27551
LC18	HK	283.16444
LC19	VYACEVTHQGLSSPVTK	1874.91965
LC20	SFNR	522.25505

Table 4. 1: Light chain peptides

Peptide Name	Amino Acid Sequence	Mass (Da)
HC01	EVQLVESGGGLVQPGGSLR	1880.99559
HC02	LSCAASGFASFSTYDMSWVR	2154.95030
HC03	QAPGK	499.27545
HC04	GLEWVATISSGGSYTYLDSVK	2395.15836
HC05	GR	231.13314
HC06	FTISR	622.34386
HC07	DSSK	435.19653
HC08	NTRYLQMNSLR	1351.69182
HC09	AEDTAVYYCAPTTVPFAYWGQGLTVTVSSASTK	3639.74432
HC10	GPSVFPLAPSSK	1185.63937
HC11	STSGGTAALGCLVK	1320.67075
HC12	DYFPEPVTVSWNSGALTSQVHTFPAVLQSSGLYSLSSVVTVP SSSLGTQTYICNVNHKPSNTK	6483.16454
HC13	VDK	360.20088
HC14	K	146.10553
HC15	VEPK	471.26930
HC16	SCDK	508.19515
HC17	THTCPPCPAPELLGGPSVFLFPPKPK	2843.45026
HC18	DTLMISR	834.42694
HC19	TPEVTCVVVDVSHEDPEVK	2138.02015
HC20	FNWYVDGVEVHNAK	1676.79471
HC21	TKPR	500.30708
HC22	EEQYNSTYR	1188.50473
HC23	VVSVLTVLHQDWLNGK	1806.99922
HC24	EYK	438.21145
HC25	CK	306.13618
HC26	VSNK	446.24890
HC27	ALPAPIEK	837.49600
HC28	TISK	447.26930
HC29	AK	217.14264
HC30	GQPR	456.24448
HC31	EPQVYTLPPSR	1285.66665
HC32	DELTK	604.30681
HC33	NQVSLTCLVK	1160.62234
HC34	GFYPSDIAVEWESNGQPENNYK	2543.12410
HC35	TTPPVLDSDGSFFLYSK	1872.91455
HC36	LTVDK	574.33263
HC37	SR	261.14370
HC38	WQQGNVFSCSVMHEALHNHYTQK	2800.25984
HC39	SLSLSPGK	787.44397

Table 4. 2: Heavy chain peptides

4.10. Assignment tables

Absolute error is calculated as the average of the absolute ppm errors of all the assigned peaks. Standard deviation is calculated as the standard deviation of the ppm errors of all the assigned peaks.

Species	Theoretical <i>m/z</i>	Sample at 4°C		Oxidised Sample	
		Observed <i>m/z</i>	ppm	Observed <i>m/z</i>	ppm
[M+H] ²⁺	941.50507	941.50497	-0.108	941.50473	-0.363
b3	357.17686	357.17753	1.873	357.17731	1.257
b5	569.32934	569.32934	0.002	*	*
b11	1069.55242	1069.55390	1.388	1069.55304	0.584
b12	1168.62083	1168.62100	0.146	1168.62121	0.326
b13	1296.67941	1296.67939	-0.013	1296.68048	0.828
b15	1450.75363	*	*	1450.75527	1.127
b16	1507.77510	1507.77898	2.575	1507.77560	0.333
b17	1594.80713	1594.80440	-1.710	1594.80136	-3.616
b18	1707.89119	1707.89121	0.011	1707.89018	-0.592
y10	983.56325	983.56582	2.608	983.56702	3.828
y8	813.45773	813.45669	-1.275	813.45626	-1.804
y7	714.38931	714.38932	0.009	714.38922	-0.131
y6	586.33074	586.32709	-6.218	586.32910	-2.790
y5	489.27797	489.27797	-0.004	489.27762	-0.719
y4	432.25651	*	*	432.25651	0.004
b4 [†]	452.25036	452.25054	0.397	452.25085	1.083
b5 [†]	551.31877	551.31824	-0.969	551.31778	-1.803
Absolute Error		1.207		1.246	
Standard deviation		1.579		1.135	

Table 4. 3: Peaks assignment for HC01 extracted fragmentation line. HC01: EVQLVESGGGLVQPGGSLR. Internal calibration points are in bold. *: not observed. †: loss of water.

Species	Theoretical m/z	Sample at 4°C		Oxidised Sample	
		Observed m/z	ppm	Observed m/z	ppm
[M+H] ²⁺	1078.48242	1078.48549	2.842	1078.48458	1.998
b13	1363.59871	1363.60237	2.681	1363.60202	2.424
b14	1478.62566	1478.62829	1.781	1478.62894	2.220
b15	1609.66614	1609.66928	1.949	1609.66986	2.310
b16	1696.69817	1696.69535	-1.662	1696.69461	-2.099
b17	1882.77748	1882.78186	2.324	1882.78173	2.255
b18	1981.84590	1981.84671	0.410	1981.84720	0.657
y14	1653.73660	1653.73186	-2.869	1653.73253	-2.464
y11	1362.61470	1362.61020	-3.301	1362.61699	1.682
y10	1291.57758	1291.57700	-0.453	1291.57585	-1.343
y9	1144.50917	1144.50688	-2.002	1144.50590	-2.858
y8	1057.47714	1057.47505	-1.979	1057.47389	-3.076
y6	793.36614	793.36623	0.119	793.36607	-0.083
y5	678.33919	678.34092	2.547	678.33914	-0.077
y4	547.29871	547.29981	2.015	547.29832	-0.708
y3	460.26668	460.26748	1.740	460.26706	0.828
y2	274.18737	274.18737	0.014	274.18733	-0.132
b8'	776.33959	776.33741	-2.803	776.33677	-3.628
b9'	847.37670	847.37669	-0.012	847.37531	-1.641
b10'	994.44511	994.44785	2.751	994.44789	2.791
b12'	1182.52482	*	*	1182.52247	-1.988
Absolute Error		1.813		1.774	
Standard deviation		1.028		1.002	

Table 4. 4: Peaks assignment for HC02 extracted fragmentation line. HC02: LSCAASGFASFSTYDMSWVR. Internal calibration points are in bold. *: not observed. ': loss of water.

Species	Theoretical <i>m/z</i>	Sample at 4°C		Oxidised Sample	
		Observed <i>m/z</i>	ppm	Observed <i>m/z</i>	ppm
[M+H] ²⁺	1198.58646	1198.59063	3.483	1198.59047	3.350
b5	585.30312	585.30483	2.915	*	*
b8	870.47198	870.47186	-0.138	870.47382	2.113
b11	1101.55750	*	*	1101.55969	1.987
b12	1158.57896	*	*	1158.57947	0.436
b13	1245.61099	1245.61526	3.426	1245.61193	0.752
b14	1408.67432	1408.68205	5.486	1408.68400	6.871
b16	1672.78533	1672.79098	3.378	1672.79010	2.852
b17	1835.84866	1835.84491	-2.041	1835.85549	3.722
b18	1948.93272	1948.93172	-0.514	1948.93462	0.974
b19	2063.95966	2063.96477	2.474	2063.96203	1.146
b21	2250.06011	2250.06992	4.361	2250.06307	1.317
y15	1639.78499	1639.78499	-0.003	1639.78093	-2.478
y14	1526.70093	1526.69645	-2.935	1526.69701	-2.568
y13	1439.66890	1439.66715	-1.217	1439.66541	-2.425
y12	1352.63687	1352.63539	-1.097	1352.63801	0.840
y11	1295.61541	1295.60904	-4.916	1295.61386	-1.196
y10	1238.59395	1238.59366	-0.231	1238.58985	-3.307
y9	1151.56192	1151.56491	2.599	1151.56596	3.510
y8	988.49859	988.49383	-4.814	988.50132	2.763
y7	887.45091	887.45017	-0.834	887.45342	2.828
y6	724.38758	724.38711	-0.652	724.38854	1.322
y5	561.32425	*	*	561.32392	-0.594
y4	448.24019	448.23912	-2.386	448.23988	-0.690
y3	333.21325	333.21333	0.251	333.21330	0.161
b7'	739.37735	739.37571	-2.220	739.37552	-2.477
Absolute Error		2.277		2.092	
Standard deviation		1.635		1.455	

Table 4. 5: Peaks assignment for HC04 extracted fragmentation line. HC04: GLEWVATISSGGSYTYLDVK. Internal calibration points are in bold. *: not observed. ′: loss of water.

Species	Theoretical <i>m/z</i>	Sample at 4°C		Oxidised Sample	
		Observed <i>m/z</i>	ppm	Observed <i>m/z</i>	ppm
[M+H] ⁺	623.35114	623.35114	0.005	623.35242	2.058
b3'	344.19687	344.19687	0.005	344.19688	0.034

Table 4. 6: Peaks assignment for HC06 extracted fragmentation line. HC06: FTISR. No internal calibration. *: not observed. ′: loss of water.

Species	Theoretical <i>m/z</i>	Sample at 4°C		Oxidised Sample	
		Observed <i>m/z</i>	ppm	Observed <i>m/z</i>	ppm
[M+H] ²⁺	676.85319	676.85455	2.014	676.85318	-0.010
b3	329.18195	329.18208	0.406	*	*
b6	733.38792	733.38907	1.577	733.38911	1.628
b7	864.42840	864.43121	3.249	864.43057	2.509
b8	978.47133	978.46836	-3.034	978.47290	1.606
b9	1065.50336	1065.50752	3.907	1065.50339	0.031
b10	1178.58742	1178.58677	-0.553	1178.58739	-0.027
y8	1024.52443	1024.52093	-3.413	1024.52272	-1.666
y7	861.46110	861.45935	-2.030	861.45934	-2.041
y6	748.37703	748.37943	3.201	748.37646	-0.768
y5	620.31846	620.31787	-0.946	620.31649	-3.171
y4	489.27797	489.27794	-0.065	*	*
y2	288.20302	288.20302	0.013	288.20302	0.013
Absolute Error		1.878		1.224	
Standard deviation		1.334		1.071	

Table 4. 7: Peaks assignment for HC08 extracted fragmentation line. HC08: NTLYLQMNSLR. Internal calibration points are in bold. *: not observed. †: loss of water.

Species	Theoretical <i>m/z</i>	Sample at 4°C		Oxidised Sample	
		Observed <i>m/z</i>	ppm	Observed <i>m/z</i>	ppm
[M+H] ⁺	1186.64665	1186.64964	2.520	1186.64958	2.470
b8	769.42430	769.42438	0.102	769.42395	-0.457
y10	1032.57242	1032.57248	0.056	1032.57289	0.453
y9	945.54039	945.54256	2.290	945.54016	-0.248
y8	846.47198	846.47185	-0.154	846.47221	0.271
y7	699.40357	699.40449	1.321	699.40343	-0.195
y5	489.26674	489.26674	0.003	489.26693	0.391
y4	418.22962	*	*	418.22956	-0.155
Absolute Error		0.921		0.580	
Standard deviation		1.031		0.722	

Table 4. 8: Peaks assignment for HC10 extracted fragmentation line. HC10: GPSVFPLAPSSK. Internal calibration points are in bold. *: not observed. †: loss of water

Species	Theoretical m/z	Sample at 4°C		Oxidised Sample	
		Observed m/z	ppm	Observed m/z	ppm
[M+H] ²⁺	661.34265	661.34479	3.233	661.34254	-0.169
b2	189.08698	*	*	189.08659	-2.080
b9	746.36791	746.37091	4.021	746.36807	0.215
b10	803.38937	803.38774	-2.033	803.39021	1.042
b12	1076.50409	1076.50626	2.020	1076.50535	1.175
b13	1175.57250	1175.57263	0.111	1175.57242	-0.068
y11	1046.56629	1046.56465	-1.569	1046.56819	1.814
y8	831.47569	831.47623	0.654	831.47178	-4.698
y7	760.43857	760.43845	-0.161	760.43706	-1.989
y6	689.40146	689.40233	1.264	689.39920	-3.276
y5	576.31739	576.31755	0.270	576.31573	-2.888
y4	519.29593	519.29597	0.076	519.29444	-2.871
y3	359.26528	359.26528	-0.006	359.26528	-0.006
b9'	728.35734	728.35513	-3.040	728.35747	0.172
b10'	785.37881	785.37752	-1.640	785.37979	1.250
b12'	1058.49352	1058.49675	3.051	1058.49465	1.067
b13'	1157.56193	1157.56353	1.378	1157.56167	-0.229
Absolute Error		1.533		1.471	
Standard deviation		1.249		1.317	

Table 4. 9: Peaks assignment for HC11 extracted fragmentation line. HC11: STSGGTAALGCLVK. Internal calibration points are in bold. *: not observed. ′: loss of water.

Species	Theoretical <i>m/z</i>	Sample at 4°C		Oxidised Sample	
		Observed <i>m/z</i>	ppm	Observed <i>m/z</i>	ppm
[M+H] ³⁺	948.82403	948.82646	2.560	948.82595	2.022
b2	239.11387	239.11387	0.013	239.11387	0.013
b3	340.16155	340.16133	-0.633	340.16164	0.279
b4	500.19219	500.19175	-0.888	500.19240	0.412
b21	2279.09876	*	*	2279.09737	-0.609
y17	1823.04657	*	*	1823.04131	-2.885
y15	1596.95121	1596.95044	-0.483	1596.95144	0.143
y13	1370.78308	1370.78288	-0.149	1370.77987	-2.345
y12	1313.76162	*	*	1313.76460	2.268
y11	1256.74016	1256.74192	1.403	1256.73663	-2.806
y8	973.58695	*	*	973.58734	0.400
y6	713.43447	713.43531	1.174	713.43362	-1.195
y5	566.36606	566.36605	-0.015	566.36598	-0.139
y2	244.16557	244.16559	0.090	244.16594	1.524
y24 ²⁺	1303.67911	1303.67775	-1.046	1303.67299	-4.697
y23 ²⁺	1253.15527	1253.15314	-1.703	1253.15229	-2.381
y22 ²⁺	1173.13995	1173.14013	0.154	1173.13741	-2.165
y21 ²⁺	1124.61357	1124.61231	-1.118	1124.61115	-2.150
y20 ²⁺	1076.08719	1076.09103	3.572	1076.08655	-0.591
y19 ²⁺	996.07186	996.06864	-3.234	996.07228	0.420
Absolute Error		1.140		1.472	
Standard deviation		1.091		1.219	

Table 4. 10: Peaks assignment for HC17 extracted fragmentation line. HC17: THTCPPCPAPPELLGGPSVFLFPPKPK. Internal calibration points are in bold. *: missing assignment. †: loss of water.

Species	Theoretical m/z	Sample at 4°C		Oxidised Sample	
		Observed m/z	ppm	Observed m/z	ppm
[M+H] ²⁺	1070.01735	1070.02085	3.270	1070.02063	3.064
b4	427.21873	427.21761	-2.612	427.21882	0.221
b9	985.50229	*	*	985.50013	-2.197
b10	1100.52924	1100.52955	0.284	1100.52894	-0.270
b11	1199.59765	1199.59556	-1.744	*	*
b13	1423.68859	1423.68629	-1.617	1423.69240	2.675
b14	1552.73118	1552.73315	1.266	1552.72892	-1.459
b15	1667.75813	1667.76452	3.833	1667.75796	-0.101
b17	1893.85348	1893.85323	-0.135	1893.85550	1.064
b18	1992.92190	1992.91563	-3.146	*	*
y10	1154.53241	1154.53339	0.850	1154.53568	2.834
y9	1039.50547	1039.50585	0.370	1039.50557	0.101
y8	940.43705	940.43719	0.147	940.43851	1.551
y7	853.40502	853.40663	1.883	853.40490	-0.144
y6	716.34611	716.34712	1.408	716.34374	-3.310
y5	587.30352	587.30349	-0.048	587.30350	-0.031
y4	472.27658	472.27635	-0.476	472.27647	-0.222
y2	246.18122	246.18122	0.008	246.18122	0.008
b18 ²⁺	996.96459	996.96864	4.065	996.96916	4.586
y16 ²⁺	906.44583	906.44878	3.250	906.44336	-2.729
y17 ²⁺	970.96713	970.96955	2.492	970.97135	4.346
Absolute Error		1.645		1.627	
Standard deviation		1.328		1.510	

Table 4. 11: Peaks assignment for HC19 extracted fragmentation line. HC19: TPEVTCVVVDVSHEDPEVK. Internal calibration points are in bold. *: not observed. †: loss of water.

Species	Theoretical <i>m/z</i>	Sample at 4°C		Oxidised Sample	
		Observed <i>m/z</i>	ppm	Observed <i>m/z</i>	ppm
[M+H] ²⁺	839.40463	839.40678	2.562	839.40621	1.883
b3	448.19793	448.19651	-3.170	448.19804	0.244
b4	611.26126	611.26171	0.737	*	*
b5	710.32967	*	*	710.32993	0.362
b6	825.35662	*	*	825.35492	-2.055
b11	1346.61641	1346.61519	-0.908	1346.61647	0.043
b12	1460.65934	1460.65798	-0.931	1460.65567	-2.513
b13	1531.69645	1531.69673	0.180	1531.69638	-0.048
y11	1230.61133	1230.60635	-4.045	1230.61310	1.440
y10	1067.54800	1067.54778	-0.205	1067.54527	-2.556
y9	968.47958	968.47744	-2.215	968.47981	0.232
y8	853.45264	853.45353	1.041	853.45482	2.552
y7	796.43118	*	*	796.42864	-3.187
y6	697.36276	697.36280	0.051	697.36229	-0.680
y5	568.32017	568.32015	-0.037	568.32017	-0.002
y4	469.25176	469.25106	-1.486	469.25190	0.304
y3	332.19285	332.19265	-0.588	332.19259	-0.769
y2	218.14992	218.14992	0.009	218.14992	0.009
y12 ²⁺	708.84896	708.84822	-1.042	708.84723	-2.438
b4''	594.23471	594.23512	0.690	594.23491	0.336
b5''	693.30312	693.30398	1.235	693.30328	0.225
b6''	808.33007	808.33136	1.599	808.33054	0.585
b8''	964.41994	964.42122	1.322	964.42028	0.348
b9''	1093.46254	1093.46397	1.310	1093.45945	-2.824
b10''	1192.53095	1192.53329	1.961	1192.53312	1.818
Absolute Error		1.242		1.144	
Standard deviation		1.019		1.065	

Table 4. 12: Peaks assignment for HC20 extracted fragmentation line. HC20: FNWYVDGVEVHNAK. Internal calibration points are in bold. *: not observed. ': loss of water. '': loss of NH₃.

Species	Theoretical m/z	Sample at 4°C		Oxidised Sample	
		Observed m/z	ppm	Observed m/z	ppm
[M+H] ²⁺	904.50689	904.50849	1.774	904.50862	1.917
b9	948.58768	948.58427	-3.594	948.58799	0.328
b10	1076.64626	1076.64644	0.171	1076.64469	-1.455
b11	1191.67320	1191.67482	1.360	1191.67502	1.528
b12	1377.75251	1377.75282	0.223	1377.75475	1.624
b13	1490.83658	1490.83603	-0.366	1490.83633	-0.165
b14	1604.87950	1604.87949	-0.009	1604.87507	-2.763
b15	1661.90097	1661.89581	-3.103	1661.90594	2.992
y11	1310.68516	1310.68071	-3.396	1310.68893	2.876
y10	1209.63748	1209.63682	-0.548	1209.63581	-1.383
y9	1110.56907	1110.57120	1.919	1110.56926	0.172
y8	997.48500	997.48517	0.166	997.48468	-0.325
y7	860.42609	860.42610	0.008	*	*
y6	732.36752	732.36853	1.386	732.36745	-0.089
y5	617.34057	617.34057	-0.004	617.34055	-0.036
y4	431.26126	431.26152	0.605	431.26158	0.744
y3	318.17720	318.17716	-0.111	318.17739	0.612
y2	204.13427	204.13427	0.010	204.13427	0.010
b8'	793.51820	793.51838	0.224	793.51740	-1.011
b7'	680.43414	680.43434	0.296	680.43376	-0.556
b6'	581.36572	581.36594	0.371	581.36569	-0.059
b5'	480.31805	480.31795	-0.200	480.31832	0.571
b4'	367.23398	*	*	367.23452	1.465
Absolute Error		0.902		1.031	
Standard deviation		1.128		0.933	

Table 4. 13: Peaks assignment for HC23 extracted fragmentation line. HC23: VVSVLTVLHQDWLNGKK. Internal calibration points are in bold. *: not observed. †: loss of water.

Species	Theoretical m/z	Sample at 4°C		Oxidised Sample	
		Observed m/z	ppm	Observed m/z	ppm
[M+H] ⁺	838.50328	838.50334	0.071	838.50396	0.810
b7	692.39775	692.39752	-0.336	692.39747	-0.408
y6	654.38210	654.38228	0.271	654.38172	-0.585
y4	486.29223	486.29222	-0.010	486.29235	0.257
Absolute Error		0.172		0.515	
Standard deviation		0.135		0.206	

Table 4. 14: Peaks assignment for HC27 extracted fragmentation line. HC27: ALPAPIEK. Internal calibration points are in bold. *: not observed. †: loss of water.

Species	Theoretical <i>m/z</i>	Sample at 4°C		Oxidised Sample	
		Observed <i>m/z</i>	ppm	Observed <i>m/z</i>	ppm
[M+H] ²⁺	643.84060	643.84028	-0.500	643.84117	0.882
b3	355.16121	*	*	355.16121	-0.003
b7	831.4246958	831.42469	-0.007	*	*
y4	456.2565083	456.25651	0.004	456.25651	0.004
Absolute Error		0.170		0.296	
Standard deviation		0.233		0.414	

Table 4. 15: Peaks assignment for HC31 extracted fragmentation line. HC31: EPQVYTLPPSR. Internal calibration points are in bold. *: not observed. ′: loss of water.

Species	Theoretical <i>m/z</i>	Sample at 4°C		Oxidised Sample	
		Observed <i>m/z</i>	ppm	Observed <i>m/z</i>	ppm
[M+H] ⁺	605.31408	605.31406	-0.038	605.31503	1.515
b4	459.208555	459.20850	-0.120	459.20863	0.163
y4	490.2871397	490.28721	0.143	490.28664	-1.019
y3	361.2445466	361.24455	0.009	361.24481	0.729
Absolute Error		0.778		0.857	
Standard deviation		0.056		0.489	

Table 4. 16: Peaks assignment for HC32 extracted fragmentation line. HC32: DELTK. Internal calibration points are in bold. *: not observed. ′: loss of water.

Species	Theoretical <i>m/z</i>	Sample at 4°C		Oxidised Sample	
		Observed <i>m/z</i>	ppm	Observed <i>m/z</i>	ppm
[M+H] ⁺	1161.62962	1161.62969	0.060	1161.62971	0.077
y8	919.52812	919.52597	-2.333	*	*
y7	820.45970	820.45952	-0.221	820.45845	-1.525
y6	733.42767	733.42780	0.173	733.42746	-0.291
y5	620.34361	620.34425	1.033	620.34379	0.291
y4	519.29593	519.29592	-0.021	519.29589	-0.078
b6′′	626.31442	626.31490	0.771	626.31567	2.000
b8′	898.44511	898.44462	-0.550	898.44337	-1.941
b9′	997.51353	997.51272	-0.810	997.51325	-0.279
Absolute Error		0.778		0.857	
Standard deviation		0.056		0.489	

Table 4. 17: Peaks assignment for HC33 extracted fragmentation line. HC33: NQVSLTCLVK. Internal calibration points are in bold. *: not observed. ′: loss of water. ′′: loss of NH₃.

Species	Theoretical m/z	Sample at 4°C		Oxidised Sample	
		Observed m/z	ppm	Observed m/z	ppm
[M+H] ²⁺	937.46455	937.46664	2.230	937.46508	0.566
b4	397.20816	397.20816	-0.003	397.20754	-1.564
b15	1640.78427	*	*	1640.77981	-2.716
y14	1574.77370	*	*	1574.76926	-2.820
y12	1378.65252	1378.65278	0.186	1378.65186	-0.481
y11	1265.56846	1265.56262	-4.614	1265.56814	-0.252
y10	1150.54152	1150.54107	-0.388	1150.53831	-2.787
y9	1063.50949	*	*	1063.51181	2.183
y8	948.48255	948.48229	-0.269	948.48009	-2.588
y7	891.46108	*	*	891.46008	-1.123
y6	804.42905	804.42815	-1.122	804.42836	-0.861
y5	657.36064	657.36071	0.108	657.35929	-2.052
y4	510.29223	510.29255	0.637	510.29116	-2.087
y3	397.20816	397.20816	-0.003	397.20754	-1.564
y2	234.14483	*	*	234.14483	-0.011
y15 ²⁺	836.41687	836.41645	-0.503	836.41453	-2.799
b6'	591.35007	*	*	591.34898	-1.851
b7'	706.37702	*	*	706.37571	-1.851
b14''	1460.69439	*	*	1460.70005	3.876
Absolute Error		0.915		1.791	
Standard deviation		1.323		1.010	

Table 4. 18: Peaks assignment for HC35 extracted fragmentation line. HC35: TPPVLDSGDGSFFLYSK. Internal calibration points are in bold. *: not observed. ': loss of water.

Species	Theoretical m/z	Sample at 4°C		Oxidised Sample	
		Observed m/z	ppm	Observed m/z	ppm
[M+H] ⁺	660.35628	660.35624	-0.063	660.35715	1.315
b2	201.12337	*	*	201.12333	-0.193
b3	288.15540	288.15546	0.218	288.15536	-0.129
b5	488.27149	488.27163	0.287	488.27098	-1.044
y5	460.24019	460.24008	-0.238	460.23987	-0.694
y3	260.12410	260.12410	0.011	260.12401	-0.335
Absolute Error		0.164		0.618	
Standard deviation		0.107		0.442	

Table 4. 19: Peaks assignment for HC39 extracted fragmentation line. HC39: SLSLSPG. Internal calibration points are in bold. *: not observed. ': loss of water.

Species	Theoretical <i>m/z</i>	Sample at 4°C		Oxidised Sample	
		Observed <i>m/z</i>	ppm	Observed <i>m/z</i>	ppm
[M+2H] ²⁺	939.94673	<i>939.97064</i>	<i>25.438</i>	<i>939.97066</i>	<i>25.460</i>
b3	357.17686	*	*	357.17699	0.361
b4	488.21735	*	*	488.2171	-0.504
b5	589.26502	*	*	589.26402	-1.705
b6	717.32360	*	*	717.32131	-3.195
b7	804.35563	804.35487	-0.945	804.3542	-1.778
b11	1188.55652	1188.55580	-0.602	1188.55865	1.796
b12	1275.58854	1275.58519	-2.629	1275.59026	1.346
b13	1346.62566	1346.62526	-0.295	1346.62550	-0.117
b14	1433.65769	1433.65640	-0.897	1433.66059	2.026
b15	1532.72610	1532.72782	1.122	1532.72805	1.273
b16	1589.74756	1589.74801	0.281	1589.74501	-1.606
b17	1704.77451	1704.77499	0.284	1704.77381	-0.408
y15	1522.71660	1522.72067	2.674	1522.71484	-1.154
y14	1391.67611	*	*	1391.67611	-0.002
y12	1162.56986	1162.57444	3.943	1162.5718	1.672
y11	1075.53783	1075.54150	3.414	1075.53837	0.504
y10	978.48506	978.48372	-1.374		
y7	691.33694	691.33697	0.038	691.33682	-0.179
y6	604.30492	*	*	604.30567	1.249
y5	533.26780	533.26896	2.173	533.26675	-1.971
y4	446.23577	*	*	446.23602	0.554
y3	347.16736	347.16736	0.003	347.16736	0.003
Absolute Error		1.378		1.114	
Standard deviation		1.237		0.824	

Table 4. 20: Peaks assignment for LC01 extracted fragmentation line. LC01: DIQMTQSPSSLASVGD. Internal calibration points are in bold. *: not observed. †: loss of water. Italic: high ppm assignments due to overlapping of peaks.

Species	Theoretical <i>m/z</i>	Sample at 4°C		Oxidised Sample	
		Observed <i>m/z</i>	ppm	Observed <i>m/z</i>	ppm
[M+H] ⁺	721.39129	721.39093	-0.496	721.39132	0.045
b4	415.25511	415.25483	-0.677	415.25513	0.045
b5	575.28576	575.28510	-1.147	575.28511	-1.130
y4	521.27520	521.27574	1.045	521.27515	-0.087
y3	408.19113	408.19065	-1.179	408.19104	-0.224
y2	307.14345	307.14348	0.088	307.14345	-0.009
Absolute Error		0.772		0.256	
Standard deviation		0.394		0.396	

Table 4. 21: Peaks assignment for LC02 extracted fragmentation line. LC02: VTITCK. Internal calibration points are in bold. *: not observed. †: loss of water.

Species	Theoretical <i>m/z</i>	Sample at 4°C		Oxidised Sample	
		Observed <i>m/z</i>	ppm	Observed <i>m/z</i>	ppm
[M+H] ⁺	674.35801	674.35796	-0.079	674.35907	1.567
b5	500.24634	500.24645	0.225	500.24673	0.785
y5	603.32090	603.32101	0.183	603.32051	-0.645
y4	516.28887	516.28870	-0.331	*	*
y2	274.18737	*	*	274.18736	-0.022
Absolute Error		0.205		0.755	
Standard deviation		0.090		0.550	

Table 4. 22: Peaks assignment for LC03 extracted fragmentation line. LC03: ASQNV. Internal calibration points are in bold. *: not observed. †: loss of water.

Species	Theoretical <i>m/z</i>	Sample at 4°C		Oxidised Sample	
		Observed <i>m/z</i>	ppm	Observed <i>m/z</i>	ppm
[M+H] ²⁺	702.88534	702.88627	1.318	702.88536	0.023
b5	557.30821	557.30820	-0.017	*	*
b6	720.37154	720.37156	0.031	*	*
b7	848.43012	*	*	848.43149	1.620
b8	976.48869	976.48925	0.570	976.48858	-0.116
b9	1104.58366	1104.58364	-0.015	1104.58377	0.103
γ4	429.28199	429.28206	0.152	429.28034	-3.855
γ3	301.18703	301.18703	-0.006	301.18703	-0.006
γ10 ²⁺	602.82730	602.82713	-0.278	602.82603	-2.103
γ9 ²⁺	553.29309	553.29310	0.017	553.29276	-0.598
γ5'	539.33001	539.33087	1.599	539.32840	-2.981
γ7'	830.45191	*	*	830.45090	-1.221
b4'	353.21833	*	*	353.21845	0.334
b5'	539.29764	539.29747	-0.324	539.29732	-0.602
b6'	702.36097	702.36097	-0.005	702.35910	-2.667
b11 ²⁺	620.82730	620.82815	1.373	620.82566	-2.638
Absolute Error		0.439		1.348	
Standard deviation		0.569		1.247	

Table 4. 23: Peaks assignment for LC04 extracted fragmentation line. LC04: TVVAWYQQKPGK. Internal calibration points are in bold. *: not observed. ′: loss of water.

Species	Theoretical <i>m/z</i>	Sample at 4°C		Oxidised Sample	
		Observed <i>m/z</i>	ppm	Observed <i>m/z</i>	ppm
[M+H] ⁺	753.40021	753.40078	0.751	753.40028	0.090
b4	395.20374	395.20360	-0.365	395.20393	0.470
b6	579.28854	579.28866	0.213	579.28837	-0.288
γ5	515.29362	515.29358	-0.082	515.29373	0.209
γ3	359.20374	359.20384	0.266	359.20374	-0.012
Absolute Error		0.335		0.214	
Standard deviation		0.227		0.159	

Table 4. 24: Peaks assignment for LC07 extracted fragmentation line. LC07: HTGVPSR. Internal calibration points are in bold. *: not observed. ′: loss of water.

Species	Theoretical m/z	Sample at 4°C		Oxidised Sample	
		Observed m/z	ppm	Observed m/z	ppm
[M+H] ²⁺	973.51712	973.51669	-0.438	973.51811	1.021
b7	626.35080	626.35093	0.203	626.35028	-0.834
b9	886.50328	886.50618	3.271	886.50326	-0.023
b10	1033.57169	1033.57441	2.627	1033.57521	3.401
b14	1429.73619	1429.73883	1.844	1429.73497	-0.856
b16	1686.83736	*	*	1686.83938	1.195
b17	1799.92143	1799.92205	0.346	1799.92140	-0.016
y14	1603.83664	1603.83080	-3.639	1603.84100	2.721
y12	1419.75184	*	*	1419.75283	0.695
y11	1320.68343	1320.67897	-3.377	1320.68594	1.901
y10	1173.61502	1173.61212	-2.467	1173.61234	-2.280
y9	1060.53095	1060.52923	-1.623	1060.53098	0.027
y8	913.46254	913.45916	-3.698	913.46220	-0.370
y7	816.40977	816.40763	-2.626	816.40740	-2.908
y6	719.35701	719.35517	-2.558	719.35683	-0.250
y5	632.32498	632.32288	-3.324	632.32400	-1.553
y4	517.29804	517.29757	-0.906	517.29703	-1.950
y3	388.25545	388.25544	-0.015	388.25545	0.011
y15 ²⁺	837.94051	837.93786	-3.166	837.93847	-2.438
y14 ²⁺	802.42196	802.42004	-2.388	802.42374	2.223
y16 ²⁺	873.45907	873.45863	-0.504	873.45785	-1.397
b4'	325.18703	*	*	325.18807	3.193
b8'	755.40865	755.40748	-1.551	755.40796	-0.916
Absolute Error		2.054		1.337	
Standard deviation		1.247		1.032	

Table 4. 25: Peaks assignment for LC11 extracted fragmentation line. LC11: TVAAPSVFIFPPSDEQLK. Internal calibration points are in bold. *: not observed. ': loss of water.

Species	Theoretical m/z	Sample at 4°C		Oxidised Sample	
		Observed m/z	ppm	Observed m/z	ppm
[M+H] ²⁺	899.45125	899.45151	0.285	899.45303	1.975
b11	1102.55612	1102.55662	0.452	1102.55761	1.350
b12	1216.59905	1216.60008	0.848	1216.60348	3.642
b13	1363.66746	1363.66623	-0.904	1363.66719	-0.200
b14	1526.73079	1526.72575	-3.302	1526.72748	-2.169
y6	810.38931	810.38748	-2.262	810.38955	0.292
y5	696.34639	696.34513	-1.804	696.34589	-0.712
y4	582.30346	582.30315	-0.530	582.30338	-0.135
y3	435.23504	435.23392	-2.584	435.23531	0.610
y2	272.17172	272.17171	-0.022	272.17172	0.015
Absolute Error		1.299		1.110	
Standard deviation		1.057		1.113	

Table 4. 26: Peaks assignment for LC12 extracted fragmentation line. LC12: SGTASVCLLNFFYPR. Internal calibration points are in bold. *: not observed. ‘: loss of water.

Species	Theoretical m/z	Sample at 4°C		Oxidised Sample	
		Observed m/z	ppm	Observed m/z	ppm
[M+H] ²⁺	1068.48800	1068.49033	2.176	1068.48795	-0.048
b8	785.37881	*	*	785.37816	-0.828
b12	1243.55493	1243.55942	3.607	*	*
b14	1429.65538	1429.65594	0.394	1429.65561	0.163
b15	1530.70306	*	*	1530.70500	1.272
b16	1659.74565	1659.74546	-0.114	1659.74947	2.302
b17	1787.80423	*	*	1787.79971	-2.526
b18	1902.83117	1902.82526	-3.104	1902.83091	-0.136
y15	1623.70926	1623.71400	2.917	1623.71405	2.948
y14	1495.65069	1495.65610	3.620	1495.65094	0.170
y13	1408.61866	*	*	1408.62495	4.467
y8	893.42107	893.42069	-0.422	*	*
y6	707.32062	707.32076	0.191	707.31974	-1.251
y4	477.23035	*	*	477.22988	-0.991
y2	234.14483	*	*	234.14483	-0.011
y18 ²⁺	961.44032	961.44133	1.049	961.43903	-1.344
b9''	882.39519	*	*	882.39604	0.967
Absolute Error		1.838		1.425	
Standard deviation		1.452		1.319	

Table 4. 27: Peaks assignment for LC15 extracted fragmentation line. LC15: VDNALQSGNSQESVTEQDSK. Internal calibration points are in bold. *: not observed. ‘: loss of water. ‘’: loss of NH₃.

Species	Theoretical m/z	Sample at 4°C		Oxidised Sample	
		Observed m/z	ppm	Observed m/z	ppm
[M+H] ²⁺	751.88286	751.88405	1.582	751.88161	-1.664
b2	203.06625	*	*	203.06663	1.882
b7	754.32538	754.32580	0.563	754.32536	-0.021
b10	1055.48915	1055.49090	1.661	1055.48921	0.060
b11	1156.53682	1156.53647	-0.307	1156.53785	0.886
b12	1269.62089	1269.62049	-0.314	1269.62122	0.261
b13	1356.65292	1356.65017	-2.025	1356.65286	-0.042
y8	836.47237	836.47269	0.374	836.47263	0.300
y7	749.44035	749.43945	-1.191	749.43945	-1.194
y6	662.40832	*	*	662.40658	-2.618
y5	561.36064	561.35959	-1.867	*	*
y4	448.27658	448.27584	-1.649	448.27581	-1.715
y3	347.22890	347.22900	0.298	*	*
y2	234.14483	234.14481	-0.096	234.14483	-0.011
Absolute Error		0.994		0.888	
Standard deviation		0.700		0.867	

Table 4. 28: Peaks assignment for LC16 extracted fragmentation line. LC16: DSTYLSSTLTLSK. Internal calibration points are in bold. *: not observed. †: loss of water.

Species	Theoretical m/z	Sample at 4°C		Oxidised Sample	
		Observed m/z	ppm	Observed m/z	ppm
[M+H] ⁺	625.28278	625.28115	-2.611	625.28216	-0.996
b4	479.17725	479.17727	0.032	479.17726	0.011
y3	439.21873	439.21872	-0.013	439.21872	-0.013
Absolute Error		0.885		0.340	
Standard deviation		1.220		0.464	

Table 4. 29: Peaks assignment for LC17 extracted fragmentation line. LC17: ADYEK. Internal calibration points are in bold. *: not observed. †: loss of water.

Species	Theoretical m/z	Sample at 4°C		Oxidised Sample	
		Observed m/z	ppm	Observed m/z	ppm
[M+H] ²⁺	938.46710	938.46911	2.138	938.46971	2.784
b5	623.24937	*	*	623.24980	0.683
b8	960.42438	960.42443	0.053	960.42395	-0.446
b9	1088.48296	1088.48328	0.297	1088.48517	2.034
b10	1145.50442	1145.49994	-3.913	1145.50596	1.344
b11	1258.58848	1258.58832	-0.130	1258.59151	2.404
b12	1345.62051	1345.62005	-0.344	1345.62031	-0.150
b13	1432.65254	1432.64982	-1.899	1432.65327	0.509
b15	1628.77372	1628.77386	0.087	1628.77369	-0.017
y12	1253.68483	1253.68090	-3.135	1253.68529	0.370
y11	1154.61641	1154.61576	-0.565	1154.61519	-1.059
y10	1053.56873	1053.56775	-0.934	1053.56713	-1.523
y8	788.45124	788.45179	0.691	788.45155	0.387
y6	618.34572	618.34652	1.298	618.34572	0.005
y5	531.31369	531.31393	0.454	531.31362	-0.129
y4	444.28166	444.28166	-0.001	444.28159	-0.158
y2	248.16048	*	*	248.16048	-0.011
y15 ²⁺	807.40123	807.39896	-2.811	807.39975	-1.833
y13''	1365.70087	*	*	1365.69933	-1.125
Absolute Error		2.054		1.337	
Standard deviation		1.247		1.032	

Table 4. 30: Peaks assignment for LC19 extracted fragmentation line. LC19: VYACEVTHQGLSSPVTK. Internal calibration points are in bold. *: not observed. ‘: loss of water. ‘’: loss of NH₃.

CHAPTER 5.

Conclusion and Outlook

Conclusion and outlook

This thesis contributes to the analysis of post translational modifications in high resolution instruments.

Dissociation with collision gas, electrons, and photons were investigated to fragment phosphopeptides in chapter 2. The various dissociation mechanisms produced various fragmentation profiles, which could give complementary information in the characterisation of phosphopeptides. The results of the comparison of the three phosphopeptides were intriguing. Further investigations with more phosphopeptides, would permit to highlight the trends, and would result in more extensive conclusions.

Methodologies to identify and localise PTMs in complex mixtures using 2DMS were developed.

In chapter 3, the extraction of phosphate loss lines quickly identified the phosphopeptides in the mixture. The further analysis of their extracted precursor lines permitted to characterise the peptides and localise the phosphorylation. This method is not limited to the analysis of phosphorylation but could be used for the analysis of all labile modifications or analytes which produce specific neutral losses.

The resonance of phosphate vibrational modes with IR radiation, resulting in the higher fragmentation efficiency of phosphopeptides compared to their unphosphorylated counterpart, directed the choice for an IRMPD dissociation. However, the methodology is also transferable to other dissociation techniques, with selective cleavage at the labile modifications.

In chapter 4, a stressed sample was compared to a control sample, using 2DMS analysis. The comparison of the 2DMS spectra highlighted the difference between the two samples, and the extraction of horizontal lines allowed the identification and localisation of PTMs. This methodology is especially interesting in the analysis of therapeutic

antibodies, and could be implemented, with automation, and shorter 2DMS run, as a quality control (QC) analysis to monitor the critical quality attributes (CQAs) while still retaining the information on the full samples. Shorter 2DMS run could be possible with the use of UVPD dissociation instead of IRMPD, as the irradiation time is higher with IRMPD and double the experiment time. A shorter transient could also be recorded, or a shorter number of scans could be acquired, as the high resolution would not be necessary in a QC workflow.

This analysis could also be developed for N-glycan analysis, after deglycosylation, labelling and purification of the N-released glycans. No need for high resolution would be needed as the sample would be less complex, and 10 minutes run should be enough to record the glycosylation profile.

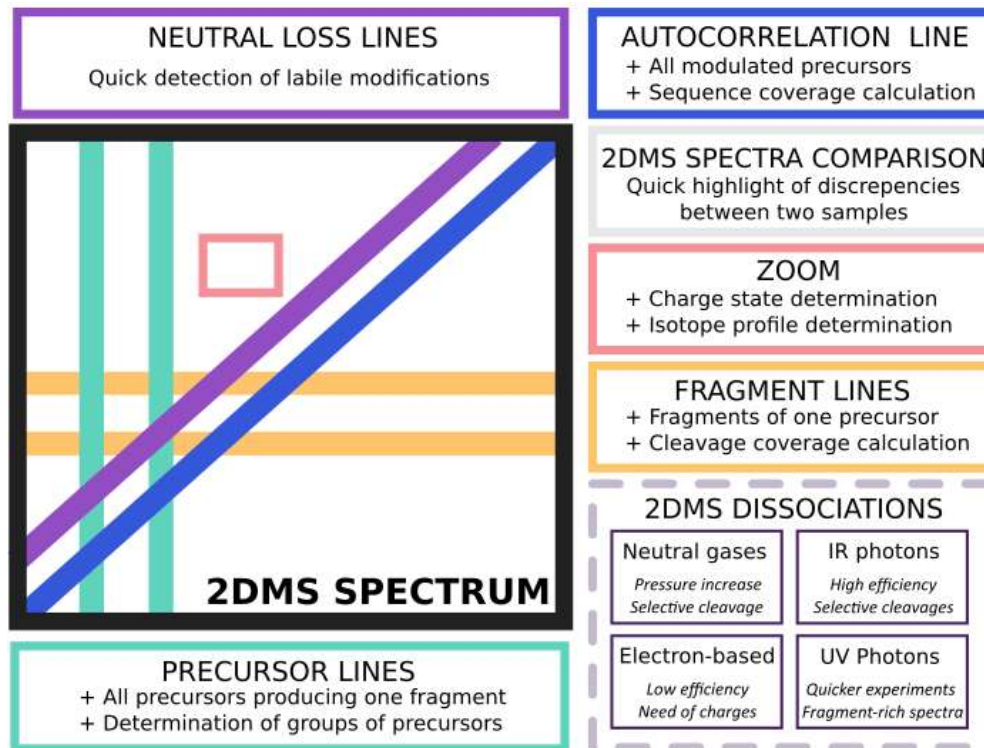


Figure 5. 1: Summary of 2DMS specifics useful for the analysis of proteomics samples.

The future of 2DMS

Moving forward in two-dimensional mass spectrometry developments, recent works to improve the resolution were completed independently (non-uniform sampling, narrow band 2DMS, phase correction, SANE algorithm, and 3D peak picking) and could be implemented in the same experiment. UVPD was implemented in the 2DMS workflow but could be further used. This dissociation technique has the advantage of quick fragmentation event, reducing the duty time of 2DMS without reducing the resolution of the experiment and still resulting in fragment-rich spectra. UVPD scores higher fragmentation efficiency than ECD, and higher cleavage coverage than IRMPD; therefore, UVPD 2DMS is extremely promising for top-down MS/2DMS experiments.

Two-dimensional mass spectrometry used to be underdeveloped, difficult to implement, and the obtained data hard to analyse. But the development of computers as well as software to visualise and analyse the data, the writing of algorithms no denoise and peak picked the data, the improvement of the resolution of the experiment, and the method development of the technique in the last decade make it now an alternative tool in the analysis of complex mixtures. Further efforts could be done to transfer the method to industrial laboratories, according to their needs (full automation of the data analysis, detection of discrepancies between two samples), or to transfer the method to other mass spectrometry instrument.

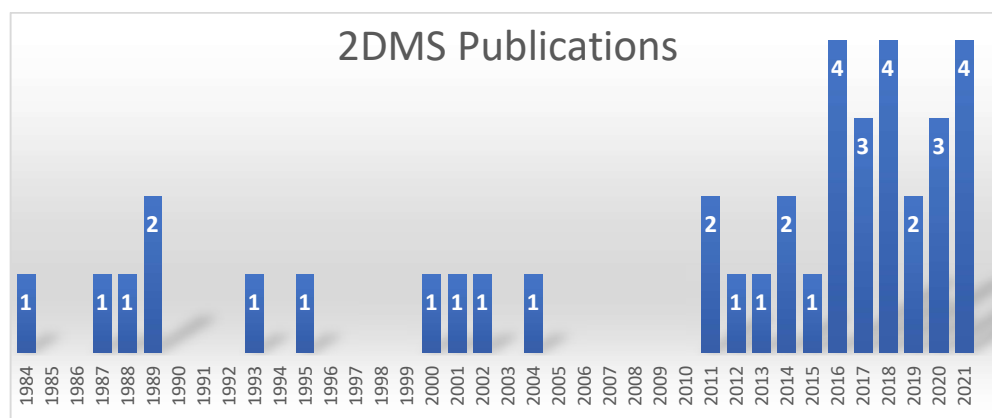


Figure 5. 2: Number of 2DMS publications.